CANADIAN THESES

THÈSES CANADIENNES

NOTICE

The quality of this microfiche is heavily dependent upon the quality of the original thesis submitted for microfilming. Every effort has been made to ensure the highest quality of reproduction possible.

If pages are missing, contact the university which granted the degree.

Some pages may have indistinct print especially if the original pages were typed with a poor typewriter ribbon or if the university sent us an inferior photocopy.

Previously copyrighted materials (journal articles, published tests, etc.) are not filmed.

Reproduction in full or in part of this film is governed by the Canadian Copyright Act, R.S.C. 1970, c. C-30.

AVIS

La qualité de cette microfiche dépend grandement de la qualité de la thèse soumise au microfilmage. Nous avons tout fait pour assurer une qualité supérieure de reproduction.

S'il manque des pages, veuillez communiquer avec l'université qui a conféré le grade.

La qualité d'impression de certaines pages peut laisser à désirer, surtout si les pages originales ont été dactylographiées à l'aide d'un ruban usé ou si l'université nous a fait parvenir une photocopie de qualité inférieure.

Les documents qui font déjà l'objet d'un droit d'auteur (articles de revue, examens publiés, etc.) ne sont pas microfilmés.

La reproduction, même partielle, de ce microfilm est soumise à la Loi canadienne sur le droit d'auteur, SRC 1970, c. C-30.

THIS DISSERTATION HAS BEEN MICROFILMED EXACTLY AS RECEIVED

LA THÈSE A ÉTÉ MICROFILMÉE TELLE QUE NOUS L'AVONS REÇUE

Canada

RATE DEPENDENT CONSTITUTIVE EQUATIONS OF CYCLIC SOFTENING AND HARDENING

By

J.S. Mshana, B.Sc.(Mech. Eng.) (Nairobi),
M.A.Sc.(Mech. Eng.) (Ottawa)

A thesis submitted to the School of Graduate Studies of the University of Ottawa in partial fulfillment of the requirements for the degree of

DOCTOR OF PHILOSOPHY

IN

MECHANICAL ENGINEERING

Department of Mechanical Engineering
University of Ottawa
May 1986

ISBN 0-315-33301-4

RATE DEPENDENT CONSTITUTIVE EQUATIONS OF CYCLIC SOFTENING AND HARDENING

PREFACE

Rate dependent plastic deformation of solids is a thermally activated process: plastic flow results from the movement of flow units over energy barriers. Accordingly, the determination of the plastic strain rate is based on deformation kinetics and on the transition state theory of rate processes. The application of these concepts to describe plastic flow during monotonic loading is now firmly established. The present study demonstrates the application of the theory to describe cyclic plastic deformation behavior.

Constitutive equations of strain and load controlled cyclic deformation were derived from the rate theory. It was assumed in the analysis that during cyclic plastic deformation the material structural characteristics (activation volume, activation free energy, and mobile dislocation density or flow units) remain constant and that the internal stress increases linearly with plastic strain. The study showed that over the high stress and low temperature range where the description of plastic flow in cyclic deformation can be approximated with activation over two consecutive energy barriers, strain controlled cyclic deformation is well related to stress relaxation while load controlled cyclic deformation is essentially a creep process. The constitutive equations described well the cyclic deformation behavior of a near eutectoid, Zn-Al alloy. The material structural characteristics (activation volume and activation free energy) determined

from the analysis of stress relaxation, creep, and cyclic loading experimental results were identical, leading to the conclusion that during cyclic loading the variations in the material structural characteristics were insignificant and that stress relaxation, creep, and cyclic deformation were controlled by the same dislocation mechanism. Subsequently, it was shown that within the high stress and low temperature range, the material structural characteristics determined from the analysis of stress relaxation experimental results can be used to predict the cyclic deformation behavior of the alloy using the constitutive equations developed in this report.

Previous experiments have shown that for many metals and alloys the dislocation- obstacle structure that produces the internal stress often changes upon cyclic loading: the material may thus soften and/or harden during cyclic loading. It was considered in the present study that within a high stress and low temperature range the rate of plastic flow during softening and hardening can be approximated with activation over single energy barriers and that the material structural characteristics were constant during cyclic deformation. In the analysis of the deformation behavior it was assumed that during hardening the internal stress increases linearly with plastic strain and that for the softening process the internal stress decreases linearly with time. When the internal stress increases upon cyclic loading, the study showed that the rate of cyclic strain accumulation and the accumulated cyclic strain were smaller than the corresponding creep (at a stress equal to the peak stress during cyclic loading) strain and strain rate. For a simple model where the material hardens during the loading part of the cycle and softens upon unloading, the analysis

showed that the rate of cyclic strain accumulation and the accumulated cyclic strain were larger than the corresponding creep (at peak stress) strain and strain rate. The increase in creep rate under cyclic loading was thus attributed to the softening that results from cyclic loading. Because the predicted cyclic deformation behavior with alternating softening and hardening is similar to that observed experimentally in many (engineering) metals and alloys, it is anticipated that the analytical model can be used to evaluate the accumulated damage (in highly stressed machine components); an essential data for design and lifetime determination of structural components.

ACKNOWLEDGEMENTS

The author wishes to express his deep sense of gratitude to his advisor, Dr. A.S. Krausz, not only for the guidance, encouragement, and critical suggestions, but also for the teaching of the art of carrying out a research project. The helpful discussions with members of the Advisory Committee: Dr. S.C. Cheng, Dr. R.C. Flanagan, and Dr. W. Wallace are very much appreciated.

Sincere thanks are due to all the staff members of the Department of Mechanical Engineering, especially to Mr. D. Seaman and to Mr. G. Toth for their help in the solution of administrative and technical problems.

The author is indebted to his employer, the University of Dar-es-Salaam, for granting him study leave, to Prof. A.S. Krausz for providing generous financial assistance from his NSERC grant, and to the German Academic Exchange Service for financial support.

Finally, the author wishes to thank members of his family for their support and encouragement. In particular, my thanks go to my wife Marietha, our son Munga, and our daughter Kithio: they have been both tolerant and sympathetic during the three years that it has taken to carry out this research project and without their support it could never have been completed.

TABLE OF CONTENTS

PAGE

PAGE

LIST OF FIGURES

PAGE

PAGE

PAGE

PAGE

LIST OF TABLES

NOMENCLATURE

a	cross section area
b	Burger's Vector
h	Planck's constant
k	Boltzmann constant
ℓ	distance moved after activation or gage length or mean free length of dislocation
m	number of cycles or mean
p	cycle period
t	deformation time
v	dislocation velocity
y	defined integral
A	constant
B	dislocation multiplication coefficient
C	softening coefficient or integration constant
E	Young's Modulus or energy
E^1	combined elastic modulus
F	flow over an energy barrier
G	Gibb's free energy
H	work hardening coefficient
K	stiffness
M	Taylor orientation factor
N	number of cycles, degrees of freedom
P	load
Q	partition function
S	nominal cross-head speed
T	absolute temperature

V	activation volume
W	work

Greek Letters

∂	partial derivative
δ	contribution to the deformation after activation
ε	normal strain
η	constant of integration
κ	transmission coefficient
ρ	dislocation density
σ	normal stress
ξ	defined integral
τ	shear stress
ϕ	angle (radians)
Δ	change of
π	constant
$\sum$	summation
Ψ	defined integral
k	rate constant

SUPERSCRIPTS

$\cdot$	rate
$\neq$ or $\ddagger$	activation
$-$	average
$*$	transition
0	initial

SUBSCRIPTS

a	applied
b	backward
e	elastic
eff	effective
exp	experimental
f	forward
h	hardening
i	internal
i,m	internal stress at m^{th} cycle
m	machine, mean
max	maximum
min	minimum
o	initial
p	plastic or product
p,c	complementary function
p,0	constant
r	reactant or range
s	softening
t	total
1,2,i,j	index
I,II	region I or II

Note: The rate constants, activation energies, are labelled as, for example, ${}_ik^j$ or ${}^jk_i$, where i represents the reactant state and j the product state. The numerals i and j are arranged as ${}_ik^j$ in the case of forward activation and as ${}^jk_i$ in the case of backward activation.

CHAPTER 1

INTRODUCTION

Progress in the sciences has been made through faltering steps, "accidents", humble attempts at a specific task, not through grandiose experiments designed to solve all the riddles of the universe with one fell swoop. Historically, men and women have formulated laws on the basis of the available experimental evidence. Further experiments are then conducted to test such laws outside of their established realm of validity. The results of such experiments then serve to investigate further the domain of validity of such laws and, where appropriate, to construct others which are more encompassing.

(K.C. Valanis, Int. J. Solids Structures, Vol. 17, pp. 249-265, 1981)

Modern machinery is required to perform reliably under a variety of operating conditions. Power generation equipment such as nuclear reactors and steam and gas turbines have to respond quickly to the changing power demands of our technological society; aircraft structures and jet engines are to perform reliably under frequent take-off, cruise, and landing operations. These are but typical examples of machinery in which the structural components are subjected to cyclic loading. Over the lifetime of the machinery, the components are subjected to many cycles of stress (or strain). Each cycle often causes a permanent damage (plastic deformation) in the components. Design of critically stressed components, therefore, requires the evaluation of stresses and strains and the assessment of the accumulated damage by following through the operating history of the components. During the projected lifetime of the machine, the total accumulated damage in highly stressed components will have to be less than the damage which will lead to mechanical failure. Consequently, the determination of time and/or cycle dependence of cyclic deformation behavior and its subsequent application in design and lifetime determination is indispensable.

The development of materials and the subsequent design of the components for such applications is a formidable task. The difficulty of the problem is primarily due to the fact that the deformation behavior of materials under cyclic loading conditions is often different from that under monotonic stress and cannot be predicted by simple extrapolation of data obtained from conventional tests: tensile, creep, and stress relaxation tests [1-8]*. The cyclic stress leads to complex submicroscopical and microscopical changes which are of a cumulative and irreversible type [7,9]. These changes manifest themselves by changes in measurable mechanical, electrical, magnetical, and other properties. For machine component and structural design purposes, the changes in mechanical properties are of utmost concern. The yield stress and the resistance to plastic deformation (internal stress) may vary in a complex manner. When plastic deformation leads to an increase in internal stress, the phenomenon is referred to as **hardening** while if the internal stress decreases, it is known as **softening.** The later effect is of particular interest because it is associated with an increase in the rate of cyclic strain accumulation which leads to premature failure of structural components. Whether the material will harden and/or soften upon cyclic loading depends on the material, its initial state, the magnitude and history of the cyclic strain (or load), and the test temperature.

There have been three approaches to the problem of deformation behavior under cyclic loading. In the first approach, testing methods simulating

---

* Numbers in brackets indicate references listed at the end of the thesis.

stressing conditions actually encountered in service are adopted and test data directly useful for design purposes are obtained for specific materials [9,10]. Nevertheless, the wide diversity of service conditions and the need for material properties for long service times usually eliminate the possibility of obtaining design data under conditions that duplicate service lives. In the second approach, the basic aspects of the cyclic stress deformation are investigated. The mechanisms of cyclic plastic deformation are studied from a metallurgical standpoint [3,5,7,9,11-18], for instance, mechanism of slip, dislocation movements, and other changes in the microstructure during cyclic deformation. The information thus obtained is extremely useful both for materials development and manufacturing processes. The third approach is the exploration of gross deformation behavior during cyclic loading. The objective of these studies [1,6,8,10,19-26] and of the present thesis is to formulate the constitutive equations; the mathematical description of the cyclic deformation behavior. When the material response to cyclic loading after long service times cannot be determined accurately from the testing methods, designs of highly reliable structures and components are usually based on predictions of mathematical models.

Constitutive equations describing the material behavior during cyclic loading have often been empirical or phenomenological [1,6,8,10,19-26]. Most of these relations [1,2,8,10,19-22] were derived from the continuum theory of plasticity and utilize the so called power creep law. For other relationships [23-26] various forms of viscoplasticity theory have been used to describe cyclic plastic deformation. However, despite some success, these empirical constitutive equations cannot, as a rule, be identified with the basic material parameters and in most cases they cannot represent the

effect of the important service and manufacturing parameter - the temperature. In addition, they do not refer to physical processes of deformation that occur (within the crystal) at the atomic level.

A sound constitutive equation must be based on a rigorously derived theory, and conform to experimental observations. It was shown by Krausz and Eyring [27] and others [28-30] that plastic flow and chemical reactions are essentially identical processes, since both are solely the consequence of breaking and establishing of atomic bonds. Because of this fundamental and general fact, plastic deformation was considered as a chemical reaction in which the composition remains unchanged but the atomic configuration changes. Subsequently, chemical kinetics, based on statistical mechanics was widely utilized [27-36] to describe plastic flow during monotonic loading. The present thesis demonstrates the application of the theory of deformation kinetics to describe cyclic plastic deformation behavior. It will be shown from the theory and experimental results that under certain physically reasonable conditions, the constitutive parameters determined from the analysis of stress relaxation test results can be used to predict the cyclic deformation behavior. The application of the theory to describe cyclic deformation behavior with increasing internal stress and with both increasing and decreasing internal stress will also be discussed.

The experimental part of the thesis describes the cyclic deformation behavior of a commercial grade, near eutectoid Zinc-Aluminum alloy. The alloy was selected because it exhibits [34,35] stress relaxation behavior to the extent of complete unloading, even at room temperature. Its extreme deformation behavior lends itself to illustrate the application of

deformation kinetics to describe cyclic plastic deformation and to the investigation of the rate controlling mechanism.

In this chapter, the theory of deformation kinetics and the conventional testing methods are reviewed while in the subsequent chapters, the application of the theory to describe cyclic deformation behavior will be discussed.

1.1 THEORY OF DEFORMATION KINETICS

1.1.1 Introduction to Deformation Kinetics

Atoms in condensed phases occupy equilibrium positions and are vibrating about the minimum of the free energy wells (Fig. 1.1). When stress is applied, the atoms are displaced elastically from their equilibrium position. The potential energy of the system is increased and stored in a reversible manner. On the removal of the stress, the atoms move back to vibrate about their equilibrium position, and a corresponding quantity of energy is released. Superimposed on this elastic deformation is the time-dependent, thermally activated plastic deformation. Plastic flow occurs when the atoms move under the combined effect of the applied stress and thermal vibrations into a new equilibrium valley while breaking the previous bonds and establishing new bonds. The higher the temperature, the greater the vibrational amplitude, and the greater the rate of moving into a new equilibrium atomic configuration. When the stress is removed the atoms remain in the new equilibrium valley, and a permanent local plastic deformation results.

The plastic flow of any material is, by the nature of the process, solely the consequence of breaking atomic bonds and establishing new bonds. The macroscopically observed shape change is the sum of the individual atomic events. Because of this fundamental and general fact the process of

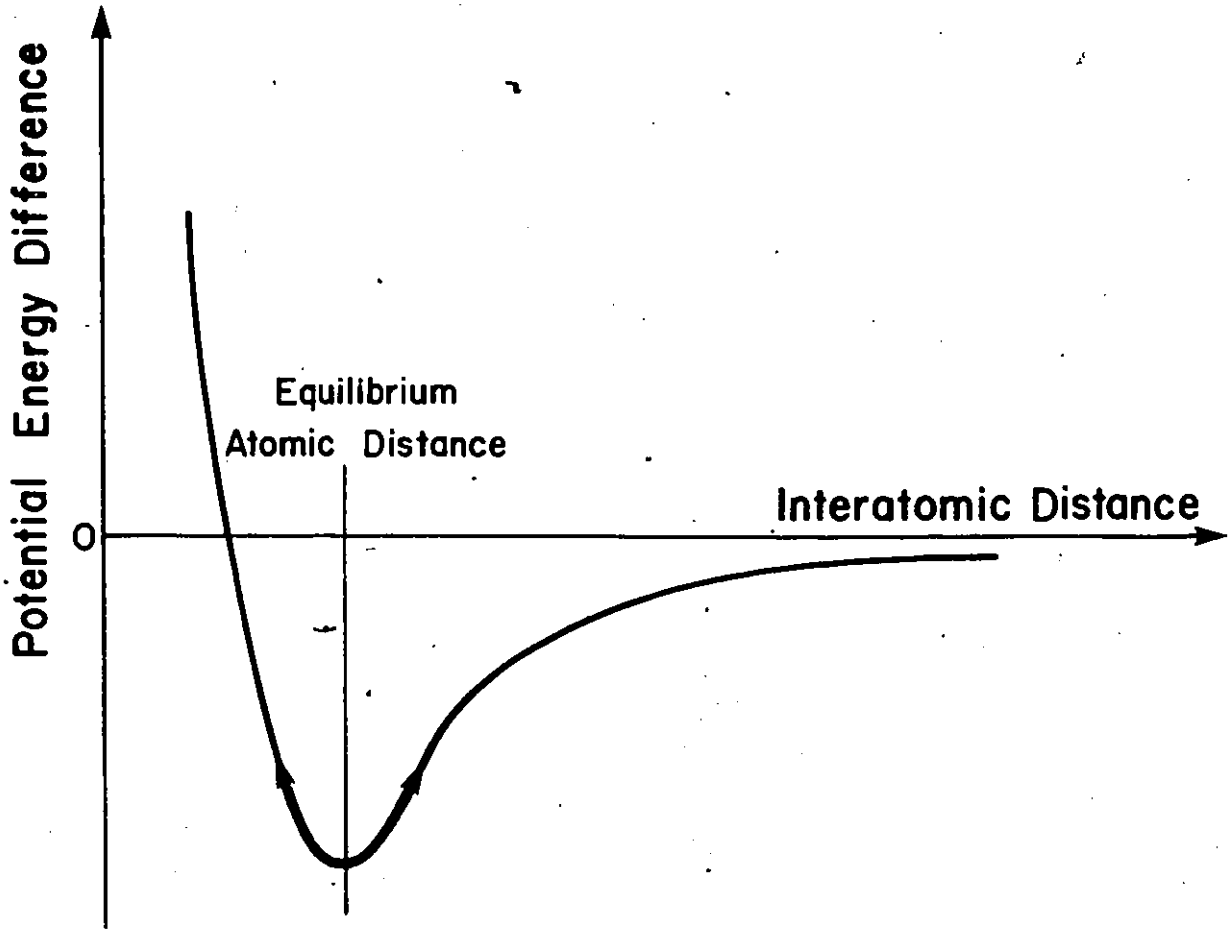

Figure 1.1. The potential energy versus atomic-distance relation for a diatomic molecule. In a solid the potential-energy well is repeated at each atom. The figure also illustrates that with the change of atomic distance the potential energy always increases.

plastic flow in crystalline materials and in polymers was considered as a chemical reaction in which the composition remains constant but the bond structure of the molecules changes. Consequently, plastic deformation is similar to isomerization of a giant molecule the specimen. Deformation kinetics is, therefore, identical to chemical reaction kinetics.

1.1.2 Deformation of Crystalline Materials

The most general case of plastic deformation occurs in polycrystalline specimens in which slip takes place over several slip systems. Theoretical considerations showed that glide cannot occur by a rigid body displacement of one part of the specimen over the other. The process occurs stepwise, by consecutive bond breaking and establishment events. Orowan [37], Taylor [38], and Polanyi [39] suggested that the linear atomic disorders, dislocations, weaken the crystal by introducing loose-structured atomic groups. Subsequently, the concept of dislocations was used to explain the discrepancy between the predicted (high) [40] and the observed (low) yield stress of metals. The effect of an applied shear stress on potential energy along a dislocation slip plane is shown in Fig. 1.2. It is clear from the schematic diagram that the energy barrier is low at the dislocation core. The barrier is lowered further and biased by the applied shear stress, and thence bond breaking takes place under the effect of a small thermal energy increase with high probability. The random thermal fluctuations, therefore, facilitate the displacement of the dislocations in the direction favored by the shear stress. The macroscopically observed plastic strain is the sum of the individual dislocation movements. Extensive studies on the properties

of dislocations have been carried out [41-46] and numerous observations have been made [47].

The plastic strain rate, $\dot{\varepsilon}_p$, resulting from the displacement of dislocations moving at an average velocity $\bar{v}$ is evaluated from Orowan's equation [48] as

$$\dot{\varepsilon}_p = \left(\frac{1}{M}\right) b\rho_t \bar{v} \qquad (1.1)$$

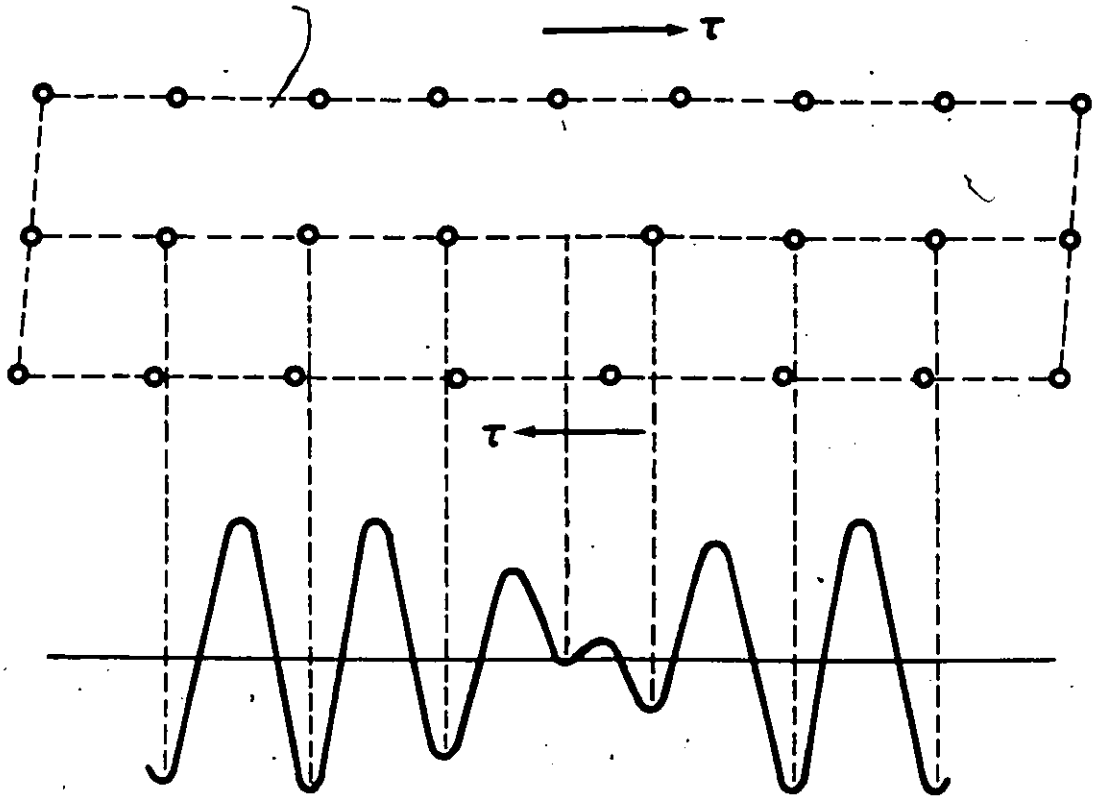

Figure 1.2. The effect of shear stress on the potential energy across an edge dislocation [38]. Bond breaking and establishment is biased by the stress so that the hole in the core of the dislocation line moves to the right.

where M is the Taylor orientation factor relating the tensile stress σ and tensile strain ε to the shear stress $\tau(=\sigma/M)$ and shear strain $\gamma(=M\varepsilon)$ resolved in the rate-controlling slip system, b is the Burger's vector and ρ_t is the mobile dislocation density (dislocations per unit area). The Taylor orientation factor for polycrystalline materials varies between 2 to 4. The limiting velocity of a dislocation is the speed of transverse - sound - waves [46]. Within the usual experimental stress and temperature ranges, the motion of dislocations occur at a much lower rate because it is impeded by obstacles. A dislocation overcomes an obstacle when it has acquired enough energy from the combined effect of the applied stress and the thermal energy (random thermal fluctuations).

Following Seeger [49], two types of obstacles to dislocation motion are usually considered: those that raise long-range stress fields, and those that raise short-range stress fields. For example, clusters of point defects are a source of a relatively short-range stress field, in comparison with the stress field of a dislocation pile-up which is long-range. It is generally considered [51-54] that the large amount of energy required to overcome the long-range obstacles can only be acquired through the applied stress. The random thermal fluctuations or thermal activations can assist dislocations in overcoming the short-range obstacles. The applied stress is in equilibrium with the internal stresses. It follows, therefore, that the applied stress, τ_a, is the sum of two components: the internal (or athermal) stress, τ_i, that is needed to overcome long-range obstacles, and the effective (or thermal) stress, τ_{eff}, that is needed to overcome short-range

obstacles. The athermal stress depends weakly on the temperature through the elastic modulus, and the thermal stress depends strongly on the strain rate and temperature.

Fig. 1.3 illustrates some of the common thermally activated dislocation motion mechanisms. Obstacles to the motion of dislocation in the slip plane are Peierls-Nabarro stress field (periodic stress field of the lattice) (Fig. 1.3a), forest dislocations (Fig. 1.3b, dislocations threading the glide plane), and the motion of jogs in screw dislocations (Fig. 1.3c). Mechanisms that produce motion of dislocations out of the slip plane are: cross-slip of extended screw dislocations (Fig. 1.3d), and the climb of edge dislocations (Fig. 1.3e).

The rate of plastic flow caused by the thermally activated motion of dislocations over the obstacles is expressed as [48].

$$\dot{\varepsilon}_p = \left(\frac{1}{M}\right) b \rho_t \bar{v} = \left(\frac{1}{M}\right) b \rho_t \bar{\ell} k \qquad (1.2)$$

where $\bar{\ell}$ is the average distance travelled by the dislocation between obstacles, and k is the net rate of activation over the velocity-limiting energy barrier. The rate of activation k depends on the kinetics of the process, and is usually a combination of elementary rate constants. Each rate constant is obtained from the properties of the energy barrier, according to the transition state theory.

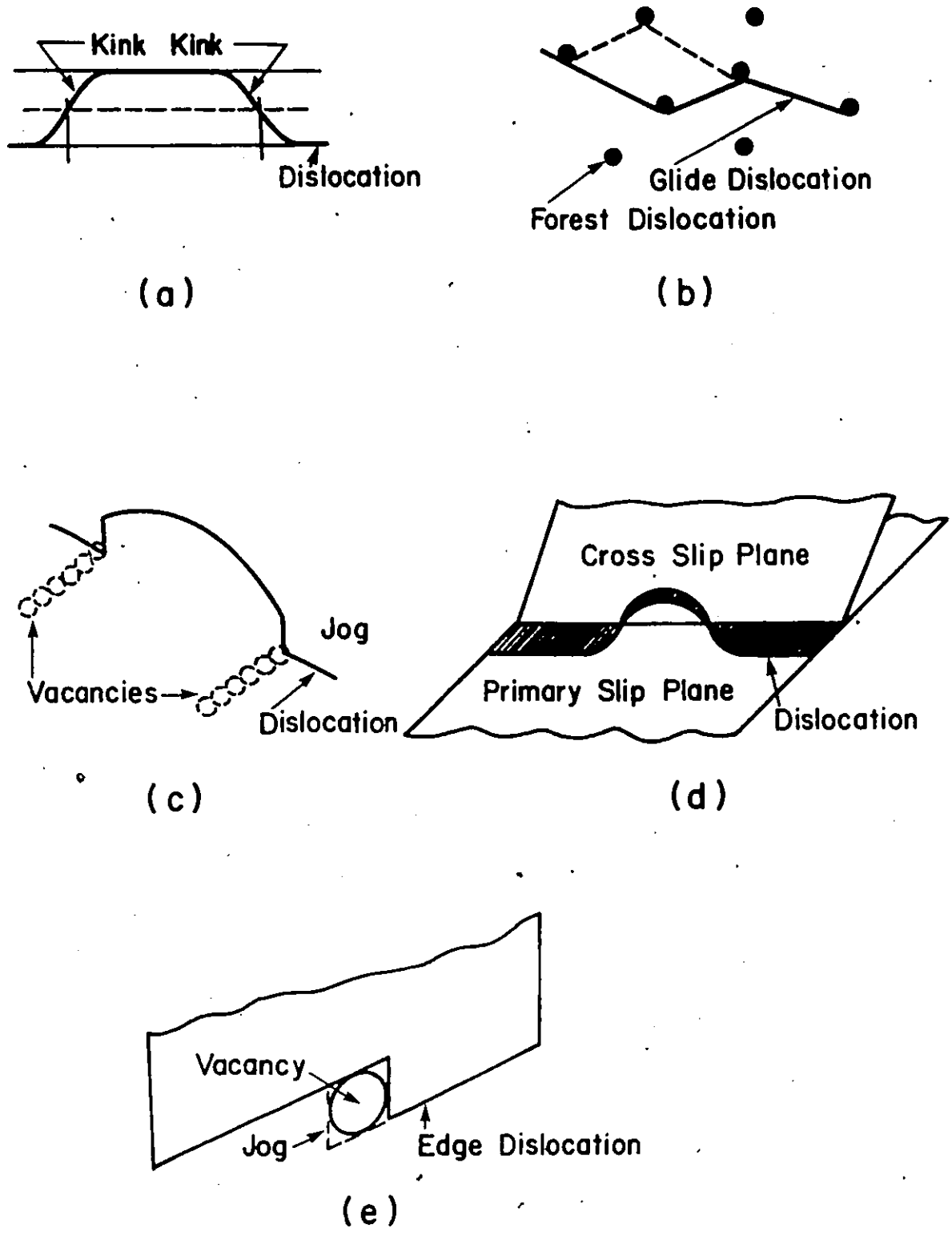

Figure 1.3. Thermally activated dislocation mechanisms [52].

1.1.3 Transition State Theory

The development of the transition state theory (usually known as rate theory or activated complex theory or absolute rate theory [27]) was initiated by Arrhenius [55] when he suggested that the rate of a chemical reaction, k, can be expressed as

$$k = A_e \exp - [\frac{\Delta E_e}{kT}] \qquad (1.3)$$

where A_e is a frequency factor, ΔE_e is an empirical activation energy, k is the Boltzmann constant, and T is the absolute temperature. Although the expression described well the temperature dependence of the rate of chemical reactions, it was purely empirical. As will be shown later, the rate theory, based on statistical (mechanics) thermodynamics leads to a similar equation.

It was recognized by Marcellin [56] that, in the language of statistical mechanics, the reaction rate is controlled by the passage of reacting molecules from the part of the phase space corresponding to the reactants to the part that corresponds to the products through a critical (or activated state) surface in the phase space. Once the activated state is reached the reaction takes place spontaneously. The concept that reactants must be in an activated state before the reaction takes place was further developed by Rodebush [57-60] and by Rice and Gershinowitz [61,62]. The theory was brought to its present form by Eyring [63,64], Evans and Polanyi [65,66], and its relevance to plasticity was already considered

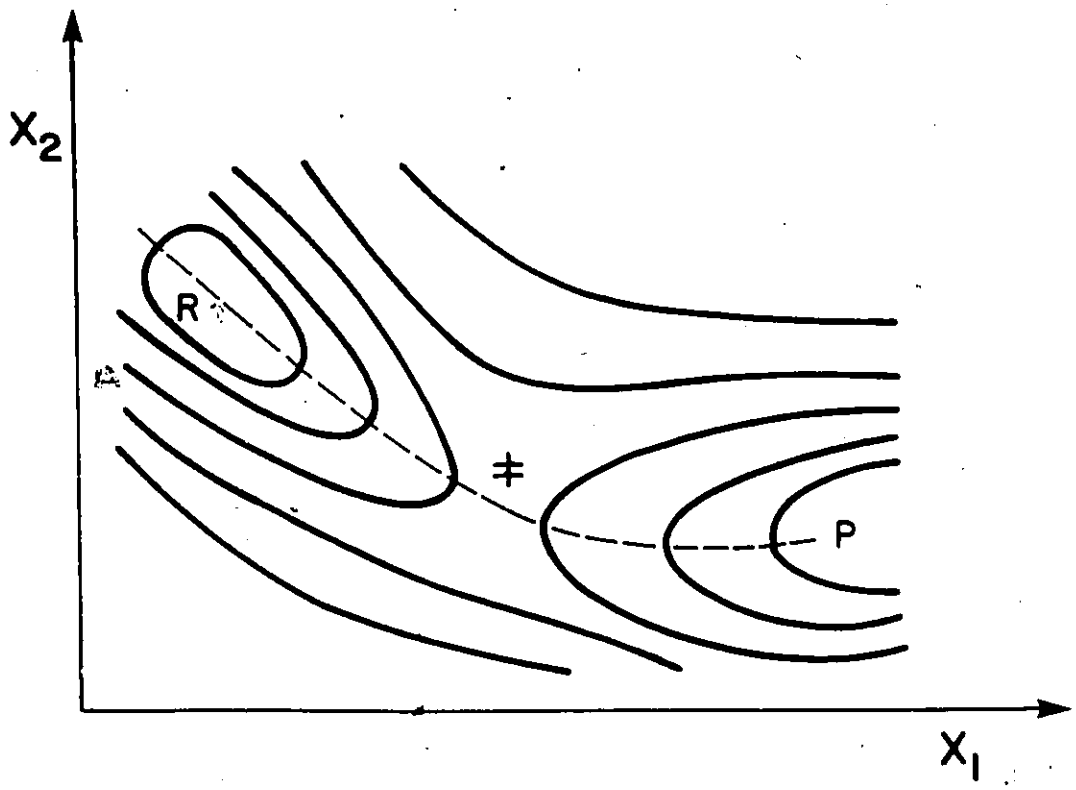

Figure 1.4. Equipotential lines in phase space, and the reaction path.

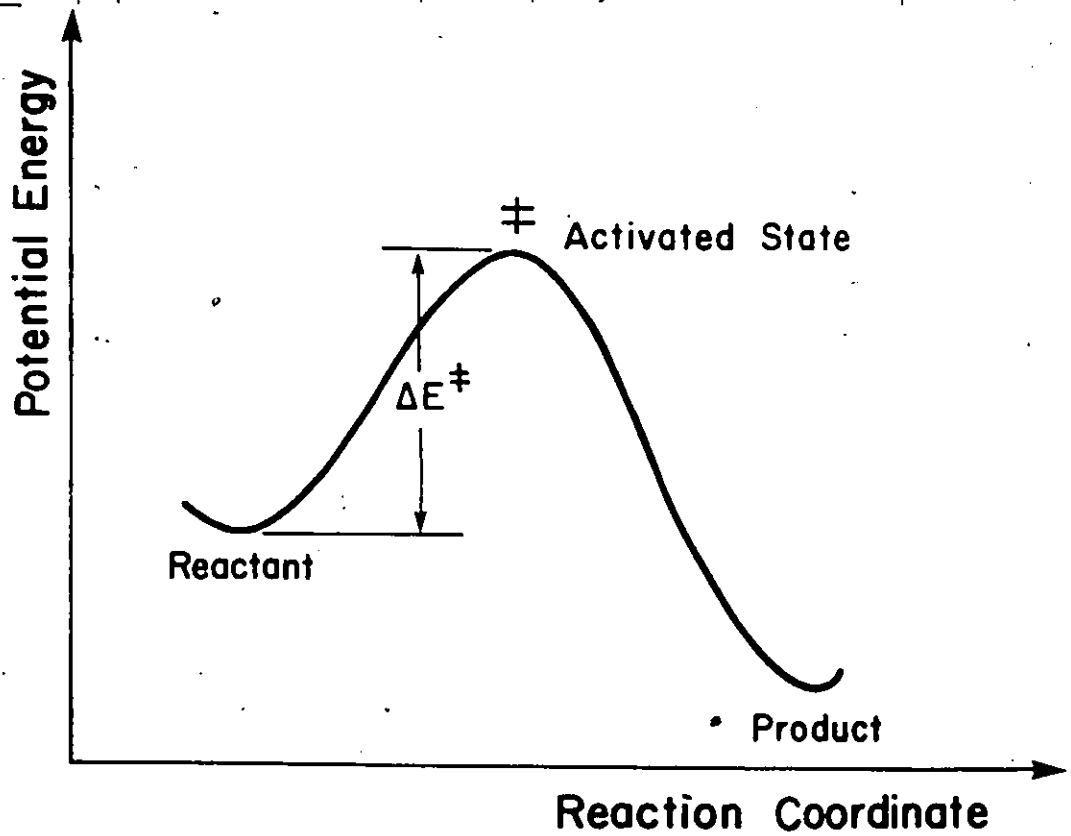

Figure 1.5. Variation of the potential energy along the reaction coordinate.

[67,68]. The transition state theory [69] and its application to deformation kinetics [27] are now firmly established.

During the thermally activated plastic flow caused by dislocation movements, the reacting molecule is analogous to the N atoms around the dislocation (which form atomic groups or flow units). The potential energy of the molecule is represented in a configuration space of 3N-5 dimensions and may theoretically be calculated from quantum mechanics. Fig. 1.4 shows schematically, in two dimensions, the configuration associated with the passage of the dislocation over an obstacle. A molecule (or flow unit) in the low energy level - indicated as R - corresponding to the reactant state can go to the low energy level - indicated as P - corresponding to the product state, only if it becomes activated to the transition state - indicated as $\neq$. The activated state is a saddle point, that is, presents negative curvature in the direction corresponding to the reaction path - the reaction coordinate, indicated with a dashed line - and positive curvature in all other orthogonal directions. The passage of the activated complexes over the top of the energy barrier may be treated as a translation or as a loose vibration [70]. The frequency of decomposition in both cases (translation and loose vibration) was found to be kT/h, where h is the Planck's constant. The potential energy along the reaction coordinate is shown schematically in Fig. 1.5. According to Scheffer and Kohnstamm [71], the molecules go both from the reactant state to the product state in the "forward" direction and products go to the reactant state in the "backward" direction. Consequently, the rates of reaction in the forward and backward directions are, respectively [27,69,70],

$$\text{Rate}_f = \rho_r k_f^{\neq} = \rho_r \kappa \frac{kT}{h} \frac{Q^{\neq}}{Q_r} \exp - \left(\frac{\Delta E_f^{\neq}}{kT}\right)$$

and (1.4)

$$\text{Rate}_b = \rho_p k_b^{\neq} = \rho_p \frac{kT}{h} \kappa \frac{Q^{\neq}}{Q_p} \exp - \left(\frac{\Delta E_b^{\neq}}{kT}\right)$$

where $\Delta E^{\neq}$ is the energy of activation at absolute zero, that is, the difference between zero-point energy of the activated complexes and that of the reactants or products, $Q^{\neq}$ represents the partition functions of the 3N-7 degrees of vibrational freedom in the activated state (the degrees of freedom corresponding to the reaction coordinate have been utilized), Q represents the partition function of the reactant or product state, ρ is the number of reacting molecules (similar to the groups of atoms forming dislocations), κ is the transmission coefficient that takes into account the possibility that a complex may be reflected back or tunnel through the energy barrier. The subscripts r and p represent the reactant and product states, respectively. Similarly, the subscripts f and b refer to the forward and backward directions, respectively over a single energy barrier. From the statistical thermodynamics definition of Gibbs free energy, ΔG, the rate constants $k_f^{\neq}$ and $k_b^{\neq}$ may be written as [27]

$$k_f^{\neq} = \kappa_f \frac{kT}{h} \exp - \left(\frac{\Delta G_f^{\neq}}{kT}\right)$$

and

$$k_b^{\neq} = \kappa_b \frac{kT}{h} \exp - \left(\frac{\Delta G_b^{\neq}}{kT}\right). \qquad (1.5)$$

In Eqs. (1.5), the rate constants $k_f^{\neq}$ and $k_b^{\neq}$ represent the number of activations in unit time, in the abscence of the applied stress. The applied stress leads to mechanical work, $W(\tau_{eff})$, on the dislocations. Due to the mechanical energy, the corresponding potential energy barrier changes by the corresponding amount. Consequently, the rate constants are expressed as [27]

$$k_f = \kappa_f \frac{kT}{h} \exp - \left[\frac{\Delta G_f^{\neq} - W_f(\tau_{eff})}{kT}\right] = k_f^{\neq} \exp \frac{W_f(\tau_{eff})}{kT}$$

and (1.6)

$$k_b = \kappa_b \frac{kT}{h} \exp - \left[\frac{\Delta G_b^{\neq} + W_b(\tau_{eff})}{kT}\right] = k_b^{\neq} \exp - \frac{W_b(\tau_{eff})}{kT}.$$

That is, the height of the energy barrier is decreased by $W_f(\tau_{eff})$ for the flow units moving in the forward direction and increased by $W_b(\tau_{eff})$ in the backward direction.

It has been assumed in the absolute theory of rate processes that the complexes in the stable configuration (reactant or product states) are in equilibrium with the activated complexes. This assumption expresses only an approximation of the dynamic conditions and is rigorously valid only when the system is in equilibrium. Studies by Prigogine, Nicolis and Allen [72] using non-equilibrium statistical mechanics have confirmed the validity of the equilibrium assumption, provided that $\Delta G/kT > 10$.

1.1.4 Deformation Kinetics

During plastic deformation a dislocation is stopped in front of an obstacle which acts as an energy barrier. It has to wait there until the combined effect of the stress and thermal energy increases sufficiently the energy of the atoms which take part in the overcoming of the barrier. When the energy and the configuration of these atoms correspond to that of the activated state, the dislocation is free to move at a very high velocity until it is stopped again by an obstacle. Eqs.(1.6) represent the expected number of activations in unit time; the rate constants k_f and k_b, in the forward and backward directions, respectively over a single energy barrier (obstacle). However, thermally activated plastic flow is often controlled by a system of energy barriers which may form either a parallel system, a consecutive system, or a combination of these two types. Hence, to obtain a physically meaningful description of the experimental results, a kinetics analysis [27] has to be carried out first: that will give an appropriate system of energy barriers. Then, as it is practiced in chemical kinetics studies, the combination of the individual rate constants or the overall rate constant can be determined. A step by step method to determine the energy barrier system and to evaluate the constitutive parameters from the experimental results and testing conditions is now well established [27,73].

In the following, the kinetics associated with fundamental processes will be discussed: backward activation over a single energy barrier, parallel, and consecutive energy barrier systems. When necessary, more elaborate systems may be constructed [27].

1.1.4.1 Single Energy Barrier Kinetics

The net rate of reaction, that is, the difference between forward and backward rates is expressed as

$$\text{Rate} = \rho_f k_f - \rho_b k_b \qquad (1.7)$$

During plastic flow, however, there is no difference between product and reactant states since after overcoming an energy barrier, the dislocations are usually stopped in front of a similar energy barrier. The situation, as outlined by Gifkins [47] is very different from that in chemical kinetics. The difference between forward and backward directions results only from the work, $W(\tau_{eff})$, done by the effective stress, τ_{eff}, during activation. Fig. 1.6 illustrates the effect of the shear stress on the energy barrier associated with the plastic flow. The plastic strain rate is then expressed from Eqs.(1.2) and (1.6) as

$$\dot{\varepsilon}_p = \left(\frac{1}{M}\right) b\bar{\ell}\rho_t \, (k_f - k_b)$$

or (1.8)

$$\dot{\varepsilon}_p = \frac{2}{M} b\bar{\ell}\rho_t k^{\neq} \sinh \left[\frac{W(\tau_{eff})}{kT}\right]$$

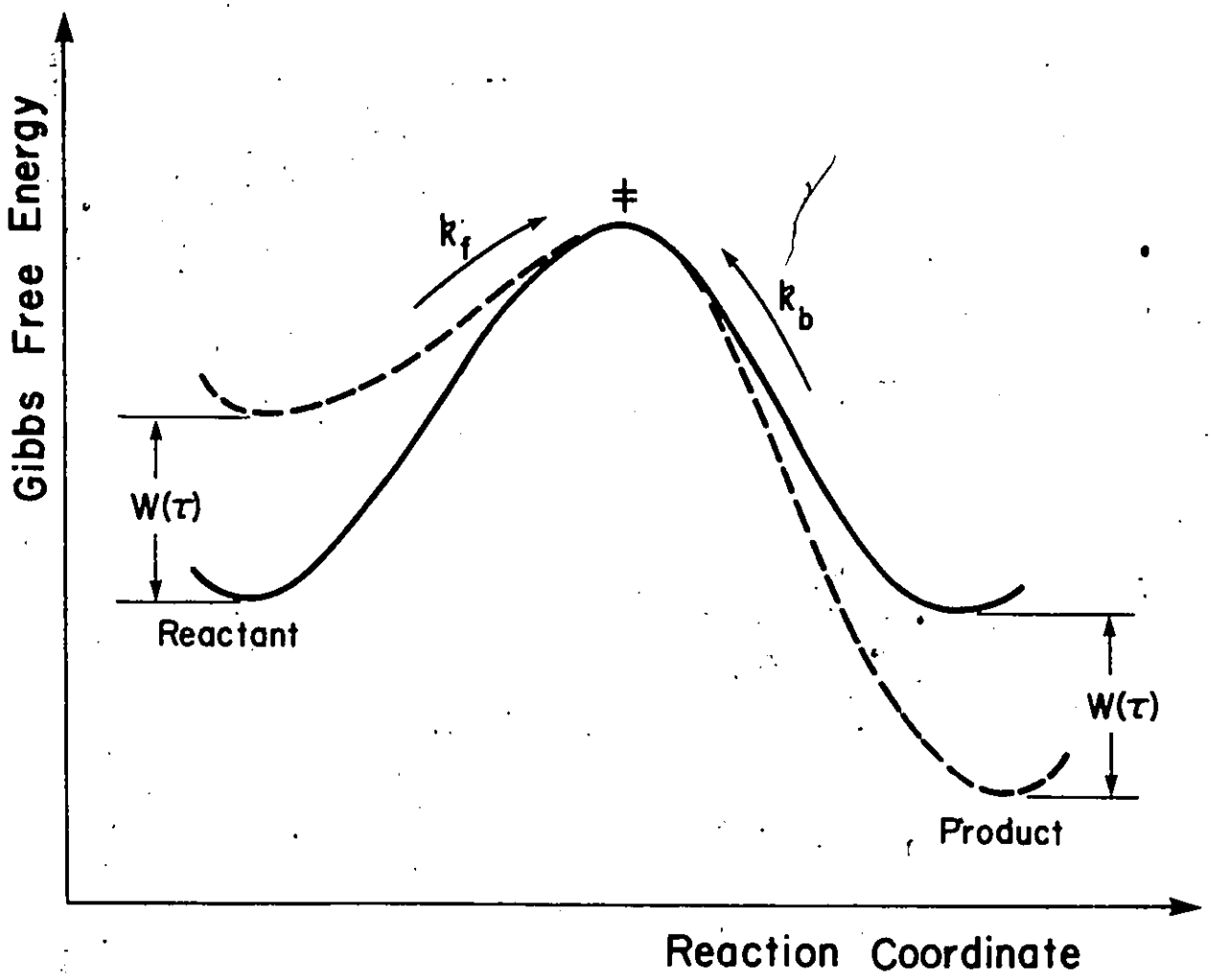

Figure 1.6. Schematic representation of the effect of the shear stress on the energy barrier associated with the plastic flow.

where $k^{\neq} = k_f^{\neq} = k_b^{\neq} = \kappa \frac{kT}{h} \exp - \left(\frac{\Delta G^{\neq}}{kT}\right)$ and

$\rho_t = \rho_f = \rho_b$.

The mechanical energy is often assumed to be a linear function of the effective stress [27], ie

$$W = V \tau_{eff} \tag{1.9}$$

where the "activation volume" V is defined as

$$V = -\left(\frac{\partial \Delta G}{\partial \tau_{eff}}\right)\Big|_T .$$

At low stress level or high temperature, when $W(\tau_{eff})$ is much less than kT, eq.(1.8) becomes

$$\dot{\varepsilon}_p = \frac{2}{M} b \bar{\ell} \rho_t k^{\neq} \frac{V \tau_{eff}}{kT} . \tag{1.10}$$

The relation expresses the often observed linear relationship between the plastic strain rate and the stress. At high stress level and low temperature, when $W(\tau_{eff})$ is much larger than kT, the constitutive equation can be expressed as

$$\dot{\varepsilon}_p = \left(\frac{1}{M}\right) \bar{\ell} b \rho_t k^{\neq} \exp \frac{V \tau_{eff}}{kT} . \tag{1.11}$$

That is, within the high stress and low temperature range, the backward activation over the energy barrier is negligible.

Alefeld [75] showed that even with constant activation volume, Eq.(1.8) could describe adequately some experimental results. Krausz [76] considered the more general case of a non-symmetrical energy barrier. The plastic strain rate is then expressed as

$$\dot{\varepsilon}_p = \frac{1}{M} \rho_t b \ (\bar{\ell}_f k_f - \bar{\ell}_b k_b) \qquad (1.12)$$

where

$$k_f = k_f^{\neq} \exp \left(\frac{V_f \tau_{eff}}{kT}\right)$$

and

$$k_b = k_b^{\neq} \exp - \frac{V_b \tau_{eff}}{kT}$$

Non-symmetrical energy barrier takes into account the facts that the structure, and hence the Gibb's free energy, of the group of atoms around the dislocation may change after activation, and that the activation distance, and hence the activation volume, may be different for the forward and backward activations. Using Eq.(1.12), Krausz [76] then elucidated the observed stress dependence of dislocation velocity in LiF, Ge, Si, etc., as

well as the effect of temperature on the deformation behavior of Ge, Si, CaF_2 etc. [77].

1.1.4.2 Parallel Energy Barrier Systems

In general, plastic deformation occurs over several slip planes, while simultaneous processes may occur in each slip plane. The macroscopically observed strain rate is the sum of all individual events [27,48,73,74] and is expressed as

$$\dot{\varepsilon}_p = \sum_i \frac{1}{M_i} \rho_t \, b_i \bar{\ell}_i k_i \qquad (1.13)$$

where the k_i's are of the form

$$k_i = k_{i_f} - k_{ib} .$$

The largest term in Eq.(1.13) controls the rate of deformation, and, in general, it can be used to describe the plastic strain rate at a given temperature.

1.1.4.3 Consecutive Energy Barrier Systems

A consecutive system operates when the deformation mechanism is such that a series of obstacles has to be overcome by the dislocation (flow unit)

before a contribution is made to the strain by the flow unit. In this case each step (activation over a barrier) can be performed only after the previous step (the overcoming of the previous barrier) has been completed.

The mechanism is therefore composed of dependent unit processes. The Peierls-Nabarro mechanism (Fig. 1.7 (a)), diffusive climb, and glide of jogged dislocations (Fig. 1.7 (b)) are examples of processes associated with consecutive energy barrier systems.

The constitutive equation associated with consecutive energy barriers is often written as [74,79,80,81]

$$\dot{\varepsilon}_p = \frac{\varepsilon_{p,0}}{\sum_i t_i} \qquad (1.14)$$

where t_i is the waiting time in front of the i-th energy barrier and $\varepsilon_{p,0}$ is a constant.

Consider the two-consecutive-energy-barrier system shown in Fig. 1.8. The net flow F_1 and F_2 over each individual barrier is [27,82]

$$F_1 = \rho_1 \, {}_1k^1 - \rho_2 \, {}^1k_2 = F_2 = \rho_2 \, {}_2k^2 - \rho_1^2 k_1 \qquad (1.15)$$

where ${}_ik^j$ represents the rate of activation in the forward direction from barrier i to the top of barrier j, and ${}^jk_i$ represents the rate of activation in the backward direction. Because the total number of dislocations is

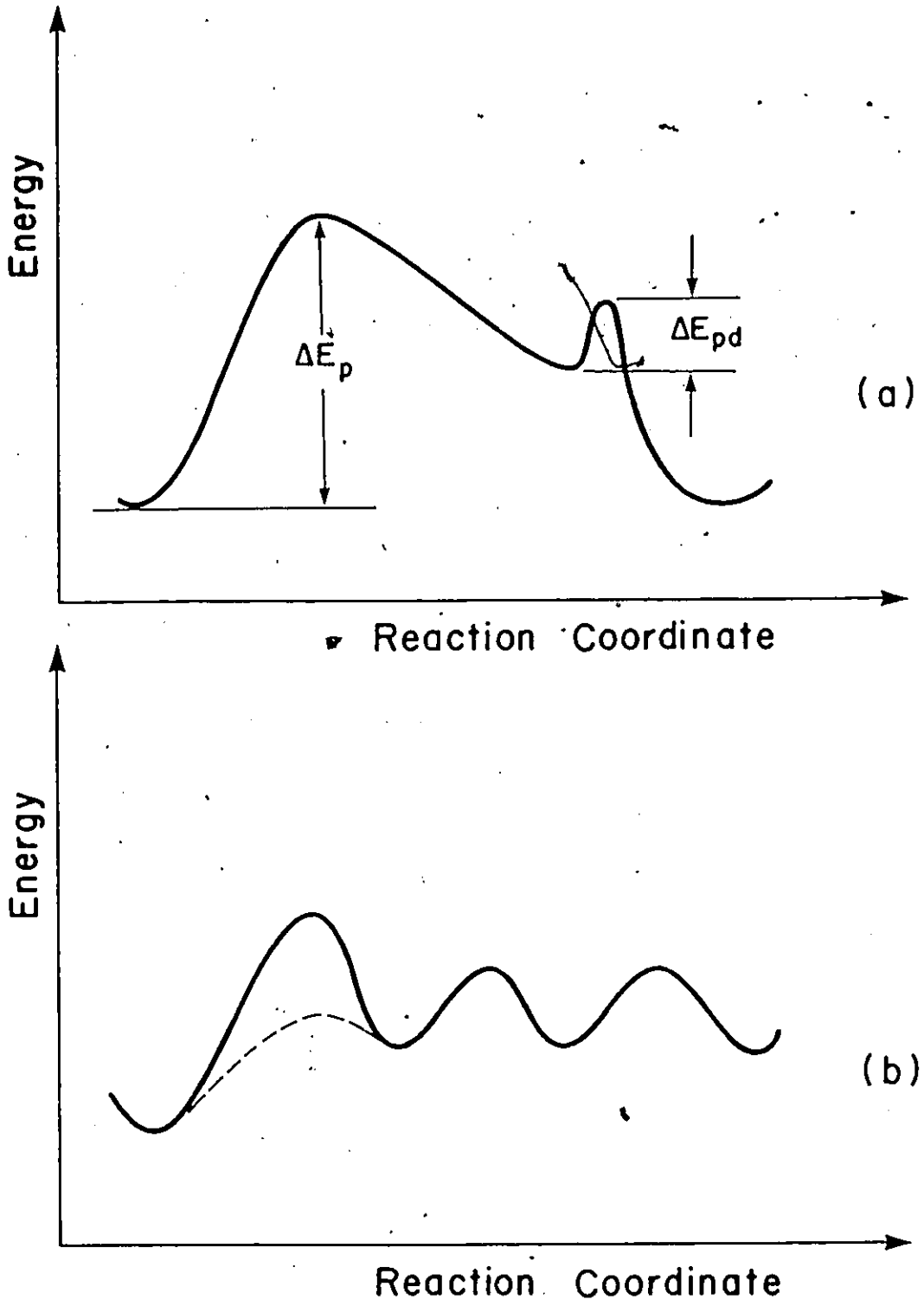

Figure 1.7. Two examples of consecutive energy barriers. (a) Peierls mechanism [78]. The first barier is associated with Peierls stress and the second with the dragging by point defects. (b) Two alternatives for the glide of jogged dislocations [46]. The first barrier is associated with the motion of the jog and the subsequent diffusion of the vacancy in the lattice.

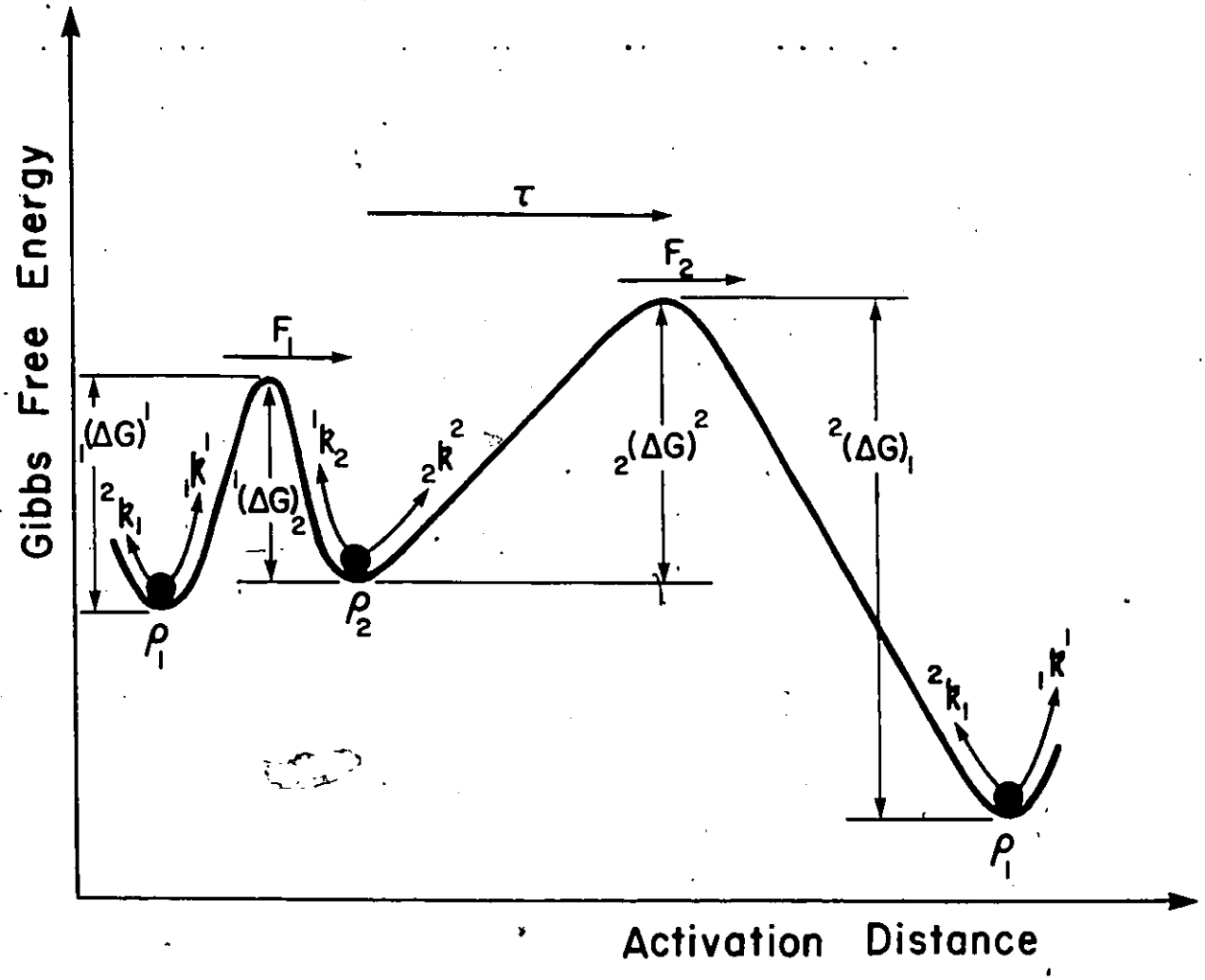

Figure 1.8. Schematic representation of a system of two consecutive energy barriers under the influence of a shear stress.

$$\rho_t = \rho_1 + \rho_2,$$

it follows that

$$\rho_1 = \rho_t - \rho_2 = \rho_t \frac{{}_2k^2 + {}^1k_2}{{}_1k^1 + {}_2k^2 + {}^1k_2 + {}^2k_1}. \tag{1.16}$$

The constitutive equation then is

$$\dot{\varepsilon}_p = \frac{1}{M} b\bar{\ell} F_1 = \frac{1}{M} b\bar{\ell}\rho_t \frac{{}_1k^1{}_2k^2 - {}^1k_2{}^2k_1}{{}_1k^1 + {}_2k^2 + {}^1k_2 + {}^2k_1}$$

$$\text{or} \quad \dot{\varepsilon}_p = \delta\rho_t \frac{1 - \dfrac{{}^1k_2{}^2k_1}{{}_1k^1{}_2k^2}}{\dfrac{1}{{}_1k^1} + \dfrac{1}{{}_2k^2} + \dfrac{1}{{}_1k^2} + \dfrac{1}{{}_2k^1}} \tag{1.17}$$

where ${}_1k^2 = {}_1k^1{}_2k^2/{}^1k_2$ . . . ${}_2k^1 = {}_2k^2{}_1k^1/{}^2k_1$ and

$\delta = \frac{1}{M} b\bar{\ell}$.

In Eq.(1.17), the numerator is

$$1 - \exp\left[\frac{{}_1\Delta G^{\neq 1} + {}_2\Delta G^{\neq 2} - {}^1\Delta G_2^{\neq} - {}^2\Delta G_1^{\neq} - ({}_1W^1 + {}_2W^2 + {}^1W_2 + {}^2W_1}{kT}\right]$$

where $W = W(\tau_{eff})$.

Since the strain rate is zero when the stress is zero it follows immediately that for the investigated system,

$$ {}_1\Delta G^{\neq 1} + {}_2\Delta G^{\neq 2} = {}_1\Delta G_2^{\neq} + {}_2\Delta G_1^{\neq} . \tag{1.18} $$

The first two terms in the denominator of Eq.(1.17) are of the form

$$ \frac{1}{{}_i k^i} = \frac{h}{\kappa kT} \exp\left[\frac{{}_i\Delta G^{\neq i} - {}_i W^i(\tau_{eff})}{kT}\right]. \tag{1.19} $$

They are the waiting times for activation over each of the energy barriers in the forward direction. The third term is expressed explicitly as

$$ \frac{1}{{}_1 k^2} = \frac{{}_1 k_2}{{}_1 k^1 \, {}_2 k^2} = \frac{h}{\kappa kT} \exp\left[\frac{{}_1\Delta G^{\neq 1} + {}_2\Delta G^{\neq 2} - {}_1\Delta G_2^{\neq} - {}_1 W^1 - {}_2 W^1 - {}_2 W^2}{kT}\right] $$

or using Eq.(1.18)

$$ \frac{1}{{}_1 k^2} = \frac{h}{\kappa kT} \exp\left[\frac{{}_2\Delta G_1^{\neq} - {}_1 W^1 - {}_2 W^1 - {}_2 W^2}{kT}\right]. \tag{1.20} $$

This term is identical to a waiting time for activation over an energy barrier corresponding to the forward free energy difference between position 1 and the top of the second barrier. Similarly, the fourth term in the

denominator of Eq.(1.17) is identical to a waiting time for activation over an energy barrier corresponding to the forward free energy difference between position 2 and the top of the first barrier. Eq.(1.17) describes the properties of a system of two consecutive energy barriers. It can be extended to describe the plastic strain rate for a system of more than two energy barriers [83].

1.2 CONVENTIONAL TESTING METHODS

1.2.1 Deformation Surface

Several experimental methods were developed for the determination of the deformation kinetics of materials. Mechanical models help the visualization of the behavior of material under the various experimental conditions. The models are made up of springs and dashpots; the springs represent the elastic and the dashpots the time dependent, dissipative flow components. The deformation behavior of materials may then be represented by the combination of springs and dashpots as shown in Fig.1.9 [Ref.27 p.129]. The deformation of the dashpot is usually non-Newtonian and is described by a constitutive relation of the form

$$f(\tau_{eff}, \varepsilon, \dot{\varepsilon}, T) = 0. \qquad (1.21)$$

The exact form of Eq. (1.21) depends on the kinetics associated with the mechanisms that control the plastic flow. The constitutive equation defines

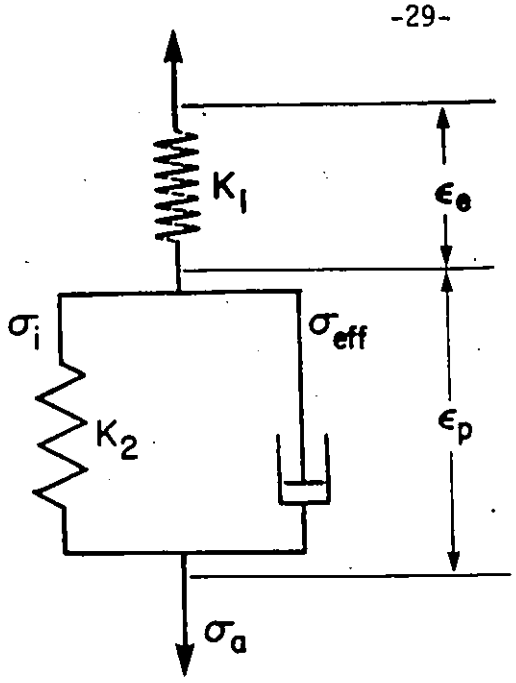

Figure 1.9. The mechanical model used in the study of plastic deformation.

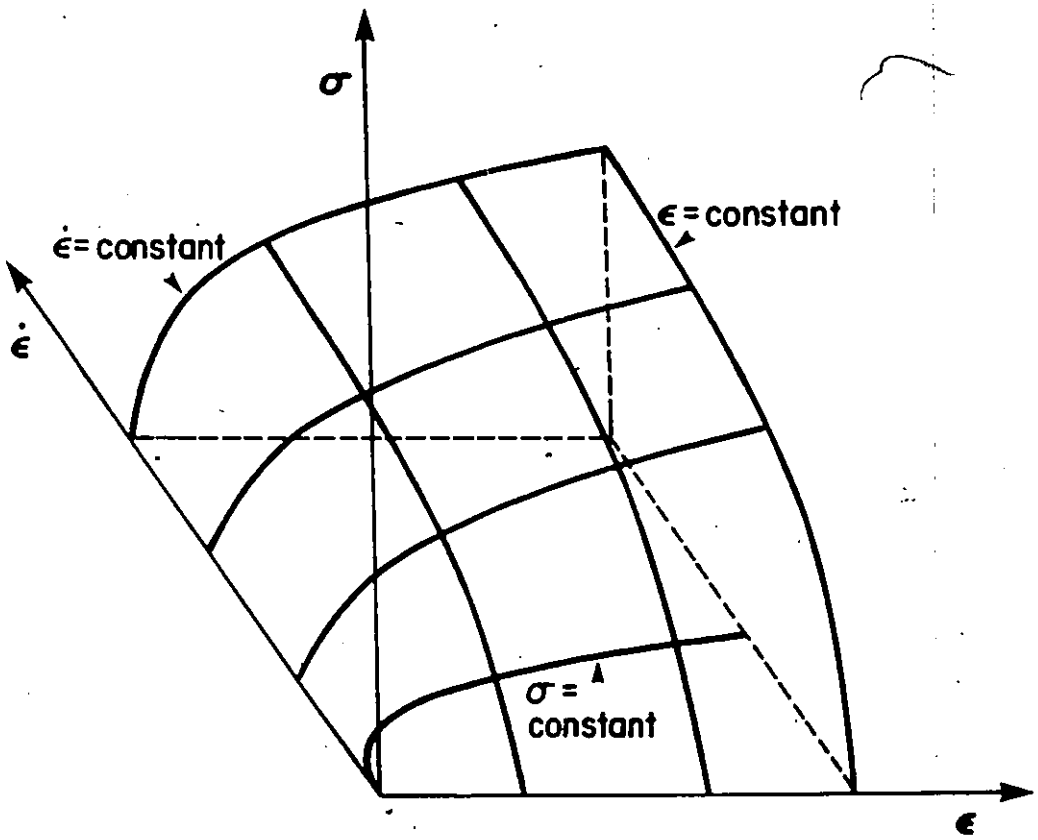

Figure 1.10. Deformation surface for the model of Fig. 1.9 (Ref. 84 p.418)

the deformation surface [84] as illustrated in Fig. 1.10. The surface is determined by various tests during which one of the variables is usually kept constant. The tests are represented by intersections of the surface with planes perpendicular to the axis: constant strain rate test (or tensile test), constant stress (or creep test), and constant strain (or stress relaxation test).

1.2.2 Constant Strain Rate Test

Fig. 1.11(a) shows schematically the input corresponding to a constant strain rate test, and the response of the model shown in Fig. 1.9. The elongation rate of the dashpot is zero at the beginning of the test, and reaches the imposed rate at the end of the test. The elastic modulus of the specimen, E (initial slope in Fig. 1.11a), is represented by the spring K_1 while spring K_2 represents the work hardening coefficient, H (final slope). Depending on the properties of the dashpot, materials may exhibit an upper and lower yield stress as indicated with the dashed line in Fig. 1.11a.

The tensile test is probably the oldest method used for the investigation of the plastic properties of materials [84]. In modern hard testing machines, the test is carried out at constant crosshead velocity. The machines provide a good approximation of the constant strain rate condition at small elongations. Tensile tests may be carried out over a very large temperature range and at various strain rates. The strain rate change test is often used to determine the experimental activation volume,

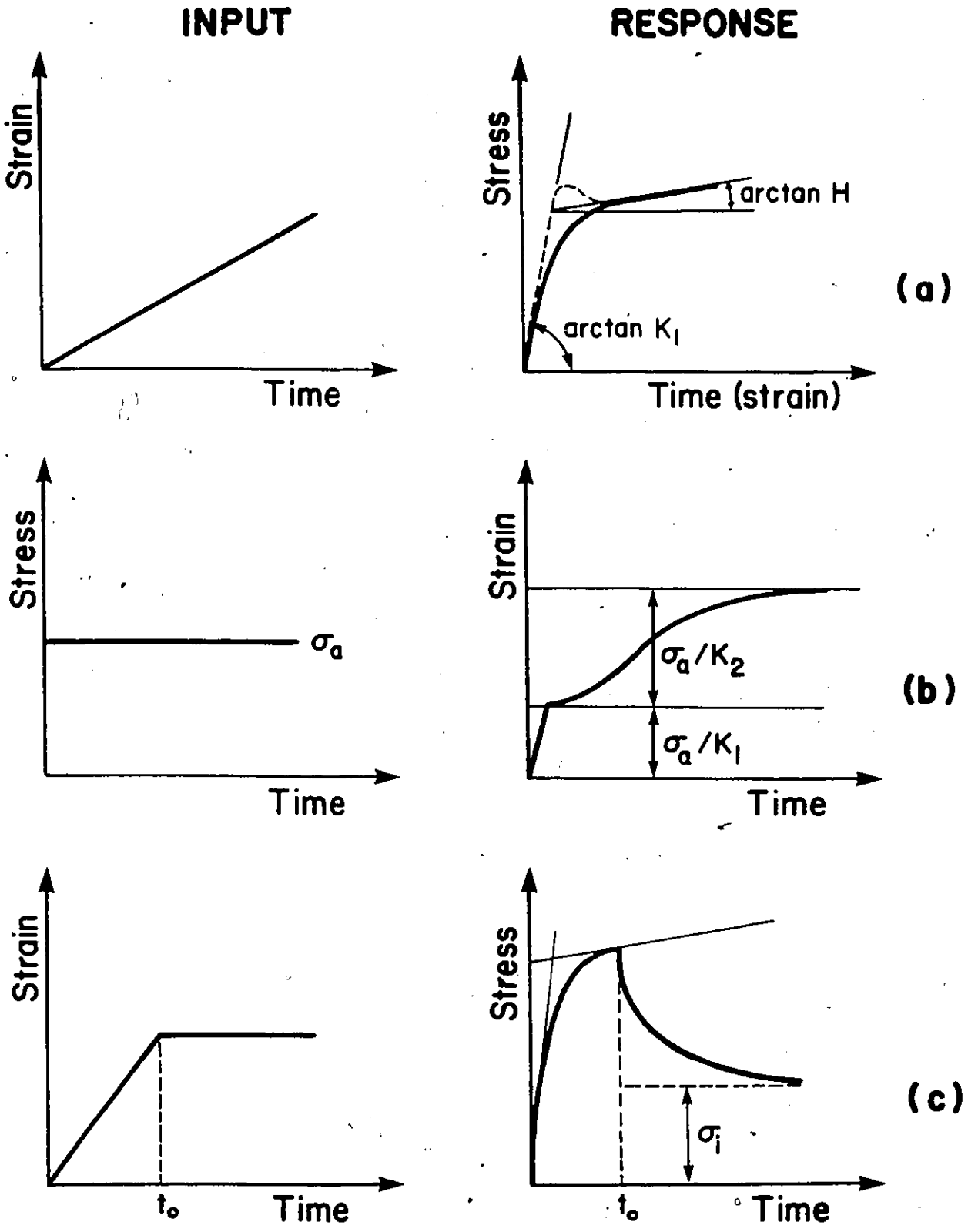

Figure 1.11. Schematic representation of the constant strain rate (a), creep (b), and stress relaxation (c) experiments (Input) and of the response of the model in Fig. 1.9.

V_{exp}, defined as

$$V_{exp} = kT \frac{\partial \ell n \dot{\epsilon}_p}{\partial \tau} .$$

1.2.3 Creep Test

Creep test is usually approximated by a constant load test, even if the applied stress changes slightly as a result of the deformation of the specimen. The constant stress input and the typical, low temperature creep response are illustrated in Fig. 1.11(b). The initial strain results from the deformation of the spring K_1. As the dashpot displaces, the load is transferred to the spring K_2 until the effective stress is zero. That is, the material undergoes work hardening: the internal stress, σ_i, increases (often linearly) with the plastic strain, ϵ_p. For some materials, however, the work hardening coefficient may be small leading to negligible internal stress increase. Discrete stress change tests in creep [85,86] allow for the determination of the experimental activation volume, similar to strain rate change tests. The experimental activation energy may be calculated from temperature change tests in creep [87,89].

1.2.4 Stress Relaxation

The behavior under constant strain or constant elongation is shown schematically in Fig. 1.11c. The specimen is pulled at a predetermined

extension rate (cross-head speed) to some desired extension or load level at which point the machine cross-head motion is stopped. Just before the motion is stopped, the dashpot (Fig. 1.9) deforms (or slips) at the imposed strain rate, under the effect of the initial stress, σ_0. Immediately after stopping the cross-head, the dashpot continues to slip under the stress σ_0. However, since the total elongation (or total strain) has to remain constant, the slip in the dashpot must be equal to the contraction of the spring K_1. Consequently, the applied stress decreases (or relaxes) with time until the stress acting on the dashpot is zero.

The first investigations on stress relaxation were made as early as 1904 by Trouton and Rankine [90]. Extensive studies have since been made by Feltham [91,92] and others [27,34-36]. Stress relaxation tests are usually carried out on a hard testing machine. The decrease of the load following the arrest of the cross-head produces a small deformation of the machine. The analysis of the test, following Guin and Pratt [93], takes into consideration the interrelation between the machine and the specimen. Fig. 1.12 shows schematically the interaction between the machine and the specimen. The machine deforms elastically with a stiffness K, and the specimen deforms both elastically and plastically according to the model in Fig. 1.9. The combined elastic modulus E^1 takes into account the elastic deformation of the machine, ε_m and of the specimen, ε_e. It is defined as

$$\frac{1}{E^1} = \frac{a_0}{K\ell_0} + \frac{1}{E}$$

where a_0 and ℓ_0 are, respectively, the initial cross-sectional area and length of the specimen, and E is the elastic modulus of the specimen. The plastic strain rate, $\dot{\varepsilon}_p$, is the difference between the constant pulling rate

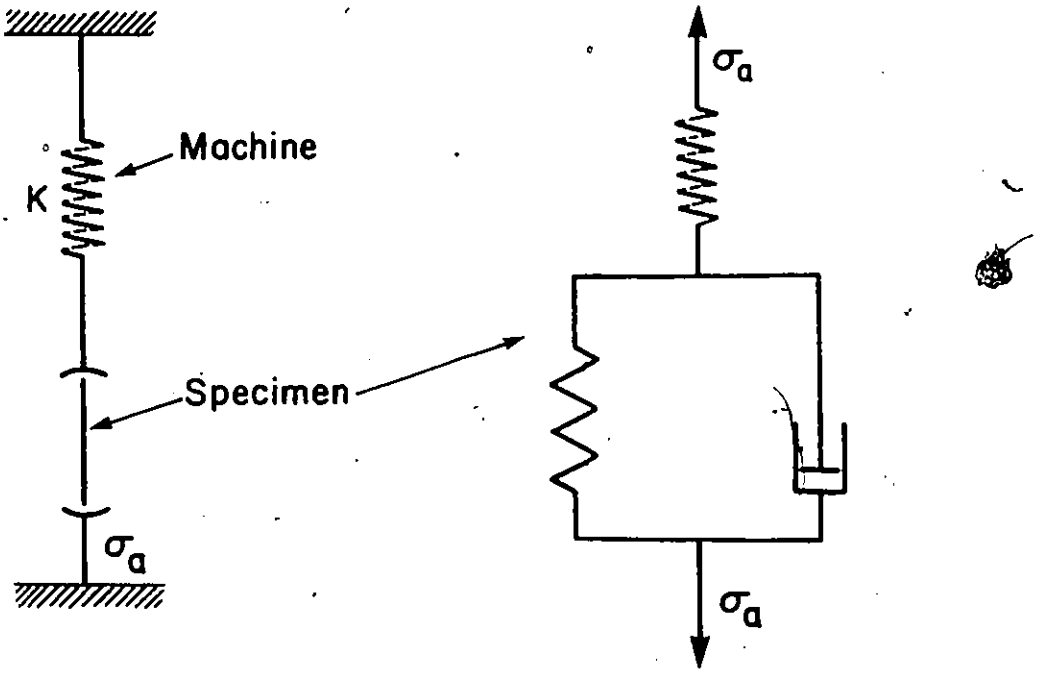

Figure 1.12 Schematic representation of the interaction between the machine and the specimen.

of the machine, $\dot{S}$, and the elastic strain rates, thus

$$\dot{\varepsilon}_p = \dot{S} - (\dot{\varepsilon}_e + \dot{\varepsilon}_m) = \dot{S} - \frac{\dot{\sigma}_a}{E} \quad .$$

Hence,

$$\dot{\sigma}_a = \xi^{-1}(\dot{S}-\dot{\varepsilon}_p). \qquad (1.22)$$

In stress relaxation, $\dot{S}=0$. Eq. (1.22) then becomes

$$\dot{\sigma}_a = -E^{-1}\,\dot{\varepsilon}_p \quad . \qquad (1.23)$$

When the deformation of the machine is not purely elastic, the total strain of the specimen, ε, should be measured. The plastic strain rate during stress relaxation is then expressed as

$$\dot{\varepsilon}_p = \dot{\varepsilon}-\dot{\varepsilon}_e = \dot{\varepsilon} - \frac{\dot{\sigma}_a}{E} \quad . \qquad (1.24)$$

Eq.(1.24) holds in all situations and shows that the plastic strain rate can be determined from the knowledge of the total strain rate and the applied stress rate.

Because plastic deformation is kept to a minimum during stress relaxation experiments, structural changes are minimized. The plastic strain rate is measured over a wide range as the stress relaxes. The fact that structural changes are minimal or non-existence during stress relaxation constitutes the main advantage of the test and makes it an indispensable tool for the development of the constitutive relations.

1.2.5 Cyclic Stress-Strain Curve

During tension-compression cyclic loading, a stable hysteresis curve develops. The development of the hysteresis curve has two stages. First is the transient stage during which changes in the material response occur. The material undergoes cyclic softening and/or hardening, leading to a nonlinear and time-dependent relationship between stress and strain. In the second stage, the steady state is approached asymptotically and is characterized by the conversion of the hysteresis curve into a loop which is traced over and over again on subsequent cycles. That is, stress and strain amplitudes have reached their saturated values. If a series of either stress - or strain - controlled tests is performed at different amplitudes, then a set of stable, saturated hysteresis loops characterizes the steady state behavior of the whole range of the loading amplitudes. The curve connecting the tips of such stable hysteresis loops gives the relationship between saturated stress and strain amplitudes and is called the cyclic stress-strain curve. Fig. 1.13 illustrates the construction of cyclic stress-strain curve from steady-state cyclic loops.

Alternative methods for obtaining cyclic stress-strain curves were suggested by Morrow [94] and also by Langdgraf and Morrow [95]. Of these, the multiple step testing and incremental step testing are used extensively. In multiple step testing, the specimen is subjected to alternating strains in blocks of increasing magnitude. Hence, from a single specimen, several stable hysteresis loops which may be used to construct the cyclic stress-strain curve are obtained. The incremental step method involves only one specimen and takes much less time than the former. The specimen is

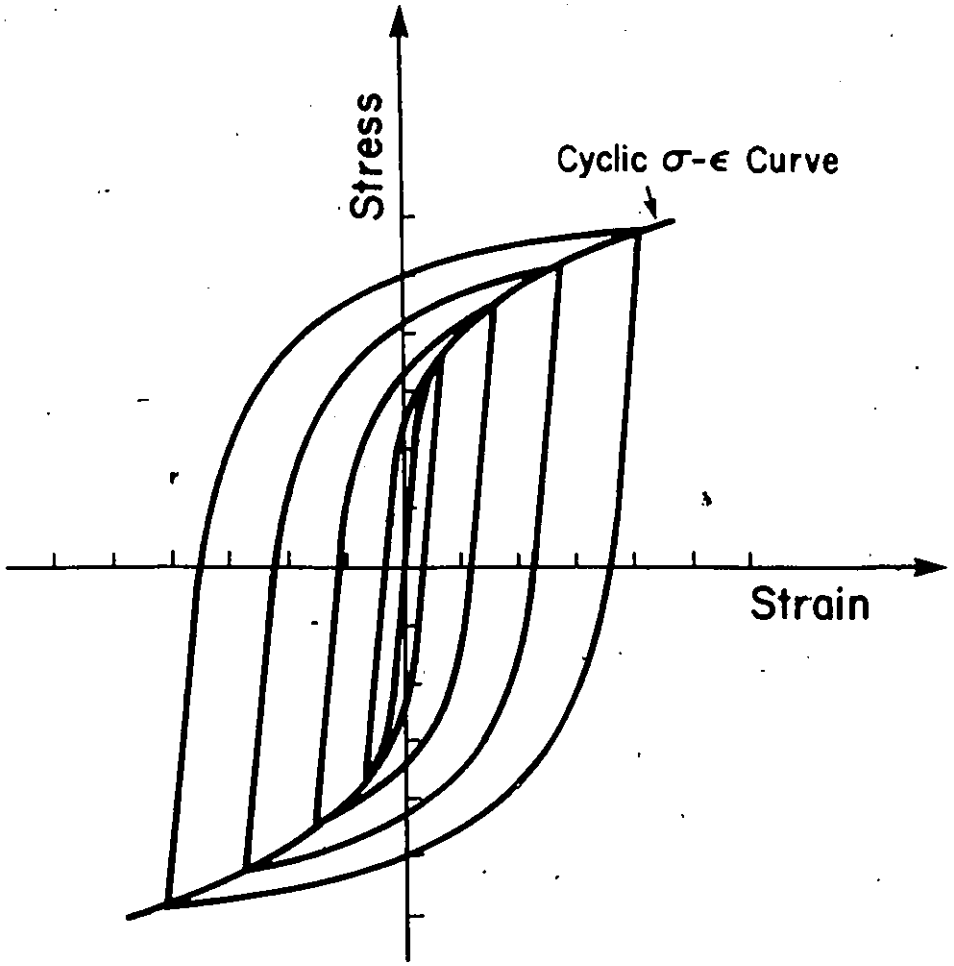

Figure 1.13. Construction of cyclic stress-strain curve from steady-state cyclic loops.

subjected to a series of blocks of gradually increasing and then decreasing strain excursions. After a relatively few such blocks, the material reached a stabilized condition. The cyclic stress-strain curve is then obtained by drawing a line through the tips of each hysteresis loop, from the smallest strain range to the largest.

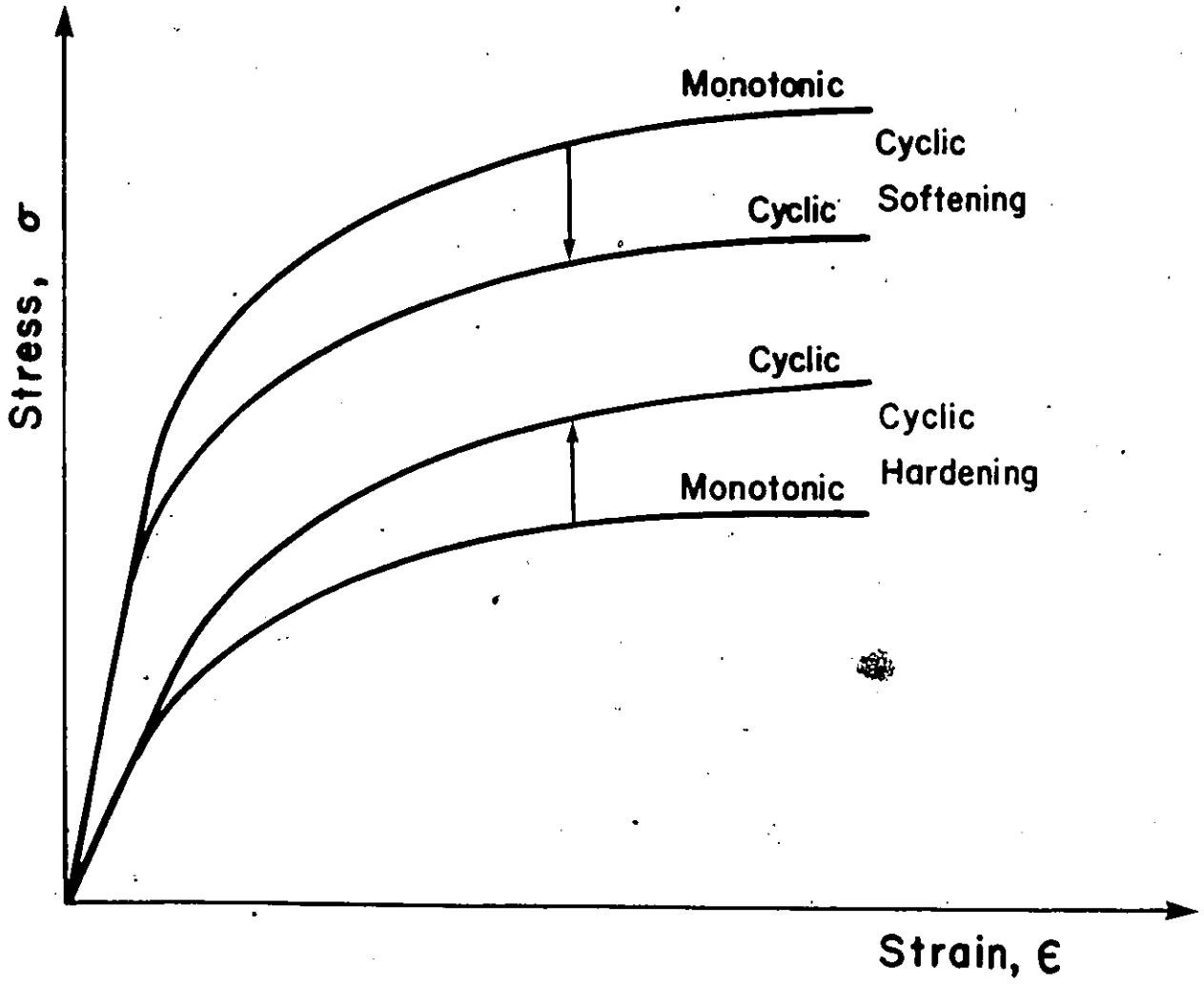

Figure 1.14. Comparison of tensile (monotonic) and cyclic stress-strain curves.

Cyclic stress-strain curve is a useful and convenient method of describing and characterizing cyclic stress-strain behavior in direct comparison with the monotonic stress-strain curve obtained from the conventional tensile test. Fig. 1.14 illustrates the positions of the monotonic and cyclic stress-strain curves. It has been demonstrated [95] that the mutual position of these two curves determines whether the material softens or hardens under cyclic loading.

1.2.6 Internal Stress Analysis

The determination of the internal stress is of great practical engineering, as well as theoretical interest. It was mentioned before that the applied stress is the sum of two components: the effective stress and the internal stress. Hence, the effective stress is expressed in function of the internal stress as

$$\tau_{eff} = \tau_a - \tau_i .$$

For the development of the constitutive equations of thermally activated plastic flow, the internal stress, and through it the effective stress has to be known. From the engineering point of view, the knowledge of the internal stress provides valuable information for the interpretation of the results obtained in materials testing. Because of the varied and great interest in the measurement of the internal stresses, a variety of methods were developed.

One of the methods was developed by Seeger [49] and is based on the variation of shear modulus with temperature. The temperature dependence of the ratio of the flow stress to the shear modulus yields the values of internal and effective stresses at each temperature. Fig. 1.15 illustrates schematically the evaluation of the internal stress, according to Seeger's method. The main disadvantage of this method is that a large number of tests are required over a wide range of temperature. Consequently, the internal structure and hence the internal stress may change with the temperature [81]. An alternative method, the incremental unloading method is, therefore, widely used instead [96-102]. Fig.1.16 illustrates the principle of the method. At zero effective stress, the plastic strain rate must be zero. At stresses below the internal stress level, negative relaxation occurs. The internal stress then is the applied stress at zero strain rate.

Despite the fact that the machine relaxation may render the measurement very difficult [100], the determination of zero strain rate is a practical impossibility. The method brackets only a stress range within which the strain rate is vanishingly small [101]. The width of this stress range depends on the sensitivity of the equipment and the properties of the material. The precaution required to use the method is further illustrated by the recent observation of a positive relaxation that followed a negative relaxation [102]. The advantage of this method is that the evaluation of the internal stress is made on the same specimen that was used in a preceding test.

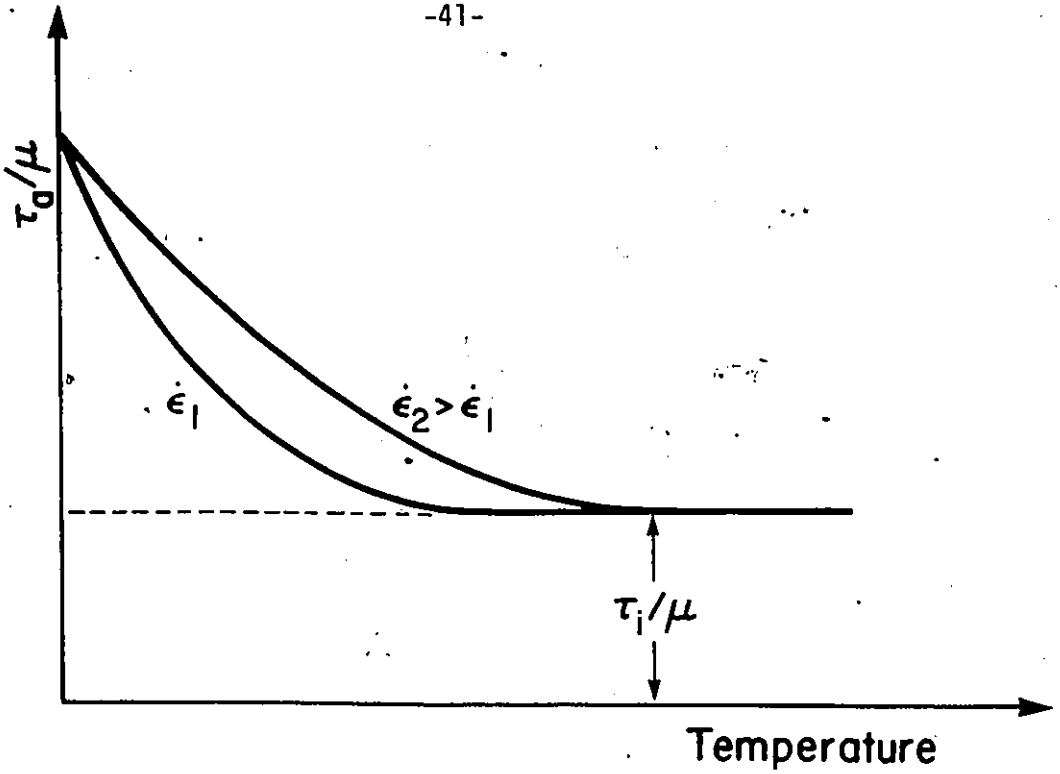

Figure 1.15. Schematic temperature dependence on τ_a/μ., τ_a is the flow stress corresponding to the strain rate $\dot{\epsilon}$, and μ is the shear modulus at the same temperature.

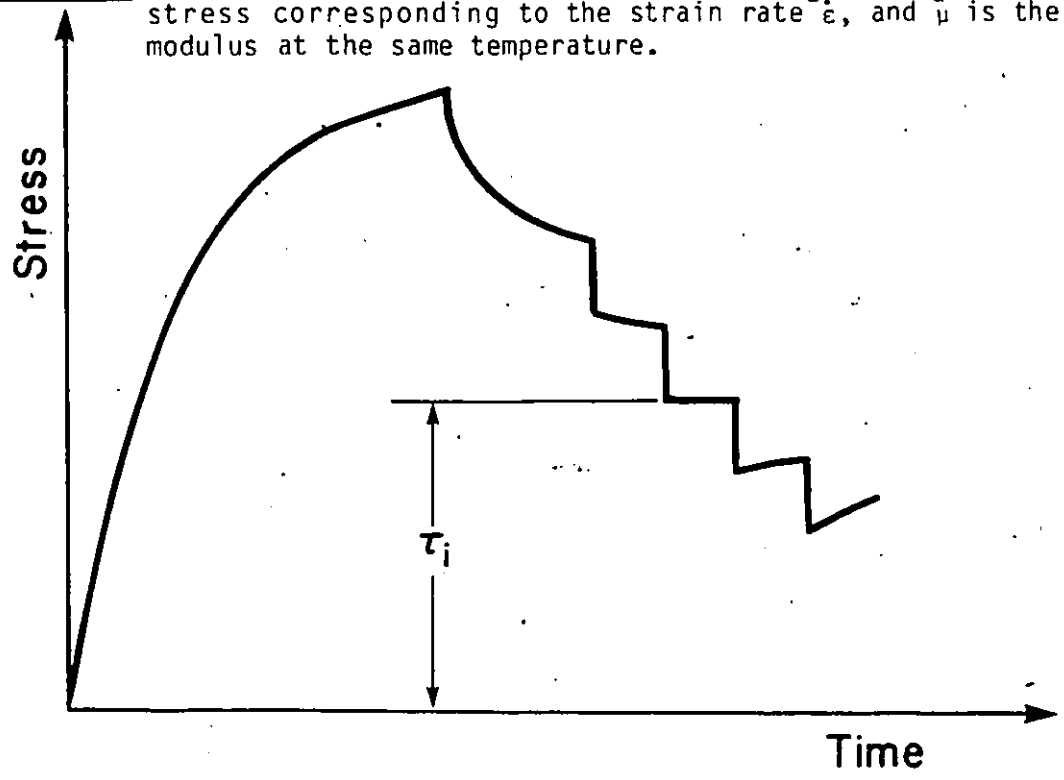

Figure 1.16. Schematic representation of the incremental unloading method to measure the internal stress.

CHAPTER 2

CONSTITUTIVE EQUATIONS OF CYCLIC LOADING

During cyclic loading, the material may experience plastic as well as elastic strain in each cycle. The dislocations undergo "to and fro" movements which often give rise to changes in mechanical properties and microstructure; the internal stress may increase and/or decrease. The to and fro dislocation movements and the resulting changes in material structural properties distinguish cyclic deformation from uniaxial, monotonic loading.

In the following, the application of constitutive equations that were derived from deformation kinetics to describe plastic deformation under cyclic loading conditions will be discussed. It is considered that cyclic deformation takes place under a cyclic stress (or strain) superimposed on a mean or directing stress (or strain). The discussion is based on materials response during which the internal stress level: (a) is constant, (b) increases linearly with plastic strain, and (c) varies in a cyclic manner-increases upon loading and decreases during the unloading part of the cycle.

2.1 STRAIN CONTROLLED CYCLIC LOADING

2.1.1 Elastic and Plastic Strain Rates

During strain controlled cyclic loading, the total strain $\varepsilon(t)$ is expressed as

$$\varepsilon(t) = \varepsilon_e + \varepsilon_p \tag{2.1}$$

or in time differential notation as

$$\dot{\varepsilon} = \dot{\varepsilon}_e + \dot{\varepsilon}_p \ . \tag{2.2}$$

The elastic strain is related to the shear stress as

$$\varepsilon_e = \frac{\sigma}{E} = \frac{M\tau}{E} \tag{2.3}$$

where E is the elastic modulus of the specimen. Consequently, the elastic strain rate is expressed as

$$\dot{\varepsilon}_e = \frac{\dot{\sigma}_a}{E} = \frac{M\dot{\tau}_a}{E} \ . \tag{2.4}$$

When plastic deformation is thermally activated, the rate of plastic flow is obtained from deformation kinetics analysis [27]. While the physical processes of plastic flow may occasionally be associated with parallel energy barrier systems, thermally activated plastic deformation is often controlled by mechanisms associated with consecutive energy barrier systems [27-30]. For the purpose of the present analysis, it is considered that the rate of plastic flow is controlled by a system of two consecutive energy barriers. The plastic strain rate, $\dot{\varepsilon}_p$, that results from the thermally activated motion of dislocations over the energy barriers is then described by Eq. (1.17) as

$$\dot{\varepsilon}_p = \delta\rho_t \frac{\left(1 - \frac{{}_1k_2 \ {}_2k_1}{{}_1k^1 \ {}_2k^2}\right)}{\frac{1}{{}_1k^1} + \frac{1}{{}_2k^2} + \frac{1}{{}_1k^2} + \frac{1}{{}_2k^1}} \ . \tag{2.5}$$

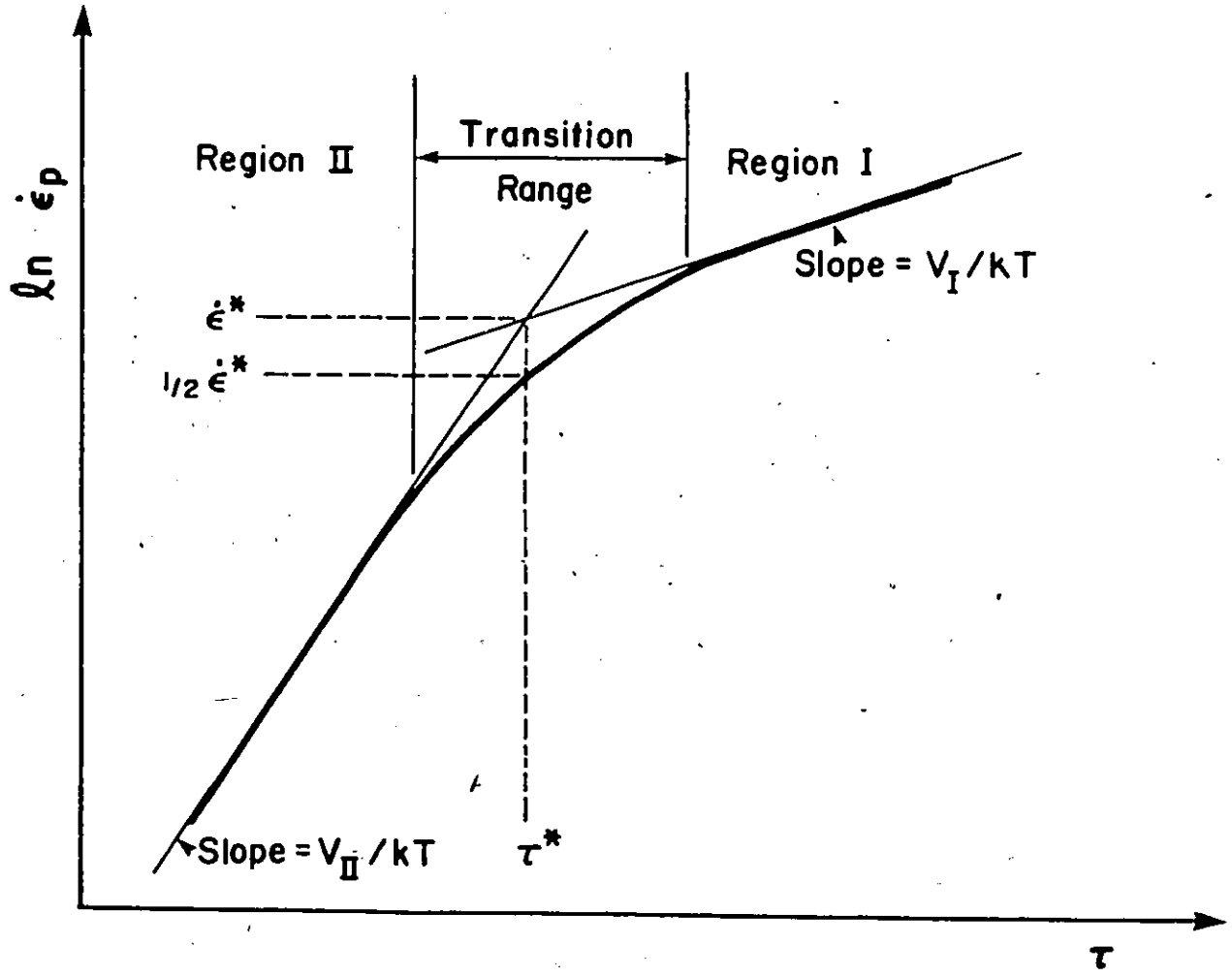

Figure 2.1. Schematic rate diagram at the transition stress.

Fig. 2.1 illustrates a typical rate diagram (for high stress range) associated with activation over a system of two consecutive energy barriers. It is characterized by two lines, regions I and II, joined by (convex curvature) a transition region. A straight line in the rate diagram indicates that the activation volume remains constant during the plastic flow. It also indicates that the Gibb's free energy (or experimental

activation energy) is a linear function of the stress, and can be expressed, in this range, as

$$\Delta G(\tau_{eff}) = \Delta G^{\neq} - V\tau_{eff} \qquad (2.6)$$

where $\Delta G^{\neq}$ is the value - or the extrapolated value - of $\Delta G(\tau_{eff})$ at zero stress. The straight line also implies that the pre-exponential factor, and hence the mobile dislocation density, ρ_t, in the rate equation is constant.

Recent studies [27,30,36,103] have shown that at high stress levels, the second term in the numerator of Eq. (2.5) is zero. For the terms in the denominator of Eq. 2.5, the studies showed that it is not experimentally possible to isolate all the four terms, and that only three of the four terms may have a separate effect. At high stress levels, however, only two terms are rate controlling (Fig. 2.1). In the stress range where one of the two terms in the denominator is effective (larger than the others because the associated free energy is larger), the plastic strain rate is expressed as

$$\dot{\varepsilon}_p = \delta\rho_t k_I = \kappa\, \delta\rho_t \frac{kT}{h} \exp - \frac{\Delta G_I(\tau_{eff})}{kT} \quad . \qquad (2.7)$$

Similarly, within the stress range (region II) where the other term in the denominator is rate-controlling, the plastic strain rate is expressed as

$$\dot{\varepsilon}_p = \delta\rho_t k_{II} = \kappa\delta\rho_t \frac{kT}{h} \exp - \frac{\Delta G_{II}(\tau_{eff})}{kT} \quad . \qquad (2.8)$$

The transmission coefficient $\kappa=1$ for plastic deformation [27]. In the transition stress range, the plastic strain rate is, therefore, expressed as

$$\dot{\varepsilon}_p = \frac{\delta \rho_t}{\frac{1}{k_I} + \frac{1}{k_{II}}} = \frac{\rho_t \, \delta \, kT/h}{\exp\left[\frac{\Delta G_I(\tau_{eff})}{kT}\right] + \exp\left[\frac{\Delta G_{II}(\tau_{eff})}{kT}\right]} \quad . \qquad (2.9)$$

Eqs.(2.9) and (1.14) are identical and can be written as

$$\dot{\varepsilon}_p = \frac{\varepsilon_{p,0}}{t_I + t_{II}} \qquad (2.10)$$

where $\varepsilon_{p,0}$ is a constant, and t_I and t_{II} are the "waiting times" for activation over each barrier. It should be noted, however, that Eq. (2.9) is valid only in a limited stress range, and, moreover, that the interpretation is different; one of the terms $(1/k_{I,II})$ may be a combined term $(1/_i k^j,\ j \neq i)$ and thus does not represent the waiting time for activation over the second energy barrier.

2.1.2 Governing Differential Equation (DE): Region I

Within the high stress and low temperature range*, (region I in Fig. 2.1) the effective stress can be expressed from Eq. (2.7) as

$$\tau_{eff} = \frac{kT}{V_I} \ln \left(\frac{\dot{\varepsilon}_p}{A_I}\right) \qquad (2.11)$$

where $A_I = \delta \rho_t \frac{kT}{h} \exp - \frac{\Delta G_I^{\neq}}{kT}$.

---

* Low temperature range is defined as $T \leq 0.4 T_m$ where T_m is the melting temperature (absolute).

Assuming that the internal stress increases linearly with the plastic strain, the applied stress is

$$\tau_a = \frac{kT}{V_I} \ell n \left(\frac{\dot{\varepsilon}_p}{A_I}\right) + \tau_i^0 + \frac{H}{M} \varepsilon_p \qquad (2.12)$$

where τ_i^0 is the internal stress at the beginning of the experiment. The applied stress rate then is

$$\dot{\tau}_a\Big|_T = \frac{kT}{V_I} \frac{1}{\dot{\varepsilon}_p} \frac{d\dot{\varepsilon}_p}{dt} - \frac{\tau_{eff}}{V_I} \frac{dV_I}{dt} - \frac{kT}{V_I} \frac{1}{A_I} \frac{dA_I}{dt} + \frac{H\dot{\varepsilon}_p}{M} \qquad (2.13a)$$

However, it was established by Krausz and Eyring [27] that in the high stress and low temperature range the activation volume is independent of stress (and hence independent of time): no structural change. Also, the evaluation of experimental results [27,106,107] for some materials has shown that when the total strain amplitude is small, the component of the shear stress rate due to mobile dislocation density (and/or microstructure) changes is negligible compared to the components due to the rate of change of the plastic strain rate and to the rate of change of the internal stress. Hence the applied stress rate within the high stress and low temperature range (region I) and during strain controlled cyclic deformation can be approximated as

$$\dot{\tau}_a\Big|_{T,\ struct.} \simeq \frac{kT}{V_I} \frac{1}{\dot{\varepsilon}_p} \frac{d\dot{\varepsilon}_p}{dt} + \frac{H}{M} \dot{\varepsilon}_p \qquad (2.13b)$$

While the above assumptions are physically reasonable, they are by no means necessary and should not be taken as restrictions on the validity of the theory. The combination of Eqs. (2.2), (2.4), and (2.13b) results in

$$\frac{MkT}{EV_I}\frac{1}{\dot{\varepsilon}_p}\frac{d\dot{\varepsilon}_p}{dt} + \dot{\varepsilon}_p\left(1 + \frac{H}{E}\right) = \dot{\varepsilon}. \qquad (2.14)$$

The DE (2.14) describes the deformation behavior during strain controlled, cyclic deformation with increasing internal stress. The solution of the DE expresses the variation of the plastic strain rate with time. The analysis is, however, valid for cyclic deformation within region I, that is, the stress and temperature range where the plastic strain rate can be approximated with activation over a single energy barrier (Eq. (2.7)), and when the material structural characteristics do not change appreciably during cyclic deformation.

2.1.3 Solution of DE

Equation (2.14) is a nonlinear, first order DE that can be solved by using the method of variation of parameters [104]. According to the procedure, the nonlinear term of Eq.(2.14) is removed, leaving the linear part as

$$\frac{d\dot{\varepsilon}_p}{dt} - \frac{EV_I}{MkT}\dot{\varepsilon}_p\dot{\varepsilon} = 0. \qquad (2.15)$$

The complementary function, $\dot{\varepsilon}_{p,c}$, then is

$$\dot{\varepsilon}_{p,c} = \eta \exp \frac{EV_I \varepsilon}{MkT} \tag{2.16}$$

where η is a constant which must be evaluated from initial conditions. The particular integral is obtained by allowing the constant η to vary with respect to time. Substituting Eq. (2.16) into Eq. (2.14) with $\eta=\eta(t)$ leads to

$$\frac{1}{\eta^2} \frac{d\eta}{dt} + \frac{EV_I\left(1 + \frac{H}{E}\right)}{MkT} \exp \frac{EV_I \varepsilon}{MkT} = 0$$

or

$$-\frac{d\eta}{\eta^2} = \frac{EV_I\left(1 + \frac{H}{E}\right)}{MkT} \exp \frac{EV_I \varepsilon}{MkT}\, dt \tag{2.17}$$

Integration of Eq.(2.17) results in

$$\frac{1}{\eta} = \frac{EV_I\left(1 + \frac{H}{E}\right)}{MkT} \int_0^t \exp \frac{EV_I \varepsilon}{MkT}\, dt + \frac{1}{\eta_0}$$

or

$$\eta = \frac{1}{\frac{EV_I\left(1 + \frac{H}{E}\right)}{MkT} \int_0^t \exp \frac{EV_I \varepsilon}{MkT}\, dt + \eta_1} \tag{2.18}$$

where $\eta_1 = \frac{1}{\eta_0}$ = constant. The particular integral then is

$$\dot{\varepsilon}_p = \frac{\exp \frac{EV_I\varepsilon}{MkT}}{\frac{EV_I(1+\frac{H}{E})}{MkT} \int_0^t \exp \frac{EV_I\varepsilon}{MkT}\, dt + \eta_1} . \qquad (2.19)$$

Because at time t=0, $\varepsilon=\varepsilon_0$, and $\tau_a=\tau_0$, the integration constant, η_1, is expressed as

$$\eta_1 = \frac{\exp \frac{EV_I\varepsilon_0}{MkT}}{A_I \exp \frac{V_I(\tau_0-\tau_i^0)}{kT}} .$$

The constitutive equation of strain controlled cyclic deformation within the specific stress and temperature range is, therefore, described as

$$\dot{\varepsilon}_p = \frac{A_I \exp \frac{EV_I\varepsilon}{MkT}}{\frac{EA_IV_I(1+\frac{H}{E})}{MkT} \int_0^t \exp \frac{EV_I\varepsilon}{MkT}\, dt + \exp\left[\frac{V_I}{MkT}\{E\varepsilon_0 - M(\tau_0-\tau_i^0)\}\right]} . \qquad (2.20)^1$$

It follows immediately from Eq.(2.20) that while the plastic strain rate is a function of time, material structural characteristics, and temperature,

---

1 In Eq. (2.20) the plastic strain rate becomes indeterminate at finite time t when $\varepsilon, \varepsilon \to \infty$. However, at high strain rates the velocity of dislocations is limited by the velocity of transverse sound waves in the material. Thermally activated dislocation movement ends - fades out - at strain rates several orders of magnitude below this [27,30].

it does not depend on time derivatives for any quantity and is, therefore, continuous upon a discontinuous change in strain rate or stress rate. This behavior of the constitutive equation is a common property of the viscoplasticity theories (or unified theories) [23-26] where the total strain rate is the sum of the plastic strain rate and the elastic strain rate (Eq. 2.2).

2.1.4 Stress-Time Relationship

Region I

The stress rate-time relationship during strain controlled cyclic loading is evaluated from Eqs. (2.2), (2.4), and (2.20) as

$$\dot{\tau}_a = \frac{E\dot{\varepsilon}}{M} - \frac{\frac{EA_I}{M}\exp\frac{EV_I\varepsilon}{MkT}}{\frac{EA_IV_I(1+\frac{H}{E})}{MkT}\int_0^t \exp\frac{EV_I\varepsilon}{MkT}\,dt + \exp\left[\frac{V_I}{MkT}\{E\varepsilon_0 - M(\tau_0-\tau_i^0)\}\right]} \quad (2.21)$$

The applied stress is then expressed in function of time, after integration of Eq. 2.21, as

$$\tau_a = \tau_0 + \frac{E(\varepsilon-\varepsilon_0)}{M} - \frac{kT}{V_I(1+\frac{H}{E})}\ln\left[\frac{EA_IV_I(1+\frac{H}{E})}{MkT}\exp\frac{V_I(\tau_0-\tau_i^0)}{kT}\int_0^t \exp\frac{EV_I(\dot{\varepsilon}-\dot{\varepsilon}_0)}{MkT}\,dt + 1\right] + C_1 \quad (2.22)$$

where C_1 is a constant of integration. Because at $t=0$, $\tau_a=\tau_0$, and $\varepsilon=\varepsilon_0$, it follows that $C_1=0$. Over the temperature, stress, and time range (region I)

where thermally activated plastic flow in strain controlled cyclic deformation can be approximated with activation over a single energy barrier, Eq. (2.22) can be used to evaluate the constitutive parameters, V_I and A_I, for the cyclic deformation process.

Eq. 2.22 describes the stress-time relationship during the strain controlled cyclic deformation, within the specific stress and temperature range. The applied stress is expressed in function of time, temperature, initial loading condition, and the material structural characteristics ($E, H, V_I, \Delta G_I^{\neq}$, and ρ_t). However, the total strain, ε, must be known explicitly before the applied stress can be evaluated. Depending on the function ε, the integration on the RHS of Eq. (2.22) may be difficult to evaluate analytically. The simplest function of the total strain is $\varepsilon=\varepsilon_0$=constant. It represents the condition during a stress relaxation experiment carried out on a very rigid machine. The stress-time relation during stress relaxation, therefore, follows from Eq. (2.22) and is expressed as

$$\tau_a = \tau_0 - \frac{kT}{V_I(1+\frac{H}{E})} \ln \left[\frac{EA_I V_I(1+\frac{H}{E})}{MkT} \left\{\exp \frac{V_I(\tau_0-\tau_i^0)}{kT}\right\} t + 1\right]. \quad (2.23)$$

Eq. (2.23) is formally identical to that derived by Wielke and Shoek [105] and also by Krausz and Eyring [27] (for H=0). It was widely utilized to describe stress relaxation in many materials (iron, Cu, Zn, Aℓ, steels, Pb, many polymers, graphite, etc.). The conclusion that follows from Eqs. (2.22) and (2.23) is an important one: stress relaxation is a special case of strain controlled cyclic deformation. Consequently, it is anticipated

that stress relaxation experiments can be used to measure the constitutive parameters, V_I and A_I, that represents the microstructure which can then be used in the development of the constitutive equation of the more complicated strain controlled cyclic deformation.

Region II

The constitutive equation for plastic deformation in Region II is expressed by Eq. (2.8). The derivation of the stress-time response during strain controlled cyclic loading, within this stress range, can be carried out using the procedure described in the previous section. The applied shear stress during cyclic deformation is then expressed in function of time as

$$\tau_a = \tau_0 + \frac{E(\varepsilon-\varepsilon_o)}{M} - \frac{kT}{V_{II}(1+\frac{H}{E})} \ln \left[\frac{EA_{II}V_{II}(1+\frac{H}{E})}{MkT} \exp \frac{V_{II}(\tau_0-\tau_i^0)}{kT} \int_0^t \exp \frac{EV_{II}(\varepsilon-\varepsilon_0)}{MkT} dt + 1\right] \quad (2.24)$$

while during stress relaxation, $\varepsilon=\varepsilon_0$=constant and the stress-time relation becomes

$$\tau_a = \tau_0 - \frac{kT}{V_{II}(1+\frac{H}{E})} \ln \left[\frac{EA_{II}V_{II}(1+\frac{H}{E})}{MkT} \left\{\exp \frac{V_{II}(\tau_0-\tau_i^0)}{kT}\right\} t + 1\right]. \quad (2.25)$$

Transition Stress Range

While the rate of plastic flow in regions I and II can be approximated with activation over the energy barriers I and II, respectively, plastic flow in the transition stress range is controlled by activation over the two consecutive energy barriers. If $\xi(t)$ is defined as

$$\xi_{I,II} = \int_0^t \exp \frac{EV_{I,II}(\varepsilon-\varepsilon_0)}{MkT}\, dt, \qquad (2.26)^2$$

then it can be shown from Eqs. (2.22) to (2.25) that when the first term in the argument is much greater than unity,

$$\xi_{I,II} = \frac{MkT}{EV_{I,II}(1+\frac{H}{E})A_{I,II}} \exp\left[\frac{V_{I,II}}{kT}\left\{(1+\frac{H}{E})\left(\frac{E(\varepsilon-\varepsilon_0)}{M}-\tau_a\right)+\frac{\tau_0 H}{E}+\tau_i^0\right\}\right]. \qquad (2.27)^2$$

Recently, Mshana and Krausz [106,107] have shown that when the applied stress is measured in function of strain cycles such that t=mp, where m is the number of cycles and p is the cycle period, the change in the shear stress≠, $-\Delta\tau$, is a linear function of the natural logarithm of time. Consequently, a method was developed to determine the constitutive

---

≠ The shear stress change is defined as $\Delta\tau = \tau_a - \tau_0$ where τ_a is the shear stress at the end of the m-th cycle. If mean shear stress change is desired, then it is calculated as

$$\Delta\tau = \tau_a - (\tau_0 + \frac{E\varepsilon_{mean}}{M}).$$

2 ξ_I (and hence t_I) is calculated using V_I and A_I in the equations while for ξ_{II} (and hence t_{II}), A_{II} and V_{II} are used. For stress relaxation $\varepsilon=\varepsilon_0$=constant and thus ξ=t.

parameters from the analysis of experimental results in regions I and II. Fig. 2.2 illustrates regions I and II, and the transition stress range on a stress change versus natural logarithm of time coordinate system. For consecutive processes or energy barriers, the slowest process controls the rate of plastic flow. Hence, in region I, $\xi_{II} << \xi_I$ and $\xi_I \propto t=mp$ while in region II, $\xi_I << \xi_{II}$ and $\xi_{II} \propto t=mp$. Because at $t=mp$ $\epsilon-\epsilon_0=0$ [106,107], the deformation time t ($\xi_I+\xi_{II} \propto t$) within the transition stress range can be evaluated from Eqs. (2.26) and (2.27) (using the constitutive parameters determined from the analysis of the experimental results in regions I and II) in function of the applied stress. Thence, from the constitutive equations, the stress-time response is fully described in regions I and II, and in the transition stress range.

It follows from Fig. 2.2 and from Eq. (2.2) that at $t=mp$ where $\epsilon=\epsilon_0$ [106,107], the plastic strain rate in region I is described as

$$\dot{\epsilon}_{pI} \simeq - \frac{M\dot{\tau}}{E} = \frac{MkT}{Et_I V_I} \qquad (2.28a)$$

(with $\xi_I \propto t_I = t$) while in region II it is expressed as

$$\dot{\epsilon}_{pII} \simeq - \frac{M\dot{\tau}}{E} = \frac{MkT}{EV_{II}t_{II}} \qquad (2.28b)$$

where $\xi_{II} \propto t_{II} = t$. At the transition stress, τ_a^*, $\dot{\epsilon}_{pI}=\dot{\epsilon}_{pII}$ and hence $V_I t_I = V_{II} t_{II}$. Eq. (2.9) then becomes [36]

$$\dot{\epsilon}_p^* = \frac{\dot{\epsilon}_{pI}}{2} = \frac{MkT}{2EV_I t_I} = \frac{MkT}{2EV_{II}t_{II}} \qquad (2.28c)$$

where $\dot{\varepsilon}_p^*$ is defined as the plastic strain rate at the transition stress. The "waiting times" $t_I(\xi_I \propto t_I)$ and $t_{II}(\xi_{II} \propto t_{II})$ for activation over each energy barrier are evaluated from Eqs. (2.26) and (2.27). Consequently,

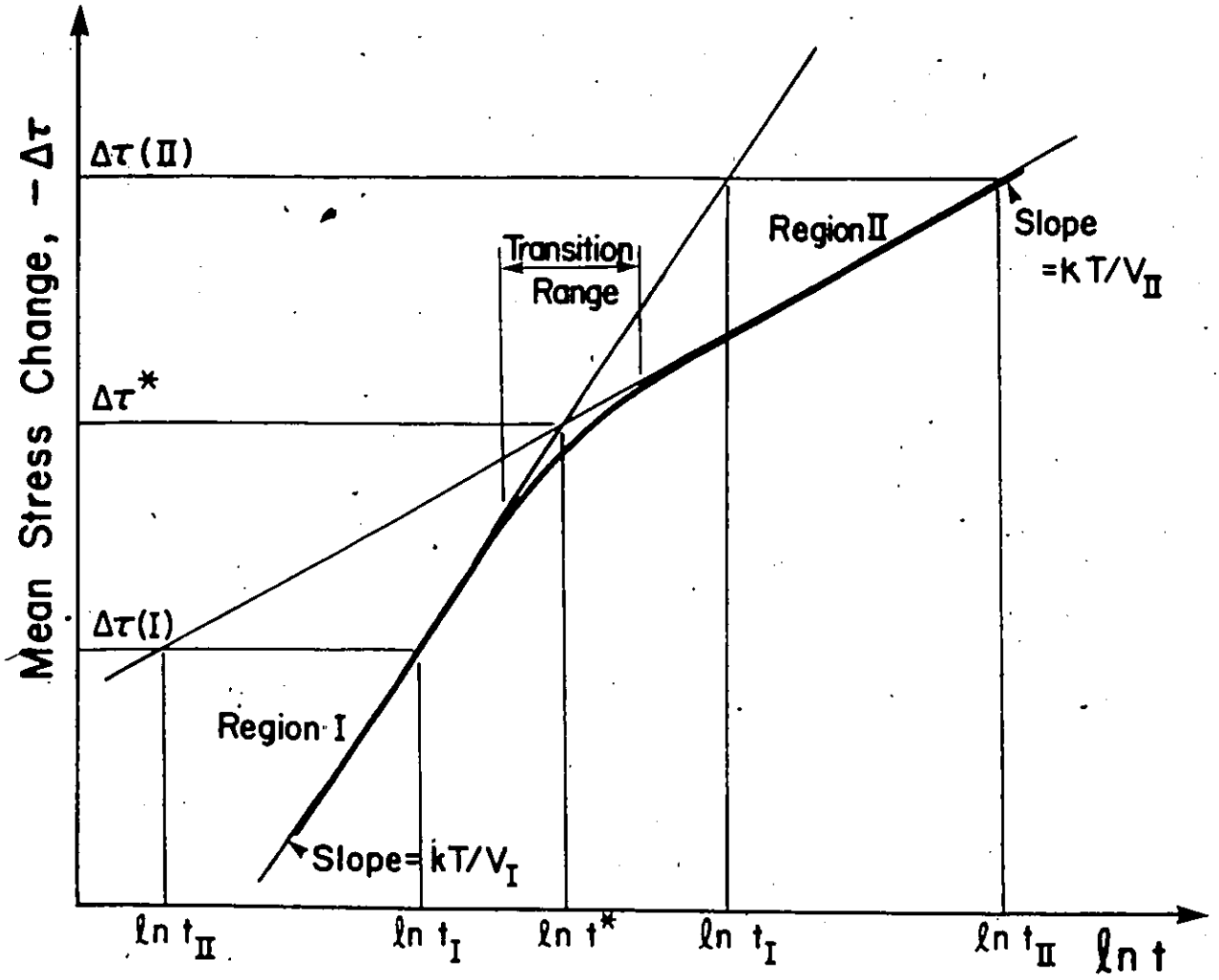

Figure 2.2. The figure illustrates schematically the stress ranges for regions I and II, and the transition stress range on a stress change versus natural logarithm of time coordinate system. In region I, $t_{II} \ll t_I$ and $t \approx t_I$ while in region II, $t_I \ll t_{II}$ and $t \approx t_{II}$. Within the transition stress range, $t = t_I + t_{II}$. It was assumed in the analysis of constitutive parameters that $H = 0$.

$$\dot{\varepsilon}_p^* = \frac{\dot{\varepsilon}_{p,0}}{2} \exp - \frac{\Delta G^*}{kT} \tag{2.29}$$

where $\Delta G^* = \Delta G_I^{\neq} - V_I \tau_a^* = \Delta G_{II}^{\neq} - V_{II} \tau_a^*$ and $\dot{\varepsilon}_{p,0} = \delta \rho_t \frac{kT}{h}$.

Accordingly [36], the temperature dependence of $\dot{\varepsilon}_p^*$ allows for the determination of ΔG^* and hence $\Delta G_I^{\neq}$ and $\Delta G_{II}^{\neq}$. The Gibb's free energy at the transition stress, ΔG^*, is defined as

$$\Delta G^* = - k \frac{\partial \ell n(\dot{\varepsilon}_p^*/T)}{\partial(1/T)} . \tag{2.30}$$

2.2 LOAD CONTROLLED CYCLIC LOADING

2.2.1 Constant Internal Stress

In the simplest deformation kinetics where thermally activated plastic flow in load controlled cyclic deformation can be approximated with activation over a single energy barrier, the constitutive equation, as before, is expressed as

$$\dot{\varepsilon}_p = \left(\frac{1}{M}\right) b \rho_t \frac{kT}{h} \bar{\ell} \exp - \frac{\Delta G_I^{\neq} - V_I \tau_{eff}}{kT} . \tag{2.31}$$

The mobile dislocation density, ρ_t, is essentially an experimentally measurable quantity and is expressed in terms of the stress or strain. A widely used form was introduced by Johnston [108], i.e.

$$\rho_t = \rho_t^0 + B\varepsilon_p , \tag{2.32}$$

where ρ_t^0 is the mobile dislocation density measured at the beginning of plastic flow and is thus an empirical parameter that represents the previous deformation (state of the structure) history. It is outside of the theory of deformation kinetics and of the theory used here: it is also a microstructural feature to be measured by the method given in this report. The factor B is also measured by direct dislocation density observation and expresses the multiplication of dislocations in function of the strain. Equations (2.31) and (2.32) can be combined and rearranged as

$$\frac{d\varepsilon_p}{\rho_t^0 + B\varepsilon_p} = A_I^1 \exp \frac{V_I \tau_{eff}}{kT}\, dt \qquad (2.33)$$

where $A_I^1 = A_I/\rho_t$. For the purpose of the present discussion, it is considered that cyclic plastic deformation takes place at constant internal stress. During load controlled cyclic deformation, the applied stress is a periodic, random, or complex function of time. If y(t) is defined as

$$y = \int_0^t \exp \frac{V_I(\tau_a - \tau_i^0)}{kT}\, dt, \qquad (2.34)$$

then the integration of Eq. (2.33) leads to

$$\frac{1}{B} \ln \left(1 + \frac{B\varepsilon_p}{\rho_t^0}\right) = A_I^1\, y$$

or $$\varepsilon_p = \frac{\rho_t^0}{B} \left[\exp A_I^1 B y - 1\right]. \qquad (2.35)$$

That is, when cyclic plastic deformation can be approximated with activation over a single energy barrier and occurs by dislocation movement and multiplication, the plastic strain increases exponentially with time since $t \propto y$. However, as straining proceeds, some of the mobile dislocations may lose their mobility through interactions with other dislocations (annihilation), pinning by solute atoms or will be lost by emission through the surface. Microstructural studies [9] have shown that during cyclic loading, the mobile dislocation density of some materials increases rapidly at the beginning of cycling and reaches saturation after a few cycles. Hence, in the lim $B \to 0$, Eq. (2.35) becomes

$$\varepsilon_p = A_I y. \tag{2.36}$$

The total strain, ε, is then expressed as

$$\varepsilon - \varepsilon_0 = M \frac{(\tau_a - \tau_0)}{E} + A_I y. \tag{2.37}$$

For creep, $\tau_a = \tau_0$ = constant and the parameter y then becomes

$$y = \{\exp \frac{V_I(\tau_0 - \tau_i^0)}{kT}\} t. \tag{2.38}$$

Hence the total strain is expressed in function of time as

$$\varepsilon = \varepsilon_0 + [A_I \exp \frac{V_I(\tau_0 - \tau_i^0)}{kT}] t \tag{2.39a}$$

while the strain rate is

$$\dot{\varepsilon} = A_I \exp \frac{V_I(\tau_0 - \tau_i^0)}{kT}. \qquad (2.39b)$$

The total strain is not proportional to the logarithm of time because τ_i = constant: a measure of constant microstructure. The conclusion that follows from Eqs. (2.37) and (2.39) is an important one: creep deformation process is a special case of stress controlled cyclic deformation. Consequently, it is anticipated that creep tests can be used to measure the constitutive parameters A_I and V_I that represents the microstructure which can then be used in the development of the constitutive equation of the more complicated cyclic deformation. Hence, over the temperature, stress and time range where thermally activated flow in stress controlled cyclic deformation and creep can be approximated with activation over a single energy barrier, Eq. (2.39) can be used to evaluate the constitutive parameters for the cyclic stress deformation process at constant internal stress.

2.2.2 Linear Work Hardening

Consider that during load controlled cyclic loading, the internal stress increases linearly with the plastic strain as

$$\tau_i = \tau_i^0 + \frac{H}{M} \varepsilon_p.$$

In the high stress and low temperature range where the rate of plastic flow

can be approximated with activation over a single energy barrier, the constitutive equation is

$$\dot{\varepsilon}_p = A_h \exp\left[\frac{V_h}{kT}\left(\tau_a - \tau_i^0 - \frac{H}{M}\varepsilon_p\right)\right]$$

or

$$\int_0^{\varepsilon_p} \exp\frac{V_h H \varepsilon_p}{kTM}\, d\varepsilon_p = A_h \int_0^t \exp\left[\frac{V_h}{kT}\left(\tau_a - \tau_i^0\right)\right] dt \qquad (2.40)$$

where the subscript h signifies that the activation parameters are associated with hardening mechanism, such as dislocation pile-up against obstacles [20], intersection mechanism [27] etc. It is considered that the variation of the mobile dislocation density with time is negligible. Krausz and Craig [86], Wyatt [85], and others [27,109,110] have shown that the activation volume, V_h, evaluated from constant stress creep and from stress relaxation experimental results is inversely proportional to the initial stress τ_0. In the special case of uniform obstacles, Essmann [111] showed that $V_h \propto \ell \propto 1/\tau_0$, where ℓ is the mean free length of mobile dislocation segments. Hence during (constant amplitude) cyclic loading, the activation volume $V_h \propto 1/\tau_{max}$ = constant since the changes in the mean free length of the mobile dislocation segments are irreversible. The plastic strain is, therefore, obtained from the integration of Eq. (2.40) as

$$\varepsilon_p = \frac{kTM}{V_h H} \ln\left[\frac{V_h H A_h}{kTM} \int_0^t \exp\frac{V_h(\tau_a - \tau_i^0)}{kT}\, dt + 1\right] . \qquad (2.41)$$

For constant stress creep, $\tau_a = \tau_0$ = constant. Eq. (2.41) then becomes

$$\epsilon_p = \frac{kTM}{V_h H} \ln \left[\frac{V_h H A_h}{kTM} \left\{\exp \frac{V_h(\tau_0 - \dot{\tau}_i^0)}{kT}\right\} t + 1\right]. \qquad (2.42)$$

Eq. 2.42 describes low temperature creep in function of time. When the first term in the argument is much greater than unity, the plastic strain versus the natural logarithm of time relation is represented by a straight line. This has been found to be the behavior in numerous experiments [27,85,86]. The slope of the curve is inversely proportional to the activation volume and from this V_h can be evaluated.

The conclusion that follows from Eq. (2.41) and (2.42) is an important one; creep deformation process is a special case of cyclic stress hardening. Consequently, it is anticipated that creep tests can be used to measure the constitutive parameters V_h and A_h that represents the microstructure which can then be used in the development of the constitutive equation of the more complicated cyclic stress hardening process. Hence, over the temperature, stress, and time range where thermally activated plastic flow can be approximated with activation over a single energy barrier, Eq. (2.42) can be used to evaluate the constitutive parameters for the cyclic (stress) hardening process.

Fig. 2.3 shows schematically a triangular stress wave form often used in stress controlled cyclic loading experiments. The applied stress for the first cycle is expressed in function of time as

$$\tau_a = \begin{cases} \tau_0 - \dfrac{2\tau_r t}{p} & \text{when } 0 < t < \dfrac{p}{2} \\ \tau_0 + \dfrac{2\tau_r}{p}(t-p) & \text{when } \dfrac{p}{2} < t < p \end{cases} \tag{2.43a}$$

where τ_r is the shear stress amplitude or range. If $\psi(t)$ is defined as

$$\psi = \int_0^t \exp \frac{V_h(\tau_a - \tau_i^0)}{kT}\, dt, \tag{2.43b}$$

then it can be shown that when t=mp, the integral becomes

$$\psi = \frac{kTt}{V_h \tau_r} \exp \frac{V_h(\tau_0 - \tau_i^0)}{kT} \left[1 - \exp - \frac{V_h \tau_r}{kT}\right]. \tag{2.44}$$

For constant stress, $\tau_a = \tau_0$ = constant and

$$\psi\Big|_\tau = \left\{\exp \frac{V_h(\tau_0 - \tau_i^0)}{kT}\right\} t. \tag{2.45}$$

It is evident from Eqs. (2.44) and (2.45) that

$$\psi\Big|_\tau > \psi.$$

Consequently, it follows from Eqs. (2.41) and (2.42) that the plastic strain (accumulation) is smaller under the cyclic stress than that under constant stress (equal to the peak or maximum stress during cyclic loading)

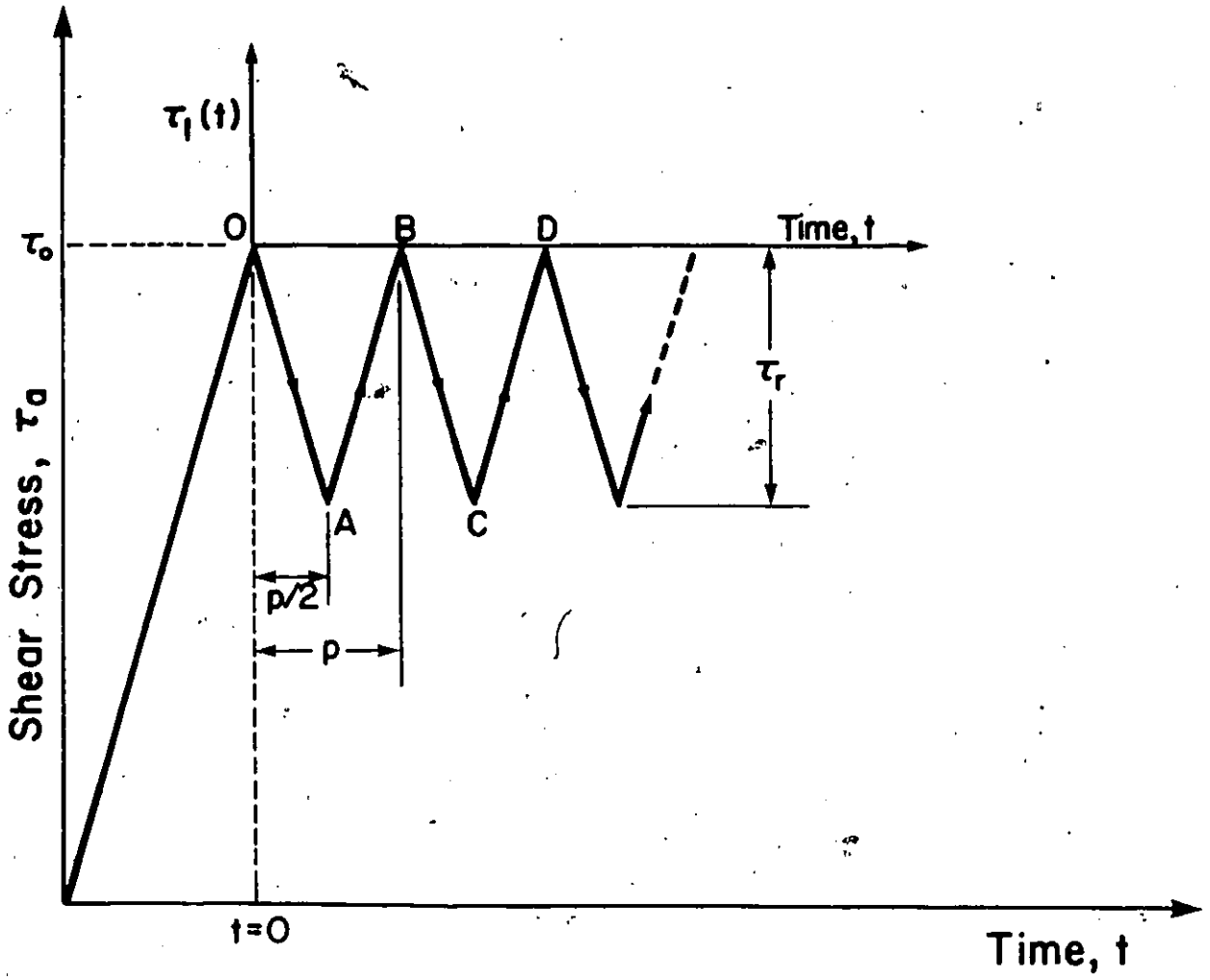

Figure 2.3 Schematic representation of stress controlled cyclic loading. The applied stress, τ_a is expressed as $\tau_a = \tau_0 - \tau_1(t)$ where τ_1 is the cyclic stress. τ_r is the shear stress amplitude or range, p is the period, and τ_0 is the initial stress at t=0.

creep. When the first term in the argument (Eqs. (2.41) and (2.42)) is much larger than unity, the strain rate for creep and for stress controlled cyclic loading are identical. It follows from the analysis that the cyclic stress hardens the material.

Fig. 2.4 shows the effect of cyclic stress hardening on plastic strain accumulation (with loading cycles). The curves were calculated by using Eq. (2.42) for creep and Eq. (2.41) for cyclic loading. The figure shows that the accumulated plastic strain is smaller under cyclic stress than that under constant stress (equal to the maximum stress during cyclic loading) creep. Also, it follows from Eqs. (2.41) and (2.42) and from Fig. 2.4 that during the first few cycles of cyclic loading, the plastic strain rate is smaller under the cyclic stress than that under constant stress creep. However, after sufficiently long time when the first term in the argument of the equations is much greater than unity, the plastic strain rates for creep and cyclic deformation are almost identical. The figure also shows that the greater the stress amplitude the smaller is the strain accumulation with cycles. The cyclic stress thus hardens the material. This behavior is sometimes referred to as "cyclic stress retardation".

The phenomenon of cyclic stress retardation has been observed experimentally by several investigators [19, 112-114]. Shetty and Meshii [19] observed the cyclic stress hardening behavior in aluminum single crystals that were tested at 77K. The behavior was also observed in zinc [112] at 303K, and in many other materials [113, 114]. The experimental observations confirm the results of the present analysis that the strain and strain rates are smaller under cyclic stress than those under constant stress (equal to the peak stress) creep. In most of these studies, a rectangular stress wave from with a minimum stress equal to zero

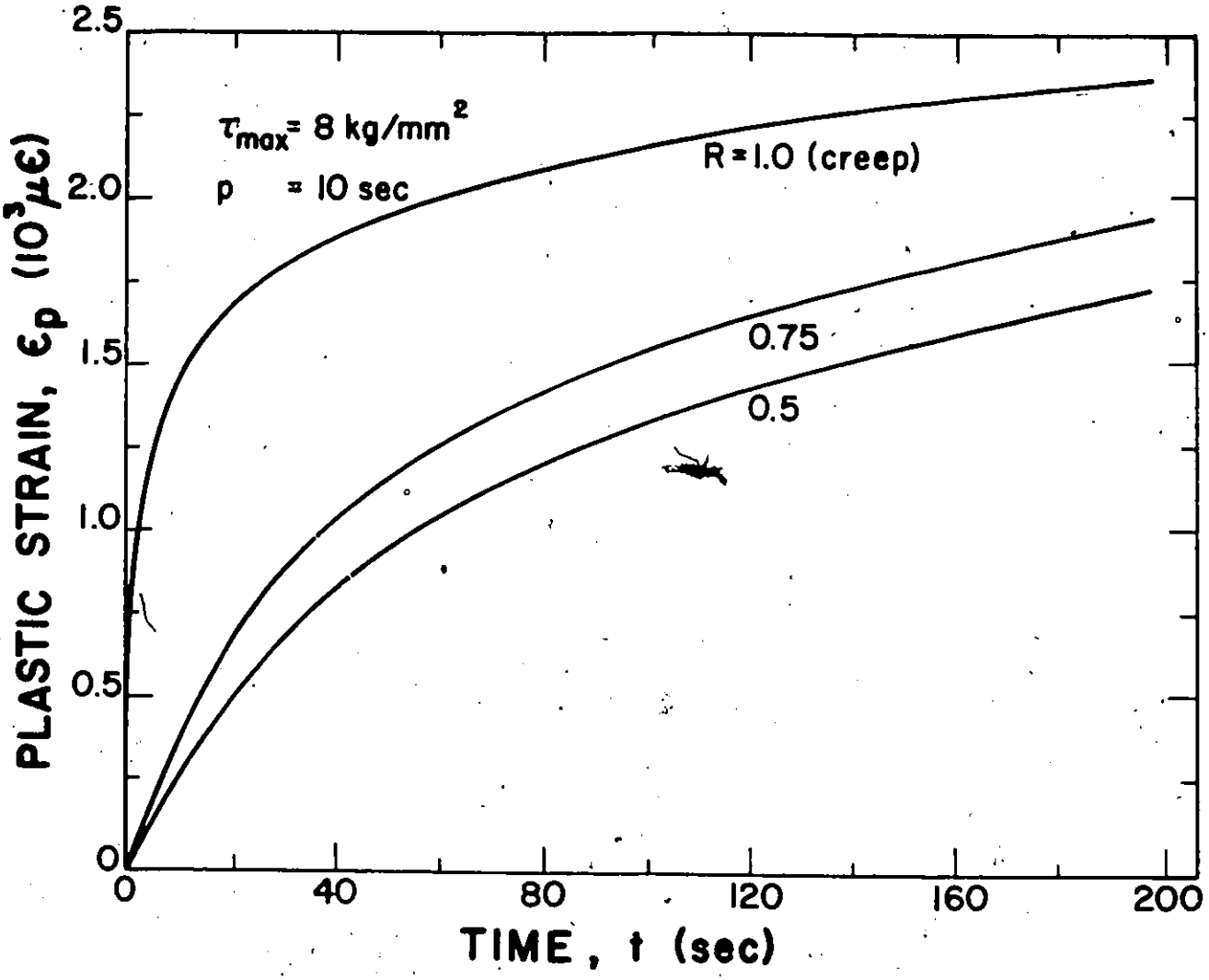

Figure 2.4. The figure shows the effect of cyclic stress hardening on the accumulated plastic strain. The curves were calculated using Eq. (2.42) for R=1 (creep) and Eq. (2.41) for cyclic loading. The parameters are: $V_h = 4.3/\tau_{max}$ eV mm^2/kg, $\Delta G_h^{\ddagger} = 3.55$ eV, H/M = 157 kg/mm^2, $\tau_i^0 = 1.78$ kg/mm^2, T=300K, $\delta\rho_t kT/h = 12$ sec^{-1}, and $\epsilon_{p,o} = 0$.

was used. Because of the wide stress range, it is likely that the deformation kinetics and hence the constitutive equations of plastic flow for stress controlled cyclic loading and creep were different. The analysis presented here indicates that within the limited high stress and low temperature range where the rate of plastic flow in both creep and cyclic stress hardening can be approximated with activation over a single energy barrier, the long range strain rates in creep and cyclic loading are identical while the accumulated cyclic strain is smaller than the creep strain (measured at the peak stress of cyclic loading). Consequently, it appears that over the high stress and low temperature range, the constitutive parameters determined from the analysis of creep test results can be used to predict the cyclic hardening behavior using the equations developed here.

2.2.3 Cyclic Softening and Hardening

It has been observed experimentally [1,2,3,7,19,20,112-114] that creep rate in metals either increases and/or decreases upon cyclic loading depending on the combination of the experimental variables (temperature, stress amplitude, frequency etc.). That is, load cycling can cause either softening of the metal which leads to increase in the strain rate or hardening which is associated with decrease in strain rate. Often, however, the hardening and softening processes are not separate: they operate simulteneously [2,7,19,20] during cyclic deformation. In static creep, the decrease in creep rate that is observed during the primary

stage is, for instance, due to the piling up of dislocations against obstacles in the slip plane. The application of a cyclic stress and the resulting to and fro motion of dislocations may increase the mobility of the piled-up dislocations by assisting them to overcome their obstacles, leading to an increase in the creep rate.

A simple approximation to express the deformation mechanism of cyclic softening and hardening was proposed by Shetty et al [20]. It was considered that the internal stress is built up (hardening) during the loading part of the cycle and is relaxed (softening) upon unloading. Consequently, the internal stress also varies in a cyclic manner. The physical mechanism is, for example, that dislocations are piled-up during loading and are dispersed during unloading.

In the simplest deformation kinetics where the plastic flow during the dislocation pile-up (hardening) and dislocation dispersening (softening) can be approximated with activation over single energy barriers, the constitutive equation is

$$\dot{\varepsilon}_{p,h} = A_h \exp \frac{V_h(\tau_a - \tau_i)}{kT} \quad (2.46a)$$

for the hardening process and

$$\dot{\varepsilon}_{p,s} = A_s \exp \frac{V_s(\tau_a - \tau_i)}{kT} \quad (2.46b)$$

for the softening process. The subscript s signifies that the activation parameters are associated with the softening process. The internal stress during hardening is expressed as

$$\tau_i = \tau_i^A + \frac{H}{M} \epsilon_p \qquad (2.47)$$

where τ_i^A is the internal stress at the beginning of the loading part of the cycle. It is assumed that during unloading the internal stress decreases in function of time as

$$\tau_i = \tau_i^0 - Ct \qquad (2.48)$$

where $0 < t < \frac{p}{2}$, τ_i^0 is the internal stress at the beginning of the unloading part of the cycle, and C is a proportionality constant (softening coefficient).

Consider the first cycle of the triangular stress wave form shown in Fig. 2.3. At the beginning of load cycling, the specimen is unloaded from 0 to A. Within the time interval, the plastic strain is evaluated from Eqs. (2.46b) and (2.48) as

$$\epsilon_p = \epsilon_{p,0} + A_s \int_0^t \exp \frac{V_s(\tau_a - \tau_i^0 + Ct)}{kT} dt \qquad (2.49)$$

where $\epsilon_{p,0}$ is the plastic strain at the beginning of unloading. Similarly, upon loading the specimen from A to B, Eqs. (2.46a) and (2.47) lead to

$$\varepsilon_p = \varepsilon_{p,A} + \frac{kTM}{V_h H} \ln \left[\frac{V_h H A_h}{kTM} \int_{p/2}^{t} \exp \frac{V_h(\tau_a - \tau_i^A)}{kT} dt + 1\right] \quad (2.50)$$

where $\varepsilon_{p,A}$ and τ_i^A are the plastic strain and internal stress ($= \tau_i^0 - \frac{Cp}{2}$), respectively at the beginning of the loading process.

Figure 2.5a shows a typical strain-time response (for two loading cycles) during the alternating softening and hardening processes. The curve was calculated using Eqs. (2.49) and (2.50). OA and BC represent the softening portions of the two cycles while AB and CD represent the hardening parts.

During the unloading process, the plastic strain rate decreases since both the applied and internal stresses are decreasing. According to the physical model, the dislocations are dispersed from the obstacles. Upon loading, however, the dislocations are piled-up against obstacles and the applied and internal stresses increase with time. At the beginning of the loading process, the effective stress is low (after unloading) and it increases slowly with time. Consequently, the plastic strain increases slowly with time until the applied stress approaches the maximum value where the dislocations acquire enough energy (from the combined effect of the mechanical and thermal energy) to overcome the obstacles. The plastic strain then increases abrubtly. The alternating softening and hardening behavior is repeated for each loading cycle. Depending on the values of softening and work hardening coefficients (C and H), the decrease in

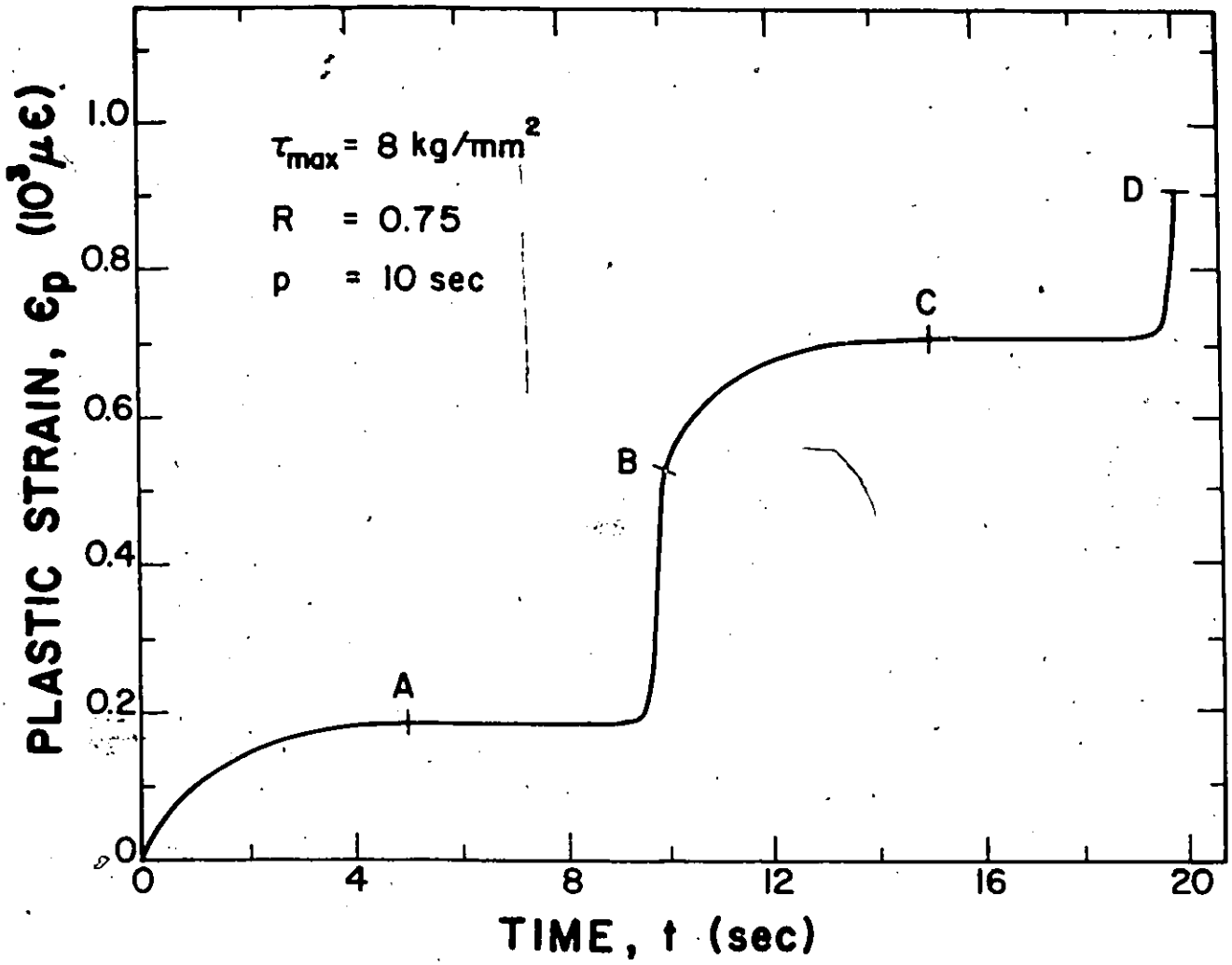
τ_{max} = 8 kg/mm^2
R = 0.75
p = 10 sec
A
B
C
D
PLASTIC STRAIN, ϵ_p ($10^3\mu\epsilon$)
TIME, t (sec)
0
0.2
0.4
0.6
0.8
1.0
4
8
12
16
20

Figure 2.5(a)

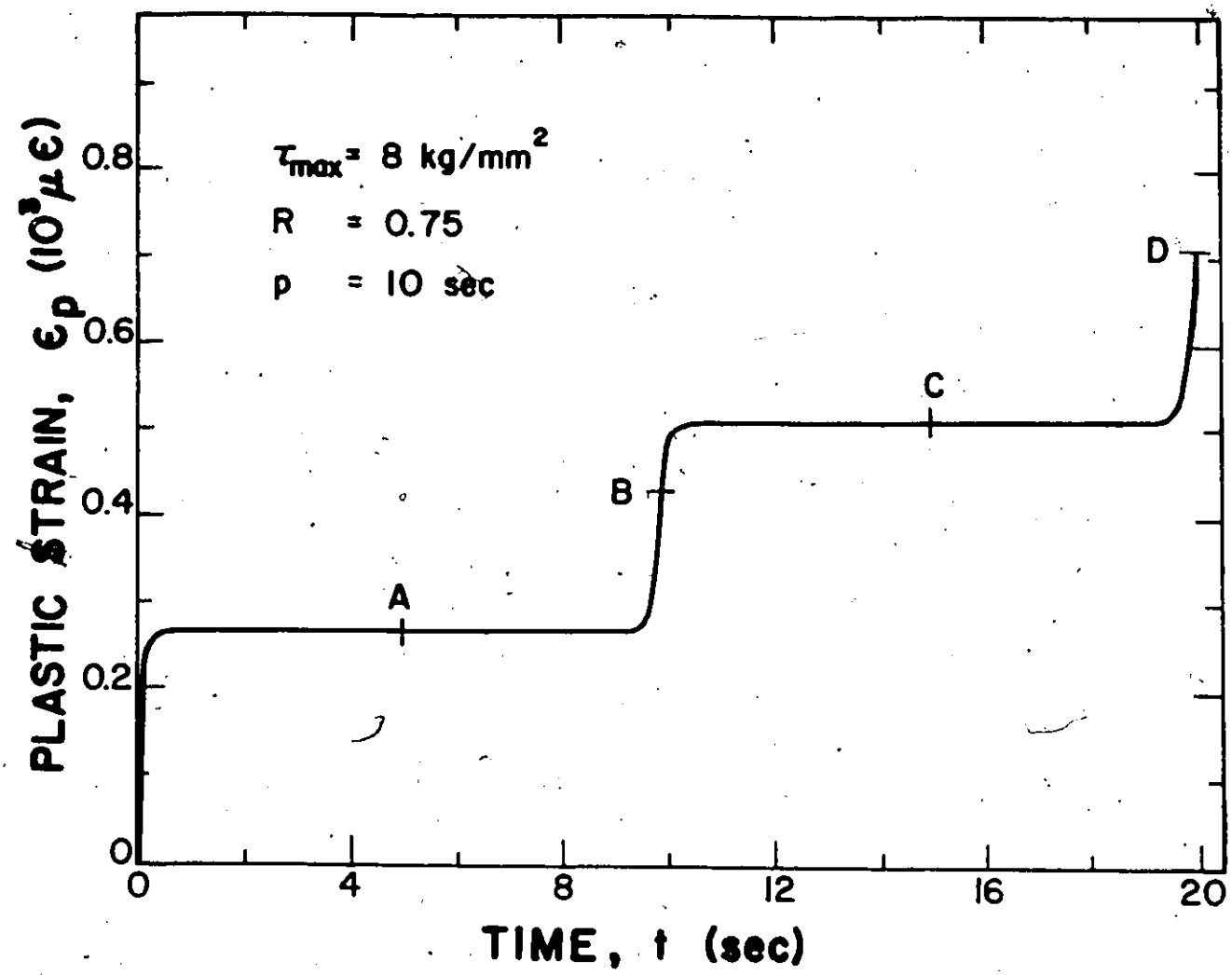

Figure 2.5 b.

Figure 2.5. The figure shows the variation of plastic strian in function of time during two loading cycles. (a) cyclic softening and hardening behavior, (b) Cyclic harderning. The curves were calculated using Eqs. (2.41) (2.49), and (2.50). The stress-time behavior is illustrated schematically in Fig. 2.3 (triangular stress wave form). The parameters are: $\Delta G_s^{\ddagger}$ = 0.61 eV, $\Delta G_h^{\ddagger}$ = 3.55 eV, T=300K, V_s/kT = 2.0 mm^2/kg , V_h = 4.3/τ_{max} eV mm^2/kg, H/M =157 kg/mm^2, τ_j^0 = 1.78 kg/mm^2, $\delta\rho_t kT/h$=12 sec., C=0.008 kg/mm^2 sec., and $\epsilon_{p,0}$=0.

internal stress during unloading may be different from the increase in the internal stress upon loading. The strain increase, therefore, may vary from one cycle to another.

Fig. 2.5b shows the cyclic deformation behavior when the softening effect is negligible and the material hardens both during loading and unloading. The strain-time response was calculated from Eq. (2.41). Upon unloading from O to A, the plastic strain initially increases rapidly; the initial strain rate is high since the internal stress is low. However, because the applied stress is decreasing with time and the internal stress is increasing (hence decreasing effective stress), the strain rate subsequently decreases to almost zero at the end of unloading (point A). On loading from A to B, the effective stress and hence the strain rate increases slowly (since the internal stress increases continuously) until the applied stress approaches the maximum value where the dislocations acquire enough energy to overcome the obstacles. The plastic strain then increases abruptly. The behavior during unloading and loading is repeated for each cycle: the plastic strain increases almost in a stepwise manner. However, due to the continuous increase in the internal stress, the greater the number of cycles, the smaller is the strain increase per cycle. It follows from Eq. (2.41) that the accumulated cyclic strain after sufficiently long time is proportional to the natural logarithm of time (or logarithm of the number of cycles).

It is apparent from Figs. 2.5a and 2.5b that after two cycles, the accumulated cyclic strain due to alternating softening and hardening is

higher than that due to cyclic hardening (without the softening effect). The figures also show that the plastic strain rate is continuous (>0), even upon a discontinuous change in stress rate (during cyclic loading).

Cyclic Strain Accumulation

The accumulated strain during cyclic softening and hardening can be evaluated by successively using Eqs. (2.49) and (2.50) for unloading and loading, respectively. The plastic strain after m cycles is then expressed as

$$\varepsilon_p-\varepsilon_{p,0} = \sum_{m=1}^{m} \{ A_s \int_0^{p/2} \exp \frac{V_s(\tau_a-\tau_{i,m}^0+ Ct)}{kT} dt + \frac{kTM}{V_h H} \ell n [\frac{V_h HA_n}{kTM}$$

$$\int_{p/2}^{p} \exp \frac{V_h(\tau_a-\tau_{i,m}^A)}{kT} dt + 1]\} \qquad (2.51a)$$

where $\tau_{i,m}^0$ and $\tau_{i,m}^A$ represent the internal stress at the m^{th} cycle, at the beginning of unloading and loading processes, respectively. For the triangular stress wave form (Fig. 2.3), the integrals can be evaluated using Eq. (2.43a) leading to an expression of the form

$$\varepsilon_p-\varepsilon_{p,o} = \sum_{m=1}^{m} \{ p \frac{kT}{V_s} \frac{A_s}{Cp-2\tau_r} \exp \frac{V_s(\tau_0-\tau_{i,m}^0)}{kT} [\exp \frac{V_s(Cp-2\tau_r)}{2kT} - 1]$$

$$+ \frac{kTM}{V_h H} \ell n [\frac{A_h Hp}{2M\tau_r} \exp \frac{V_h(\tau_0-\tau_{i,m}^A)}{kT} (1-\exp- \frac{V_h\tau_r}{kT}) + 1]\}. \qquad (2.51b)$$

Fig. 2.6 shows the accumulated cyclic strain (with cycles) in function of time (t=mp). The figure shows that after sufficiently long time, the creep strain and creep rates under cyclic softening and hardening are larger than the corresponding strain and strain rates at constant stress (equal to the maximum stress) creep. This behavior is referred to as "cyclic stress acceleration". The figure also shows that the larger the stress amplitude the smaller is the accumulated strain and strain rate. This behavior follows from the constitutive equation and also from the fact that during unloading, the applied and internal stresses decrease (hence the effective stress). Therefore, the larger the stress amplitude, the smaller is the mean effective stress and hence the smaller the strain rate.

The decrease in internal stress during the unloading process depends on the softening coefficient, C, while the increase in internal stress upon loading is proportional to the work hardening coefficient, H. Figs. 2.7 and 2.8 show the effect of softening and work hardening coefficients, respectively on creep and cyclic deformation behavior. It is evident from Fig. 2.7 that the greater the softening coefficient the greater is the decrease in internal stress and hence the larger is the accumulated cyclic strain and the rate of cyclic strain accumulation. On the other hand (Fig. 2.8), the greater the work hardening coefficient the larger is the increase in internal stress (during cyclic loading and creep) and hence the smaller is the strain and strain rate.

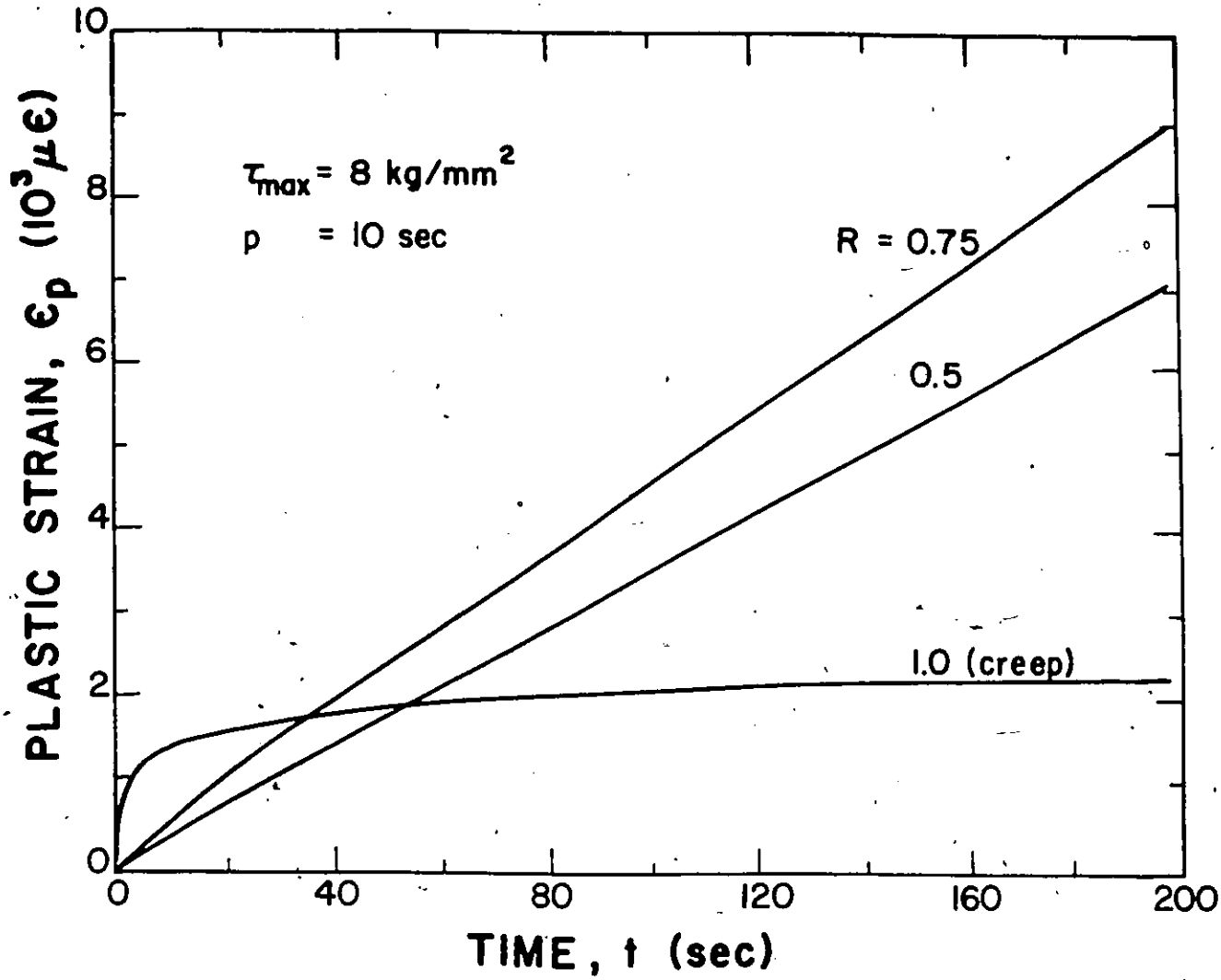

Figure 2.6. The figure shows the effect of cyclic softening and hardening on the accumulated plastic strain (with cycles). For creep, R=1 and the material hardens continuously while during cyclic loading, both softening and harderning takes place and hence the strain and strain rate are higher. The curves were calculated using Eq. (2.42) for creep and (2.51) for cyclic loading. The same parameters as in Fig. 2.5 were used.

Temperature Dependence

The temperature dependence of the cyclic softening and hardening behavior follows from the constitutive equation; the higher the temperature the higher is the strain rate and the accumulated cyclic strain. In the present model a dislocation (or flow unit) overcomes an obstacle when it has acquired enough energy from the combined effect of mechanical energy (due to the applied stress) and thermal energy (due to the random thermal vibrations of the dislocation). Because the mean amplitude of the thermal vibrations (or thermal energy) is proportional to temperature, it follows that for a given effective stress, the higher the temperature the higher is the energy supplied to the dislocation and hence the higher is the plastic strain rate. Fig. 2.9 shows typical deformation behavior during cyclic loading and creep at various temperatures. The solid lines represent the accumulated cyclic strain in function of number of cycles (or time) while the dashed lines represent the creep (at a stress equal to the peak stress) behavior. As expected from the model, the figure shows that for both creep and cyclic loading, the higher the temperature the higher is the accumulated plastic strain and strain rate. It was assumed that the deformation takes place within a low temperature range where annealing effects are negligible.

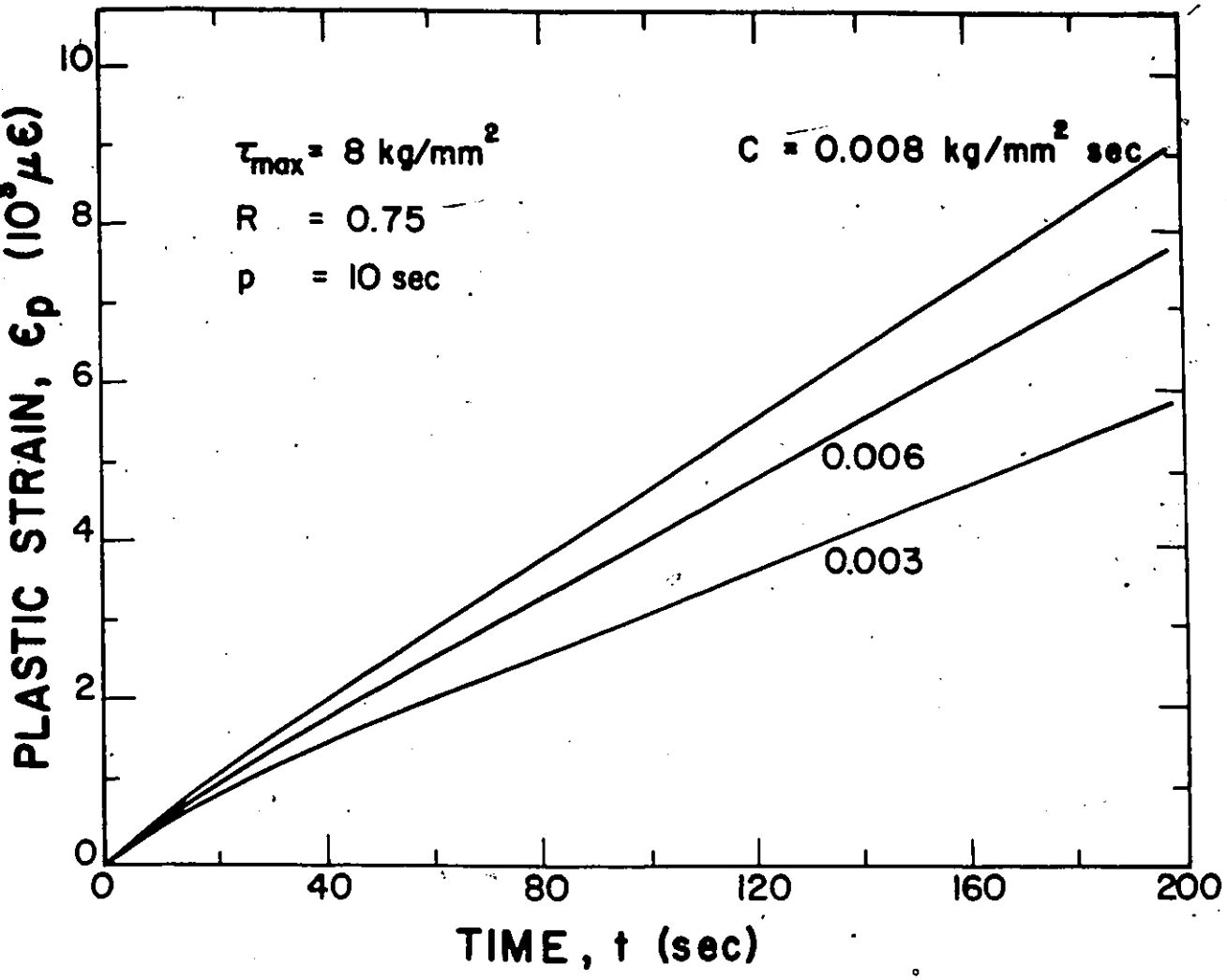

Figure 2.7. The figure shows the effect of softening pramater C on the cyclic deformation behavior. The curves were calculated using Eq. (2.51), with parameters indicated in Fig. 2.5.

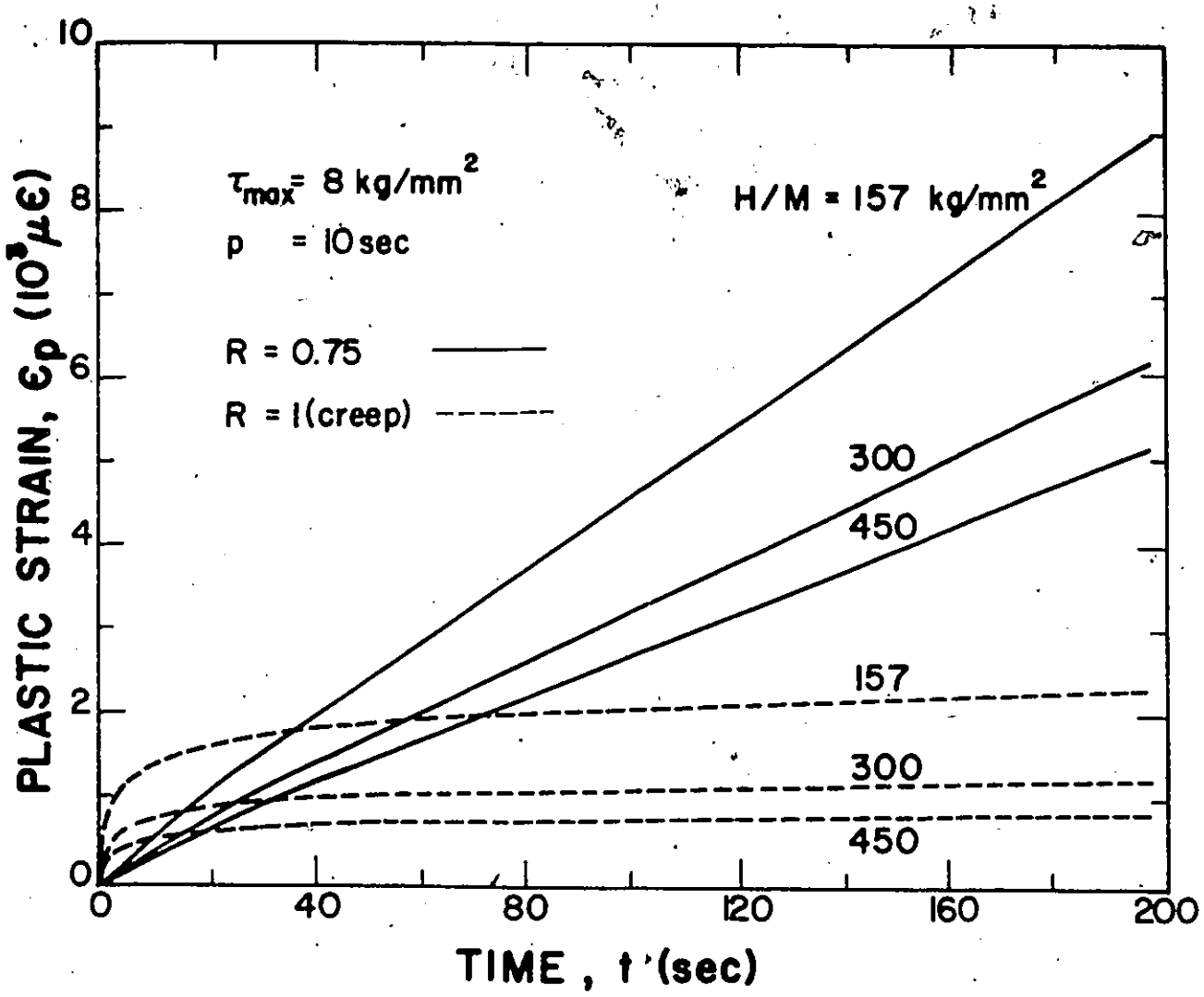

Figure 2.8. The figure shows the effect of work hardening coefficient on the cyclic softening and hardening behavior. The solid lines represent the cyclic loading behavior and were calculated using Eq. (2.51). The dashed lines show the creep behavior, calculated using Eq. (2.42). The other parameters are as shown in Fig. 2.5.

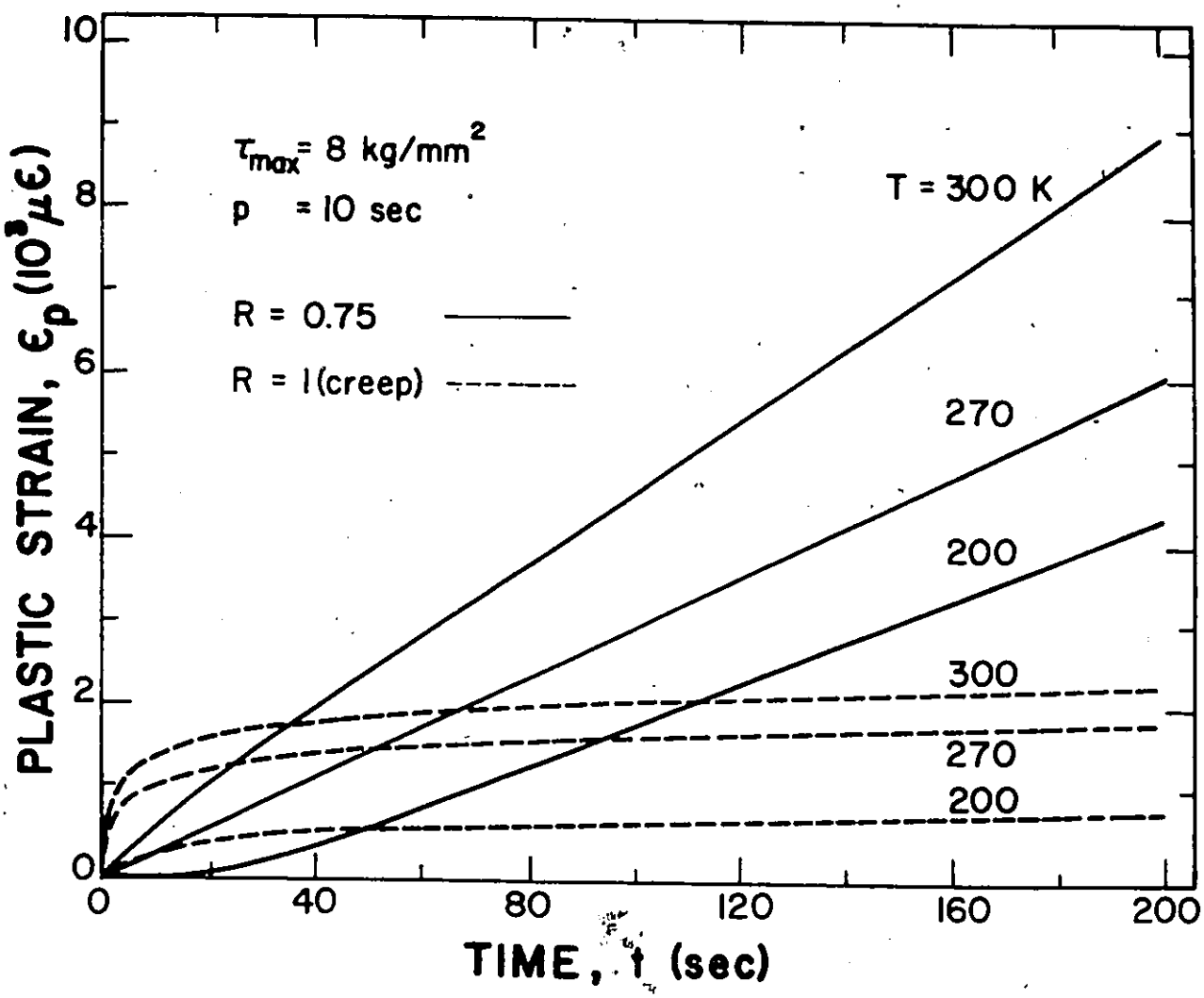

Figure 2.9. The figure shows the effect of temperature on the accumulated plastic strain during cyclic softening and hardening. The solid lines represent the cyclic deformation behavior while the dashed lines show the temperature dependence of creep. The other parameters are as shown in Fig. 2.5

Closing Comments

The increase in creep rate (or rate of cyclic strain accumulation) under a cyclic stress was observed experimentally in aluminum (polycrystaline) [3,19], copper [2,7] and lead [1]. The experimental results are in agreement with the conclusions from the present analysis that because of the alternating softening and hardening during cyclic deformation, the accumulated cyclic strain and the rate of cyclic strain accumulation are higher than the strain and strain rate under constant stress (equal to the maximum stress during cyclic loading) creep. Shetty and Meshii [19] pointed out that since the peak stress during cyclic deformation is the same as the initial static stress, the increase in creep rate necessarily means that softening can be attributed to decrease in the internal stress. The cyclic stress induces a change in the dislocation-obstacle structure that produces the internal stress.

The present analytical model is based on a rigorously derived, physical theory: rate theory based on statistical mechanics. It is not a coincidence, therefore, that the conclusions from the analysis conforms to the experimental observations. Because of the conformity between the theoretical prediction and the experimental observations, it is anticipated that the analytical model can be used to evaluate the accumulated damage (in highly stressed machine components); an essential data for design and lifetime determination of structural components.

Most of the cyclic loading experiments [1,2,3,7,19] were carried out at R=0, that is, with minimum stress equal to zero. Direct comparison of

the theoretical prediction with the experimental results was not possible since it was assumed in the analysis that cyclic deformation takes place within a high stress ($R > 0$) and low temperature range. However, in principle, the deformation kinetics can be extended to describe cyclic deformation within the stress and temperature range at which the experiments were carried out.

CHAPTER 3

EXPERIMENTAL DETAILS

3.1 EXPERIMENTAL SPECIFICATIONS

3.1.1 Material and Specimen Design

The material under investigation was a commercial grade (marketed as Noranda Z-500), near entectoid Zn-Al superplastic alloy of nominal composition: Al 25 Wt%, Cu 5 Wt%, Mg 0.05 Wt%, Zn balance. The material was selected because, as determined in a previous investigation [34,35] on constitutive laws, this alloy exhibits stress relaxation to the extent of complete unloading (it has a very low internal stress), even at room temperature. Its extreme deformation behavior lends itself to illustrate the application of deformation kinetics to describe cyclic plastic deformation and to the investigation of the rate controlling mechanisms. In addition, its deformation kinetics is well documented [34,35,115-119]. The mechanical, physical, and chemical properties of the alloy were compiled and presented in a previous thesis [119].

Test specimens were designed and machined according to ASTM standards. Round, shouldered-end (Fig. 3.1a), and sheet type (Fig. 3.1b) tensile specimens were designed and machined according to ASTM E8. The sheet type specimens were machined with axes parallel to the rolling direction and the round tensile specimens were machined from 12.5 mm diameter rods. The tensile specimens, with the usual standard grips, were used for stress relaxation, strain and stress controlled cyclic loading, and creep tests.

Specimens for tension-compression tests (Fig. 3.1c) were designed and machined according to ASTM 606-80. A special fixture, threaded specimen fixture, for the tension-compression tests was also designed and machined according to the ASTM standard.

3.1.2 Equipment

The experiments were conducted on a model TTC-M Instron machine and were controlled by means of a Motorola M6809 computer. A 10,000 kg capacity load cell was used. The specified accuracy for the overall load weighing system was better than ±0.5% of the indicated load*. The total strain of the specimen was measured with an Instron G51-11MA strain gauge extensometer, which was calibrated with an Instron A18-3C extensometer caliberator. To prevent damage to the specimen surface, small strips of cellophane tape were applied to the specimen surface where the extensometer knife edges made contact so that the knife edges imbeded in the tape rather than in the specimen. The calibration did not change by more than 1% in the temperature range of 273-370K. The deviation from linearity between the extensometer output and the strain was better than 0.25%.

The extensometer and the load cell were each connected to an analog (Instron) amplifier. The two amplifiers were then connected to the computer through an A/D (analog-digital) converter and to a Hewlett-Packard 7004B X-Y recorder. The output of the amplifiers (0-10.05 ± .05 V) dependend weakly on the operating range of the load cell. During the experiments, therefore, the load and extension (strain) readings were monitored by the computer and/or recorded by the X-Y recorder. Fig. 3.2 shows schematically the different components of the testing facility.

---

* See Operating Instructions Manual for the Instron machine.

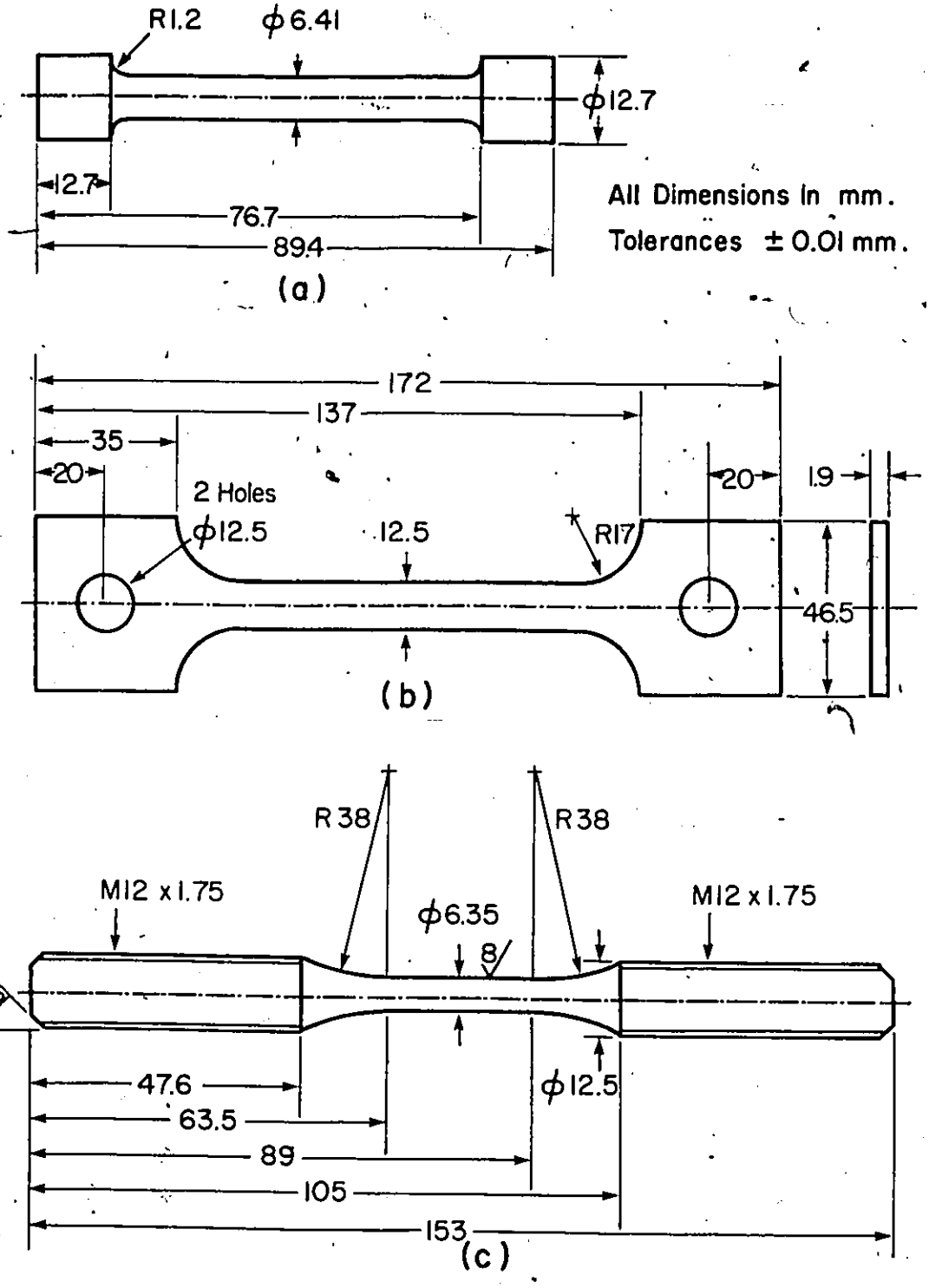

Figure 3.1. Tensile and fatigue specimens. (a) Round, shouldered-end tensile specimen, (b) Sheet type tensile specimen and (c) Tension-Compression fatigue specimen.

The test specimen and grip assembly were enclosed in an Instron temperature chamber, model 3111. The chamber had a long term temperature stability of ±1.0°C. The test temperature was also monitored with a thermometer placed near the specimen. During the experiment, the thermometer was read through the glass window of the chamber. The room temperature fluctuations were within the range ± 2.0°C. Tests below ambient

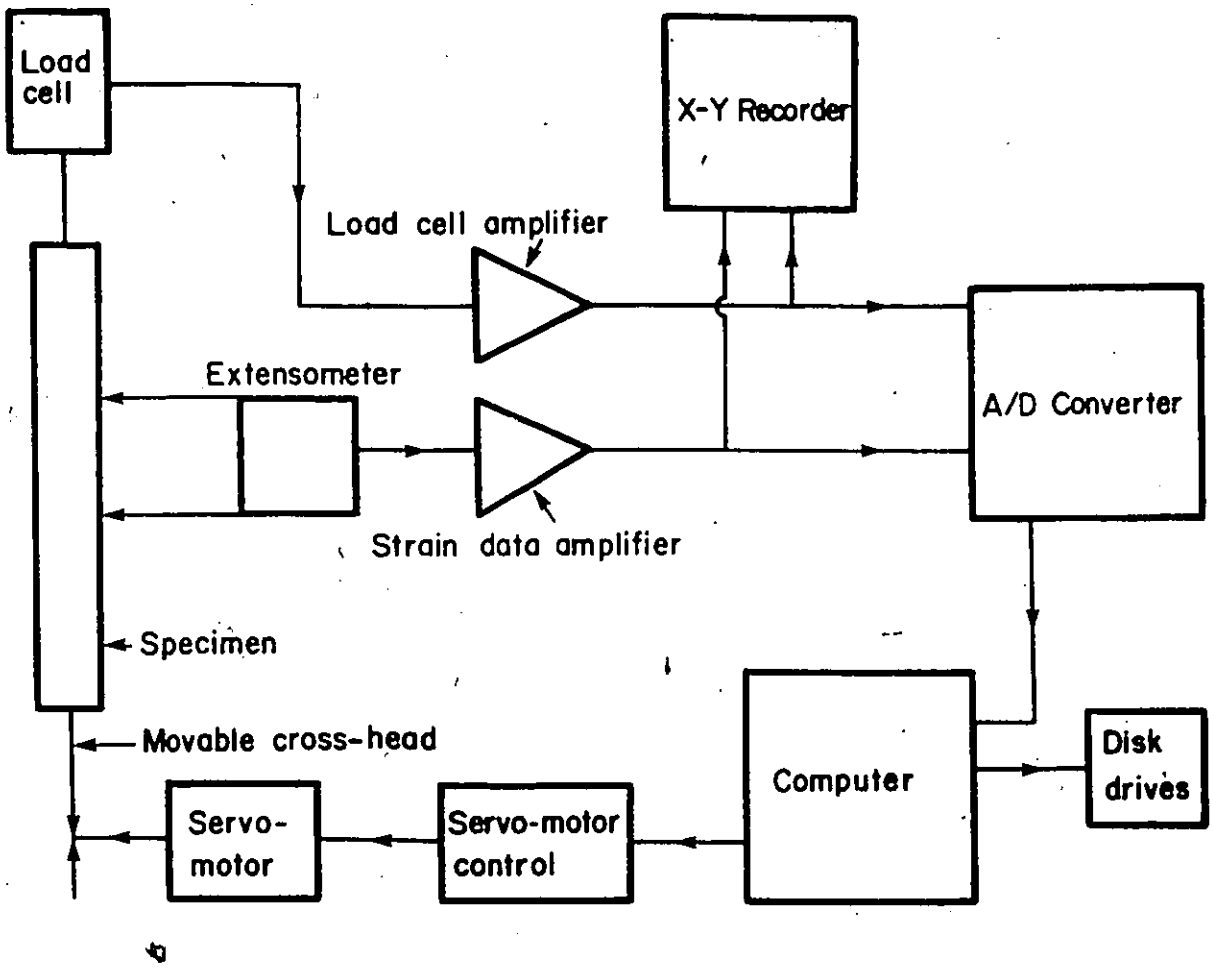

Figure 3.2. Schematic diagram of the testing facility.

temperature were carried out in a cold room. In order to minimize temperature fluctuations, the test frame of the machine was surrounded with a double styrofoam insulation. The test temperature was then monitored by a thermocouple placed near the specimen. The temperature fluctuations were typically within a ±0.5° range.

Stress relaxation measured during constant elongation tests results from the elastic contractions of the machine and the specimen that compensate the plastic elongation of the specimen. Because a small strain change produces a large stress change (the ratio is the combined elastic modulus), it is important to minimize the length changes caused by temperature fluctuations. Furthermore, to be able to measure low strain rates, the temperature has to be stable over a long period of time.

3.2 EXPERIMENTAL PROCEDURE

3.2.1 Computer Program

The movement of the machine cross-head was controlled by the computer through the servo-motor control (Fig. 3.2). The motion of the cross-head was specified by its speed, in mm/min., and its displacement in mm (magnitude and direction). Positive displacement signifies that the cross-head is moving upwards, that is, unloading the specimen while negative displacement means loading the specimen. Hence, by varying both the speed and the displacement during the experiment, it is possible to generate different load (stress) or strain wave forms. A computer program was developed to control the cross-head motion. Table 3.1 shows the description

of different commands that were used to control the cross-head motion and to read the clock or stop watch. Further details on the commands and on the computer program development are discussed in the manuals [120,121]. Figure 3.3 shows a typical flow chart of the computer (BASIC) program.

Table 3.1. Description of the different commands used in the computer program for controlling the cross-head motion.

Command	Description
INIT	The command initializes the interface program. It is issued at the beginning of the operating program.
START.	Start the cross-head motion according to the specified cross-head SPEED and DISP (displacement).
PORTC[0]=1	Stop or halt the cross-head motion.
PORTC[0]=0	Resume the cross-head motion following a halt or stop command.
RDTIME	Read the time on the clock.
ADRDAT=$12FF WR	Reset the clock to zero: use it as a stop watch.

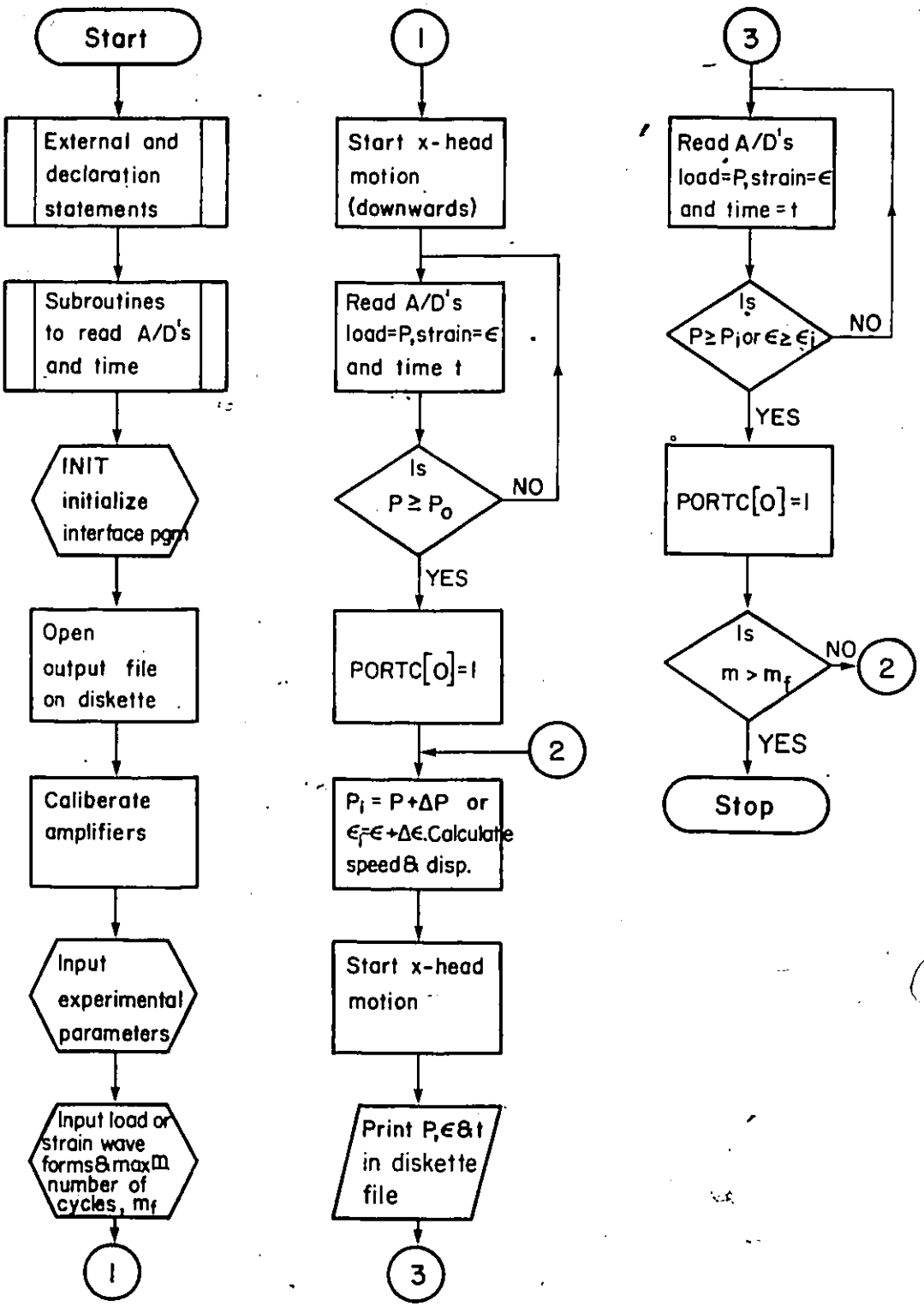

Figure 3.3. Flow chart of the computer program used to control the experiments.

3.2.2 Stress Relaxation (Constant Strain)

Stress relaxation experiments were conducted at constant total strain. The specimen was initially loaded at constant cross-head speed to a predetermined load or initial stress, σ_0, reaching the initial strain ε_0. The cross-head was then stopped and the computer was programmed to control the cross-head position so that the total strain was within the range $\varepsilon_0 \pm 100\ \mu\varepsilon$. During the cross-head position control, the (cross-head) speed was kept to a minimum, about 0.1 mm/min., in order to minimize inertia effects on the stress relaxation behavior. The applied load was continuously monitored by the computer and it was recorded on a floppy disk in function of time when the decrease in the load was 5 kg. The experiment was stopped when the load had (relaxed) decreased by about 90% of the initial load. Fig. 3.4 shows a typical stress relaxation behavior on stress versus strain axes, as recorded by the X-Y recorder.

The experimental parameters for the stress relaxation experiments are shown in Table 3.2. Each experiment was carried out on a new specimen except for test #3 where several experiments were conducted on a single specimen in order to determine the effect of temperature on the stress relaxation behavior. Round, shouldered-end tensile specimens were used for the experiments except for test #4 where a plate type tensile specimen was used. The initial cross-head speed for all the experiments was 1.0 mm/min.

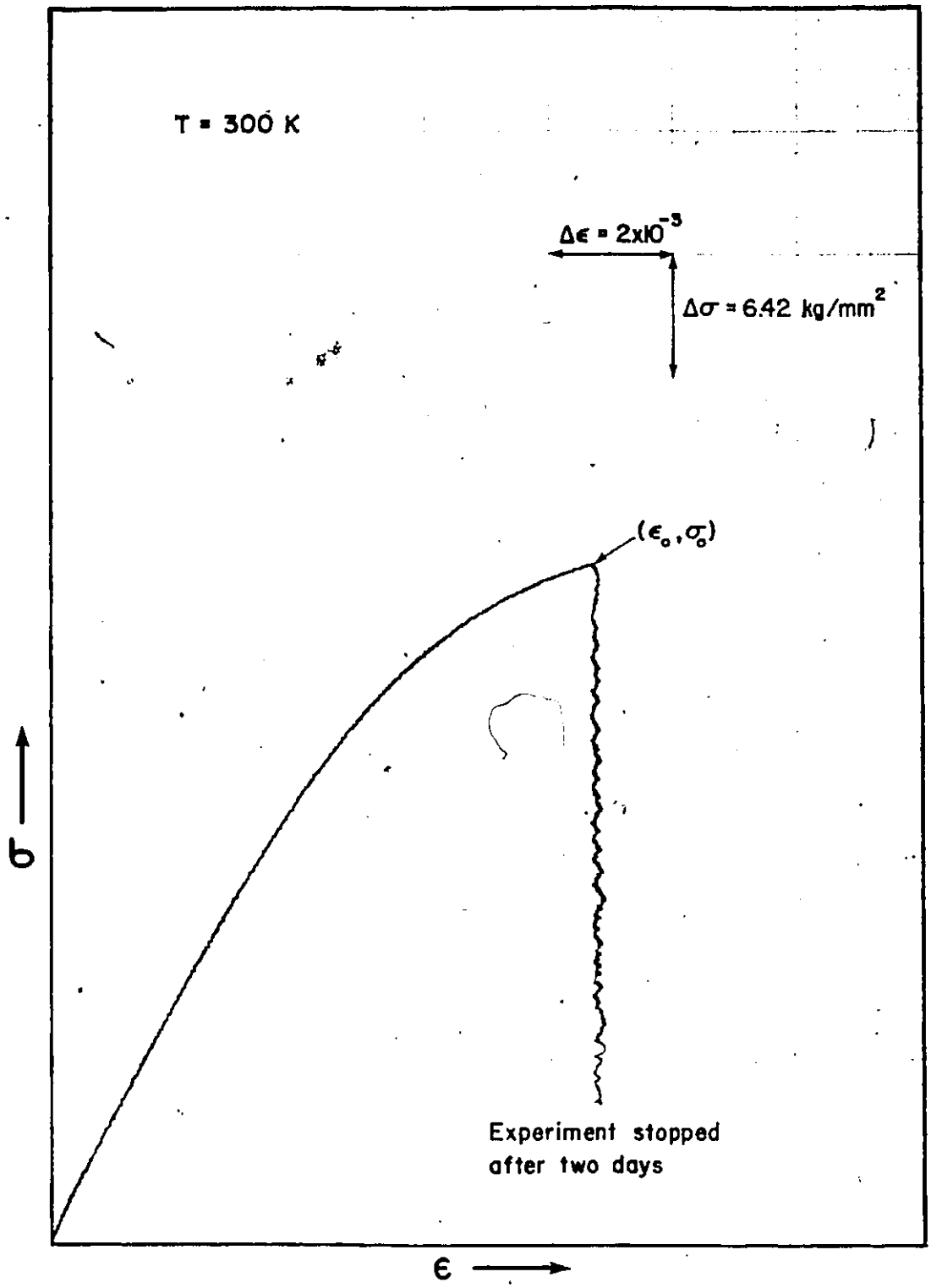

Figure 3.4. Stress Relaxation.

Table 3.2. Experimental Parameters for Stress Relaxation Tests.

Experiment No.	Temp. (K)	σ_0 (kg/mm^2)
1	293	20.3
2	298	14.1
3.1	313	13.7
3.2	323	13.7
3.3	334	13.7
3.4	343	13.7
3.5	353	13.7
4	273	10.1
5	293	15.5
6	298	17.1
7	329	14.25

3.2.3 Constant Load (Creep)

Constant load experiments were carried out on round, shouldered-end tensile specimens following a procedure similar to that for stress relaxation tests. The specimen was initially loaded at constant cross-head speed to a predetermined load P_0 (or initial stress σ_0) reaching the initial strain ε_0. The cross-head motion was then stopped and the computer was programmed to control the cross-head position such that the load was maintained constant within a maximum observable variation of 10 kg (or

about 0.4 kg/mm^2 in stress). That is, when the load had decreased by about 5kg (due to stress relaxation) the specimen was reloaded until the load was equal to P_0. During reloading, the cross-head speed was kept to a minimum (about 0.1 mm/min.) in order to minimize inertia effects on the creep rate.

The total strain was continuously monitored by the computer and it was recorded on a diskette file in function of time when the increase in strain was about 4×10^{-4}. After sufficiently long time when the strain rate had reached a steady state, the load was increased by 50 kg. Subsequently, steady state creep rate was obtained in function of the applied stress from a single specimen. Fig. 3.5 shows a stress versus strain curve recorded by the X-Y recorder during the constant load tests that were carried out at 330K. Similar experiments were conducted at 298K, 317K, and at 345K.

Effect of Temperature

Temperature change tests were carried out at a constant load of 500 kg (or at a normal stress equal to 16.3 kg/mm^2). Similarly to the constant load tests, the temperature in the chamber was increased by about 10K after sufficienly long time when the strain rate had reached a steady state. The steady state strain rate was, therefore, obtained in function of temperature (which was increased in steps of about 10K form 300K to 370K) from a single, shouldered-end, tensile specimen.

In addition, a temperature cycling experiment, between 311K and 320K was carried out at a constant load of 750kg (or normal stress equal to 25kg/mm^2). In order to avoid annealing effects, temperature changes were

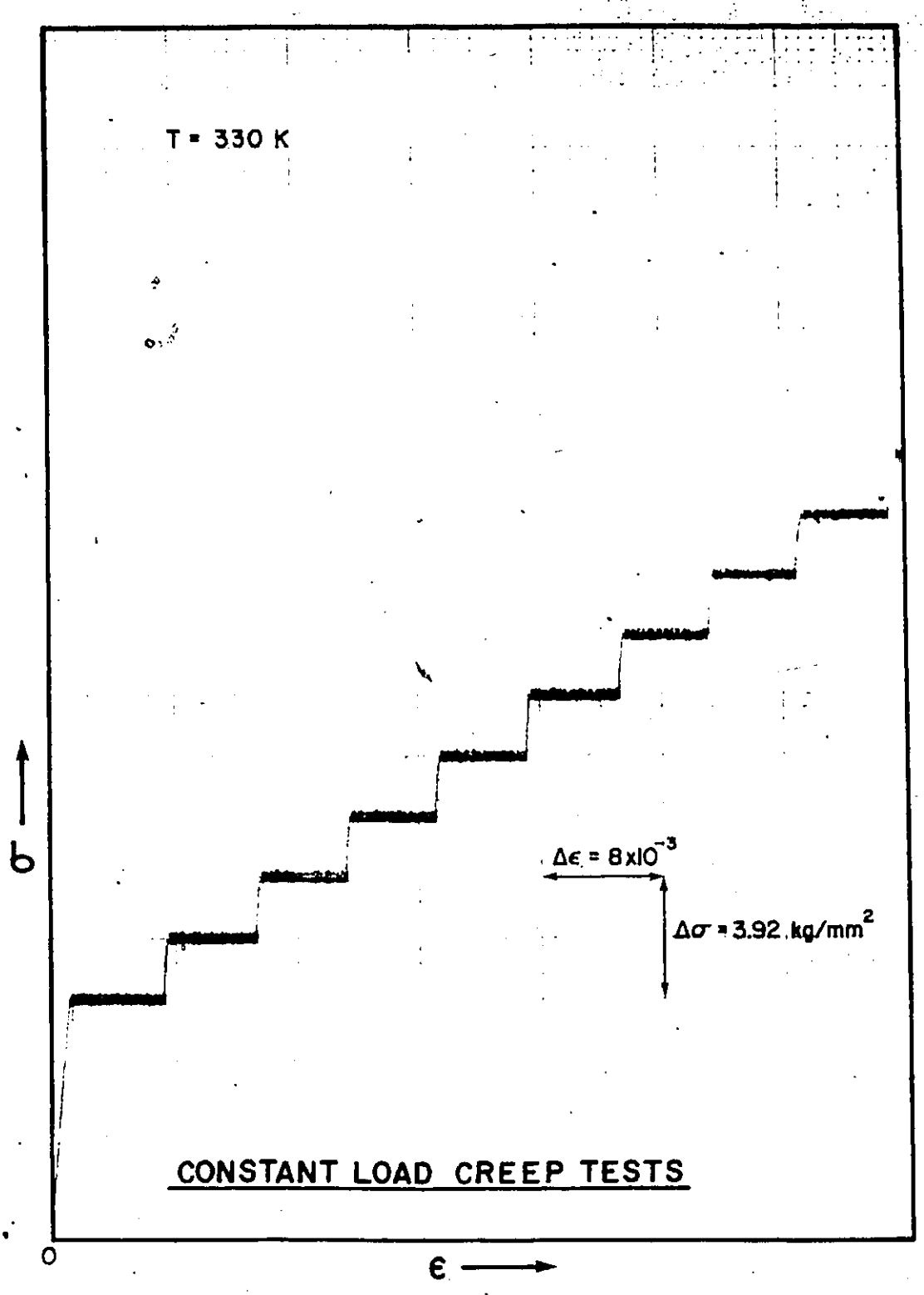
T = 330 K
b
$\Delta\epsilon = 8 \times 10^{-3}$
$\Delta\sigma = 3.92$ kg/mm^2
CONSTANT LOAD CREEP TESTS
0
ϵ

Figure 3.5.

made towards the lower temperature, that is, the temperature was cycled in both directions. Consequently, after the strain rate had reached a steady state at 320K, the temperature in the chamber was reduced to 311K thereby freezing the structure. It was then increased to 320K after the strain rate at 311K had reached a steady state. The temperature cycling procedure was repeated three times and the steady state strain rates at 311K and 320K were evaluated. When the material structural characteristics are constant with temperature, the experimental apparent activation energy is determined from the results of the temperature cycling experiment.

3.2.4 Strain Controlled Cyclic Loading

Triangular, Total Strain Wave Form

The specimen was initially loaded at constant cross-head speed to a predetermined load Po (or initial stress σ_0). The corresponding total strain, ε_0, was then the minimum strain, ε_{min}, while the maximum strain, $\varepsilon_{max} = \varepsilon_{min} + \varepsilon_r$, where ε_r is the total strain amplitude or range. Thenceforth the specimen was loaded cyclically at constant cross-head speed between the minimum and maximum total strain as shown in Fig. 3.6. For each cycle, the minimum and maximum loads were monitored by the computer and they were recorded on the diskette when the decrease in the mean load was equal to or greater than 5kg. The experiment was terminated when the mean load had decreased by more than 90% of the initial mean load (measured at the first cycle). For some experiments, the applied load was recorded in function of time at short time intervals (about 0.5 sec.) and they were

terminated after 5 cycles. Table 3.3 shows the experimental parameters for the strain controlled cyclic loading exeriments while Fig. 3.7 depicts a typical stress-strain behavior (that was recorded by the X-Y recorder) during a strain controlled cyclic loading experiment. Round, shouldered-end tensile specimens were used except for experiment #3 where a plate type tensile specimen was used.

Table 3.3. Experimental parameters for the strain controlled cyclic loading experiments.

Experiment No.	Temperature (K)	Initial Stress σ_0 (kg/mm^2)	Strain Amplitude, ϵ_r (10^3 μ ϵ)
1	293	20.2	1.24
2.1	298	14.1	1.0
2.2	298	14.1	2.0
2.3	298	14.1	3.0
3	273	10.1	0.6
4.1	293	15.5	2.0
4.2	293	15.5	3.0
5.1	298	18.2	0.8
5.2	298	19.3	1.8
6	329	14.3	1.4

For the purpose of determining the effect of cycle period (and hence the frequency) on the cyclic deformation behavior, strain controlled cyclic loading experiments were carried out at different cross-head speeds (1, 2, and 3 mm/min). The experiments which were conducted on a single specimen and with constant strain range (equal to 2×10^{-3}) were terminated after 100 cycles.

Sinusoidal Total Strain Wave Form

The sinusoidal total strain wave form was approximated by a series of linear segments and for each segment, the cross-head speed was constant. The strain change for the i-th segment was evaluated as

$$\Delta\varepsilon_i = \varepsilon_r \{ \sin (\phi_i + \Delta\phi) - \sin \phi_i \} \qquad (3.1)$$

where $\phi_i = \frac{2\pi t}{p}$ radians while the corresponding cross-head speed was determined from

$$\text{Speed} = S \cos (\phi_i + \frac{\Delta\phi}{2}) \qquad (3.2)$$

where S is the initial speed at t=0. Negative speed signifies that the cross-head is moving upwards (compressive load) while positive speed means that the cross-head is moving downwards (tensile load).

During the experiment the specimen was initially loaded at constant cross-head speed to a predetermined load P_0 reaching the initial total strain, ε_0, for which ϕ=0. Subsequently, the computer was programmed to control the cross-head motion, following the different segments (with $\Delta\phi$ = 0.1 radians) which form the sinusoidal strain wave form. For the i-th segment, the total strain was continuously monitored and compared with the

calculated value, $\varepsilon = \varepsilon_0 + \sum_{i=1}^{i} \Delta\varepsilon_i$. When the two values of strain were equal, the cross-head motion was stopped and the load and strain readings were recorded on a diskette file in function of time. With $\phi_{i+1} = \phi_i + \Delta\phi$ the strain increment, cross-head speed, and the calculated total strain were evaluated and the procedure was repeated. The test was terminated after 10 cycles.

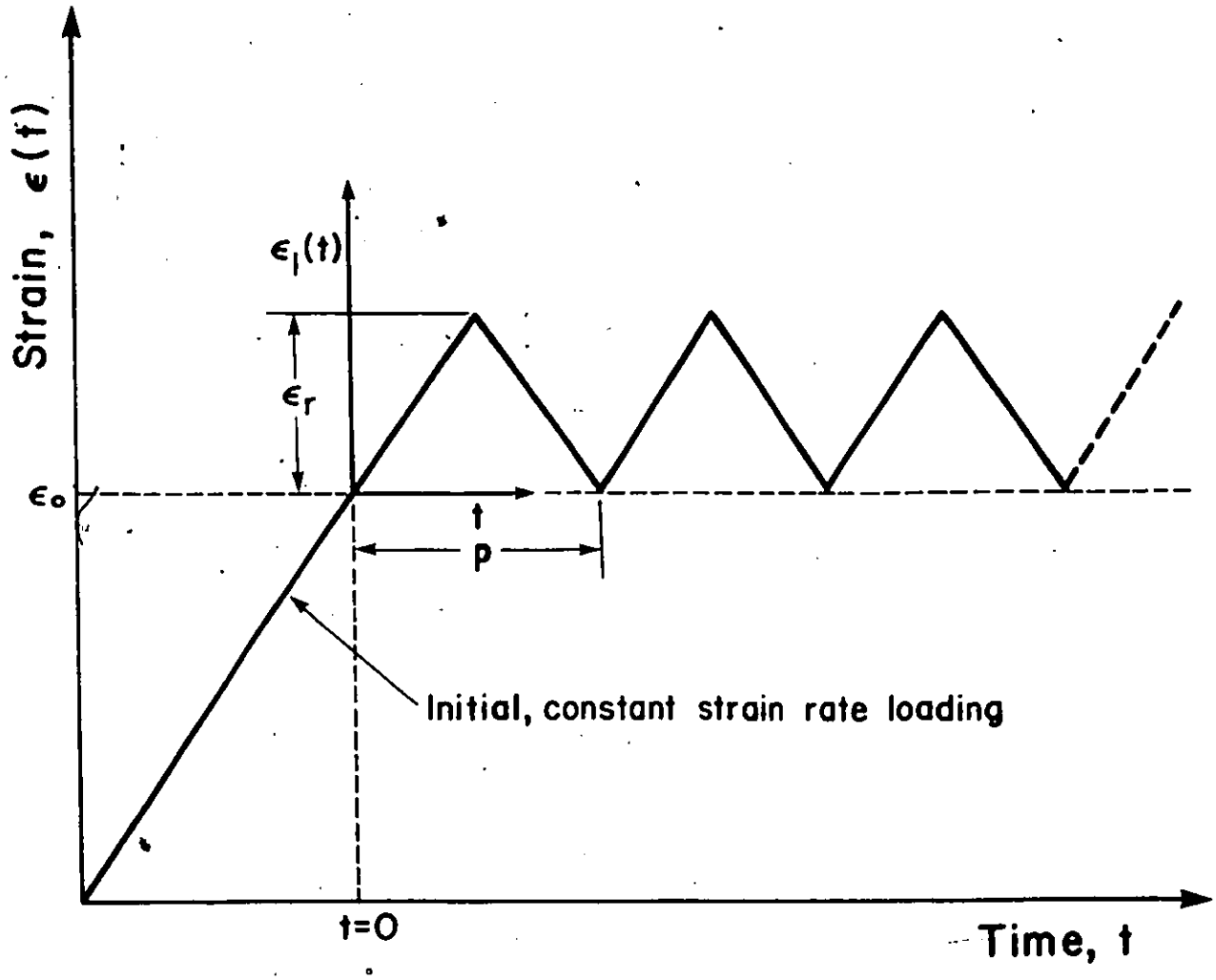

Figure 3.6. A schematic representation of a triangular strain wave form used in strain controlled cyclic loading experiments. ε_r is the strain range or amplitude, p is the cycle period, and $\varepsilon(t) = \varepsilon_0 + \varepsilon_1(t)$.

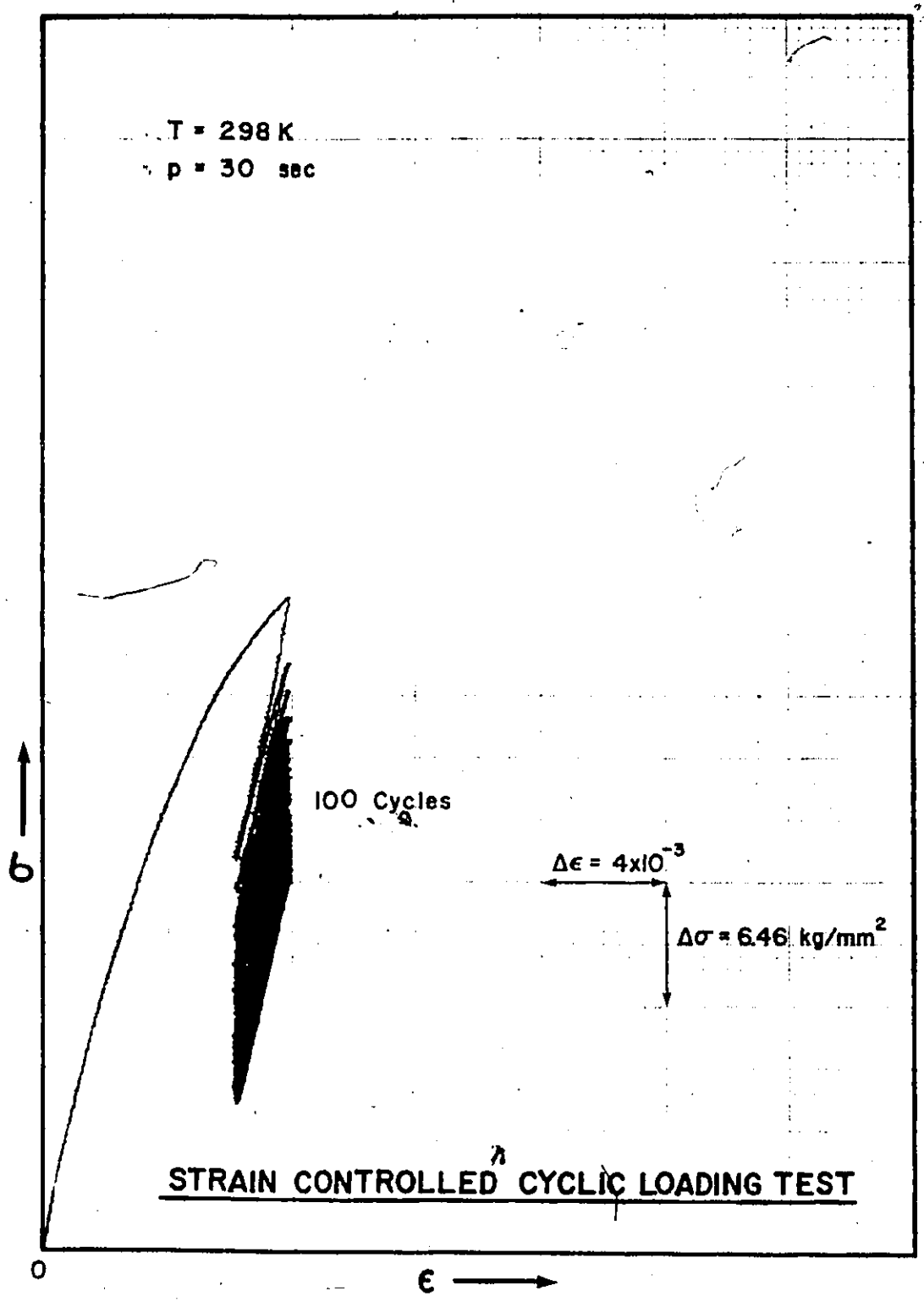
T = 298 K
p = 30 sec
100 Cycles
Δε = 4x10⁻³
Δσ = 6.46 kg/mm²
STRAIN CONTROLLED CYCLIC LOADING TEST
σ
0
ε

Figure 3.7.

Trapezoidal Total Strain Wave Form

Several strain controlled cyclic loading experiments were conducted with a (symmetrical) trapezoidal, total strain wave form. Since the wave form is a combination of constant strain and triangular strain segments, the procedure for the experiments was similar to that for stress relaxation and (triangular strain) cyclic loading experiments previously described. During the experiments (which were conducted at room termperature, 298 ± 1.0K) the applied load was monitored and recorded on the diskette at short intervals of time (about 0.5 sec.). The experiments were terminated after 5 cycles.

3.2.5 Load Controlled Cyclic Loading

Load controlled cyclic loading experiments using round, shouldered-end tensile specimens were carried out following a procedure similar to that described in the previous section (except that the applied load is the controlled function and the total strain is the independent variable). The specimen was loaded at constant cross-head speed to a predetermined initial load Po. Similar to the strain controlled cyclic loading experiments, the specimen was then subjected to cyclic loading at constant cross-head speed, between the minimum load, P_{min}, and the maximum load, $P_{max} = P_{min} + P_r$, where P_r is the load amplitude or range (Fig. 3.8). For each cycle, the maximum and the minimum total strains were monitored by the computer and they were recorded on the diskette in function of time when the mean total strain had increased by about 4×10^{-4} mm/mm. After sufficiently long time when the rate of cyclic strain accumulation had reached a steady state, the

minimum load was increased by 50kg and the load cycling was continued. Subsequently, the (steady state) rate of cyclic strain accumulation was obtained in function of the minimum (or initial) stress (for the same stress amplitude) from a single specimen. Fig. 3.9 (and also Fig. A12) shows the variation of the total strain with the applied stress during load controlled cyclic loading experiments. The curve was recorded by the X-Y recorder. The load controlled cyclic loading experiments with shear stress amplitudes of 1.6, 3.1, and 5.78 kg/mm^2 were conducted at room temperature, 298 ± 1.0K.

For the purpose of comparing the measured cyclic deformation behavior with the theoretical prediction, load controlled cyclic loading experiments during which the load-strain-time readings were recorded on the floppy diskette at short intervals of time (about 0.5 sec.) were carried out. The experiments which were conducted with both the triangular and the sinusoidal load wave forms were terminated after 10 cycles.

In order to determine the effect of cycle period on the load controlled cyclic deformation behavior, several experiments (with triangular load wave form) were carried out at various cross-head speeds. The experiments were conducted on a single specimen and with a shear stress amplitude of 3.66 kg/mm^2. During the experiments, the maximum and minimum strains for each cycle were recorded on the diskette and the experiments were terminated after 100 cycles.

Load controlled cyclic loading experiments were also carried out to determine the effect of stress ratio, $R = P_{min} / P_{max}$, on the cyclic deformation behavior. The experiments (with triangular load wave form) were

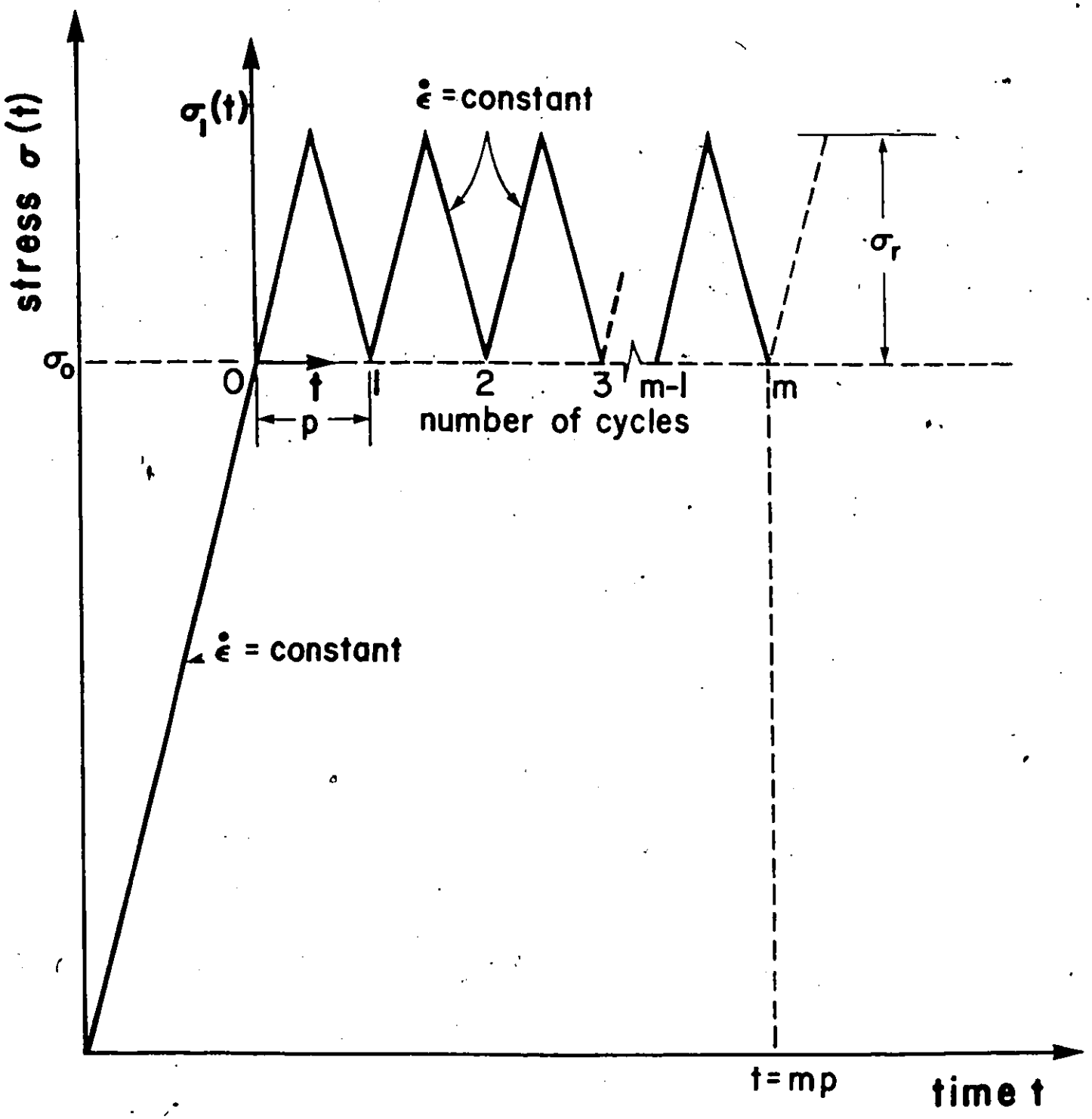

Figure 3.8. A schematic representation of a triangular load wave form often used in load (stress) controlled cyclic loading experiments. σ_r is the stress range or amplitude, p is the cycle period, and σ_0 in the initial stress.

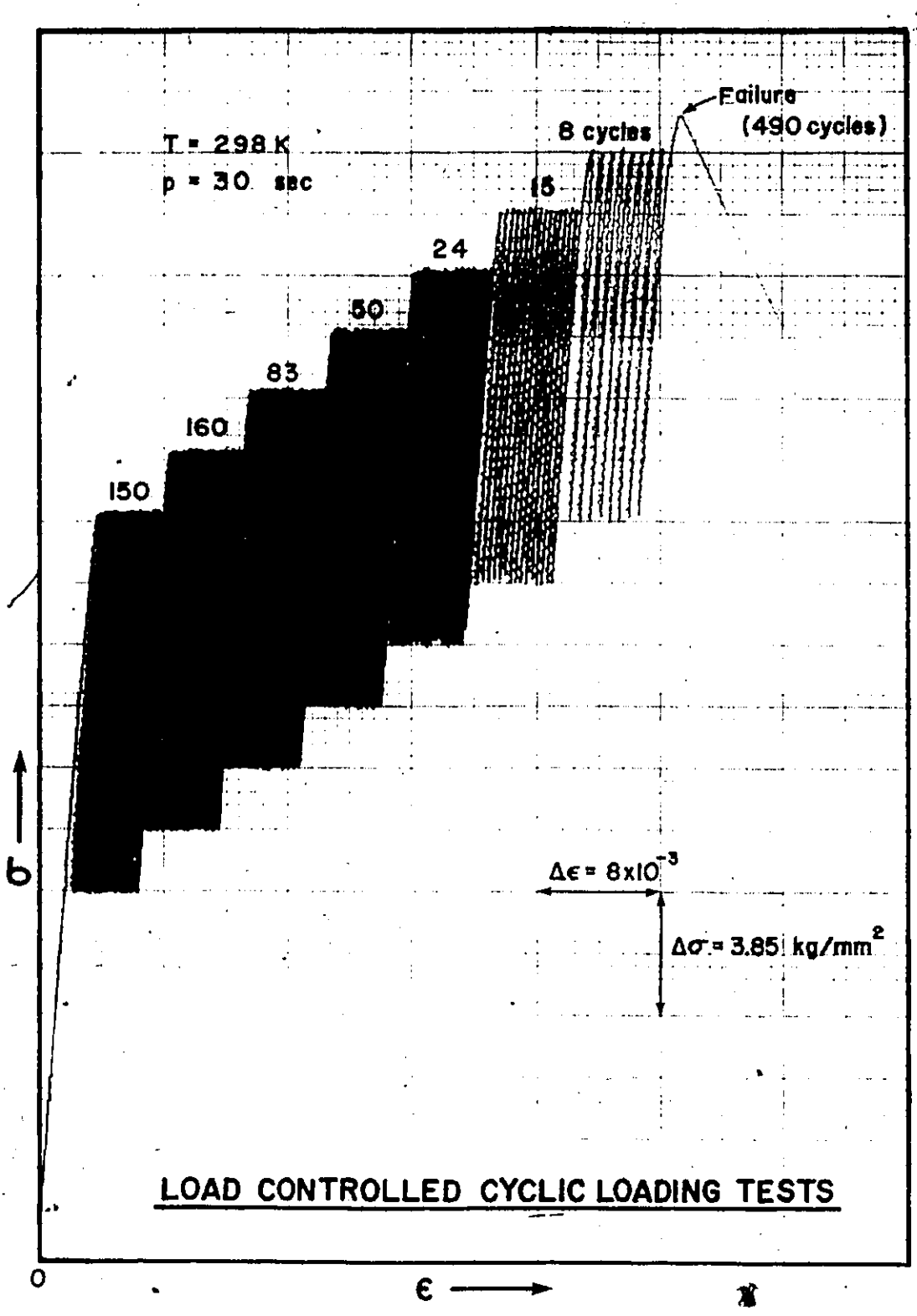
T = 298 K
p = 30 sec
Failure
(490 cycles)
8 cycles
15
24
50
83
160
150
σ
Δε = 8x10⁻³
Δσ = 3.85 kg/mm²
LOAD CONTROLLED CYCLIC LOADING TESTS
0
ε

Figure 3.9.

conducted at 329K and at a cross-head speed of 1.0 mm/min. For each experiment (at constant R) the maximum and minimum strains were recorded on the diskette when the mean total strain had increased by 4×10^{-4} mm/mm and the experiment was terminated when the mean strain rate had reached a steady state.

3.2.6 Tension - Compression Cyclic Loading

Tension-compression cyclic loading experiments were carried (using fatigue specimens) out in order to investigate the cyclic deformation behavior at zero mean strain or load. Both strain and load controlled fatigue experiments were conducted at room temperature using a triangular strain or load wave form. For each cycle, the maximum and minimum load and strain readings were monitored and recorded on the diskette. The test was discontinued after sufficiently long time when the hysteresis loop had reached a steady state. Fig. 3.10 shows a stress versus strain curve (traced by the X-Y recorder) of a typical tension-compression, cyclic loading experiment. Almost all the strain and load controlled cyclic loading experiments depicted this behavior.

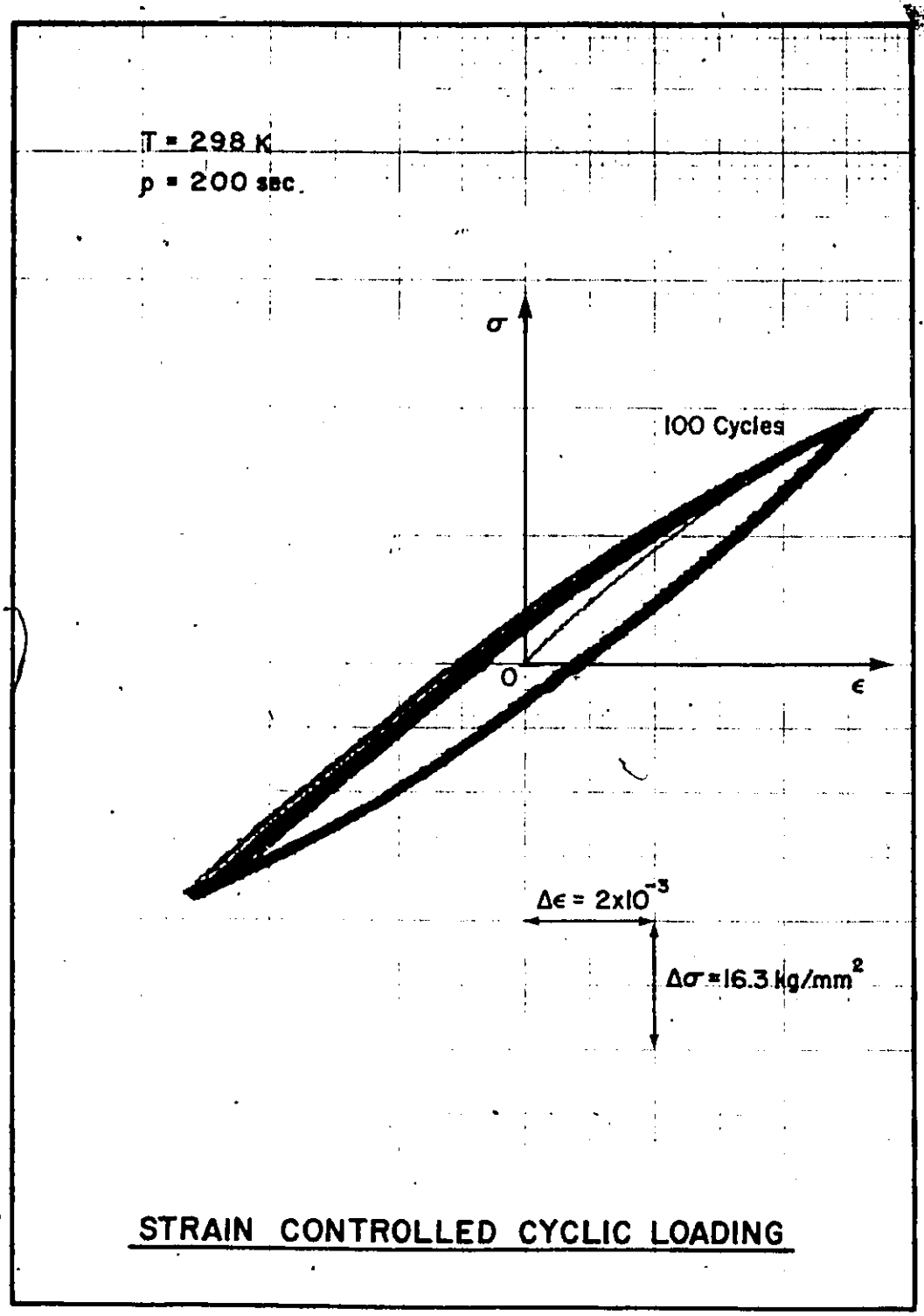
T = 298 K
p = 200 sec.
σ
100 Cycles
0
ε
Δε = 2x10⁻³
Δσ = 16.3 kg/mm²
STRAIN CONTROLLED CYCLIC LOADING

Figure 3.10.

CHAPTER 4

EXPERIMENTAL RESULTS AND DISCUSSION

4.1 STRAIN CONTROLLED CYCLIC LOADING

4.1.1 Evaluation of Constitutive Parameters

The results of strain controlled cyclic loading with a triangular total strain wave form and stress relaxation experiments were used to evaluate the constitutive parameters. For the triangular strain wave form (Fig. 3.6), the total strain $\varepsilon = \varepsilon_0 + \varepsilon_1(t)$ where

$$\varepsilon_1(t) = \begin{cases} \dfrac{2\varepsilon_r t}{p} & \text{when } 0 < t < \dfrac{p}{2} \\ \dfrac{2\varepsilon_r (p-t)}{p} & \text{when } \dfrac{p}{2} < t < p \ . \end{cases} \tag{4.1}$$

The integral in Eq. (2.26) was then carried out as follows [106, 107]. Consider the first loading cycle where $0 < t < p$. The integral for this time interval is

$$\int_0^p \exp \frac{EV\varepsilon_1(t)}{MkT}\, dt = \int_0^{p/2} \exp \frac{2EV\varepsilon_r t}{MkTp}\, dt + \int_{\frac{p}{2}}^{p} \exp \frac{2EV\varepsilon_r (p-t)}{MkTp}\, dt$$

$$= \frac{MkTp}{EV\varepsilon_r} \left[\exp \frac{EV\varepsilon_r}{MkT} - 1\right] . \tag{4.2}$$

Hence, for m cycles, $t = mp$ and the integral then is

$$\int_0^{mp} \exp \frac{EV\varepsilon_1(t)}{MkT}\, dt = \frac{Mt}{\varepsilon_r} \frac{kT}{EV} \left[\exp \frac{E\varepsilon_r V}{MkT} - 1\right]. \tag{4.3}$$

The variable ξ in Eq. (2.26) then becomes

$$\xi_{I,II} = \frac{MkTt}{E\epsilon_r V_{I,II}} \left[\exp \frac{E\epsilon_r V_{I,II}}{MkT} - 1\right]. \tag{4.4}$$

Consequently, the applied stress is expressed in function of time from Eqs. (2.24) and (4.4) as

$$\tau = \tau_0 - \frac{kT}{V_{I,II}(1 + \frac{H}{E})} \ln \left| \frac{A_{I,II}(1 + \frac{H}{E})t}{\epsilon_r} \exp \frac{V_{I,II}(\tau_0 - \tau_i^o)}{kT} \left\{\exp \frac{E\epsilon_r V_{I,II}}{MkT} - 1\right\} + 1 \right| \tag{4.5}$$

since at t=mp, $\epsilon - \epsilon_0 = 0$. It follows from Eq. (4.5) that when the first term in the argument is much greater that unity, the applied stress is proportional to the natural logarithm of time. In region I (Fig. 2.2), the slope of the curve is inversely proportional to $V_I (1 + \frac{H}{E})$ while the intercept at $\ln t=0$ is proportional to $A_I(1 + \frac{H}{E})$ and is a function of the strain amplitude, and the initial internal and applied stresses. Similarly, in region II the slope of the curve and the intercept are proportional to $V_{II}(1 + \frac{H}{E})$ (inversely) and $A_{II}(1 + \frac{H}{E})$, respectively. It follows that in order to evaluate the constitutive parameters, $V_{I,II}$ and $A_{I,II}$, the ratio H/E and the internal stress, τ_i^o, have to be determined.

The tension-compression cyclic loading experiments on the Zn-Al alloy at room temperature (Fig. 3.10) did not indicate any hardening during the deformation for many cycles. Zhu and Ramaswami [122] have carried out similar experiments on the alloy over a wide range of strain amplitudes and strain rates. They also observed that there is vary little fatigue hardening. Consequently, the work hardening coefficient, H≈0 and as was observed in a previous study [34,35], the internal stress level of the alloy is negligibly small, that is, $\tau_i^o \approx 0$.

The constitutive parameters, $V_{I,II}$ and $A_{I,II}$, were, therefore, evaluated from the experimental results which were plotted on a - $\Delta\tau$ (shear stress change) versus natural logarithm of time coordinate system. Fig. 4.1 (and also Figs. A1 and A2 in appendix) shows typical strain controlled cyclic loading and stress relaxation experimental results for region I.

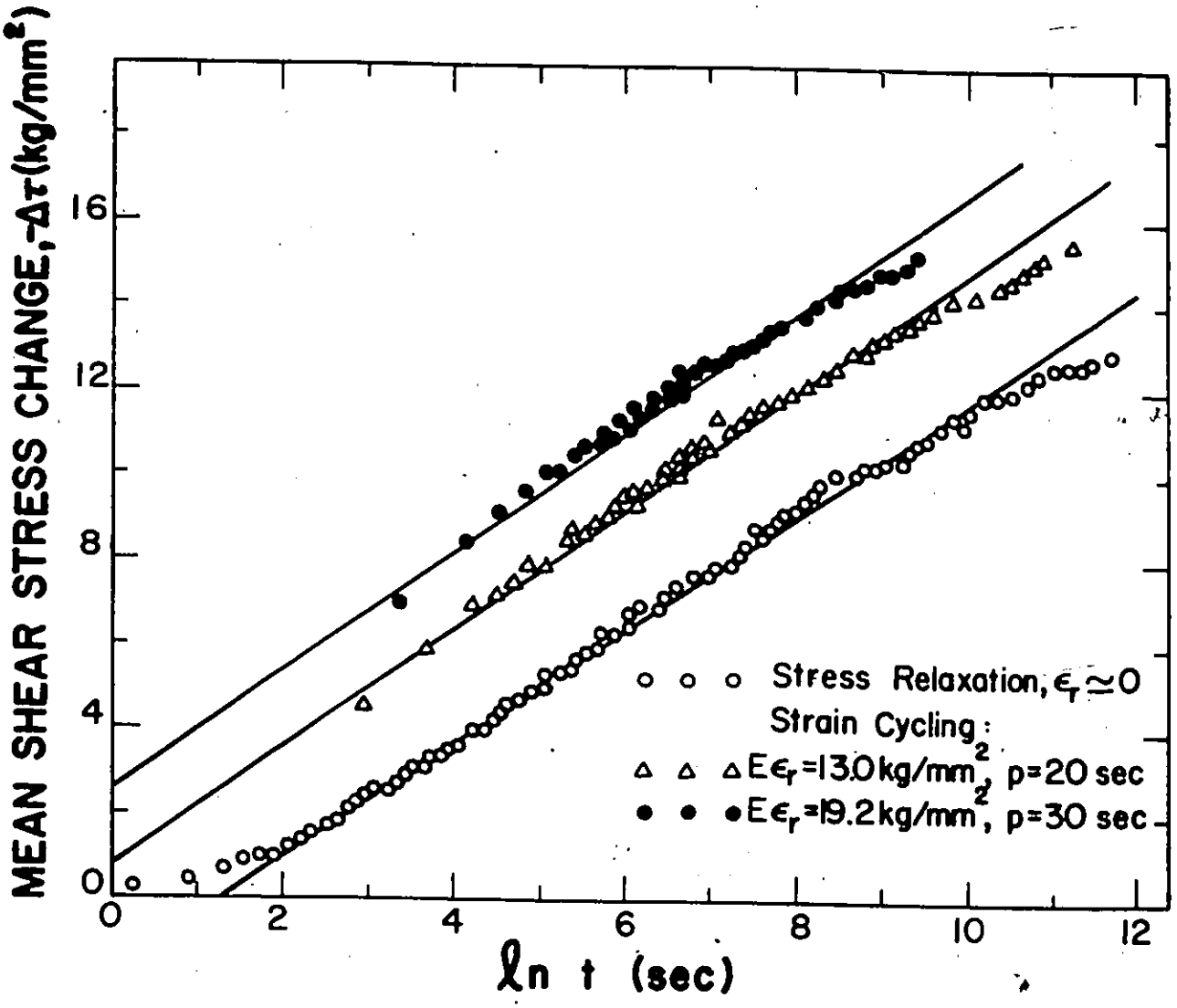

Figure 4.1. Strain controlled cyclic loading and stress relaxation mean shear stress change represented in the shear stress change versus natural logarithm of time coordinate system for the evaluation of activation volume, V_I, and the parameter A_I. The experiments were carried out on a near entectoid Zn-Aℓ alloy. The experimental variables are: τ_o = 15.5 kg/mm², and T = 293K.

The lines were obtained from least square method using Eq. (4.5) for the cyclic loading experiments and Eq. (2.23) for the stress relaxation experiment. The deviation of experimental points from the straight line during the early part of stress relaxation (for t ~ 10 sec.) was indeed expected from theoretical and geometrical considerations. It follows from Eqs. (2.23) and (4.5) that the stress change versus the natural logarithm of time relation is linear only when the first term in the argument is much greater than unity, that is, after sufficiently long time. At t=0 or at the beginning of stress relaxation, $\tau=\tau_0$ and the stress change has to be zero. From the analysis of the experimental results, V_I and A_I were evaluated. It was assumed that $\sigma_a = 2\tau_a$ or M=2.

A computer program was developed to evaluate the parameters V_I and A_I in region I and V_{II} and A_{II} in region II from the experimental results, using the least square method. For the transition stress range, the deformation time $t \alpha \xi_I + \xi_{II}$ was then evaluated from Eqs. (2.27) and (4.4) in function of the applied stress, τ_a. Consequently, the applied stress was evaluated from the theory in function of the deformation time t and the strain amplitude for regions I and II and the transition stress range. Fig. 4.2 (and also Figs. A3 and A4 in the appendix) shows the comparison between the theoretical prediction and the experimental results. The constitutive parameters $V_{I,II}$ and $A_{I,II}$ that were evaluated from the experimental results are presented in Tables 4.1 and 4.2

The constitutive parameters were determined from the analyses of stress relaxation and strain controlled cyclic loading experimental results that were obtained from different specimens. The scatter observed in the

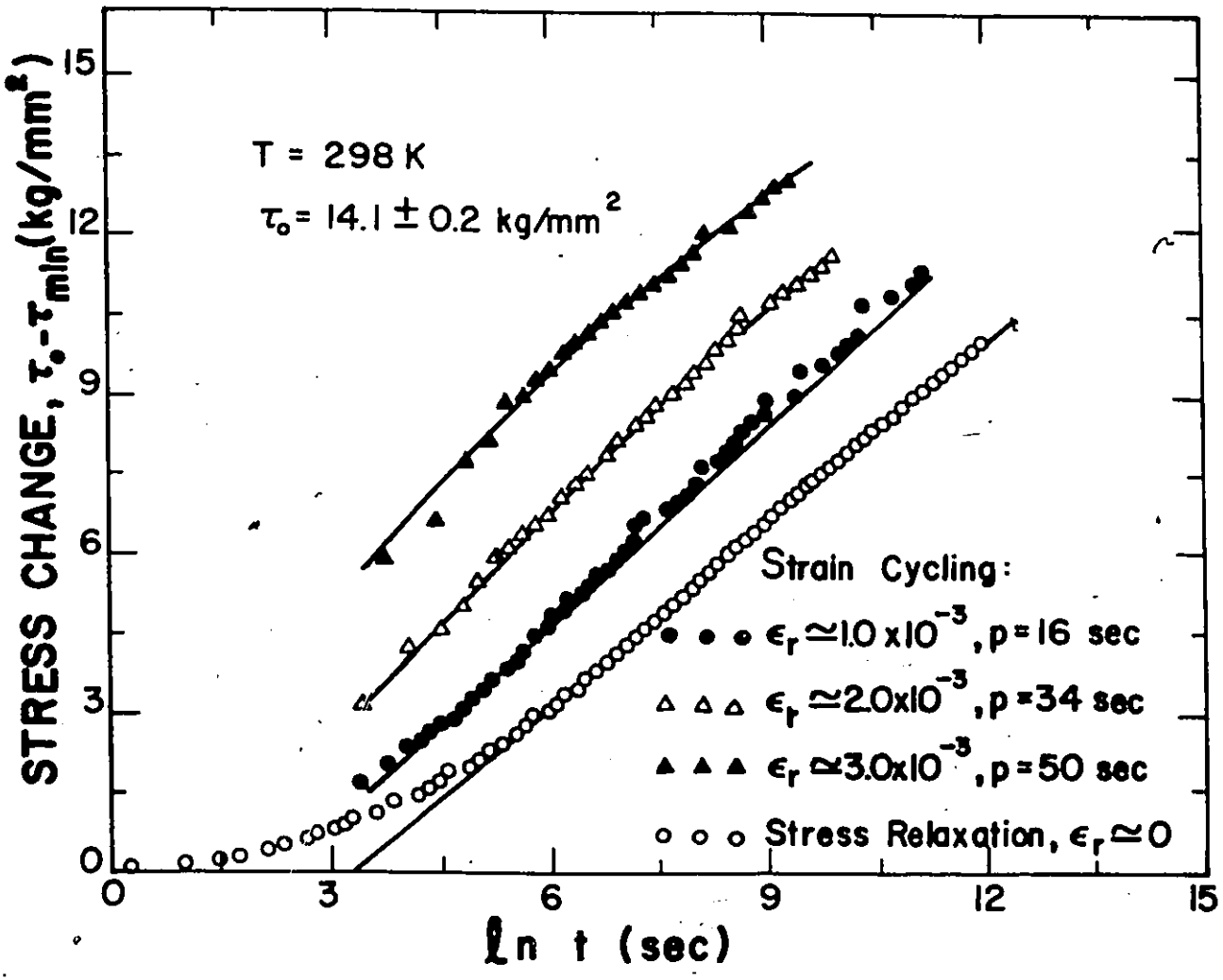

Figure 4.2. Strain controlled cyclic loading and stress relaxation experimental results for regions I and II, and the transition stress ranges. The symbols indicate the experimental results while the curves were calculated using Eqs. (2.27) and (4.4).

constitutive parameters is most likely due to the inherent variation in structural parameters ($\Delta G^{\ddagger}$, V, ρ_t) between the different specimens. Because the parameters $A_{I,II}$ are exponential functions of the activation free energies, $\Delta G^{\ddagger}_{I,II}$, the variations in the structural parameters often lead to a scattter of up to two orders of magnitude in the constitutive parameters $A_{I,II}$. The scatter in the constitutive parameters could also partly be due to inaccuracies that results from fitting exponential relations to experimental data. However, despite the scatter, the constitutive parameters determined from stress relaxation and strain controlled cyclic loading experiments are within the same range. Furthermore, the long straight parts of the curve (regions I and II in Figs. 4.1 and 4.2) indicate the validity of the assumptions in Section 2.1, that is, the material structural characteristics do not change appreciably during cyclic deformation and that the backward activations over the energy barriers are negligible. Consequently, stress relaxation can be employed to determine the constitutive parameters, and by using the equations developed in this report, the strain controlled cyclic deformation behaviour can be predicted.

4.1.2 Stress-Time Response

The constitutive parameters that were determined from the analysis of stress relaxation and strain controlled cyclic loading experimental results were used to predict the stress-time behaviour during cyclic deformation. Fig. 4.3 shows the shear stress-time response during the first few cycles of a strain controlled cyclic loading experiment (with triangular, total strain wave form). The symbols represent the experimental results while the solid

Table 4.1. Activation parameters obtained from the analysis of stress relaxation experimental results

Experiment #	Fig.	Temp (K)	τ_0 (kg/mm^2)	V_I (b^3)	V_{II} (b^3)	A_I /sec.	A_{II} /sec.	τ^* kg/mm^2
1	A_1	293	20.2	13	-	2.3×10^{-9}	-	-
2	4.2	298	14.1	18	-	7.3×10^{-11}	-	-
3.1	4.8	313	13.7	19	-	9.8×10^{-11}	-	-
3.2	4.8	323	13.7	19	30	6.4×10^{-10}	6.34×10^{-11}	3.7
3.3	4.8	334	13.7	18	37	2.17×10^{-9}	8.17×10^{-11}	3.7
3.4	4.8	343	13.7	18	44	7.34×10^{-9}	1.0×10^{-10}	3.7
3.5	4.8	353	13.7	15	41	2.48×10^{-8}	5.36×10^{-10}	3.5
4	A2	273	10.1	20	-	5.4×10^{-9}	-	-
5	4.1	293	15.5	16	-	1.09×10^{-9}	-	-
6	A3	298	17.1	15	21	4.74×10^{-10}	5.8×10^{-11}	4.6
7	A4	329	14.25	16	29	6.8×10^{-9}	3.55×10^{-10}	4.75

line (Fig. 4.3b) was calculated from Eq. (2.22) (with $H=\tau_i^o=0$). Similarly, Figs. 4.4 and 4.5 show the comparison of the predicted stress-time response with the measured response for sinusoidal and trapezoidal total strain wave forms, respectively. For the sinusodal wave form, the integral in Eq (2.22) was evaluated numerically, using a BASIC computer program [123] based on Romberg's method while for the trapezoidal wave form, the integration was carried out analytically following a procedure similar to that described in Section 4.1.1

It is observed that within the stress, time and temperature range where the constitutive equation of plastic flow during strain controlled cyclic deformation can be approximated with activation over a single energy

Table 4.2. Activation parameters evaluated from the analysis of strain controlled cyclic loading experiments

Exp. #	Fig.	Temp (k)	τ_0 (kg/mm^2)	ε_r ($10^3\mu\varepsilon$)	V_I (b^3)	V_{II} (b^3)	A_I /sec.	A_{II} /sec.	τ^* kg/mm^2
1	A_1	293	20.2	1.24	14	-	9×10^{-10}	-	-
2.1	4.2	298	14.1	1.0	16	19	1.85×10^{-10}	7.4×10^{-11}	3.9
2.2	4.2	298	14.1	2.0	15	21	3.46×10^{-10}	1.3×10^{-11}	3.8
2.3	4.2	298	14.1	3.0	13	21	3.0×10^{-9}	9.1×10^{-12}	3.6
3	A2	273	10.1	0.6	21	-	6.6×10^{-9}	-	-
4.1	4.1	293	15.5	2	15	-	3.1×10^{-10}	-	-
4.2	4.1	293	15.5	3	15	-	4.6×10^{-10}	-	-
5.1	A3	298	18.2	0.8	13	20	6.17×10^{-9}	2×10^{-10}	4.7
5.2	A3	298	19.3	1.8	13	20	1.76×10^{-9}	1.8×10^{-10}	4.6
6	A4	329	14.25	1.4	13	34	3.925×10^{-8}	5.1×10^{-11}	2.65

barrier, the applied shear stress is proportional to the logarithm of time* (and hence to the logarithm of number of cycles). Each cycle leads to a decrease in the applied shear stress. The greater the number of cycles the smaller is the decrease in the applied shear stress per cycle. It is also evident from Figs. 4.3, 4.4, and 4.5 that there is a good agreement between the calculated stress-time response and the experimental data. Again, the agreement between the predicted and the measured stress-time response indicates the validity of the assumptions that were made in the derivation of the constitutive equations.

* A similar behavior was observed experimentally in high strength T_i - 7Al-2Cb - 1Ta Titanium alloy and in AISI Type 304 Stainless Steel (E. Krempl and V.V. Kallianpur, J. Appl. Mech., Trans. of ASME, Vol. 52, p. 654, Sept. 1985).

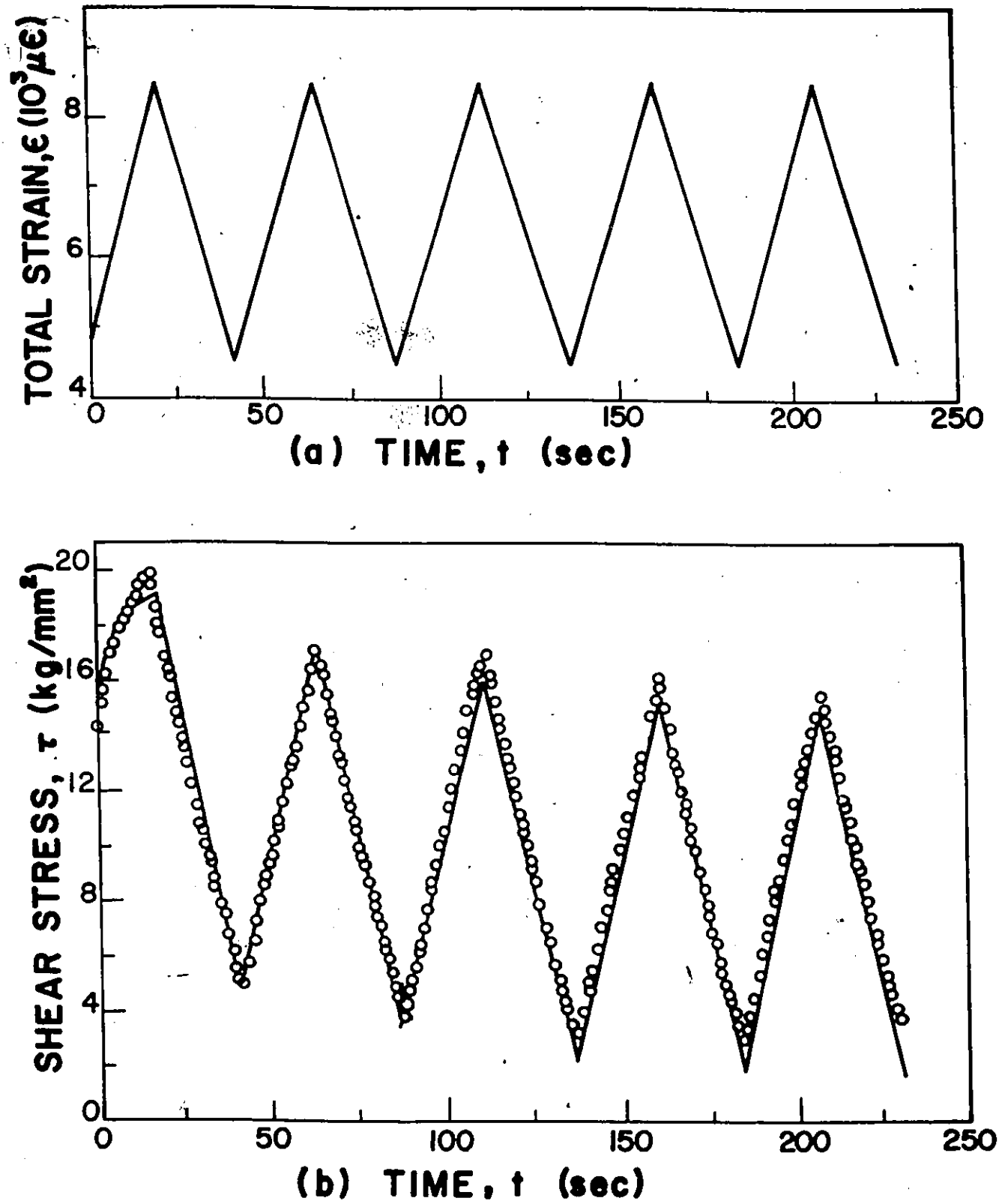

Figure 4.3. Stress-time response during the first few cycles of a strain controlled cyclic loading experiment. (a) Input, strain-time triangular wave form, (b) stress-time response. The symbols represent experimental data and the solid line was calculated from the theory. The parameters are: $V_I=16b^3$, T=293K, $A_I=10^{-9}$/sec, $\tau_o=14$kg/mm^2, $\epsilon_r=4\times10^{-3}$ and p=40 sec.

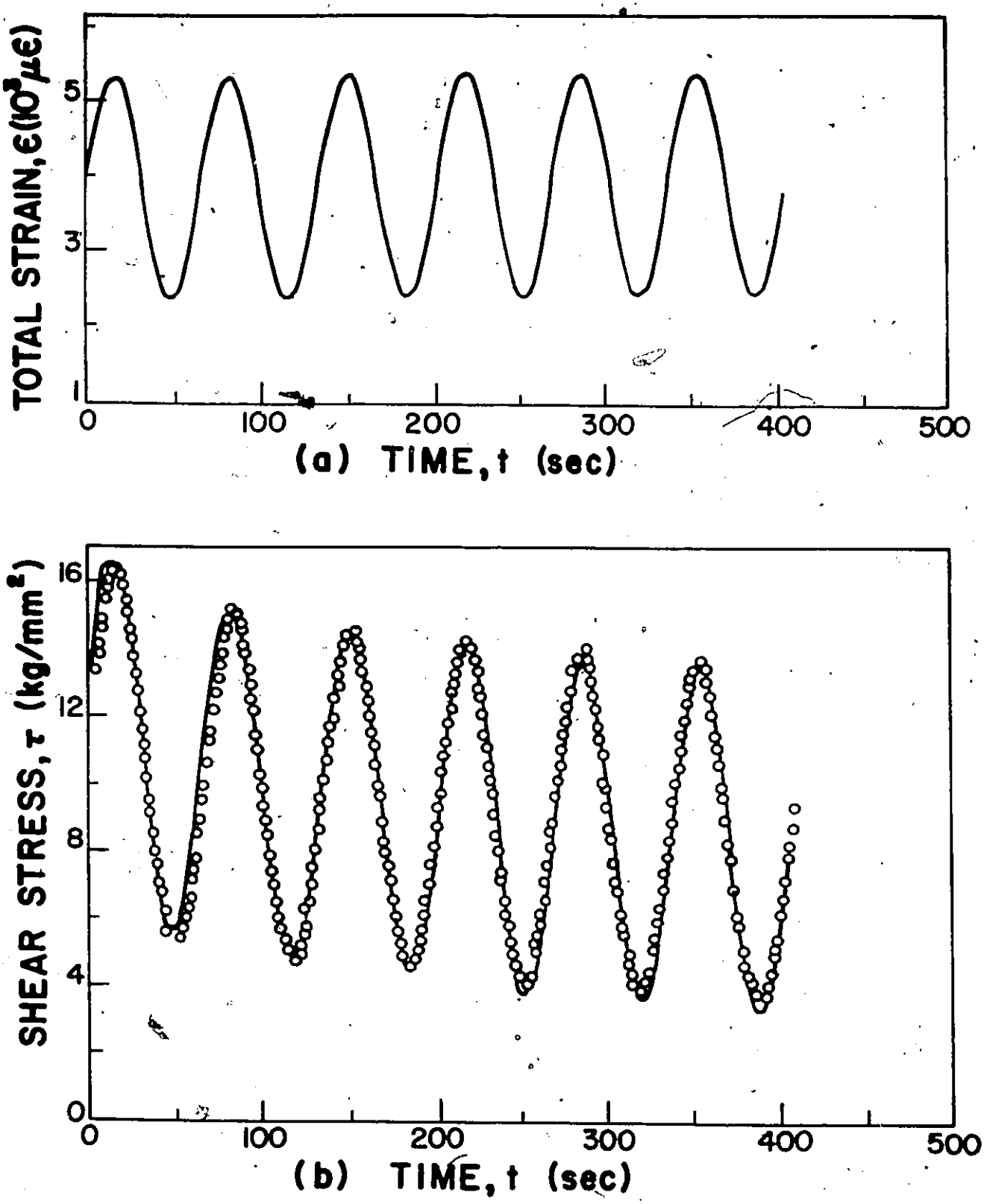

Figure 4.4. Stress-time response during the strain controlled cyclic loading. (a) Input strain-time, sinusoidal wave form, (b) stress-time response. The symbols represent experimental data and the solid line was calculated from the theory. The parameters are: $A_I = 1.3\times10^{-9}$/sec. $V_I = 16b^3$, T=293K, $\varepsilon_r = 1.5\times10^{-3}$, $\tau_0 = 13.5 kg/mm^2$ and p=68 sec.

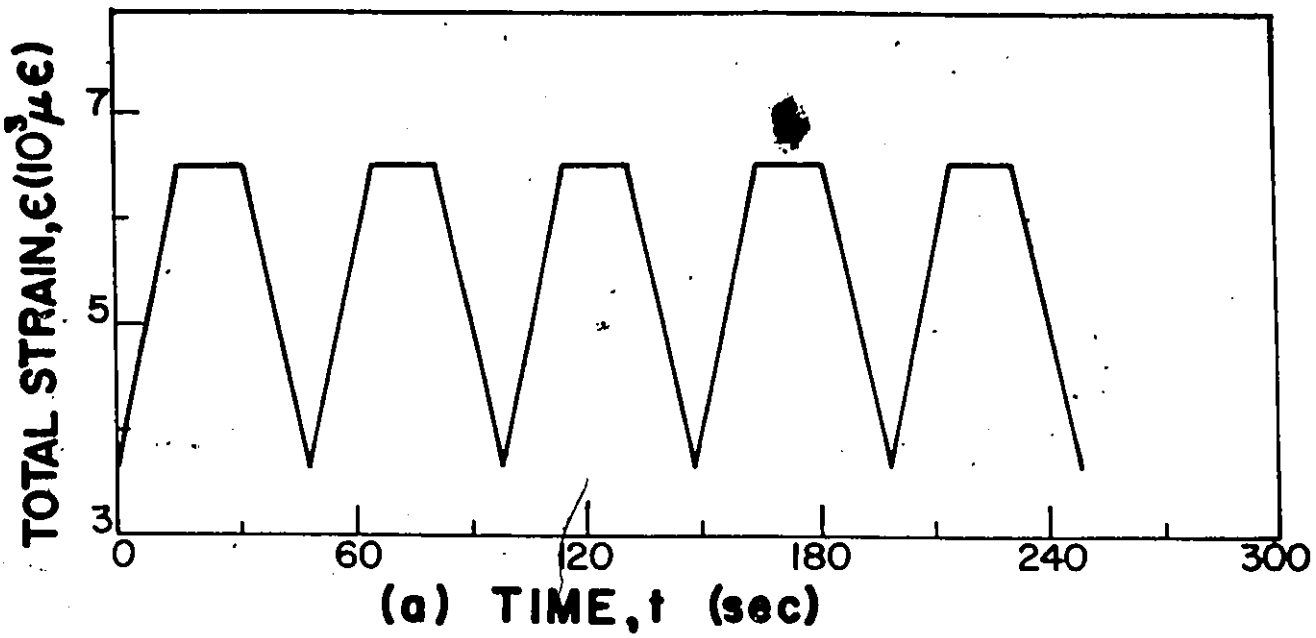

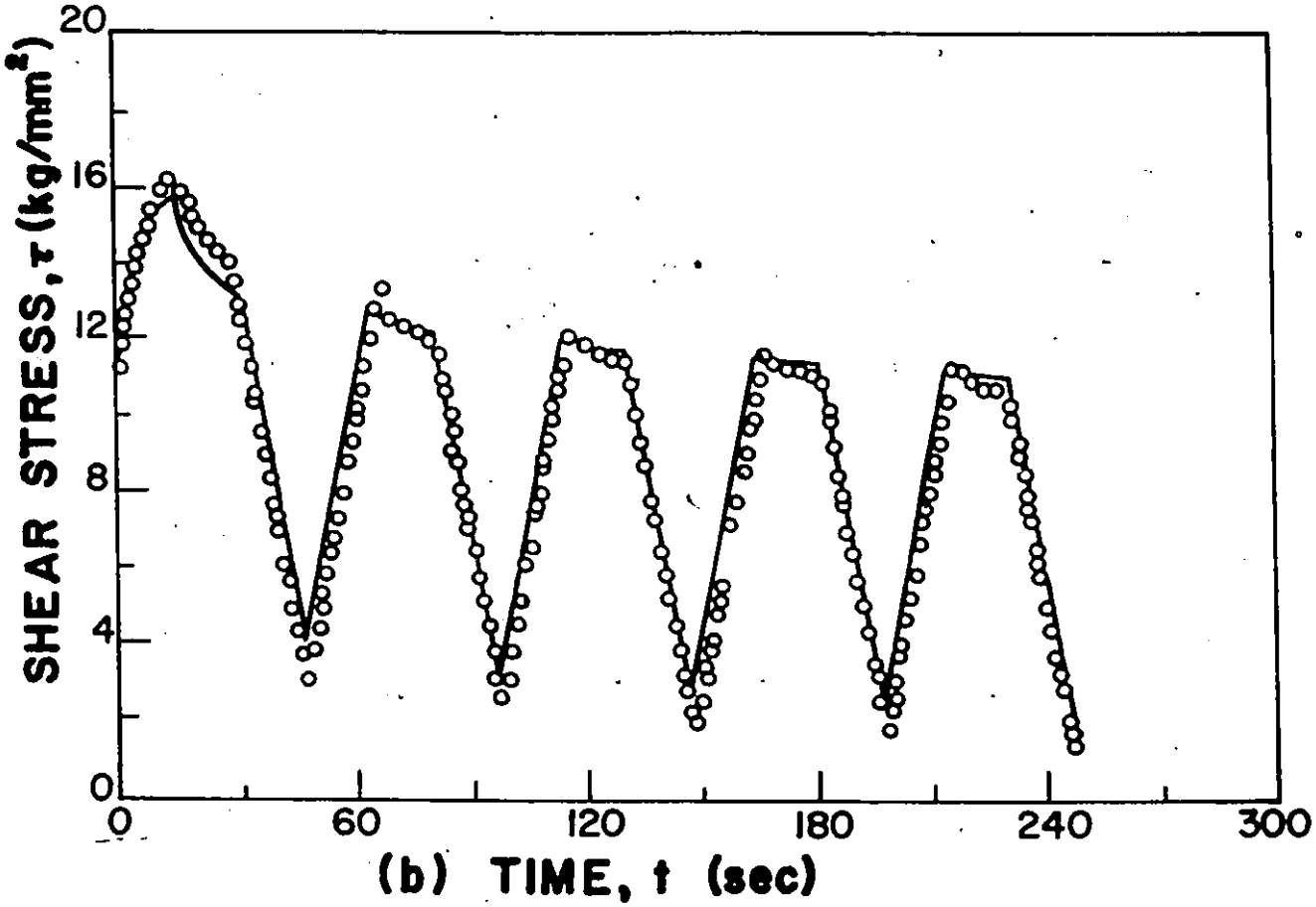

Figure 4.5. Stress-time response during strain controlled cyclic loading. (a) Input strain-time trapezoidal wave form, (b) stress-time response. The symbols represent experimental data while the solid line was calculated from the theory. The parameters are: $V_I=17b^3$, $A_I=4.5\times10^{-10}$/sec., $\epsilon_r=2.9\times10^{-3}$, p=50 sec., $\tau_0=11$kg/mm^2, and T=298K.

4.1.3 Effect of Cycle Period

The effect of cycle period on the cyclic deformation behavior was evaluated from strain controlled cyclic loading experiments that were carried out at different cross-head speeds (and hence different frequencies). A triangular total strain wave form with a strain amplitude of 2×10^{-3} was used and the experiments were carried out on a single specimen. The results are presented in Fig. 4.6 and were plotted on two sets of coordinate systems. In Fig. 4.6a, the results were plotted on stress change versus the logarithm of time coordinate system while in Fig. 4.6b they were plotted on a stress change versus the logarithm of number of cycles coordinate system.

It follows from Eq. 4.5 that when the first term in the argument is much greater than unity, the shear stress change is proportional to the natural logarithm of time. Consequently, the applied shear stress change after time t is not frequency dependent. Fig. 4.6a shows that when the shear stress change is plotted against the natural logarithm of time, the relationship is almost linear (with a large scatter) and that the cycle period has a negligible effect on the cyclic deformation. However, because t=mp, the use of the coordinate system in Fig. 4.6a obscures the effect of the cycle period on the cyclic deformation behavior. The frequency effect is illuminated when the stress change is plotted against the natural logarithm of the number of cycles (Fig. 4.6b). It is observed from the experimental results that (after N cycles) the larger the cycle period the larger is the shear stress change (or the lower is the applied shear stress). That is, since frequency = $\frac{1}{p}$, the smaller the frequency the larger is the shear stress change. Hence, the effect of the loading frequency on the cyclic deformation behavior manifests itself in the shear stress change per cycle.

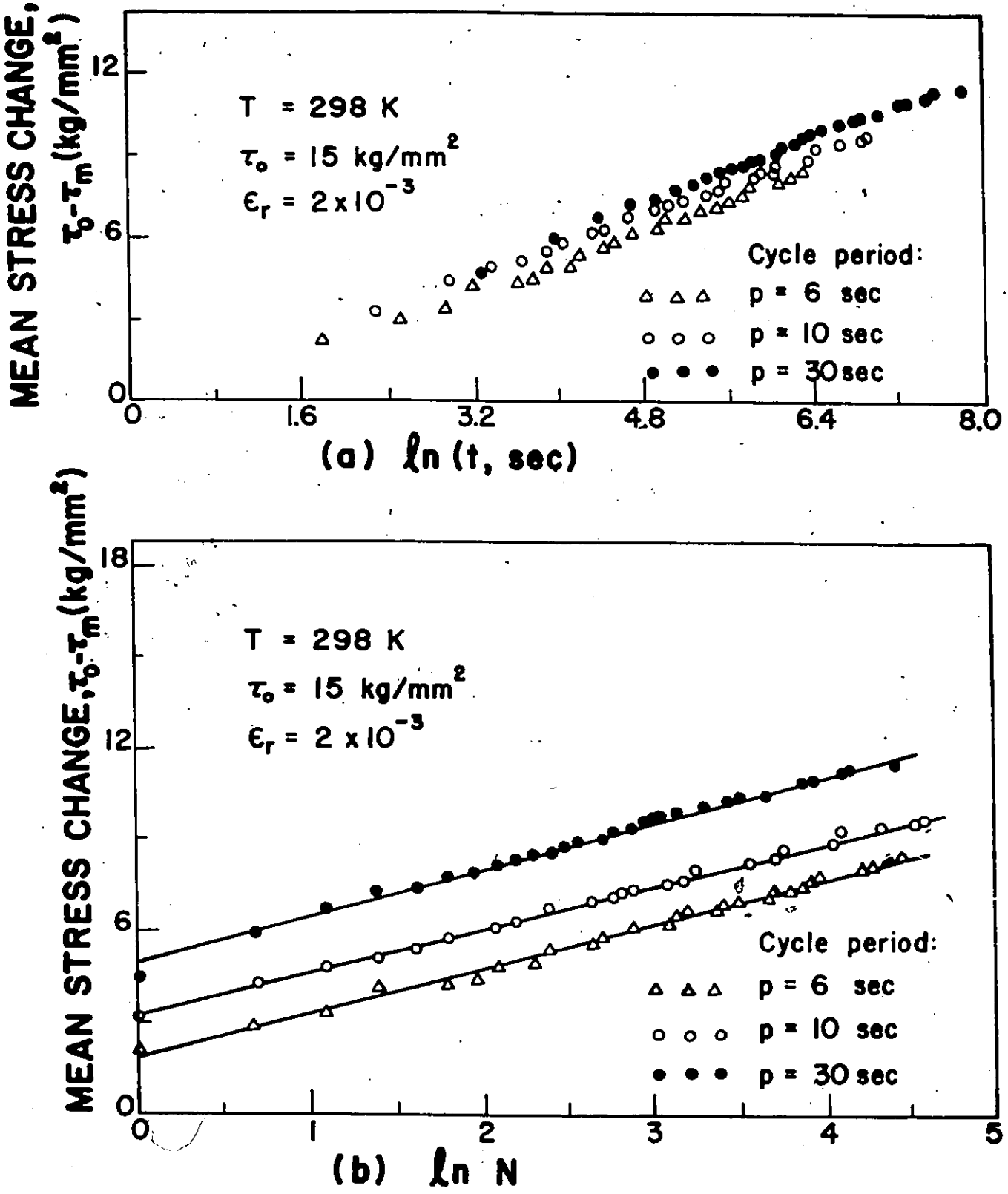

Figure 4.6. Effect of the cycle period on the strain controlled, cyclic deformation behavior. The symbols represent the experimental data while the lines were obtained from least square method, using Eq. 4.5. (a) Experimental results plotted on stress change versus logarithm of time coordinate system (b) the results were plotted on stress change versus logarithm of number of cycles coordinate system.

The constitutive parameters that were determined from the experimental results (at different frequencies) are almost identical. It seems, therefore, that the cycle period or the loading frequency has an insignificant effect on the constitutive parameters.

4.1.4 Activation Energy

Results from stress relaxation experiments that were conducted at different temperatures and on a single specimen (specimen number 3, Table 4.1) were used to determine activation energy. Following a procedure developed by Faucher [36], the activation energy at the transition stress was obtained from the temperature dependence of the transition strain rate. According to Eq. (2.29), the least square analysis (Fig. 4.7) leads to

$$\Delta G^{*} = 11.419 \times 10^{3}k = 0.983 \text{ eV}$$

and $\delta\rho_t = 7.2 \times 10^{-6}$

with a correlation factor of 0.97. The activation energies at zero stress, $\Delta G^{\ddagger}$, were determined from

$$\Delta G^{\ddagger}_{I,II} = \Delta G^{*} + V_{I,II}(\tau_a^{*} - \tau_i^{o}).$$

The transition stress is determined from the experimental results (Table 4.1) while the internal stress for the alloy is negligible. Consequently, τ_a^{*} was estimated at 3.5 ± 1.0 kg/mm^2 and the activation free energies $\Delta G^{\ddagger}_{I,II}$ were evaluated as

$$\Delta G^{\ddagger}_{I} = 1.06 \pm 0.02 \text{ eV}$$

and

$$\Delta G^{\ddagger}_{II} = 1.14 \pm 0.05 \text{ eV}.$$

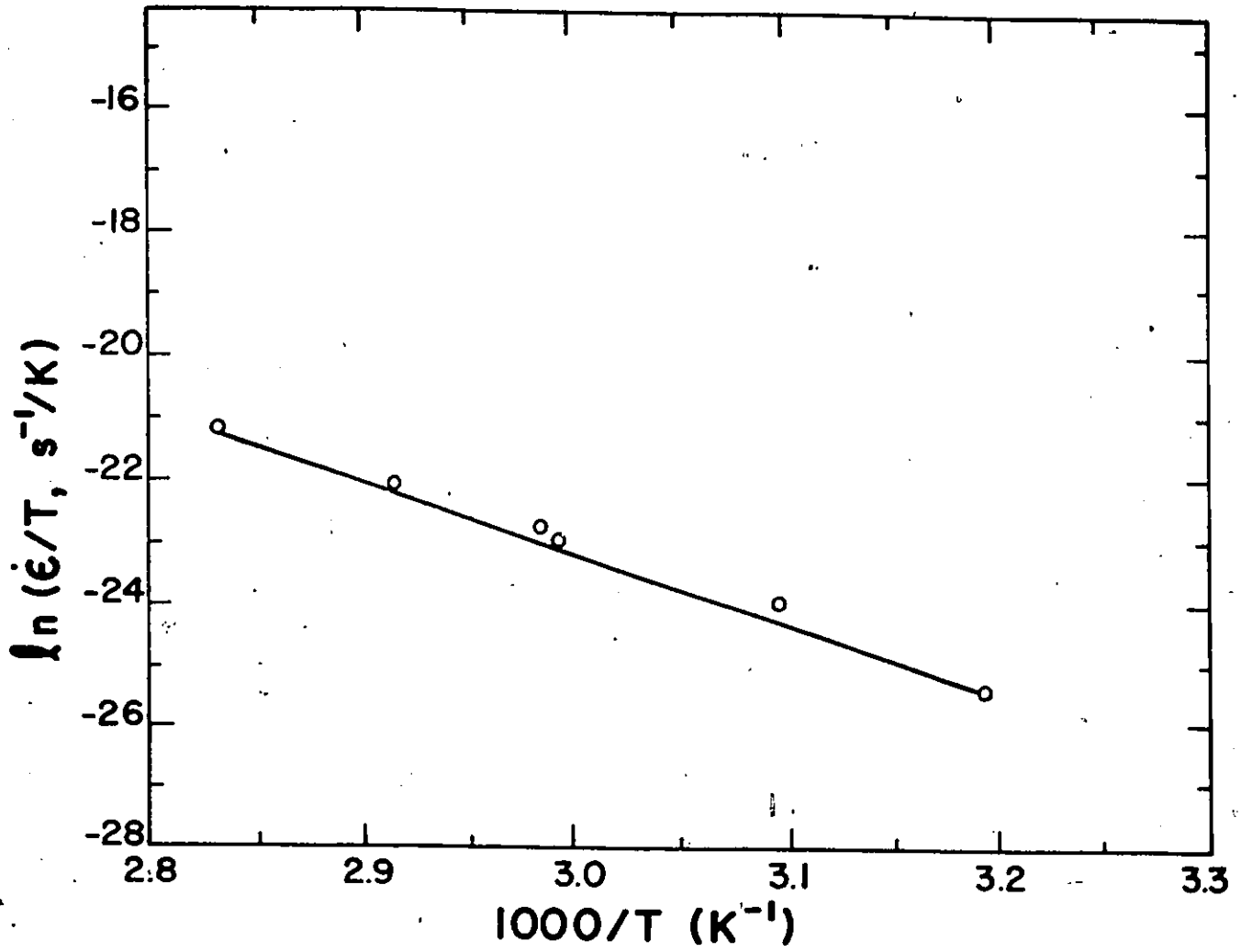

Figure 4.7. Determination of the activation energy at the transition stress for specimen 3.

The deformation behavior during stress relaxation of specimen number 3 at various temperatures is shown in Fig. 4.8. The symbols represent the experimental results while the curves were calculated from the theory, using the results of the Arrhenius plot. The excellent agreement between the theoretical prediction and the experimental results confirms the validity of the assumption that within the temperature range, the internal stress was negligible and that the material structural characteristics were constant during stress relaxation.

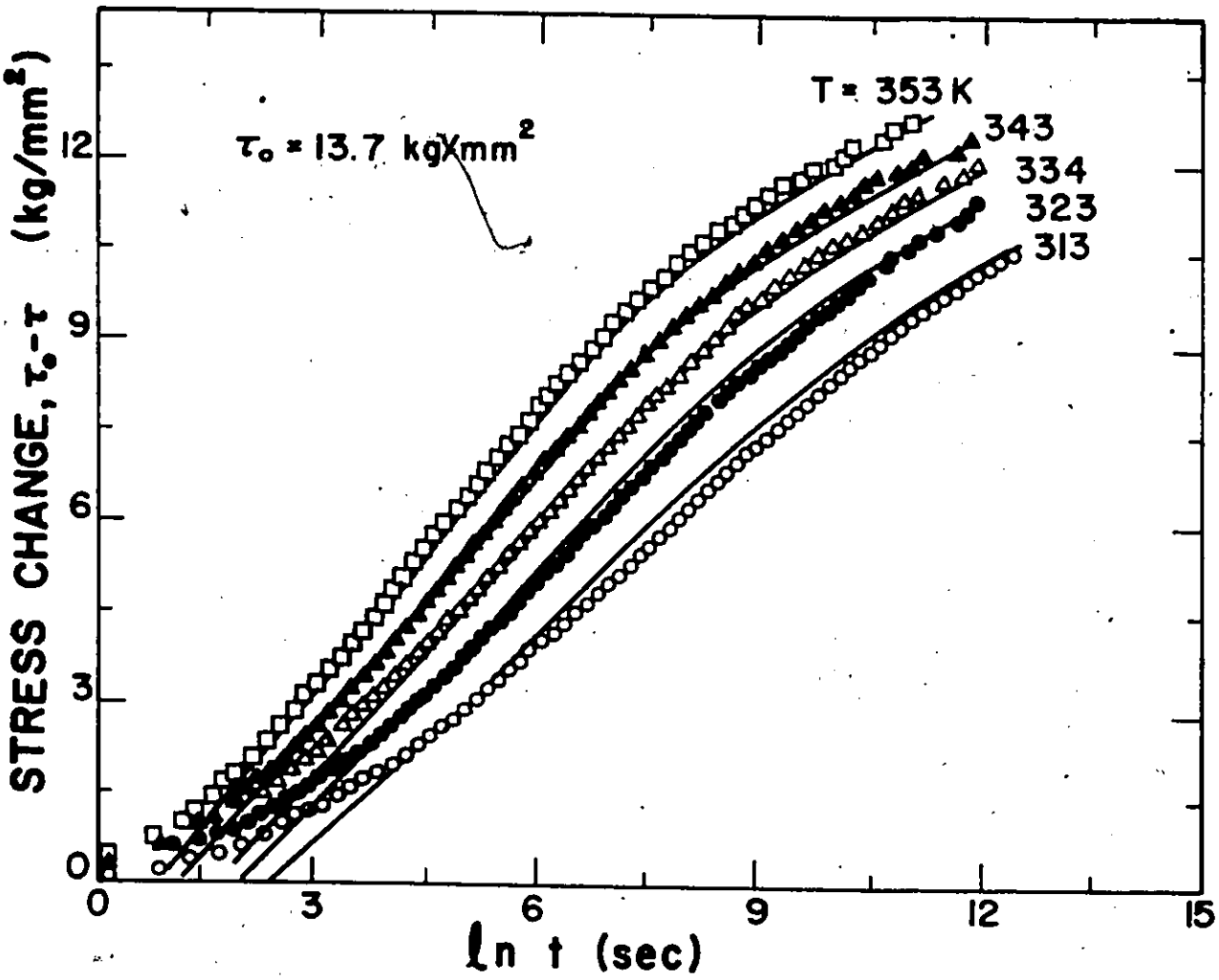

Figure 4.8. Effect of temperature on the stress relaxation behavior of specimen 3. The symbols represents the experimental data while the curves were evaluated from Eq. (2.27) (with ξ=t).

4.2 LOAD CONTROLLED CYCLIC LOADING

4.2.1 Evaluation of Constitutive Parameters

The total strain during load controlled cyclic deformation was evaluated (Section 2.2.1) as

$$\varepsilon = \varepsilon_0 + \frac{M(\tau_a-\tau_o)}{E} + A_I \int_0^t \exp \frac{V_I(\tau_a-\tau_i^o)}{kT}\, dt. \qquad (4.6)$$

For triangular load wave form, $\tau_a = \tau_o + \tau_1(t)$ (Fig. 3.8) and the integral can be evaluated following the method described in Section 4.1.1 as

$$\int_0^{mp} \exp \frac{V_I(\tau_a-\tau_i^o)}{kT}\, dt = \frac{kTt}{V\tau_r} \exp \frac{V_I(\tau_o-\tau_i^o)}{kT} \left| \exp \frac{V_I\tau_r}{kT} - 1 \right|.$$

Consequently, the total strain is evaluated in function of time t=mp and the stress amplitude as

$$\varepsilon = \varepsilon_0 + \frac{A_I\, kTt}{V\tau_r} \exp \frac{V_I(\tau_o-\tau_i^o)}{kT} \left| \exp \frac{V_I\tau_r}{kT} - 1 \right| \qquad (4.7)$$

since at t=mp, $\tau_a-\tau_o = 0$ (Fig. 3.8). The steady state total strain rate then is

$$\dot{\varepsilon} = \frac{A_I\, kT}{V\tau_r} \exp \frac{V_I(\tau_o-\tau_i^o)}{kT} \left| \exp \frac{V_I\,\tau_r}{kT} - 1 \right|. \qquad (4.8)$$

That is, during constant amplitude, load controlled cyclic deformation, the rate of strain accumulation is constant and is a function of the initial effective shear stress and the load amplitude.

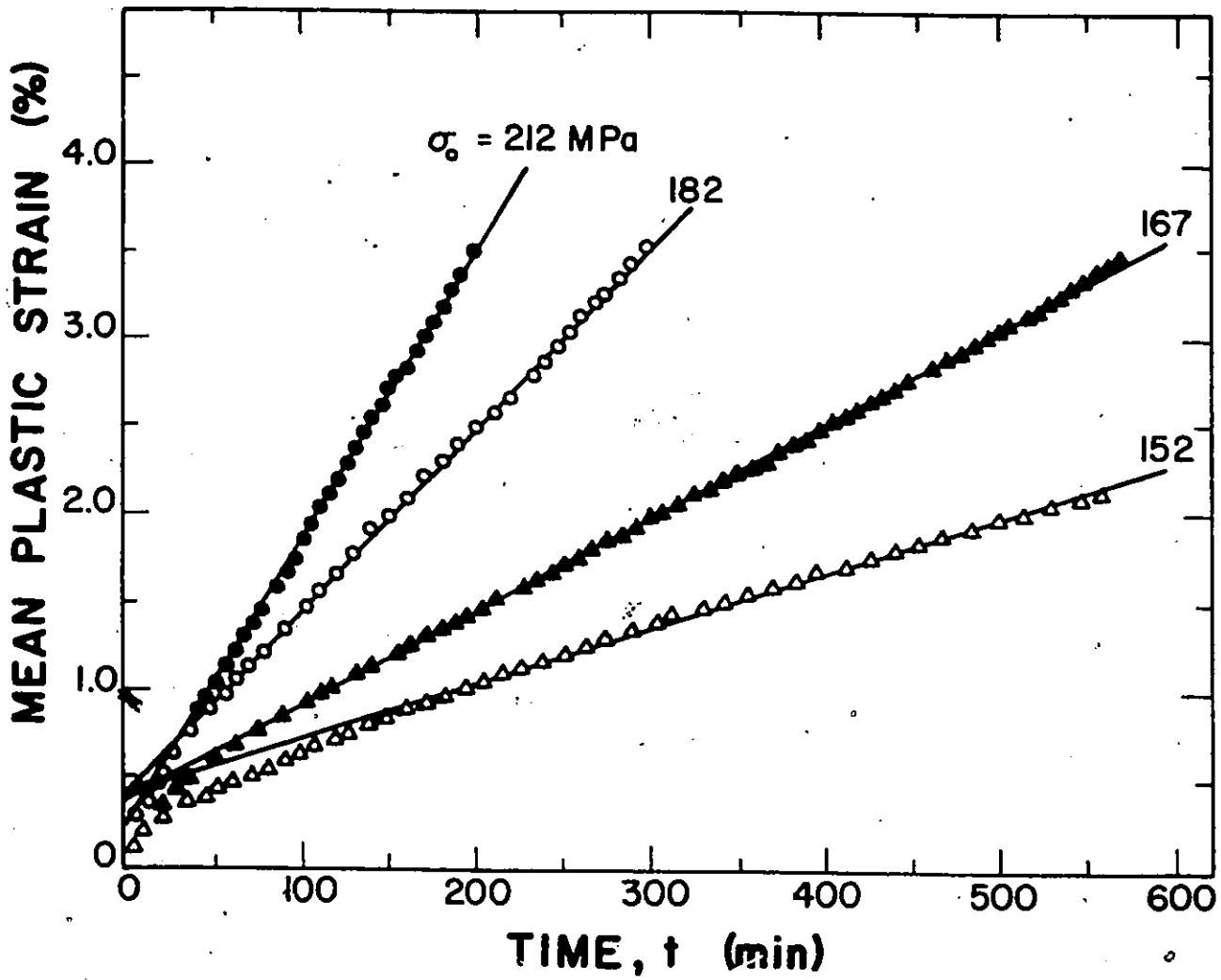

Figure 4.9. Mean plastic strain plotted in function of time for different initial stress levels. The lines were obtained from least square method using Eg. (4.7) while the symbols represent the measured values. The experimental parameters are: T=298K, σ_r=61MPa, and p=10 sec.

Fig. 4.9 shows typical experimental results that were obtained from constant amplitude, load controlled cyclic loading tests. The experiments were carried out at room temperature, 298 ± 1.0K, and with a (normal) stress amplitude of 61MPa (6.2 kg/mm^2). Each experiment was carried out on a different specimen. For each initial stress level, the mean plastic strain was plotted in function of time. The lines were obtained from least square method using Eq. (4.7). The linear time dependence of the accumulated cyclic strain indicates that no work hardening occurred: the material structural characteristics (ρ_t, V_I, and $\Delta G_I^{\ddagger}$) were constant during cyclic deformation. The slope of each of the lines represents the steady state strain rate at the corresponding initial stress and stress amplitude.

Similar cyclic loading experiments were carried out with (normal) stress amplitudes of 3.2 and 11.6 kg/mm^2 and at room temperature, 298 ± 1.0k. For each of these experiments, a single specimen was used. The procedure that was used to evaluate the steady state strain rate at each initial stress is illustrated in Fig. 4.10, both for creep (Fig. 4.10a) and cyclic loading (Fig. 4.10b).

The constitutive parameters were analyzed by plotting the strain rate in function of the initial stress on a semi-logarithm scale as shown in Fig. 4.11. According to Eq. (4.8), the plot should be a straight line; the slope of which is proportional to activation volume, V_I, while the intercept at τ_o=0 is proportional to the parameter A_I and is a function of the stress amplitude and the internal stress. However, for this alloy, the internal stress is negligible. The constitutive parameters that were evaluated from the experimental results (Fig. 4.11) are shown in Tables 4.3 and 4.4.

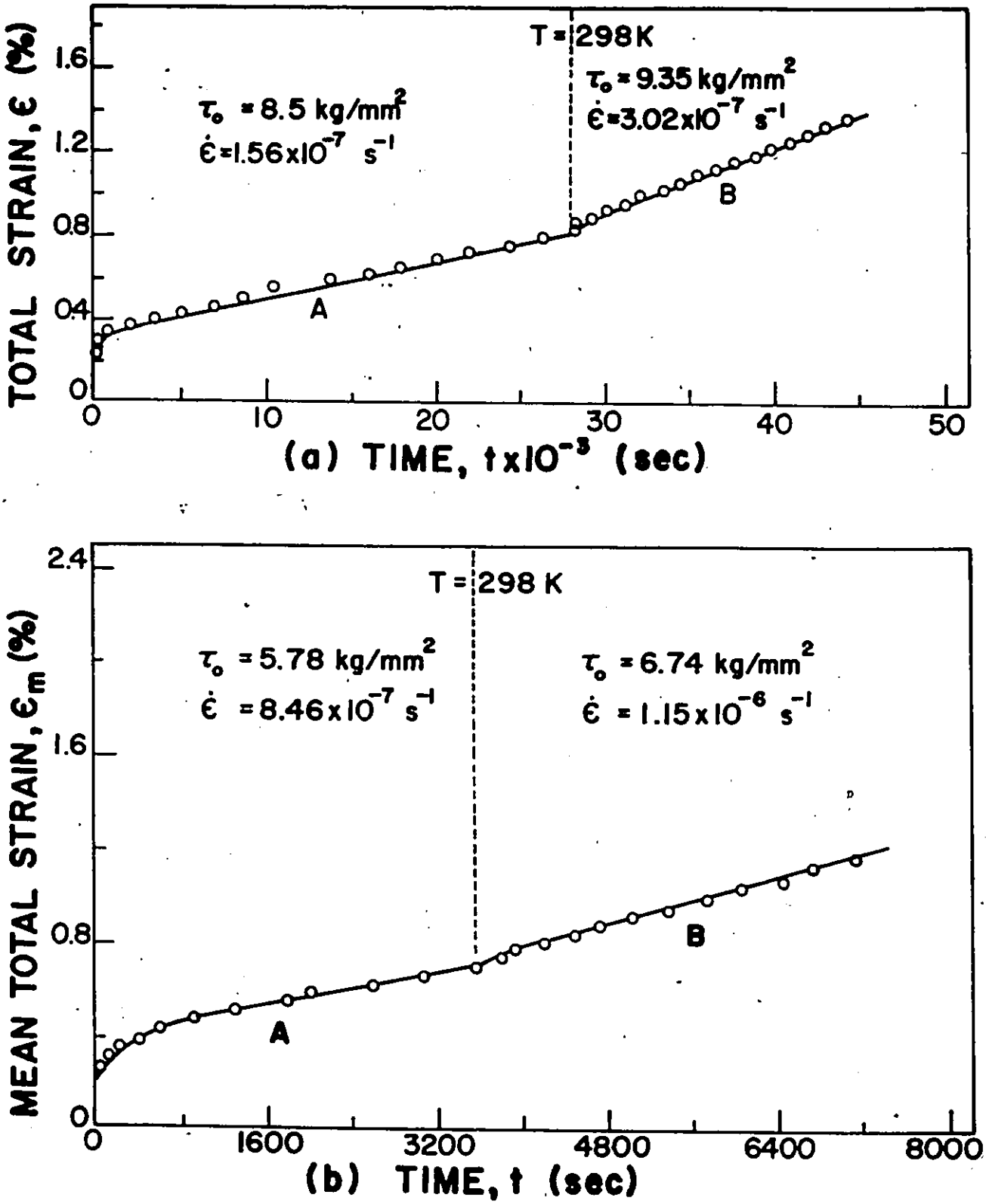

Figure 4.10. Typical strain-time curves when the (minimum) stress was increased (B) after steady state has been reached at a lower stress (A). (a) Constant load tests (b) Load controlled cyclic loading experiments with τ_r = 5.8 kg/mm^2. Notice the brief primary creep after stress was increased.

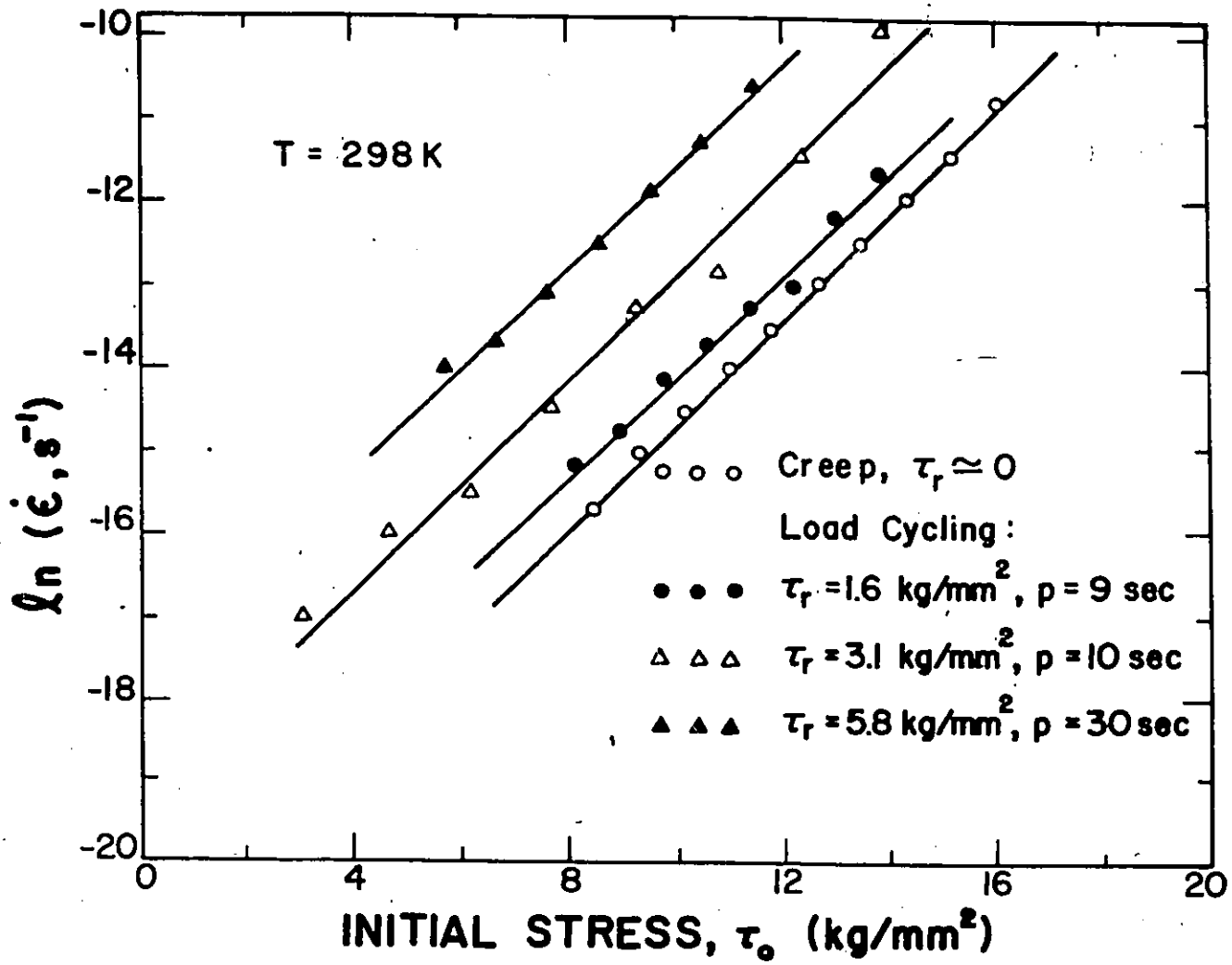

Figure 4.11. The natural logarithm of strain rate plotted in function of initial stress. The lines were obtained from least square method using Eq. (2.39b) for creep and Eq. (4.8) for load controlled cyclic loading while the symbols represent the experimental data. For τ_r = 3.1 kg/mm^2 each of the experimental point was determined from a different specimen while for the other stress amplitudes, a single specimen was used.

Table 4.3. Constitutive parameters determined from constant load experiments.

Experiment No.	Figure	Temp (K)	V_I (b^3)	A_I (sec^{-1})
1	4.11	298	13	8.3×10^{-10}
2	4.17	317	13	9×10^{-9}
3	4.17	330	13	6.42×10^{-8}
4	4.17	345	14	2.5×10^{-7}

Table 4.4. Constitutive parameters determined from load controlled cyclic loading experiments.

Experiment No.	Figure	Temp (K)	τ_r (kg/mm^2)	V_I (b^3)	A_I (sec^{-1})
1	4.11	298	1.6	13	10^{-9}
2	4.11	298	3.1	14	7.8×10^{-9}
3	4.11	298	5.78	13	2.4×10^{-9}

It follows from Tables 4.3 and 4.4 that the constitutive parameters determined from the analysis of constant load (creep) and load controlled cyclic loading experimental results are identical. The equality of the constitutive parameters indicates the validity of the assumption that the material structural characteristics remain constant during cyclic deformation. Consequently, constant load tests (creep) can be employed to determine the constitutive parameters and, by using the equations developed in this report, the load controlled cyclic deformation behavior can be predicted.

4.2.2 Strain-Time Response

The constitutive parameters that were determined from creep and load controlled cyclic loading experiments were used to calculate the load controlled cyclic deformation behavior. Fig. 4.12 shows the strain-time response during the first few cycles of a load controlled cyclic loading experiment (with a triangular load wave form). The symbols represent the experimental data while the solid line (Fig. 4.12b) was calculated from Eq. (2.37) (with $\tau_i \simeq 0$). Similarly, Fig. 4.13 (and also Fig. A8) shows the strain-time response for the sinusoidal load wave form. The symbols represent the experimental data while the solid line (Fig. 4.13b) was calculated numerically from Eq. (2.37) using a BASIC computer program [123] based on Romberg's method.

It is observed that within the stress, time, and temperature range where the constitutive equation of plastic flow during load controlled cyclic deformation can be approximated with activation over a single energy barrier, the total strain is proportional to time or number of loading cycles. The strain-time relation derived in this report describes well the cyclic deformation behavior. The excellent agreement between the predicted and the measured strain is an indication of the validity of the assumptions made in the derivation of the equations: the internal stress and the material structural characteristics remain constant during cyclic deformation.

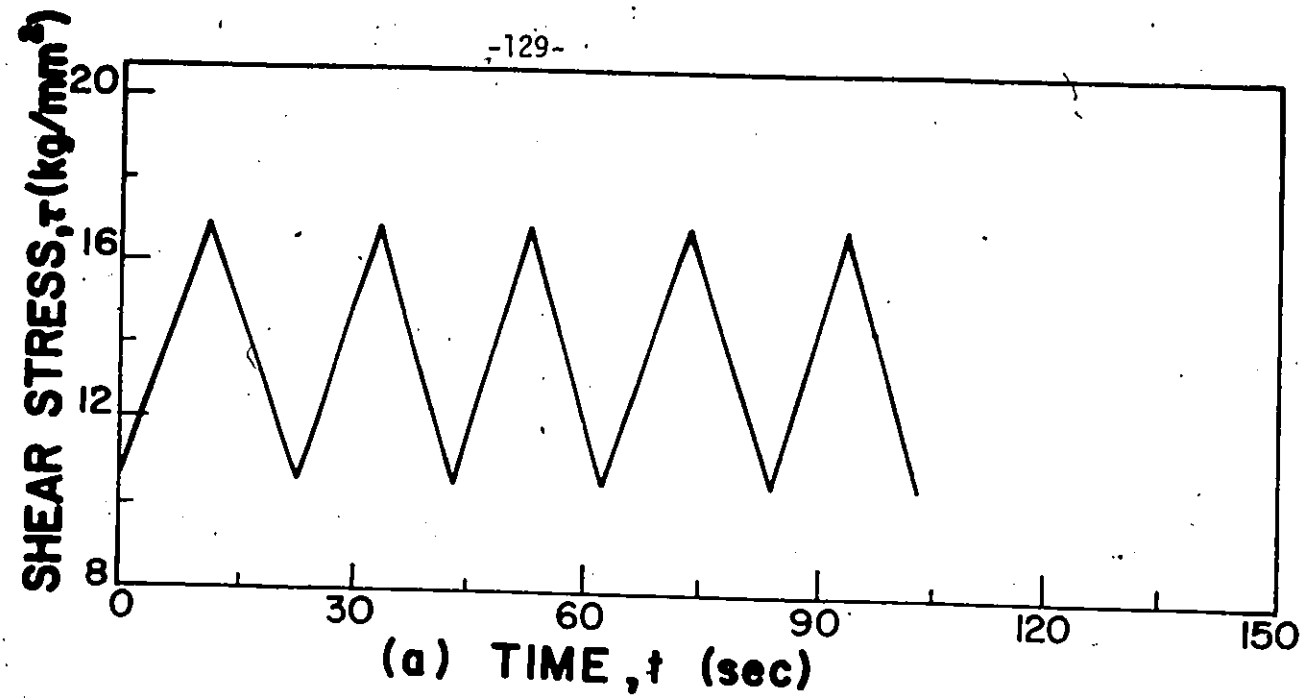

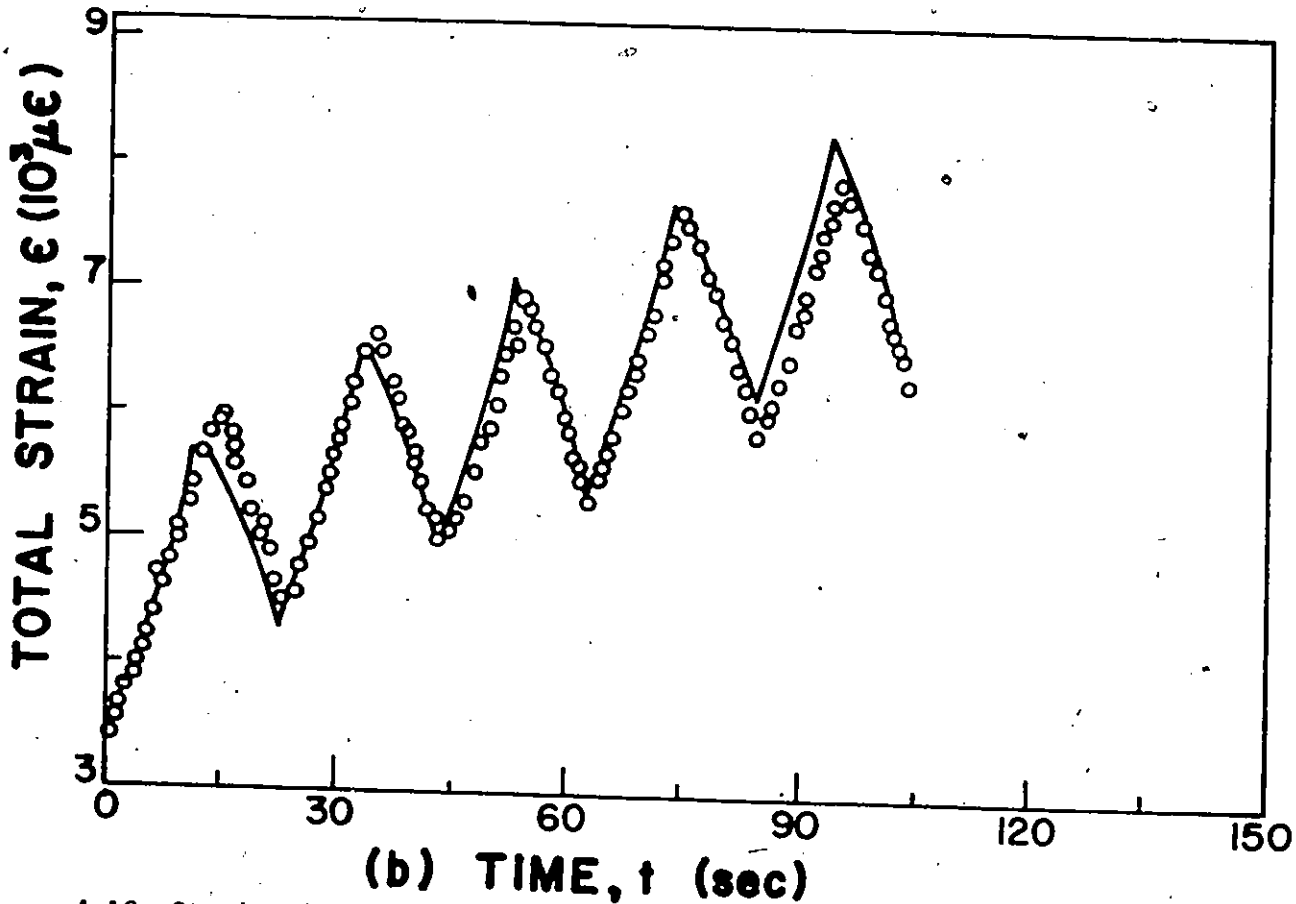

Figure 4.12. Strain-time response during load controlled cyclic loading. (a) Input stress-time triangular wave form (b) Strain-time response. The symbols represent the experimental data and the solid line was calculated from Eq. (2.37). The parameters are: $V_I = 12b^3$, $A_I = 10^{-9}$/sec, $\tau_o = 11.8$ kg/mm^2, $\tau_r = 6.2$ kg/mm^2, E=6580 kg/mm^2, p=22 sec. and T= 298K.

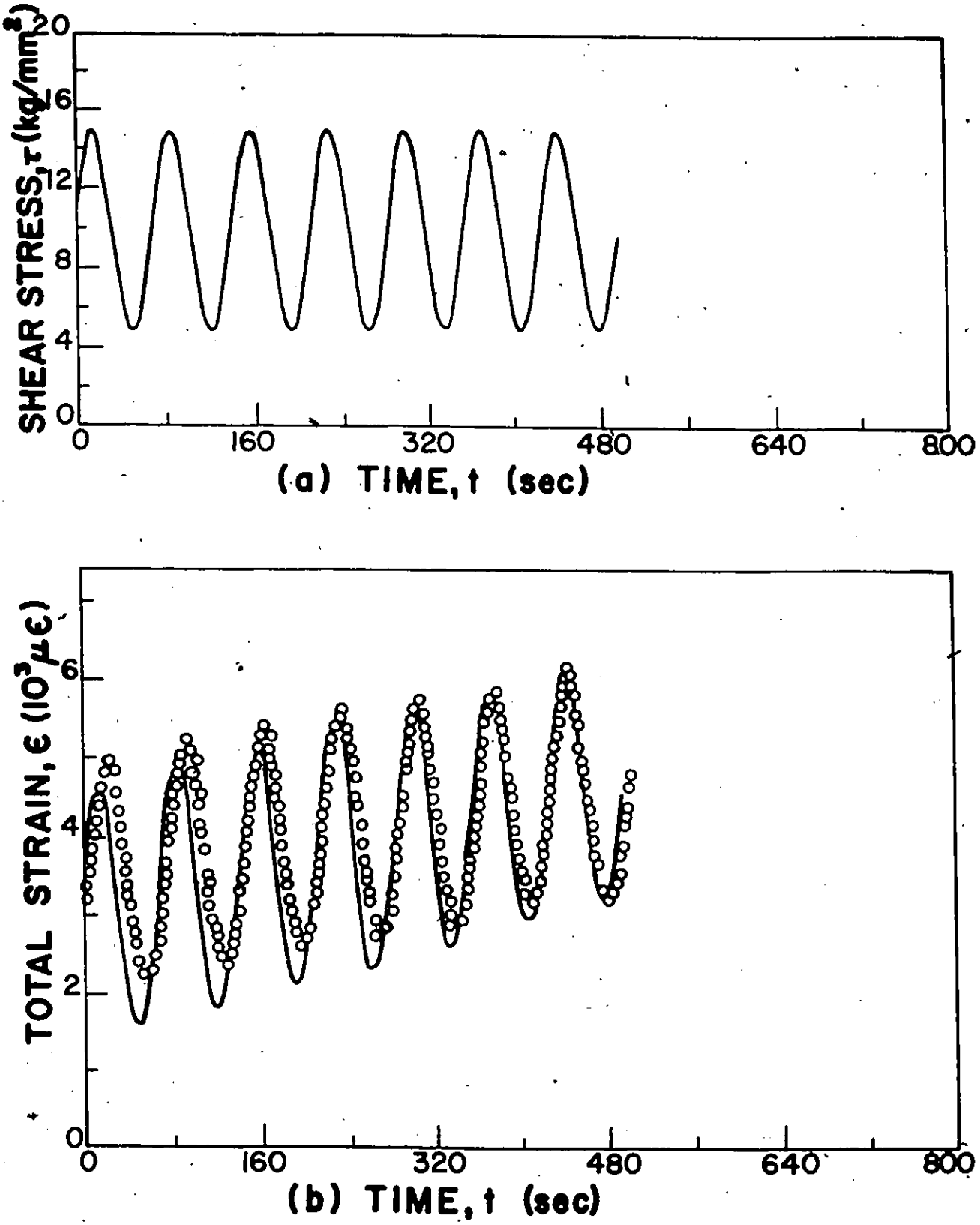

Figure 4.13. Strain-time response during load controlled cyclic loading. (a) Input stress-time, sinusoidal wave form (b) Strain-time response. The symbols represent the experimental data and the solid line was calculated numerically from the theory. The parameters are: $V_I = 13b^3$, $A_I = 10^{-9}$ sec^{-1}, $\tau_o = 10$ kg/mm^2, $\tau_r = 5$ kg/mm^2, E=6580 kg/mm^2, $p = 71$ sec., and T= 298K.

4.2.3 Effect of Cycle Period

The effect of cycle period on load controlled cyclic deformation behavior was evaluated from (load controlled) cyclic loading experiments that were carried out at different cross-head speeds (and hence different frequencies). A triangular stress wave form with stress amplitude of 3.66 kg/mm^2 was used and the experiments were carried out on a single specimen. The results were plotted on two coordinate systems as shown in Fig. 4.14 (and also Fig. A7). The strain response was plotted in function of time, Fig. 4.14a, and in function of number of loading cycles, Fig. 4.14b.

When the strain response is plotted in function of time, the strain-time relation is linear (Fig. 4.14a) and the cycle period has no significant effect on the cyclic deformation behavior. However, as pointed out earlier, the use of strain-time axes obscures the effect of cycle period on the cyclic deformation behavior because t=mp. It is clear from Fig. 4.14b that when the strain response is plotted in function of the number of loading cycles, the effect of cycle period on cyclic deformation behavior is apparent. The higher the cycle period the higher is the strain increment per cycle (slope of the curve represents the strain increment per cycle). In other words, the lower the frequency the higher is the strain increment per cycle. Hence the effect of cycle period on the cyclic deformation behavior manifests itself in the strain increment per cycle. The strain rates (rate of strain accumulation) that were evaluated from least square method were almost identical; the cycle period has no significant effect on the strain rate. The experimental results confirm the theoretical prediction (Eq. 4.8): the rate of cyclic strain accumulation is a function of the initial effective shear stress and the stress amplitude.

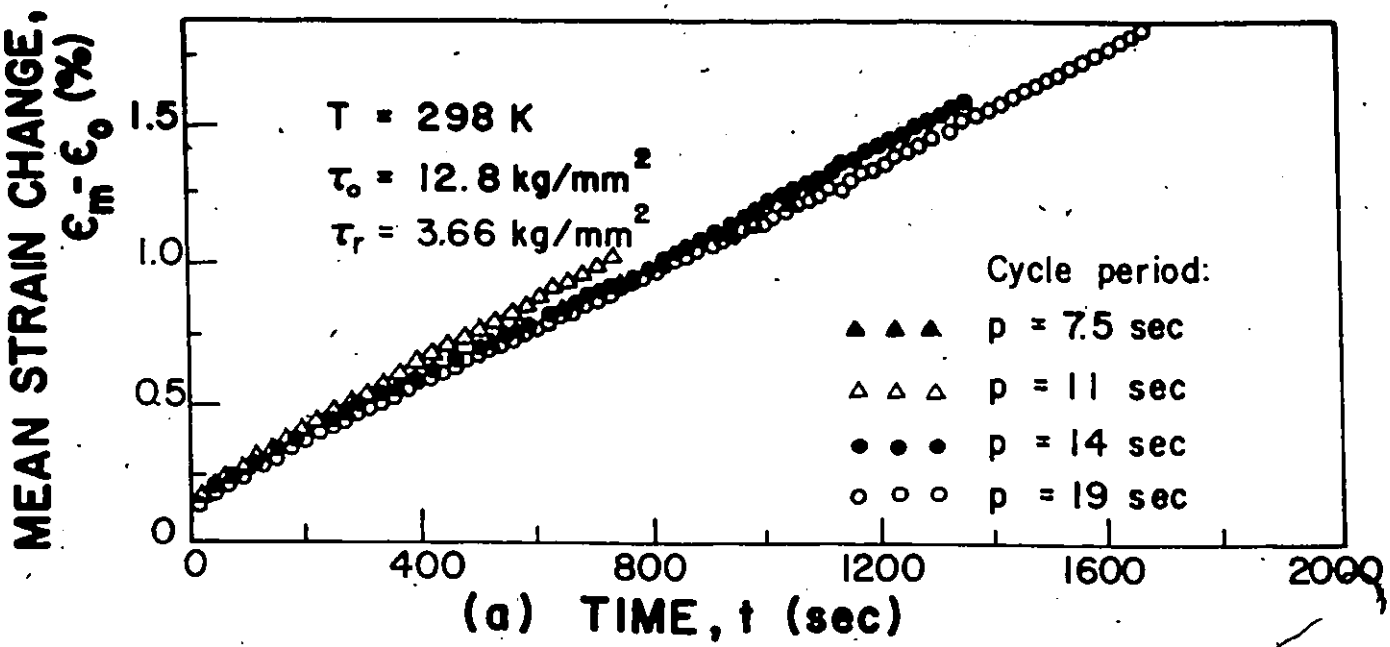

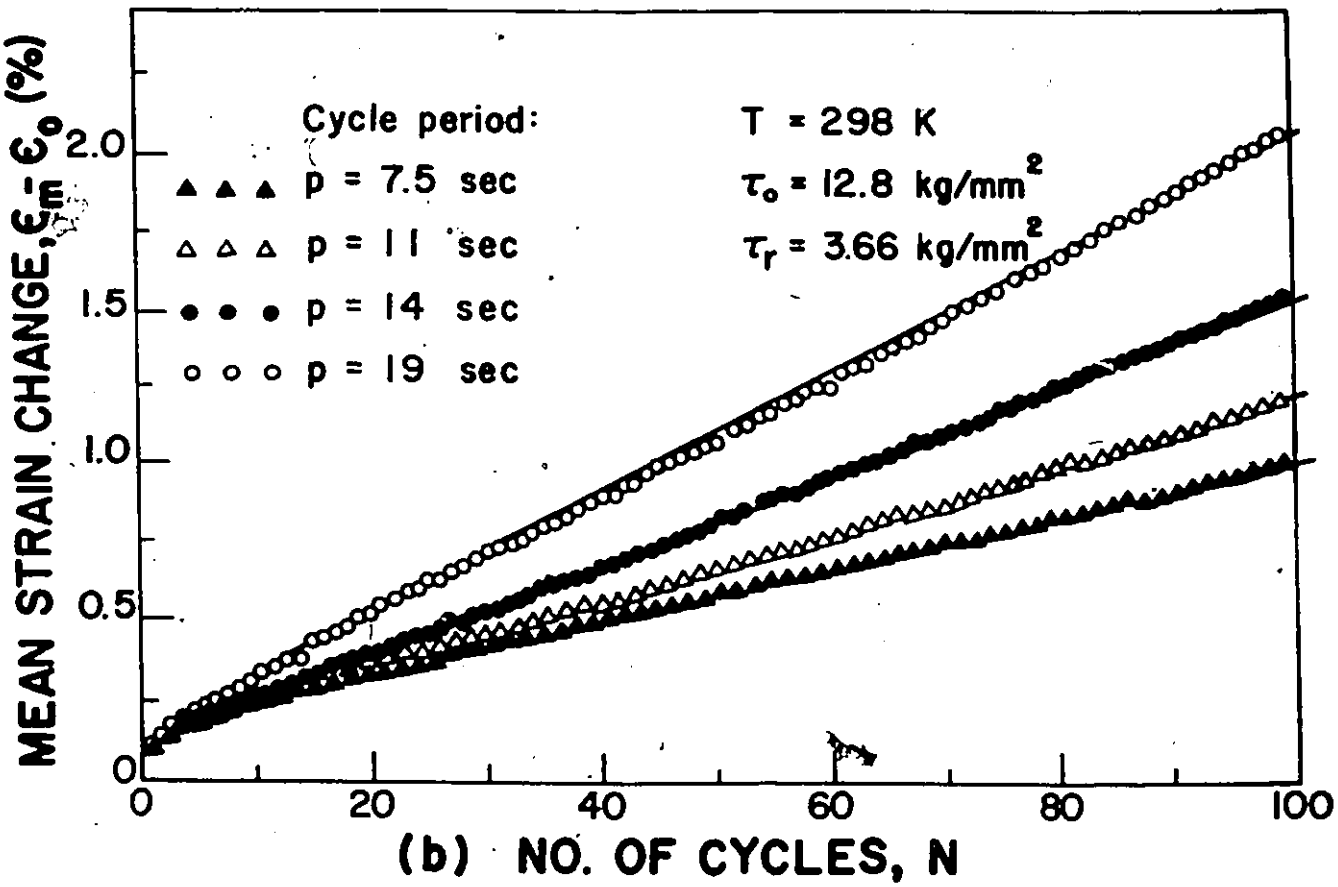

Figure 4.14. Effect of cycle period on the load controlled cyclic deformation behavior. The symbols represent the experimental data while the lines were obtained from least square method using Eq. (4.7). (a) Strain response plotted in function of time, and (b) Strain response plotted in function of number of cycles.

4.2.4 Effect of Stress Ratio

Fig. 4.15 shows results of experiments that were carried out at different stress ratios,

$$R = \frac{\tau_{min}}{\tau_{max}} = \frac{\tau_{min}}{\tau_{min} + \tau_r} \quad . \tag{4.9}$$

The experiments were conducted on a single specimen and with a cross-head speed of 1.0 mm/min, and with a triangular load wave form. The accumulated cyclic strain was measured at constant τ_{min} (Fig. 4.15a) and at constant τ_{max} (Fig. 4.15b). The experimental results show that for constant τ_{min} a decrease in the stress ratio leads to increase in both the strain and strain rate while for constant τ_{max}, a decrease in the stress ratio leads to a decrease in both the strain and strain rate. In other words, the strain and strain rate are functions of the mean stress: the higher is the mean stress the higher are the accumulated strain and strain rate. The normalized strain rates that were determined from the experimental results (Fig. 4.15) were compared with theoretical prediction, as shown in Fig. 4.16. It is evident from the figure that there is a good agreement between the calculated and the measured strain rates.

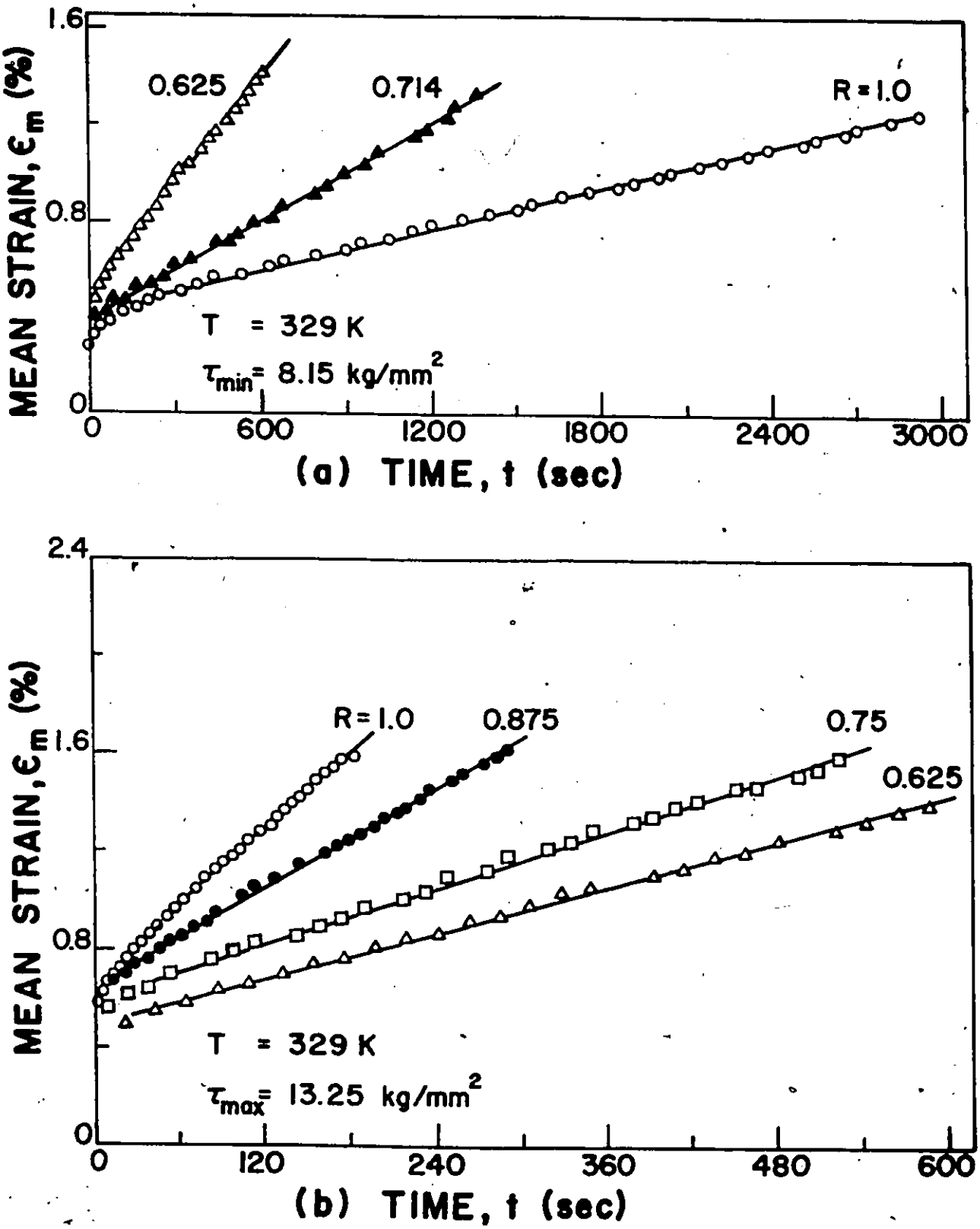

Figure 4.15. Effect of stress ratio, $R = \tau_{min}/\tau_{max}$ on the cyclic deformation behavior. (a) Deformation with constant minimum stress, τ_{min} and (b) constant maximum stress, τ_{max}. The cross-head speed was 1.0 mm/min for all the experiments.

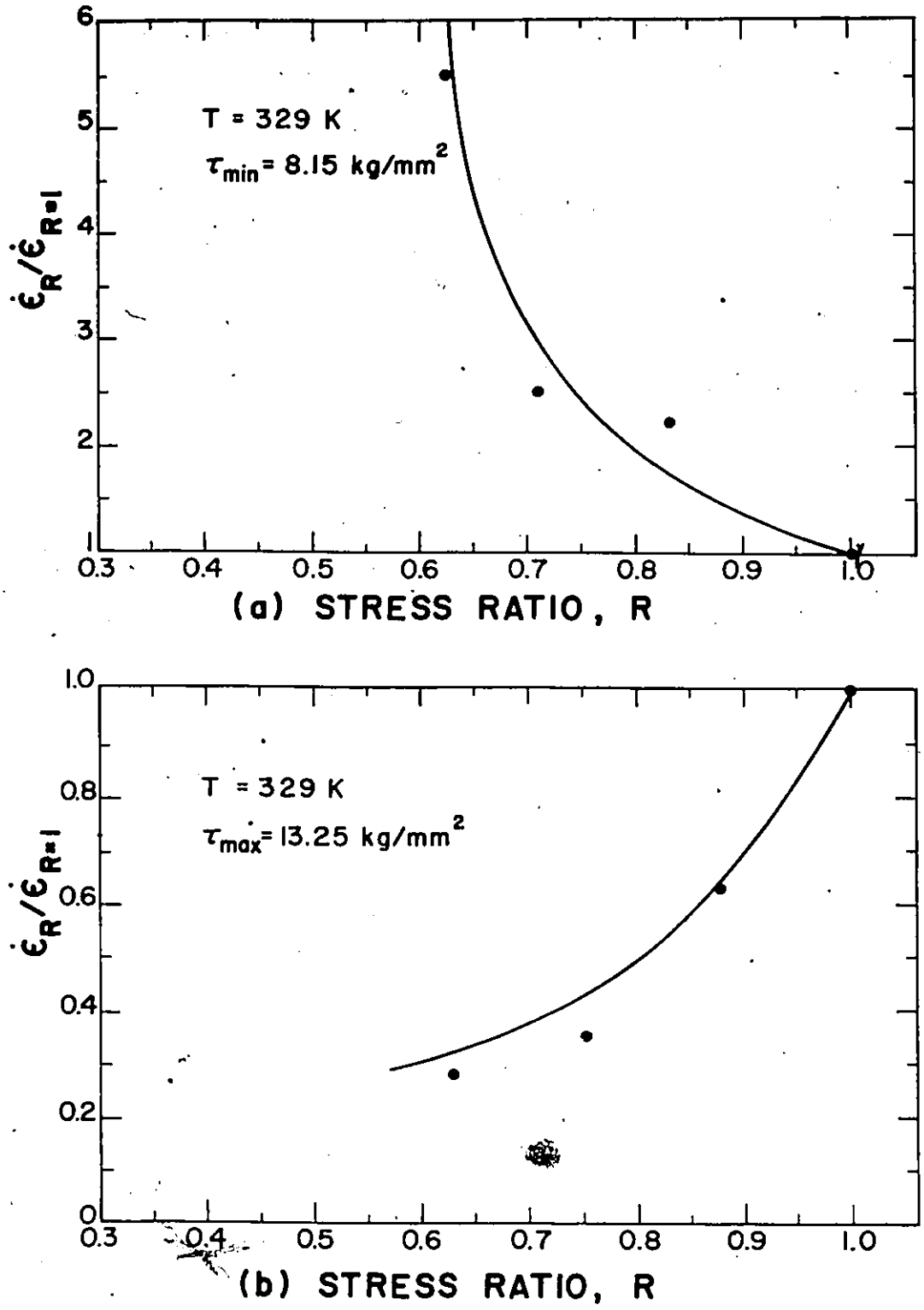

Figure 4.16. Effect of stress ratio on the strain rate. (a) Cyclic deformation with constant τ_{min} and (b) with constant τ_{max}. The curves were calculated from Eqs. (2.39b) and (4.8) with V_I/kT = 0.61 mm^2/kg and the symbols represent experimental data.

4.2.5 Activation Energy

The activation energy associated with creep was determined from temperature cycling experiments and from Arrhenius plot. The rate of plastic flow was measured over the temperature range for which the activation energy was to be determined. It was assumed that within the temperature range the material structural characteristics ($\Delta G^{\ddagger}$, ρ_t, and V) remain unchanged. That is, the material structural characteristics are constant during the activation energy measurements. When these conditions are satisfied, then it follows from Eq (2.7) that, because the strain rates measured at two different temperatures T_1 and T_2 are related, the experimental apparent activation energy ΔG_I can be expressed from

$$\frac{\dot{\varepsilon}_{p1}}{\dot{\varepsilon}_{p2}} \approx \exp\left[- \frac{\Delta G_I}{k} \left(\frac{1}{T_1} - \frac{1}{T_2}\right)\right]$$

as

$$\Delta G_I \approx \frac{-k}{\frac{1}{T_1} - \frac{1}{T_2}} \ln \left(\frac{\dot{\varepsilon}_{p1}}{\dot{\varepsilon}_{p2}}\right) \tag{4.10}$$

or

$$\Delta G_I = -k \frac{d \ln \dot{\varepsilon}_p}{d \left(\frac{1}{T}\right)} . \tag{4.11}$$

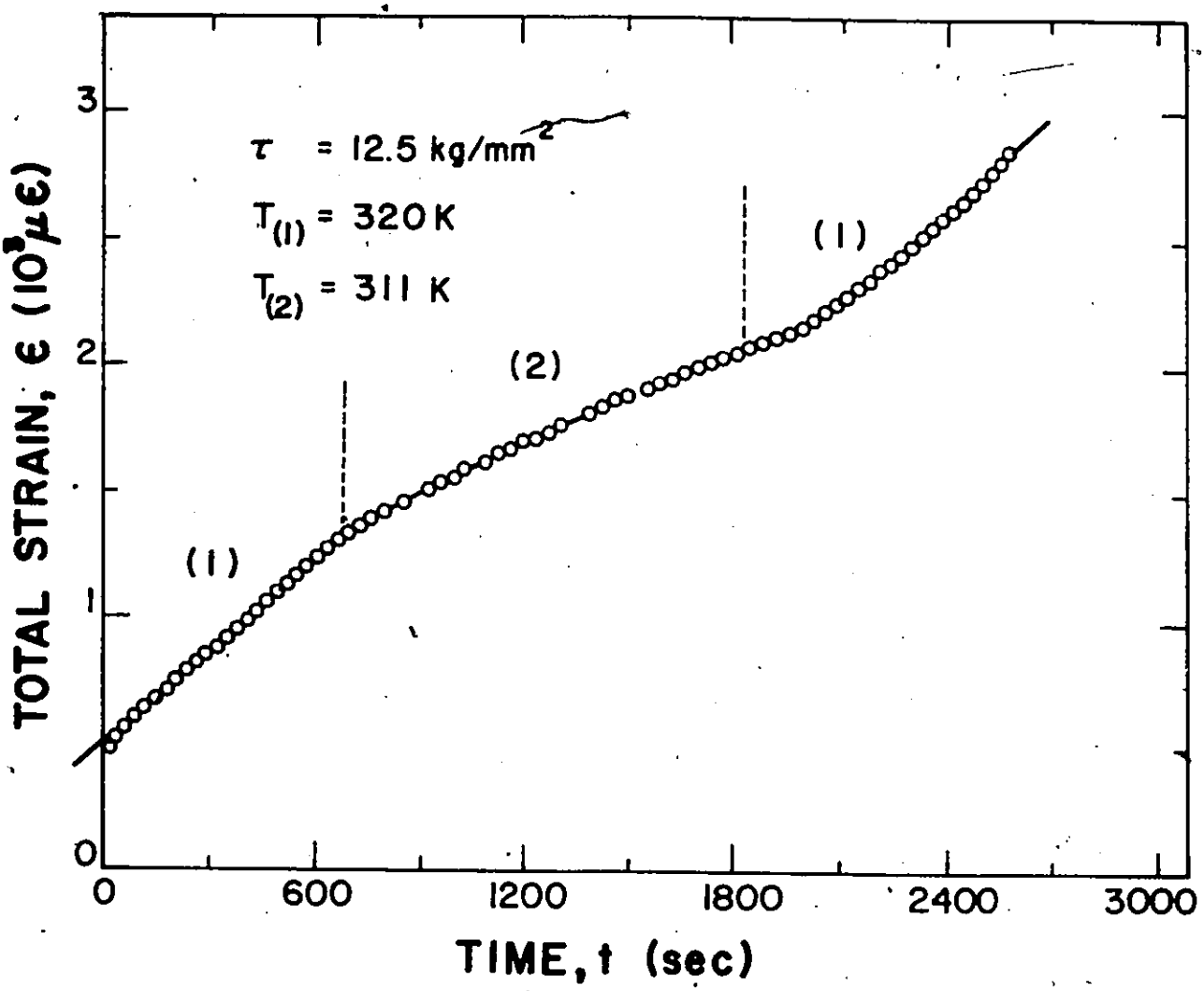

Figure 4.17. A typical strain versus time curve measured in a temperature cycling experiment. The strain rate in regions (1) is 1.2×10^{-5}/sec. while that in region (2) is 5.53×10^{-6}/sec.

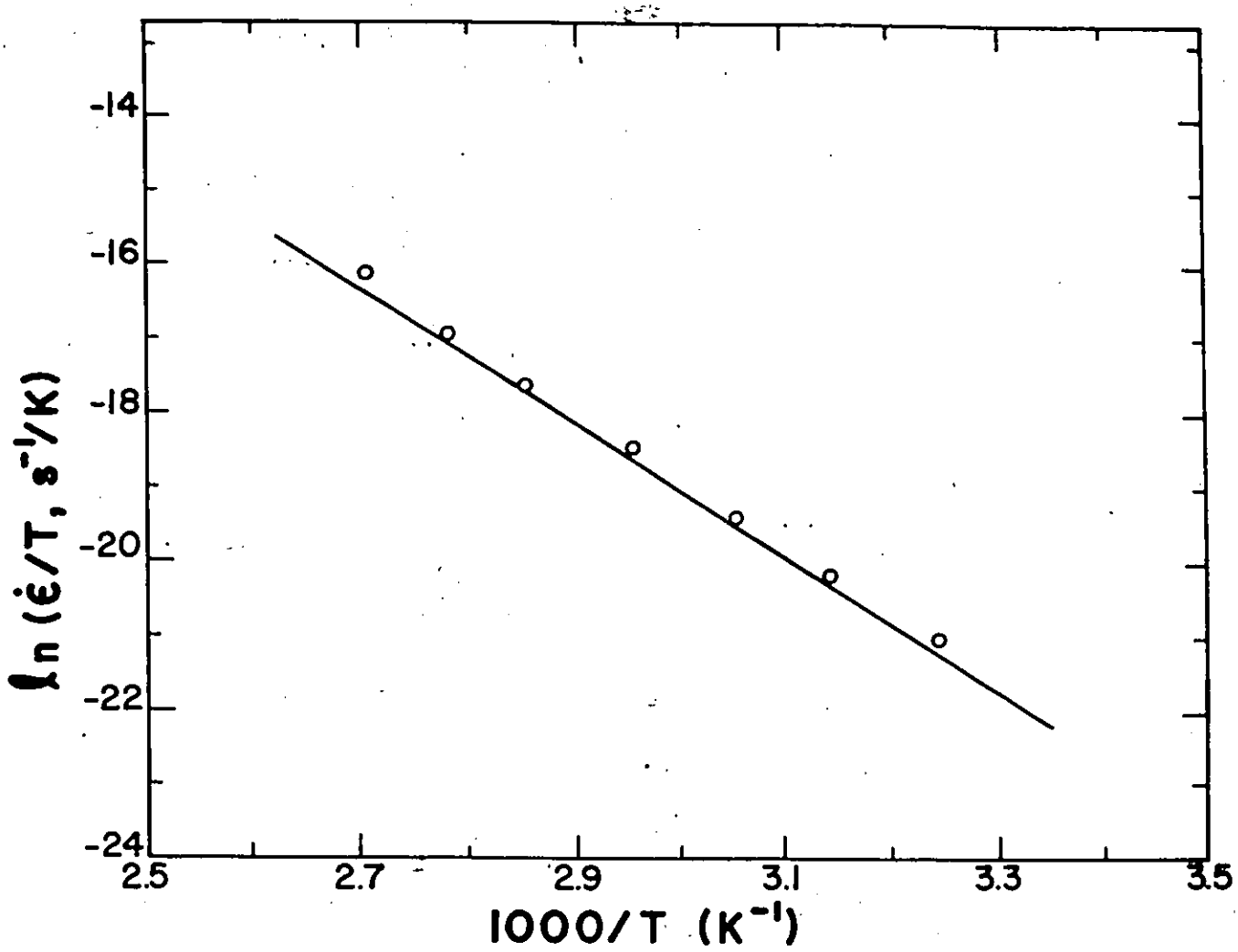

Figure 4.18. The Arrhenius type plot for creep of the near eutectoid Zn-Aℓ alloy. The experiments were carried out on a single specimen and at a constant shear stress of 8.15 kg/mm^2. The steady state strain rate was measured in function of temperature which was increased in steps of about 10K from 300K to 370K.

Fig. 4.17 shows a typical strain versus time curve measured in a temperature cycling experiment. From the results of the experiment the experimental activation energy was evaluated from Eq. (4.10) as

$$\Delta G_I \simeq \frac{k}{\frac{1}{T_2} - \frac{1}{T_1}} \ln \frac{\dot{\varepsilon}_1}{\dot{\varepsilon}_2} = 8.577 \times 10^3 \, k$$

while the activation energy at zero stress was determined from Eq. (2.6) as

$$\Delta G_I^{\ddagger} = \Delta G_I + V_I \, \tau_{eff} = 11.2 \times 10^3 k$$

or $\Delta G_I^{\ddagger} = 0.964$ eV.

The experimental activation energy was also evaluated from the Arrhenius type plot using Eq. (4.11) (Fig. 4.18) as

$$\Delta G_I = 9.054 \times 10^3 k$$

with a correlation factor of 0.95.

Similarly, the activation energy at zero stress was determined as

$$\Delta G_I^{\ddagger} = 11.106 \times 10^3 k = 0.956 \text{ eV}.$$

The least square analysis of the Arrhenius plot also leads to the evaluation of the parameter $\delta\rho_t$ as

$$\delta\rho_t \simeq 2 \times 10^{-7}$$

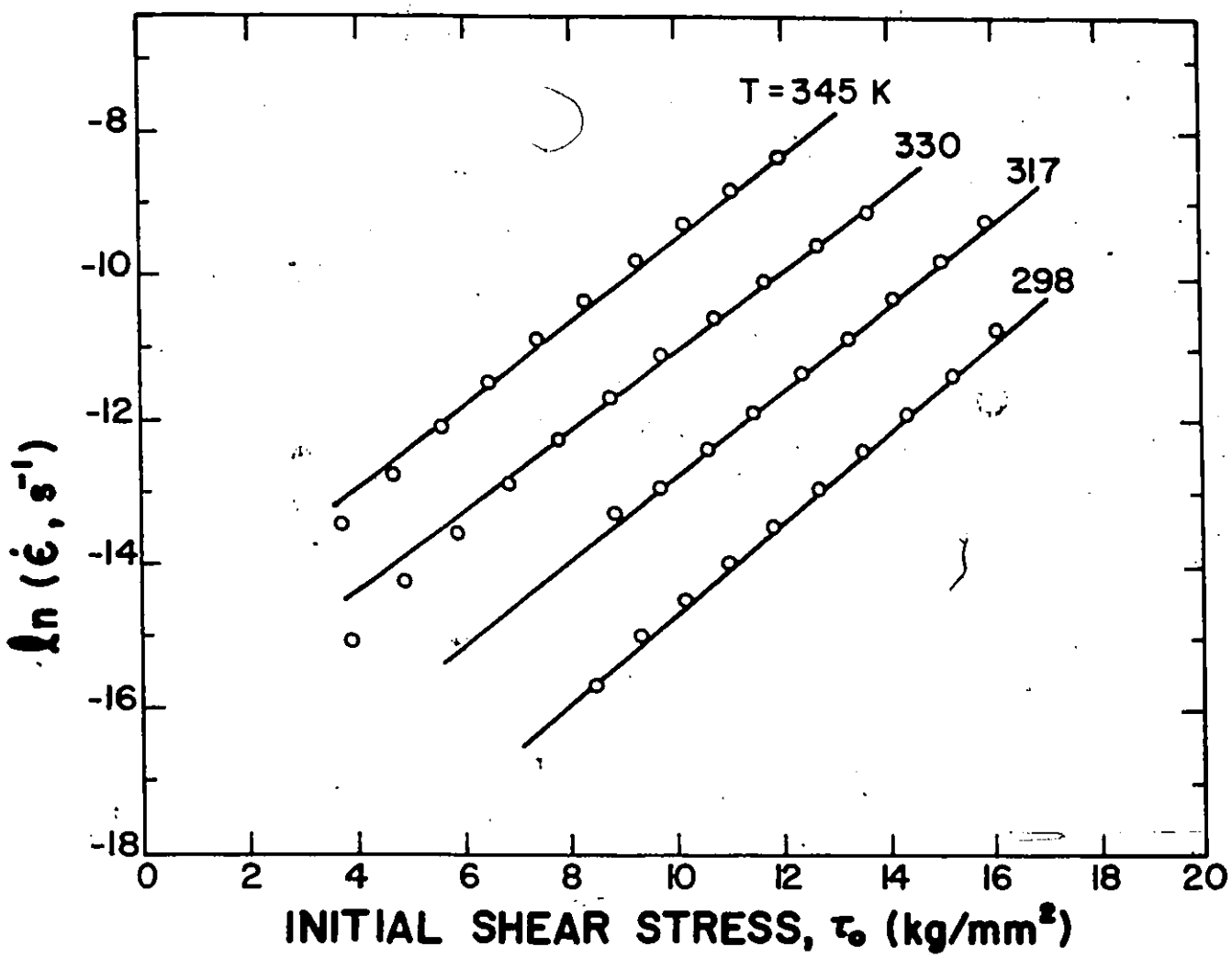

Figure 4.19. Effect of temperature on the creep rate. The symbols represent experimental data while the lines were obtained from least square method using Eq. (2.39b)

which compares well with that determined from the analysis of the stress relaxation experimental results (Fig. 4.7). Table 4.5 shows the activation energies, $\Delta G^{\ddagger}_{I,II}$, that were evaluated from temperature change tests in creep and from stress relaxation. It is observed that the activation energies (for plastic flow of the near eutectoir Zn-Aℓ alloy) that were determined from the present analysis are comparable to those obtained by other investigators.

It is evident from Fig. 4.19 that the constitutive equation describes well the temperature dependence of the creep behavior of the Zn-Aℓ alloy. Furthermore, the excellent agreement between the predicted and the measured creep rates confirms the validity of the assumption that within the high stress and low temperature range the material structural characteristics remains unchanged during creep.

4.3 CONSTITUTIVE PARAMETERS

4.3.1 Activation Volume

The activation volumes $V_{I,II}$ were determined from the analysis of stress relaxation, creep, and cyclic loading experimental results. It was considered that the internal stress was negligible and that the work hardening coefficient H = 0. However, Sargent [124] showed that the measured activation volume is related to the true activation volume V as

$$V_I = V(1 + \frac{H}{E}).$$

Table 4.5. Activation energies for plastic flow of the near eutectoid Zn-Aℓ alloy.

Testing Method	Method of Temperature Variation	Activation Energy		Investigators
		$\Delta G_I^{\neq}$ (eV)	$\Delta G_{II}^{\neq}$ (eV)	
Stress relaxation	Test at different temperature	1.06±0.02	1.14±0.05	Present study
Creep	Temperature cycling	0.964	-	Present study
Creep	Temperature change	0.956	-	Present study
Creep	Temperature change	1.09±0.04	-	Chaudhari [117]
Creep	Temperature cycling	0.82±0.05	1.23±0.06	Mohamed and Langdon [125]
Creep	Temperature change	0.82	1.25	Vaidya, Murty and Dorn [118]

For strain controlled experiments, E is the elastic modulus of the specimen while if displacement is the controlled variable, E is the combined elastic modulus describing the net elastic response of the test specimen and grip assembly. Because E is large and H was negligible, the measured activation volume $V_I \approx V$.

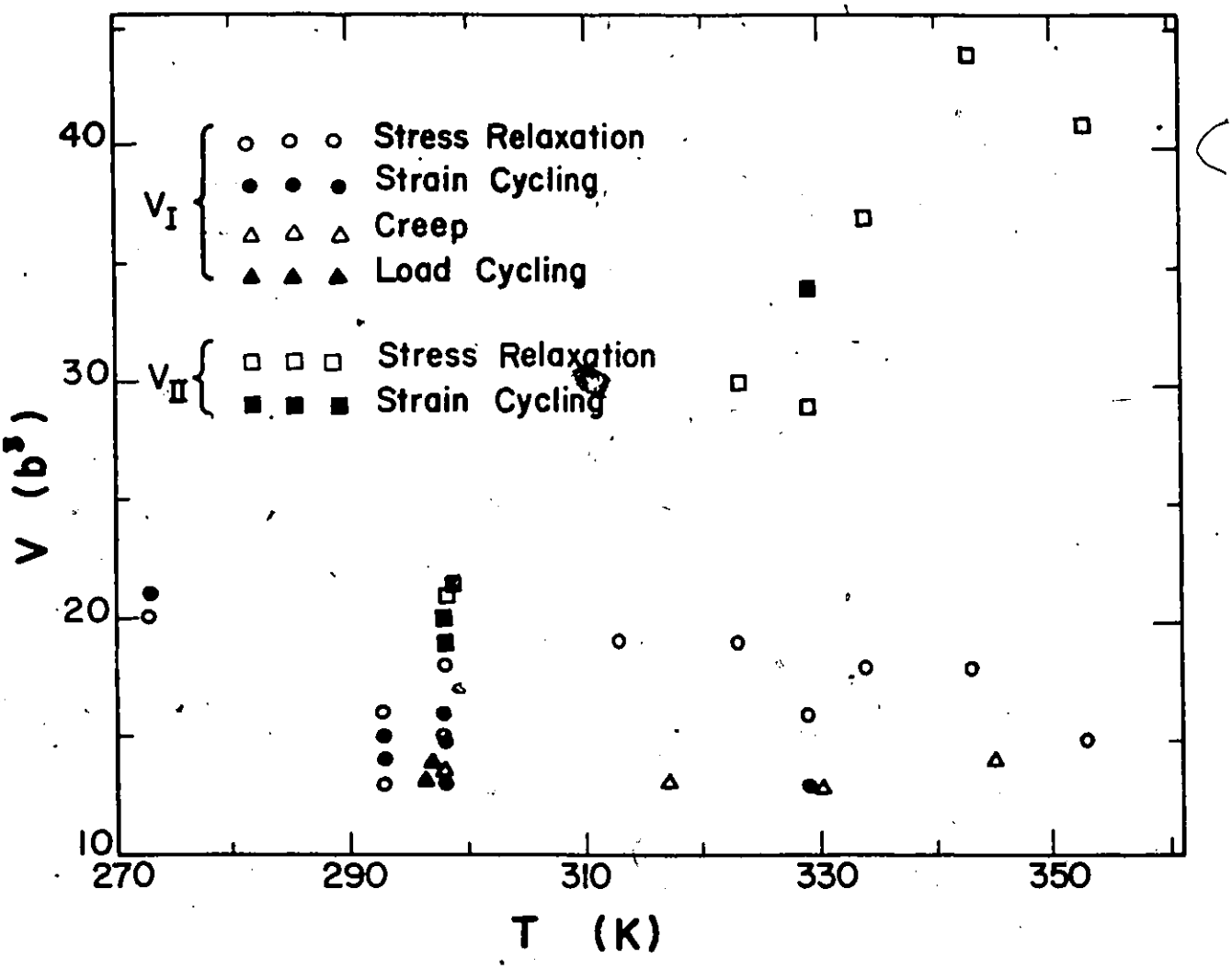

Figure 4.20. Temperature dependence of the activation volumes, $V_{I,II}$, evaluated from the analysis of stress relaxation, creep, and cyclic loading experimental results. Over 20 specimens were used in the experiments.

The measured activation volumes are also related to the dislocation density changes. Because the strain rate is

$$\dot{\varepsilon}_p = \delta \rho_t k_I,$$

the experimental activation volume, V_I, measured in stress relaxation when ρ_t changes is

$$V_I = kT \frac{\partial \ell n \dot{\varepsilon}_p}{\partial \tau_{eff}} = kT \left| \frac{\partial \ell n \rho_t}{\partial \tau_{eff}} + \frac{\partial \ell n k_I}{\partial \tau_{eff}} \right|.$$

During stress relaxation, the stress rate is proportional to the strain rate and the measured activation volume is expressed as

$$V_I = - \frac{kT}{E} \frac{\partial \ell n \rho_t}{\partial \varepsilon_p} \frac{\partial \sigma_{eff}}{\partial \tau_{eff}} + V.$$

The dislocation density is related to the strain [108] as

$$\rho_t = \rho_t^o + B\varepsilon_p.$$

The measured activation volume then becomes

$$V_I = \frac{2kT}{E} \frac{-B}{\rho_t^o + B\varepsilon_p} + V.$$

At 300K, with E = 6580 kg/mm^2, $\varepsilon_p = 8 \times 10^{-3}$ and when $\varepsilon_p \quad \rho_t^o/B$, the correction factor is only $0.8b^3$. This small correction factor is negligible and proves that it was legitimate to neglect dislocation multiplication in the analysis of the deformation behavior of the Zn-Aℓ alloy.

The measured activation volumes were plotted in function of temperature as shown in Fig. 4.20. While V_I appears to be temperature independent, the

activation volume at low stress level, V_{II}, seems to increase with temperature. Faucher and Krausz [82] have shown that this effect is a general feature of consecutive energy barrier systems. They concluded that because the true activation volumes that are associated with each of the free energies ($\Delta G^{\ddagger}_{I,II}$) are constant, the temperature dependence of the measured activation volume is only an apparent effect that results from the properties of consecutive energy barrier systems. Moreover, it was considered in the analysis of the experimental results that the backward activation over the energy barriers were negligible. In Region II the stress level is low and this assumption is not strictly valid. Nevertheless, the two energy barrier system describes well the cyclic deformation behavior.

It is apparent from Tables 4.1, 4.2, 4.3, and 4.4 that the activation volumes obtained from the analysis of stress relaxation, creep, and strain and load controlled cyclic loading experimental results are similar. Consequently, within the high-stress and low temperature range where the backward activations over the energy barriers are negligible the activation volumes determined from the analysis of stress relaxation and creep experimental results can be used to predict the cyclic deformation behavior, using the theory developed in this thesis. The measured activation volume V_I is within the range $17 \pm 4b^3$ while V_{II} is within the range $31 \pm 12b^3$. The results are well in agreement with those obtained in previous studies [34, 106, 107, 119, 126] where V_I was determined as $14 \pm 2b^3$ while V_{II} was evaluated as $39 \pm 15b^3$.

4.3.2 Constitutive Parameters $A_{I, II}$

The constitutive parameters, $A_{I,II}$, that were obtained from the analysis of stress relaxation, creep, and cyclic loading experimental results were plotted in function of the reciprocal of temperature on semi-logarithm scales as shown in Figs. 4.21 and 4.22. The figures show that the constitutive parameters determined from stress relaxation, creep, and cyclic loading are within the same range. According to Eq.(2.11), the relations should be straight lines, the slopes of which are proportional to the activation energies, $\Delta G_I^{\ddagger}$ or $\Delta G_{II}^{\ddagger}$. However, because the experimental results were obtained from different tests (stress relaxation, creep, and cyclic loading) and from a large number of specimens (over 20 specimens) which inherently have slight variations in structural parameters (ρ_t, V, and $\Delta G^{\ddagger}$), a scatter of up to two orders of magnitude is observed. Consequently, the temperature dependence of $A_{I,II}$ was used for preliminary evaluation of the activation energies associated with the deformation mechanisms. The actual activation energies were determined from the Arrhenius type plots (obtained from temperature change and temperature cycling techniques) as discussed in Sections 4.1.4 and 4.2.5.

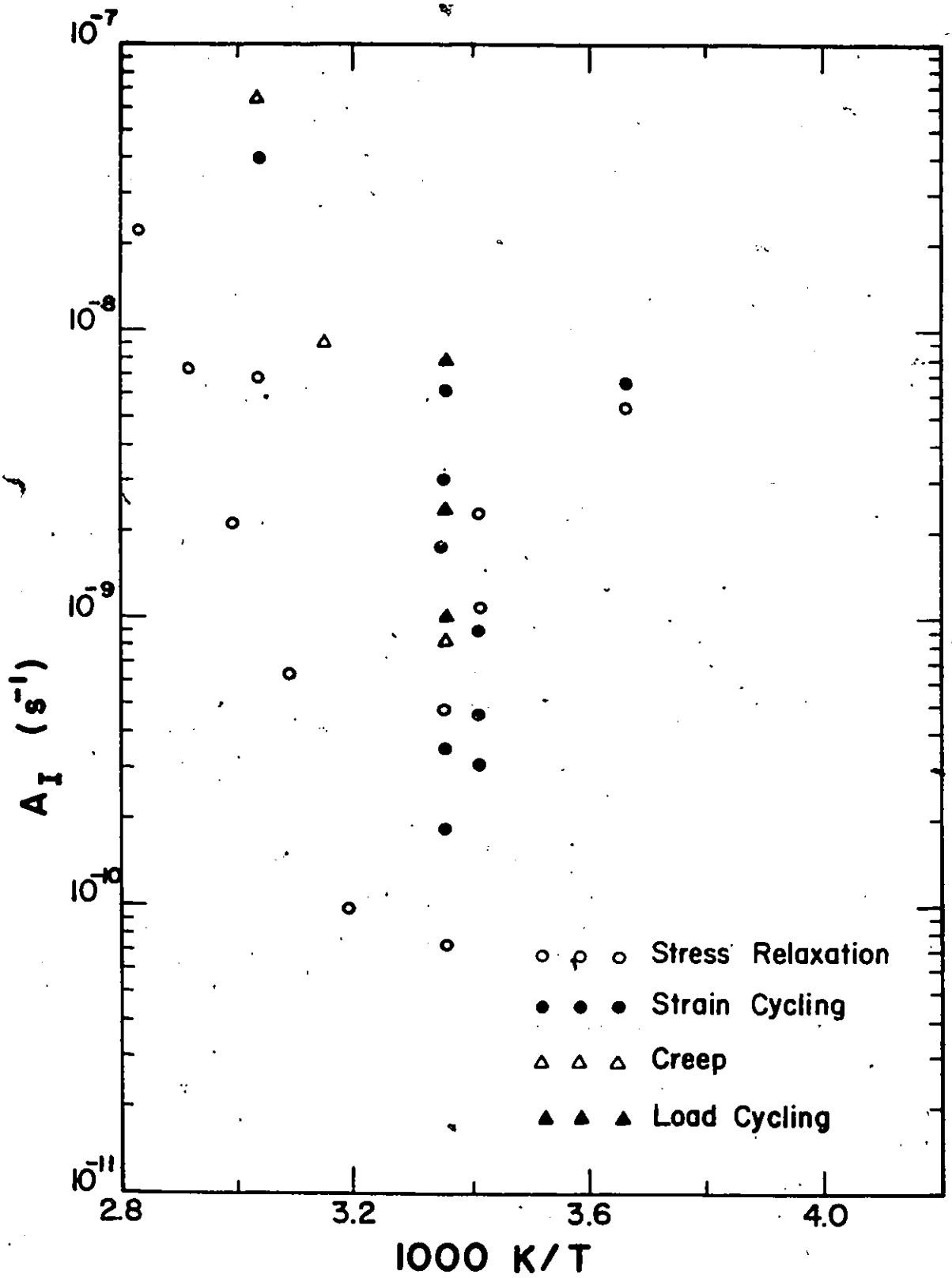

Figure 4.21. The temperature dependence of the constitutive paramter A_I evaluated from stress, relaxation, creep, and cyclic loading expeirmental results.

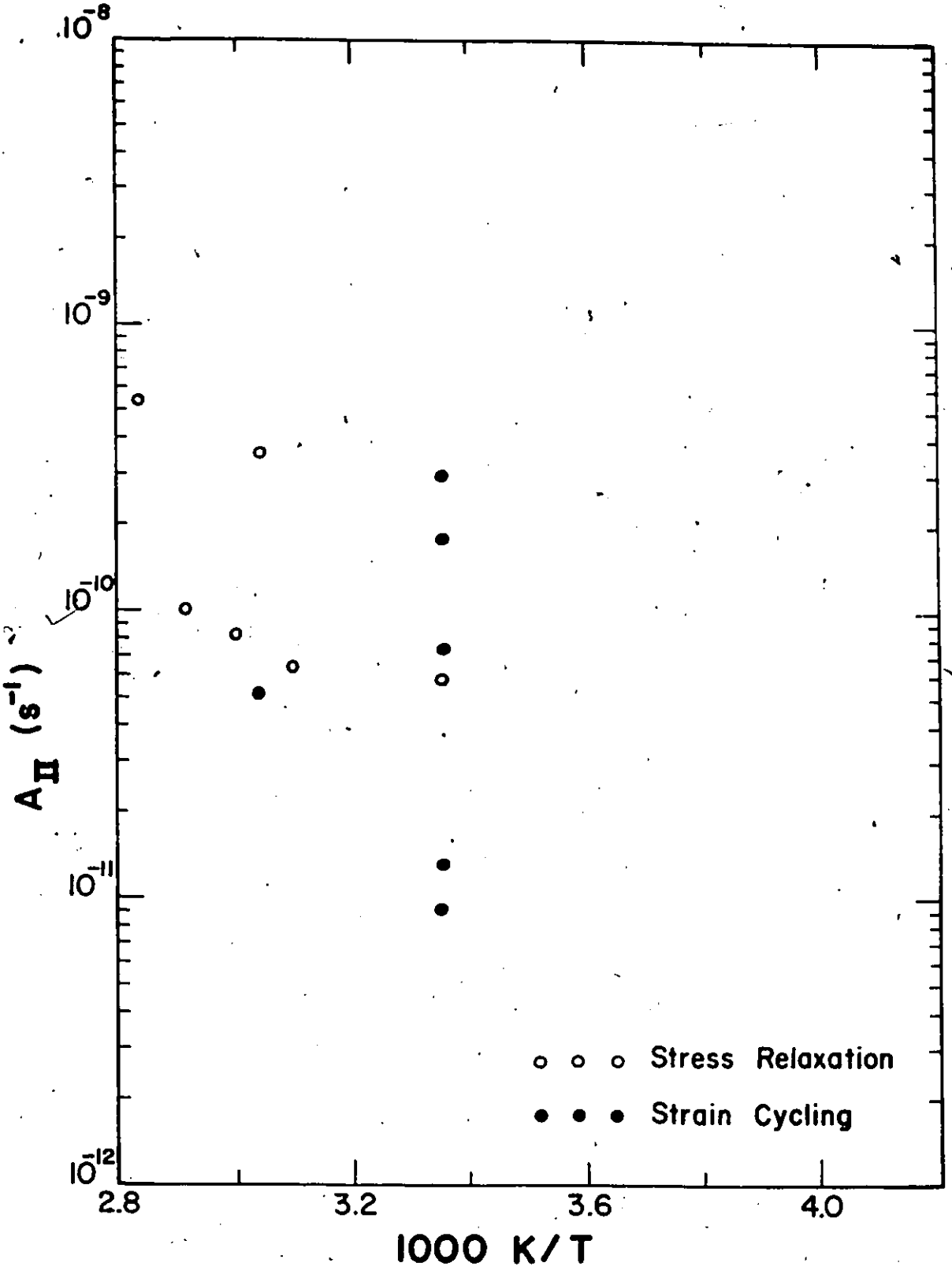

Figure 4.22. The temperature dependence of the constitutive parameter A_{II} evaluated from stress relaxation and strain controlled cyclic loading.

4.3.3 Deformation Mechanism

A deformation kinetics study [34] of the near eutectoid Zn-Aℓ alloy showed that at room temperature (below $0.4T_m$ where T_m is the melting temperature of the alloy) plastic deformation is controlled by consecutive operation of two mechanisms. Although the rate controlling mechanisms at high temperature (above $0.4T_m$, where the deformation is superplastic) have been extensively investigated [115-118, 125, 126], the rate controlling mechanisms at low temperature (where the deformation is not superplastic) have not received a great deal of attention [34, 106, 107, 117, 119]. The studies revealed that grain-boundary sliding, and hence superplastic flow, is controlled by grain-boundary diffusion and that it is frequently accompanied by dislocation motion within the grains. Furtheremore, microstructural studies [127] revealed the presence of dislocations in samples that were not deformed superplastically whereas relatively fewer dislocations were observed in superplastically deformed samples. The rate controlling deformation mechanisms of the alloy at room temperature have not been established although it is widely accepted [116, 117, 128, 129] that dislocation movements inside the grains may be rate controlling. The measured activation parameters ($V_{I,II}$ and $\Delta G^{\ddagger}_{I,II}$) at room temperature for stress relaxation, creep, and cyclic deformation indicate that the rate of plastic flow of the alloy (during stress relaxation, creep, and cyclic deformation) may be controlled by dislocation movements, either by Peierl's - Nabarro mechanism or by cross-slip mechanism. A more detailed and definitive study would be outside of the scope of this report.

4.4 CLOSURE

The analysis of the cyclic deformation behavior of the Zn-Aℓ alloy leads to the conclusion that the deformation is rate dependent, strongly dependent on the temperature and loading rate. Within the high stress and low temperature range where the rate of plastic flow can be approximated with activation over two consecutive energy barriers, the analysis of the theory and experimental results showed that the stress change (or stress drop) during strain controlled cyclic deformation is frequency dependent: the lower the frequency, the higher is the stress drop (per cycle). For a given frequency (or loading rate), it was observed that the stress change is directly proportional to the natural logarithm of time. Similarly, during load controlled cyclic deformation the study showed that the lower the frequency the higher is the strain increment per cycle while the accumulated cyclic strain is proportional to the deformation time or number of cycles. The constitutive equations that were derived from the rate theory described well the cyclic deformation behavior of the alloy.

Krempl and Kallianpur [130, 131] have recently* carried out cyclic loading experiments on high strength Ti - 7Aℓ- 2Cb-1Ta Titanium alloy and on AISI Type 304 Stainless Steel. They observed from the experiments that during strain controlled cyclic deformation of the alloys at room temperature the stress change is frequency and hence rate dependent and that

---

* September 1985 publication.

for a given frequency, the stress change is directly proportional to the logarithm of time. Because these experimental observations are similar to the (present) theoretical prediction, it follows that the constitutive equations derived in this report can also be used to describe cyclic deformation in these alloys. Krempl and Kallilanpur [130] concluded that the rate dependence (or viscous behavior) of the cyclic deformation is an important part of cyclic deformation of metals and must be considered even at room temperature.

That the constitutive equations conform to experimental observations in near eutectoid Zn-Aℓ alloy, high strength titanium alloy and AISI Type 304 stainless steel is not a coincidence. The equations are based on a rigorously derived physical theory: rate theory based on statistical mechanics. The theory has been widely used to describe plastic deformation during monotonic loading of many materials. The present study shows that the theory not only describes plastic flow during monotonic loading but also during cyclic loading.

It is realized that for some materials, the variations of the structural characteristics during cyclic deformation may be significant. The mobile dislocation density may increase significantly due to dislocation multiplication and the activation volume may change with the applied stress. For these materials, therefore, the variations of the structural characteristics must be incorporated in the development of the constitutive equations of cyclic loading.

CHAPTER 5

SUMMARY AND CONCLUSIONS

The time dependence of cyclic deformation behavior is an indispensable part of cyclic deformation of metals. When plastic flow results from thermally activated motion of dislocations (or flow units), the constitutive equation is obtained from kinetics studies and is usually of the form

$$\dot{\varepsilon}_p = \dot{\varepsilon}_0 \exp - \frac{\Delta G_{exp}(\tau)}{kt} .$$

The cyclic deformation behavior then follows from the analysis of the time dependence of the experimental parameters $\dot{\varepsilon}_0$ and ΔG_{exp}. This approach was utilized to study the time dependence of the cyclic deformation behavior of a near eutectoid Zn-Al alloy and to evaluate the deformation behavior when softening and hardening occurs upon cyclic loading.

5.1 CYCLIC DEFORMATION BEHAVIOR OF Zn-Al Alloy

While cyclic deformation behavior cannot, in general, be predicted from the analysis of creep and stress relaxation experimental results, it has been shown that under special, physically reasonable conditions the constitutive parameters determined from stress relaxation and creep can be used to predict the cyclic deformation behavior. The analysis shows that within the high stress and low temparature range where thermally activated plastic flow in creep, stress relaxation, and cyclic loading can be approximated with activation over two consecutive energy barriers, strain controlled cyclic deformation is essentially a stress relaxation process

while load controlled cyclic deformation is related to creep. It was assumed in the study that within the high stress and low temperature range, cyclic deformation, stress relaxation, and creep takes place at constant material structural characteristics (ρ_t, $\Delta G^{\neq}$, and V). The application of the model to describe cyclic plastic deformation behavior of the Zn-Al alloy lead to the following conclusions.

1. In the high stress and low temperature range, the cyclic plastic deformation of the alloy is controlled by a consecutive operation of two mechanisms. The derived constitutive equations describe well the cyclic deformation behavior of the alloy.

2. The material structural characteristics determined from the analysis of stress relaxation, creep, and cyclic loading (strain and load controlled) experimental results were similar. Consequently, it was shown that the constitutive parameters determined from a simple stress relaxation test can be used to predict the cyclic deformation behavior (within the high stress and low temperature range) using the constitutive equations derived in this report.

3. Strain and load controlled cyclic deformation are different manifestations of the same basic process depending on the control condition. The measured activation parameters (which are in agreement with the published values) suggest that within the high stress and low temperature range, cyclic plastic deformation is controlled by dislocation movement, either by Pierl's - Nabarro mechanism or by cross-slip mechanism.

4. While the rate of loading (frequency) has no effect on the rate of cyclic strain accumulation, the strain increment per cycle is frequency dependent. The lower the frequency the higher is the strain increment per cycle. A similar frequency effect was observed in strain controlled cyclic deformation. That is, the lower the frequency the larger is the stress change (decrease) per cycle. At high frequencies, however, the rate of plastic flow is limited by the velocity of transverse sound waves in the material. None-the-less, thermally activated plastic flow ends - fades out - at strain rates (or frequencies) several orders of magnitude below this.

5. Within the high stress and low temperature range, the rate of cyclic strain accumulation and the accumulated cyclic strain increases with the applied mean stress. Similarly, for strain controlled cyclic loading, the applied stress change increases with the mean total strain.

5.2 CYCLIC SOFTENING AND HARDENING

Cyclic loading may induce a change in the dislocation - obstacle structure that produces the internal stress: the material may thus soften and/or harden upon cyclic loading. It was considered that within a high stress and low temperature range the rate of plastic flow in hardening and softening can be approximated with activation over single energy barriers and that the material structural characteristics are constant during cyclic deformation. The analysis of the cyclic deformation behavior within the stress and temperature range lead to the following conclusions.

1. The rate of cyclic strain accumulation and the accumulated cyclic strain during cyclic hardening were smaller than those under constant stress (equal to peak stress during cyclic loading) creep. The long term strain rates, however, were identical. Consequently, it was anticipated that the constitutive parameters determined from the analysis of creep test results can be used to predict (within the high stress and low temperature range) the cyclic hardening deformation behavior.

2. When the internal stress decreases (softening) upon unloading and increases (hardening) during the loading part of the cycle, the rate of cyclic strain accumulation and the accumulated cyclic strain were (after sufficiently long time) larger than those under constant stress (equal to the peak stress) creep. The behavior is similar to that often (in the literature) observed experimentally during cyclic deformation of metals: the application of a cyclic load (of sufficient magnitude) results in ductile failure of specimens (copper, aluminum, etc.) in a few thousand cycles whereas the application of a steady (creep) stress (equal to peak stress) produces little deformation and no failure occurs over a period of several days. Therefore, it was anticipated that the analytical model presented here can be used to evaluate the accumulated damage in highly stressed machine components; an essential data for design and lifetime determination of machine components.

5.3 RECOMMENDATIONS FOR FURTHER RESEARCH

It is recommended that the theoretical and experimental parts of this study may be extended to include:

1. Deformation behavior under random loading (strain or load controlled). This investigation is in progress and the results will be published elsewhere [132].

2. The application of the model to describe cyclic deformation behavior of other engineering materials, particularly those with non-zero and increasing and/or decreasing internal stress.

3. The extension of the deformation kinetics to include backward activation and its application to describe cyclic deformation behavior.

4. Microstructural studies to establish the deformation mechanism during cyclic loading.

REFERENCES

1. A.J. Kennedy, Proc. Roy. Soc., A, Vol. 213, p. 492, (1952).
2. A.H. Meleka and A.V. Evershed, J. Inst. Met., Vol. 88, p. 411, (1959-60).
3. C.E. Feltner, Acta Met., Vol. 11, p. 817, (1963).
4. C.E. Feltner and C. Laird, Acta Met., Vol. 15, p. 1621, (1967).
5. C.E. Feltner and C. Laird, Acta Met., Vol. 15, p. 1633, (1967).
6. E. Shiratori and Y. Obataya, Int. J. Mech. Sci., Vol. 16, p. 433, (1974).
7. F. Lorenzo and C. Laird, Acta Met., Vol. 32, No. 5, p. 681, (1984).
8. H.D. Chandler, Acta Met., Vol. 32, No. 8, p. 1253, (1984).
9. M. Klesnil and P. Lukas, Material Science Monographs, Vol. 7, "Fatigue of Metallic Materials", Elsevier Scientific Publishing Co., (1980).
10. R.M. Wetzel, Editor, "Fatigue Under Complex Loading: Analysis and Experiments", Advances in Engineering, Vol. 6, published by the society of Automotive Engineers Inc., 1977.
11. P.J. Woods, Phil. Mag., Vol. 28, p. 155, (1973).
12. J.M. Finney and C. Laird, Phil. Mag., Vol. 31, p. 339, (1975).
13. A.T. Winter, Phil. Mag., Vol. 31, p. 411, (1975).
14. J.C. Figueroa and C. Laird, Acta Met., Vol. 29, p. 1679, (1981).
15. A.J. Winter, Acta Met., Vol. 28, p. 963, (1980).
16. F. Lorenzo and C. Laird, Acta Met., Vol. 32, No. 5, p. 671, (1984).
17. H.D. Chandler and J.V. Bee, Acta Met., Vol. 33, No. 6, p. 1121, (1985).
18. A.S. Argon, Editor, "Constitutive Equations in Plasticity", MIT Press, Cambridge, Mass., 1975.

19. D.K. Shetty and M. Meshii, Met. Trans., Vol. 6A, p. 349, (1975).

20. D.K. Shetty, T. Mura and M. Meshii, Mat. Sci. Eng., Vol. 20, p. 261, (1975).

21. T. Mura, A. Novakovic and M. Meshii, Mat. Sci. Eng., Vol. 17, p. 221, (1975).

22. L.F. Coffin and E. Krempl, Editors, Cyclic Stress - Strain Behavior - Analysis, Experimentation and Failure Prediction, ASTM, STP 519, American Society for Testing and Materials; 1973.

23. K.C. Valanis and H.C. Wu, J. Appl. Mech., Vol. 41; p. 1, (1975).

24. M.C.M. Liu, E. Krempl and D.C. Nairn, J. Engng. Mater. Technol., Vol. 98, p. 322, (1976).

25. H.C. Wu and M.C. Yip, J. Engng. Mater. Technol., Vol. 103, p. 212, (1981).

26. M.A. Eisenberg and C.F. Yen, J. Engng. Mater. Technol., Vol. 105, p. 113, (1983).

27. A.S. Krausz and H. Eyring, "Deformation Kinetics", Wiley-Intersci., New York 1975.

28. U.F. Kocks, A.S. Argon, and M.F. Ashby, Thermodynamics and Kinetics of Slip, Pergamon Press Ltd., London 1975.

29. A.S. Krausz and B. Faucher, "A Kinetics Approach to the Derivation and Measurement of the Constitutive Equations of Time-dependent Deformation", Mechanical testing for Deformation Model Development, ASTM STP 765, R.W. Rhode and J.C. Swearengen, Eds., American Society for Testing and Materials, p. 284, (1982).

30. A. Krausz and B. Faucher, "Energy Barrier Systems in Thermally Activated Plastic Flow", Reviews on the Deformation Behavior of Materials, P. Feltham, Ed., Vol. IV, No. 2, (1982).

31. M.J. Makin, Phil. Mag., Vol. 9, p. 81, (1964).

32. J. Weertman, "Rate Processes in Plastic Deformation of Materials", edited by J.C.M. Li and A.K. Mukherjee, A.S.M., Metal Park, Ohio, 1975.

33. D.H. Sastry, M.J. Luton and J.J. Jonas, Phys. Stat. Sol., Vol. 33a, p. 173, (1976).

34. C.H. Laforce, A.S. Krausz and W. Ginman, Z. Metallkde, Vol. 69, p. 622, (1978).

35. J. Mshana, A.S. Krausz and J. Denis, "An Analysis of the Constitutive Equation of Cyclic Softening", Proceedings of the Ninth Canadian Congress of Applied Mechanics, University of Saskatchewan, Saskatoon May 30 - June 3rd 1983, p. 315.

36. B. Faucher, "A study of Steady State and Non-Steady State Deformation Kinetics", Ph.D. Thesis, University of Ottawa, 1979.

37. E. Orowan, Z. Phys., Vol. 89, p. 605, 614, 634, (1934).

38. G.J. Taylor, Proc. Roy. Soc., Vol. A145, p. 362, (1934).

39. M. Polanyi, Z. Phys., Vol. 89, p. 660, (1934).

40. J. Frenkel, Z. Phys., Vol. 37, p. 572, (1926).

41. A.H. Cottrell, "Dislocation and Plastic Flow in Crystals", Oxford University Press, 1953.

42. J. Friedel, "Les Dislocations", Gauthiers - Villars, Paris, 1956.

43. H.G. Van Bueren, "Imperfections in Crystals", Interscience, New York, 1960.

44. J. Weertman, J.R. Weertman, "Elementary Dislocation Theory", Macmillan, New York, 1964.

45. F.R.N. Nabarro, "Theory of Crystal Dislocations", Oxford Clarendon Press, 1967.

46. J.P. Hirth and J. Lorthe, "Theory of Dislocations", McGraw-Hill, New York, 1968.

47. S. Amelinckx, in "Advances in Materials Research in the Nato Nations", Eds. H. Brooks, N.H. Manson, N.E. Promisel, and G.H. Cooper, Pergamon Press, Oxford, 1963.

48. E. Orowan, Proc. Phys. Soc., Vol. 52, p. 8, (1940).

49. A. Seeger, Z. Naturforsh., Vol. 9a, p. 758, 819, 856, (1954).

50. Z.S. Basinski, Phil. Mag., Vol. 4, p. 393, (1959).

51. H. Conrad, H. Wiedersich, Acta Met., Vol. 8, p. 128, (1960).

52. H Conrad, J. Metals, Vol. 16, p. 582, (1964).

53. J.P. Hirth, W.D. Nix, Phys. Stat. Sol., Vol. 35, p. 177, (1969).

54. H. Conrad, Mater Sci. Eng., Vol. 6, p. 265, (1970).

55. S. Arrhenius, Z. Phys. Chem., Vol. 4, p. 226, (1889).

56. A. Marcellin, Ann. Phys., Vol. 3, p. 158, (1915).

57. W.H. Rodebush, J. Am. Chem. Soc., Vol. 45, p. 606, (1923).

58. W.H. Rodebush, J. Chem. Phys., Vol. 1, p. 440, (1933).

59. W.H. Rodebush, J. Chem. Phys., Vol. 3, p. 242, (1935).

60. W.H. Rodebush, J. Chem. Phys., Vol. 4, p. 744, (1936).

61. O.K. Rice, H. Gershinowitz, J. Chem. Phys., Vol. 2, p. 853, (1934).

62. O.K. Rice, H. Gershinowitz, J. Chem. Phys., Vol. 3, p. 479, (1935).

63. H. Eyring, J. Chem. Physics, Vol. 3, p. 107, (1935).

64. W.F.K. Wynne-Jones, H. Eyring, J. Chem. Phys., Vol. 3, p. 492, (1935).

65. M.G. Evans, M. Polanyi, Trans. Far. Soc., Vol. 31, p. 875, (1935).

66. M.G. Evans, M. Polanyi, Trans. Far. Soc., Vol. 33, p. 448, (1937).

67. M. Polanyi, J. Chem. Soc., Vol. 59, p. 629, (1937).

68. H. Eyring, J. Chem. Phys., Vol. 4, p. 283, (1936).

69. S. Glasstone, K.J. Laidler, H. Eyring, "The Theory of Rate Processes", McGraw-Hill, New York, 1941.

70. K.J. Laidler "Theories of Chemical Reaction Rates", McGraw-Hill, New York, 1969.

71. F.E. Scheffer and P. Kohnstamm, Verlag Akad. Wetensch. Amsterdam, Vol. 19, p. 878, (1911).

72. I. Prigogine, G. Nicolis and P.M. Allen, Chemical Dynamics, J.O. Hirsch-felder and D. Henderson, Eds., Wiley, New York, 1971.

73. T. O'D. Hanley, A.S. Krausz, J. Appl. Phys., Vol. 45, p. 2013, (1974).

74. R.C. Gifkins, J. Mater. sci., Vol. 5, p. 156, (1970).

75. G. Alefeld, Z. Naturforsch., Vol. 17a, p. 899, (1962).

76. A.S. Krausz, Acta Met., Vol. 16, p. 897, (1968).

77. A.S. Krausz, Mater. Sci. Eng., Vol. 6, p. 260, (1970).

78. V. Celli, M. Kabler, T. Ninomiya, R. Thomson, Phys. Rev., Vol. 131, p. 58, (1963).

79. J.C.M. Li in "Rate Processes in Plastic Deformation of Materials", edited by J.C.M. Li and A.K. Mukherjee, ASM, 1975.

80. J. Diehl, G.P. Seidel, L. Hiemann, Phys. Stat. Sol., Vol. 12, p. 405, (1965).

81. H. Conrad, Mater. Sci. Eng., Vol. 6, p. 265, (1970).

82. B. Faucher, A.S. Krausz, J. Appl. Phys., Vol 49, p. 3946, (1978).

83. A.S. Krausz, Mater. Sci. Eng., Vol. 26, p. 65, (1976).

84. A. Nadai, "Theory of Flow and Fracture of Solids", Vol. 1, 2nd edition, McGraw-Hill, New York, 1950.

85. O.H. Wyatt, Proc. Phys. Soc., Vol. B66, p. 459, (1953).

86. A.S. Krausz, B.G. Craig, Acta Met., Vol. 14, p. 1807, (1966).

87. A.H. Cottrell, V. Aytekin, J. Inst. Met., Vol. 77, p. 389, (1950).

88. T.A. Trozera, J. Mote, J.E. Dorn, Trans. Amer. Soc. Met. 186, 1 (1960).

89. H. Conrad, L. Hays, G. Shoek, H. Wiedersich, Acta Met., Vol. 9, p. 367, (1961).

90. P. Trouton, A.O. Rankine, Phil. Mag., Vol. 8, p. 538, (1904).

91. P. Feltham, Phil. Mag., Vol. 6, pages 259, 847, (1961); Vol. 8, p. 989, (1963).

92. P. Feltham, Phys. Stat. Sol., Vol. 3, p. 1340, (1963).

93. F. Guiu, P.L. Pratt, Phys. Stat. Sol., Vol. 6, p. 111, (1964).

94. Jo Dean Morrow, Internal Friction, Damping and Cyclic Plasticity, ASTM STP 378, p. 45, 1965.

95. R.W. Landgraf, Jo Dean Morrow and T. Endo, J. Mater., JMLSA, vol. 4, No. 1, p. 176, (1969).

96. G.B. Gibbs, Phil. Mag., Vol. 13, p. 317, (1966).

97. G. Sargent, H. Conrad, Scripta Met., Vol. 3, p. 43, (1969).

98. S.R. MacEwen, O.A. Kupcis, B. Ramaswami, Script Met., Vol. 3, p. 441, (1969).

99. C.N. Ahlquist, W.D. Nix, Scripta Met., Vol. 3, p. 679, (1969).

100. R.E. Reed - Hill, J.R. Donoso, Scripta Met., Vol. 9, p. 1305, (1975).

101. F. Guiu, Scripta Met., Vol. 3, p. 753, (1969).

102. K. Okazaki, Y. Aono, T. Kaneyuki, H. Conrad, Mater. Sci. Eng., Vol. 33, p. 253, (1978).

103. B. Faucher, A.S. Krausz, J. Appl. Phys., Vol. 49, p. 3946, (1978).

104. W.J. Cunningham, Introduction Non-Linear Analysis, McGraw-Hill, New York, 1958, p. 63.

105. B. Wielke and G. Schoeck, Phys. Stat. Sol. (a), Vol. 38, p. 539, (1976).

106. J.S. Mshana and A.S. Krausz, J. Eng. Mater. and Tech., Vol. 107, p. 7, (1985).

107. J.S. Mshana and A.S. Krausz, Z. naturforsch., Vol. 40a, No. 7, p. 653, (1985).

108. W.G. Johnston, J. Appl. Phys., Vol. 33, p. 2716, (1962).

109. A. Neuhauser, N. Himstedt and Ch. Schwink, Phys. Stat. Sol. (a), Vol. 3, p. 585, (1970).

110. F. Guiu, Phys. Stat. Sol., Vol. 33, p. 785, (1969).

111. U. Essmann, Phys. Stat. Sol., Vol. 17, p. 725, (1966).

112. A.T. Price, J. Inst. Metals, Vol. 95, p. 87, (1967).

113. R. Koterazawa, Proc. Int. Conf. on Creep and Fatigue in Elevated Temperature Applications, C 214/73, 214.1, Philadelphia, Sept. 1973.

114. R. Koterazawa, Proc. Int. Conf. on Mechanical Behavior of metals, III, Kyoto, Aug. 1971, p. 135.

115. F.A. Mohamed, S.A. Shei, and T.G. Langdon, Acta Met., Vol. 23, p. 1443, (1975).

116. A. Arieli and A.K. Mukherjee, Acta Met., Vol. 28, p. 1571, (1980).

117. P. Chaudhari, Acta Met., Vol. 15, p. 1777, (1967).

118. M.L. Vaidya, K.L. Murty and J.E. Dorn, Acta Met., Vol. 21, p. 1615, (1973).

119. C.H. Laforce, "The Deformation Kinetics of a Superplastic Zn - Al Alloy", M.A.Sc. Thesis, University of Ottawa, 1977.

120. "Operators Manual for the Modified Instron Machine", Dept. of Mech. Eng., University of Ottawa.

121. Motorola Microsystems, EXOset 30, BASICM User's Guide M6809BASICM(D1), Motorola Inc., (1979).

122. X. Zhu, B. Ramaswami, "Fatigue Deformation of Superplastic Zn - 22 Percent Al Eutectoid Alloy", Presented at the International Conference on Strength of Metals and Alloys (ICSMA - 7), Montréal, Canada, August 1985.

123. A.R. Miller, "Basic Programs for Scientists and Engineers", 1st Edition, Berkeley: Sybex, 1981.

124. G.A. Sargent, Acta Met., Vol. 13, p. 663, (1965).

125. F.A. Mohamed and T.G. Langdon, Phys. Stat. Sol. 9(a), Vol. 33, p. 375, (1976).

126. J.D. Lee, P. Niessen, J. Mat. Sci., Vol. 9, pp. 1467-1477, 1974.

127. A. Ball and M.M. Hutchison, Met. Sci. J., Vol. 3, p. 1, (1969).

128. I.I. Novikov, V.K.Portnov and T.E. Terentieva Acta Met., Vol. 25, p. 1139, (1977).

129. O.A. Kaibyshev, R.V. Rodionov and Z. Valiev, Acta Met., Vol. 26, pp. 1877-1886, (1978).

130. E. Krempl and V.V. Kallianpur, Trans. ASME, J. Appl. Mech., Vol. 52, p. 654, (1985).

131. V.V. Kallianpur, Ph.D. Thesis, Rensselaer Polytechnic Institute, Troy, N.Y., May 1983.

132. Z.W. Lian, A.S. Krausz and J.S. Mshana, "An Approach to Predict the Material Stress-Strain Response Under Random Cyclic Loading", to be published.

APPENDIX

Additional Theoretical and Experimental Results

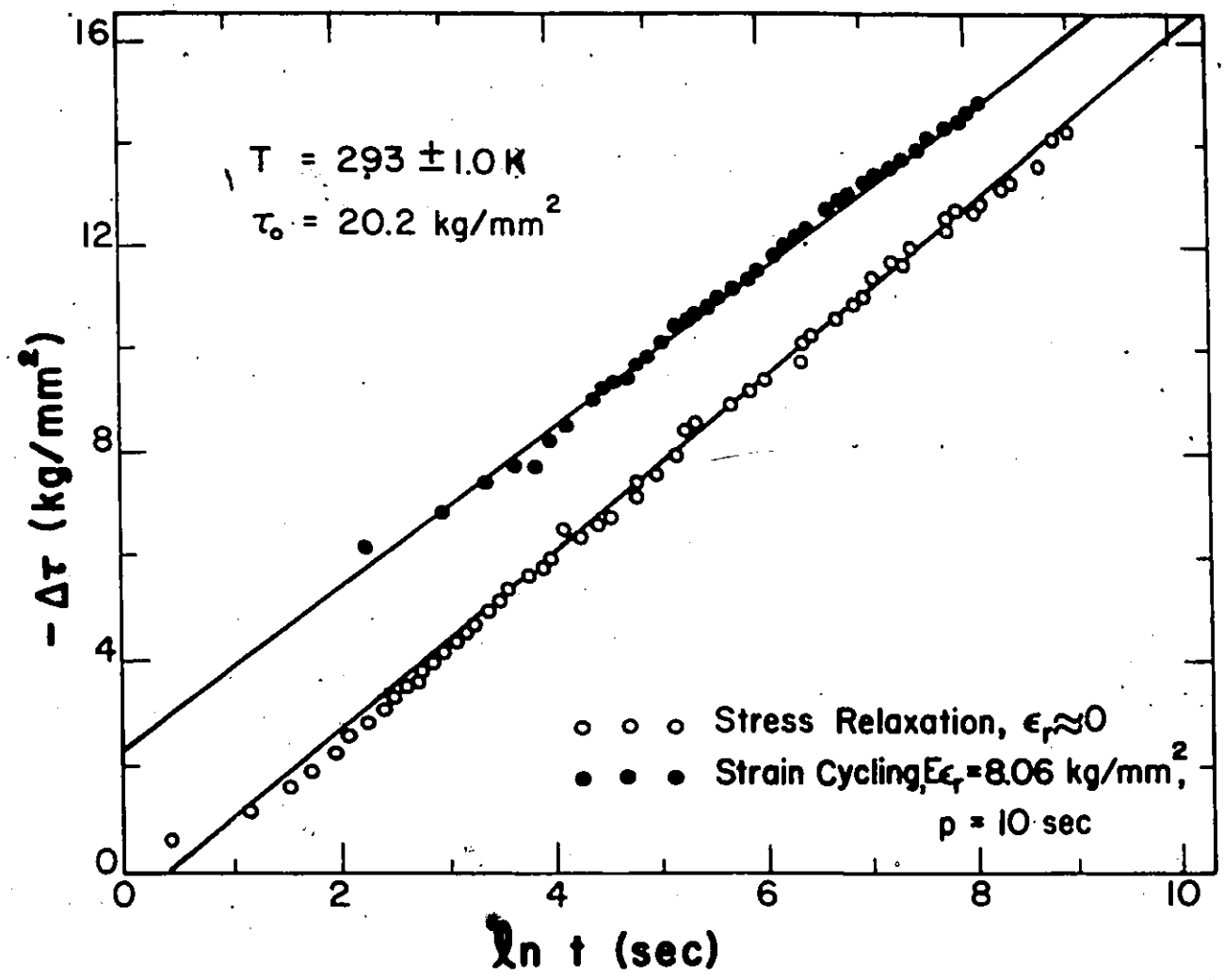

Figure A1. Stress relaxation and cyclic loading experimental results for region I (Fig. 2.2). The symbols indicate the experimental results while the lines were obtained from least square method using Eqs. (2.23) and (4.5) for stress relaxation and cyclic loading, respectively.

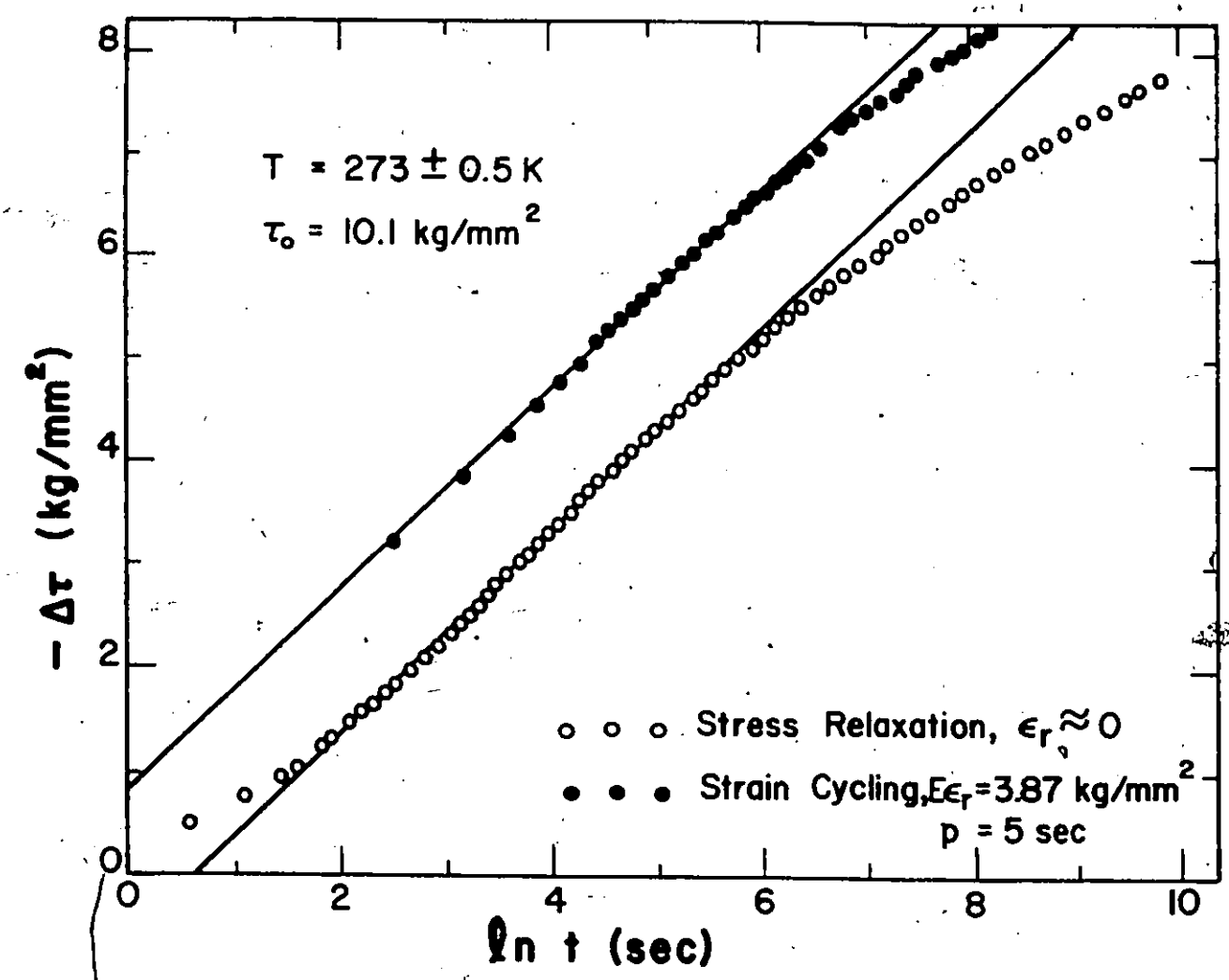

Figure A2. Stress Relaxation and cyclic loading experimental results for region I (Fig. 2.2). The symbols indicate the experimental results while the lines were obtained from least square method using Eqs. (2.23) and (4.5) for stress relaxation and cyclic loading, respectively.

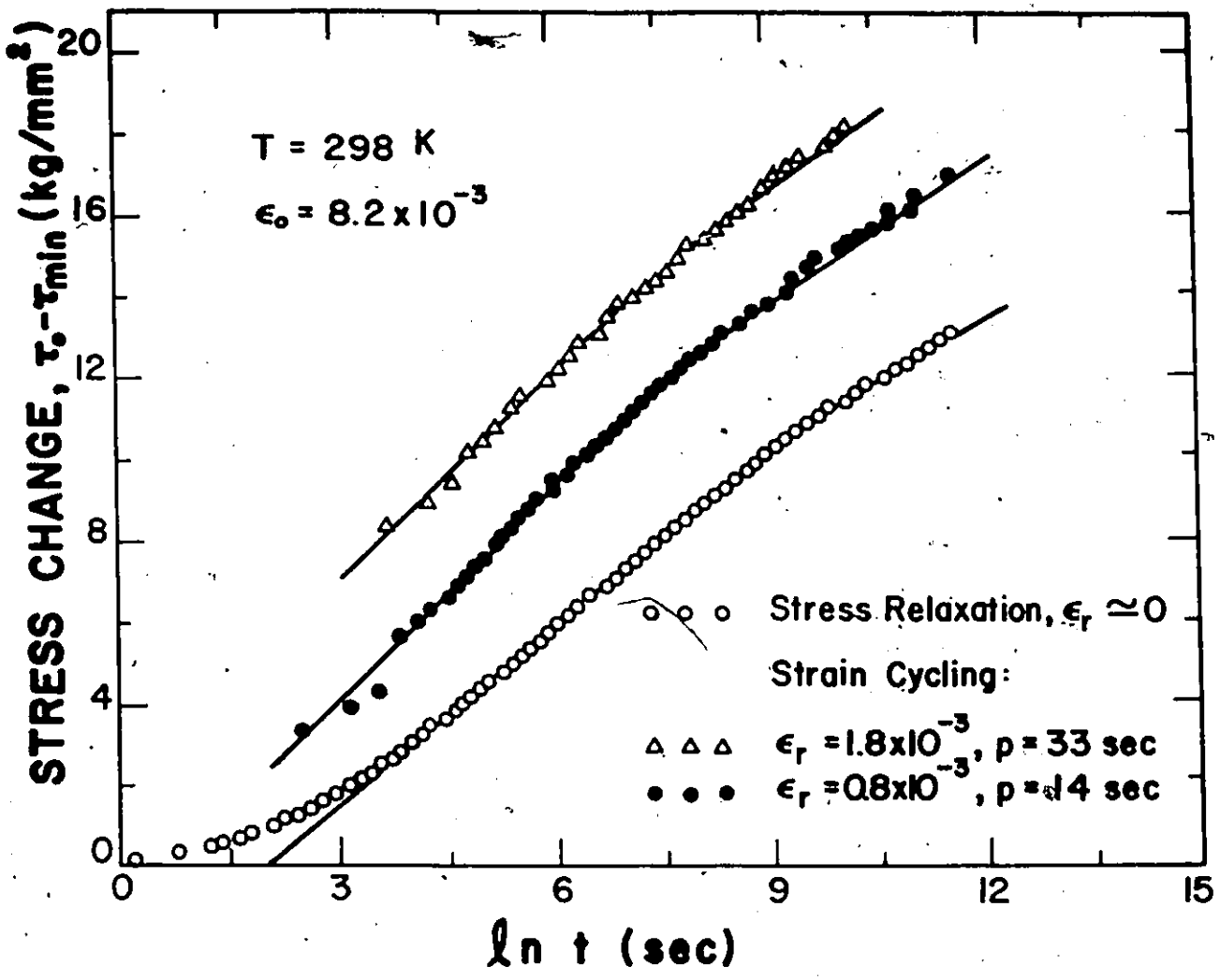

Figure A3. Stress relaxation and strain controlled cyclic loading experimental results for regions I and II, and the transition stress range (Fig. 2.2). The initial strain, ϵ_0, was the same for all the experiments while the corresponding initial stresses differed slightly. The symbols indicate the experimental results while the curves were calculated from the theory.

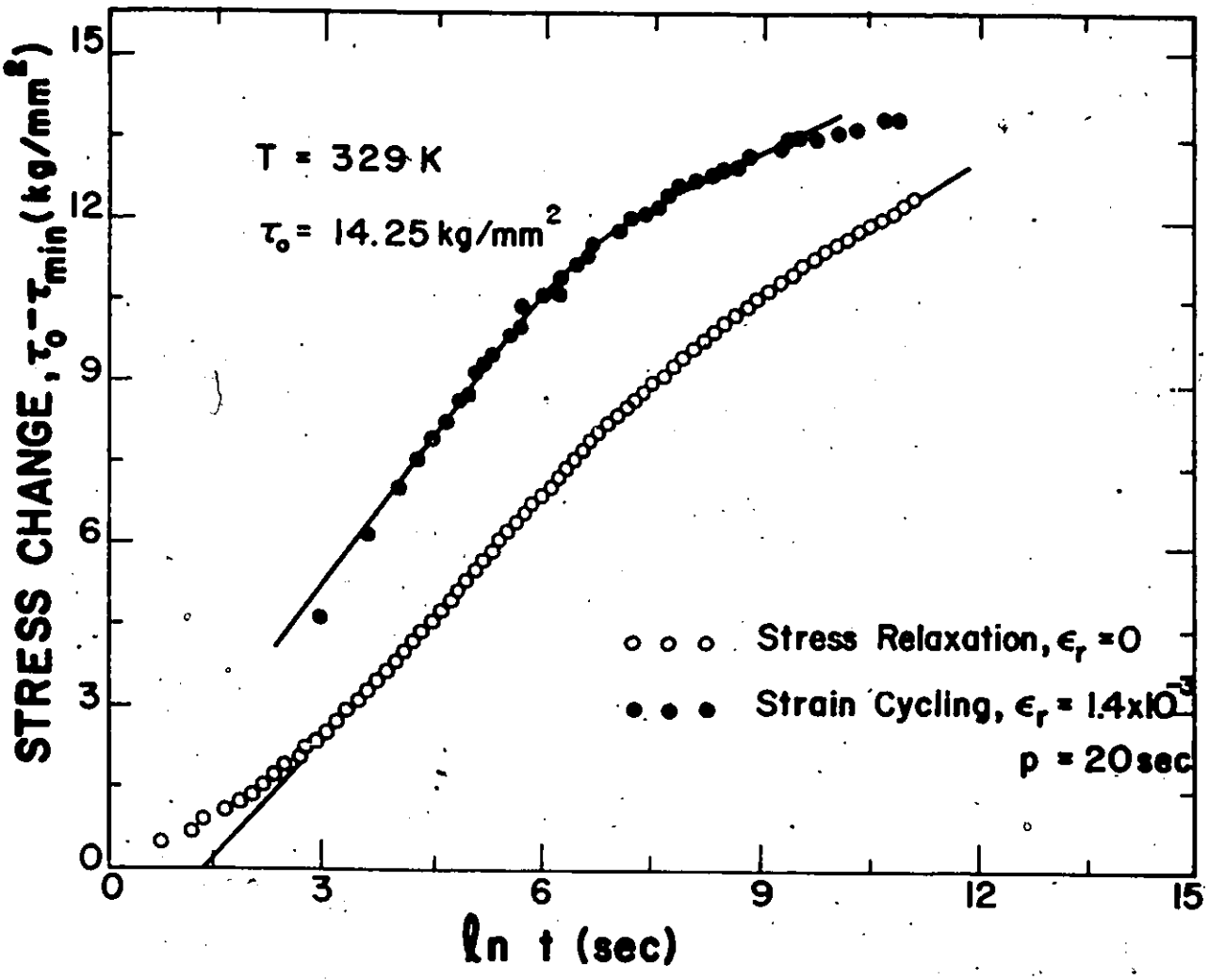

Figure A4. Stress relaxation and strain controlled cyclic loading experimental results for regions I and II, and the transition stress range (Fig. 2.2). The symbols indicate the experimental results while the curves were calculated from the theory.

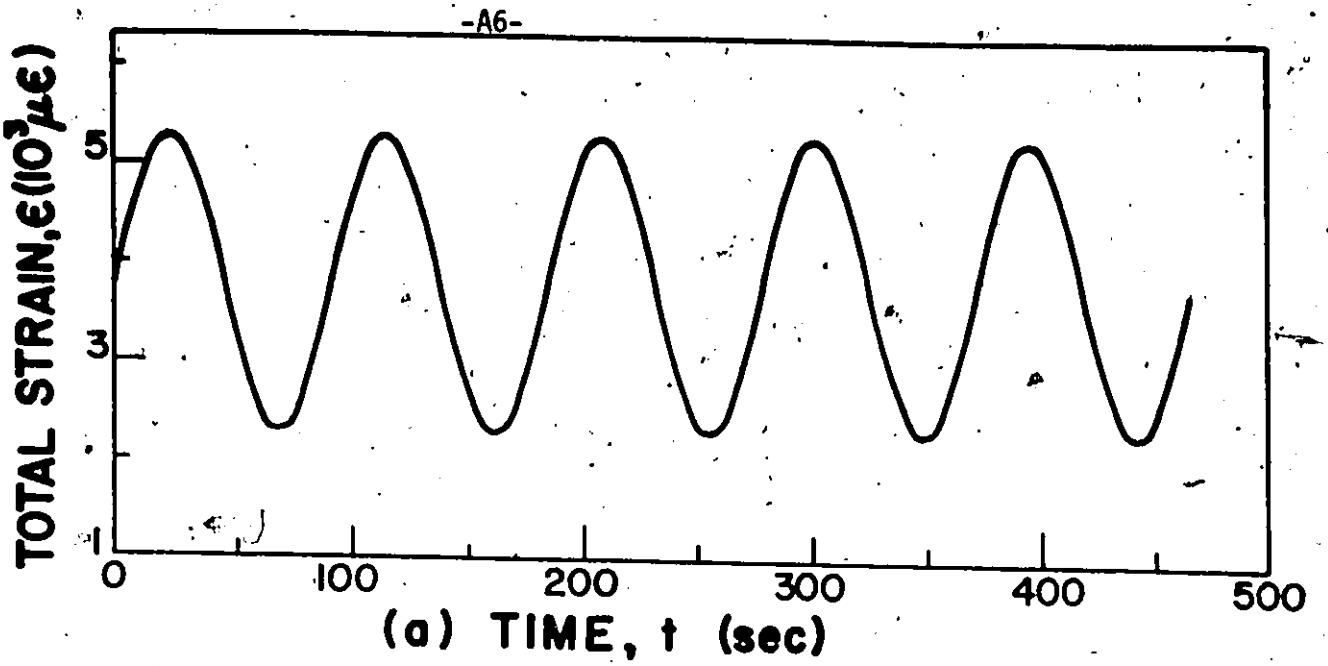

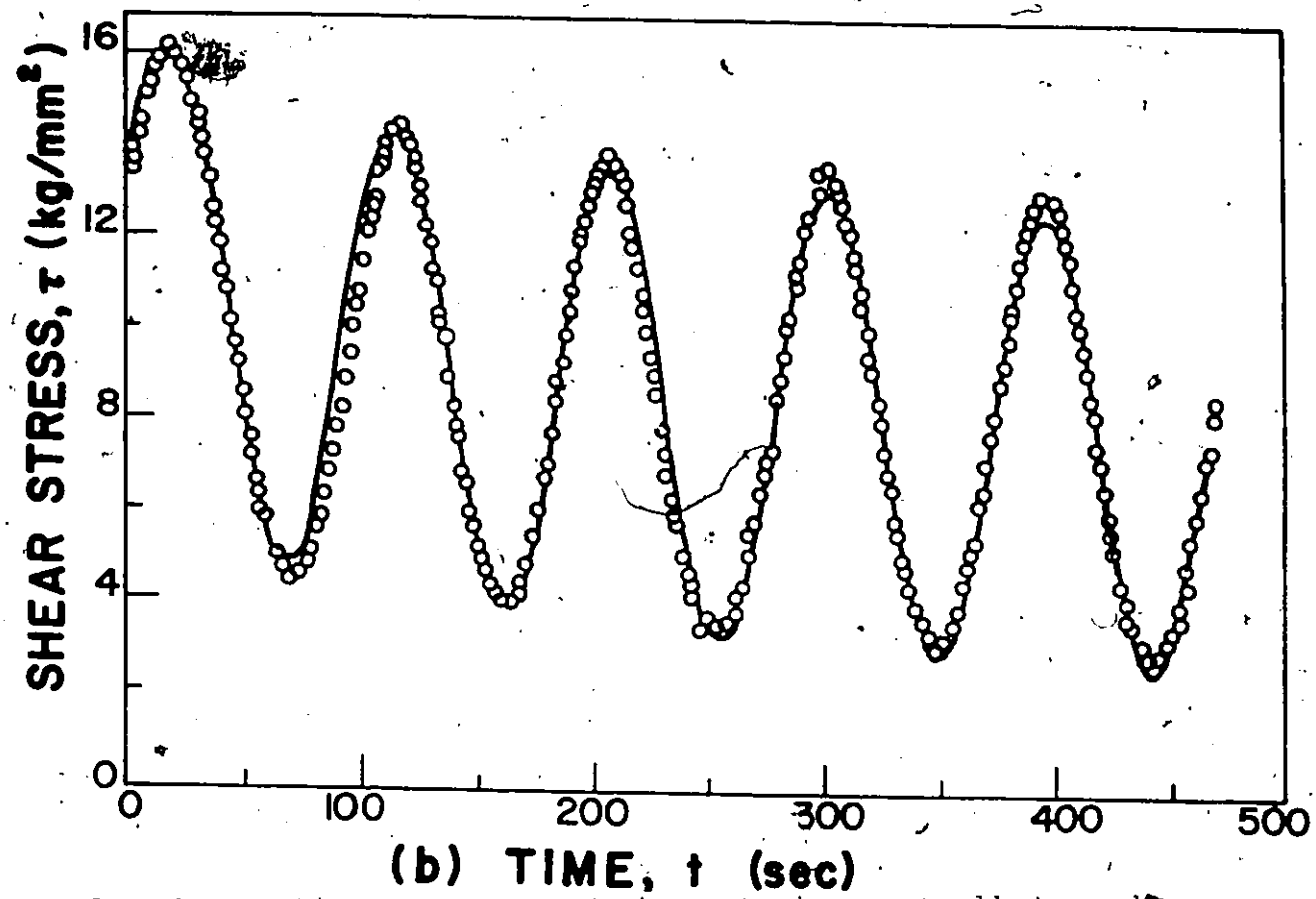

Figure A5. Stress-time response during strain controlled cyclic deformation (a) Input strain-time, sinusoidal wave form (b) stress-time response. The symbols represent experimental data and the solid line was calculated form Eq. (2.22). The cycle period p=94 sec., and the other parameters are indicated in Fig. 4.4.

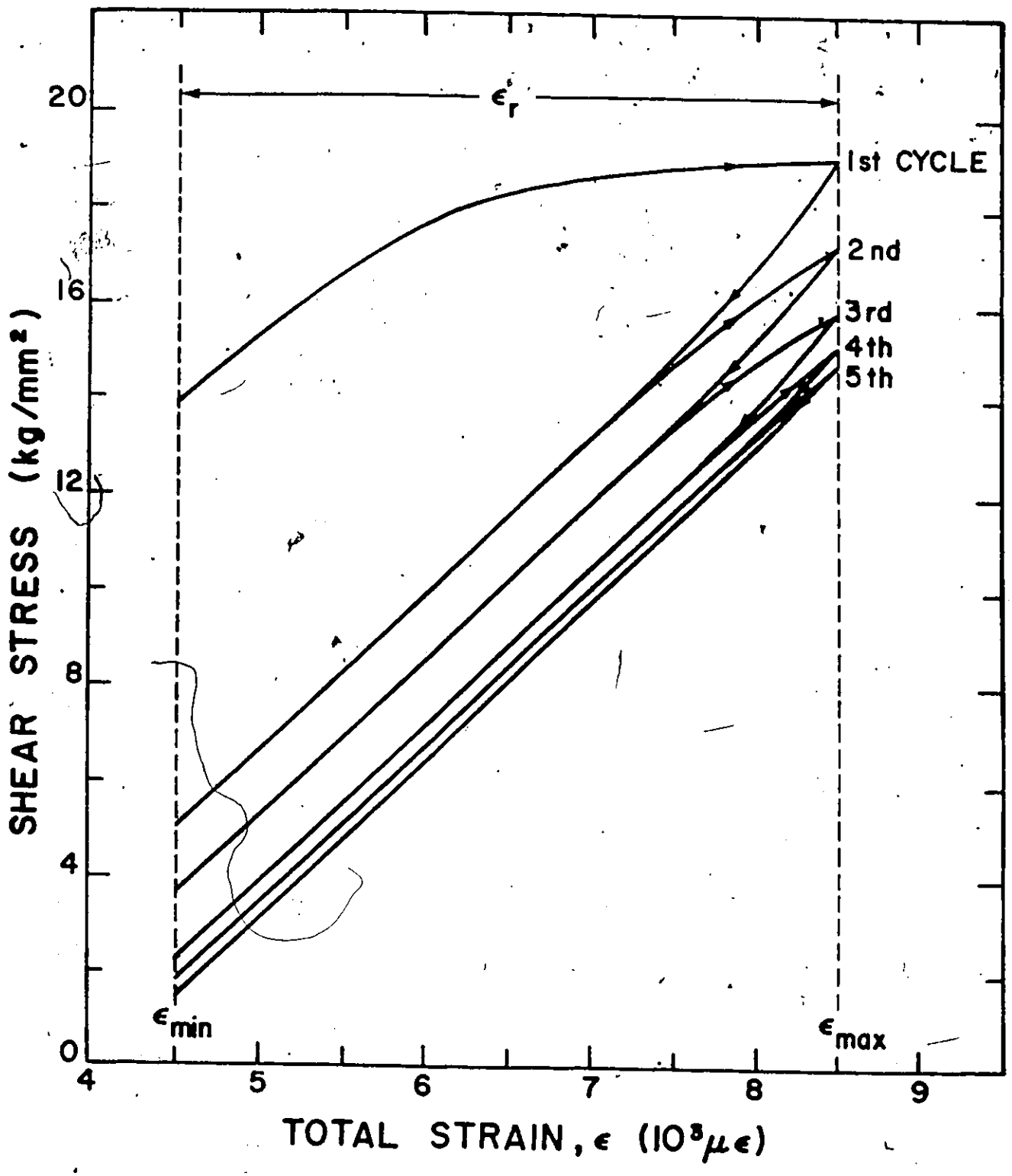

Figure A6: The figure shows the predicted hysteresis loops during the first few cycles of strain controlled cyclic deformation. The stress-time response shown in Fig. 4.3 was replotted on stress-strain axes.

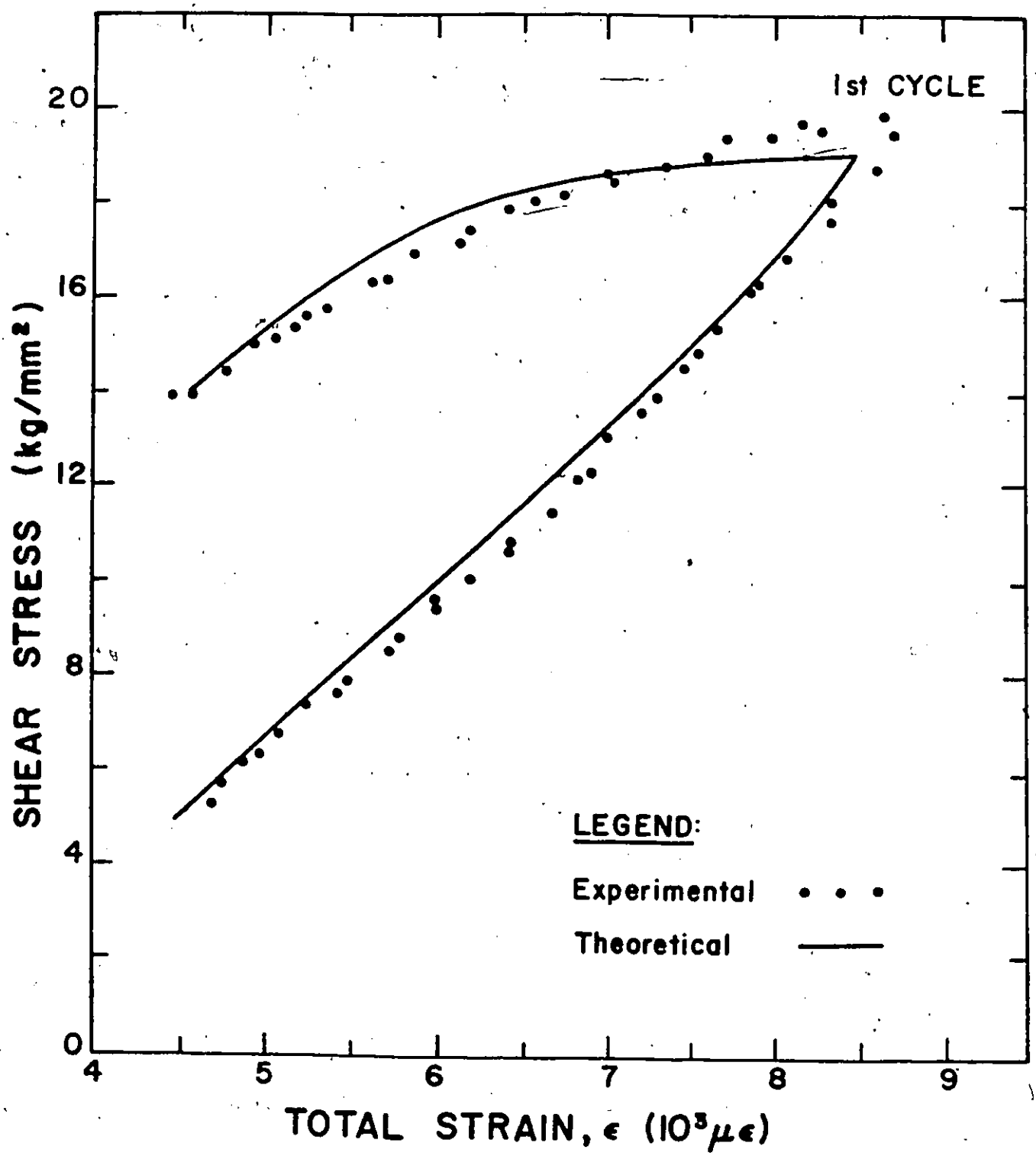
1st CYCLE
SHEAR STRESS (kg/mm²)
TOTAL STRAIN, ε (10³με)
0
4
8
12
16
20
4
5
6
7
8
9
LEGEND:
Experimental
Theoretical

Figure A7(a).

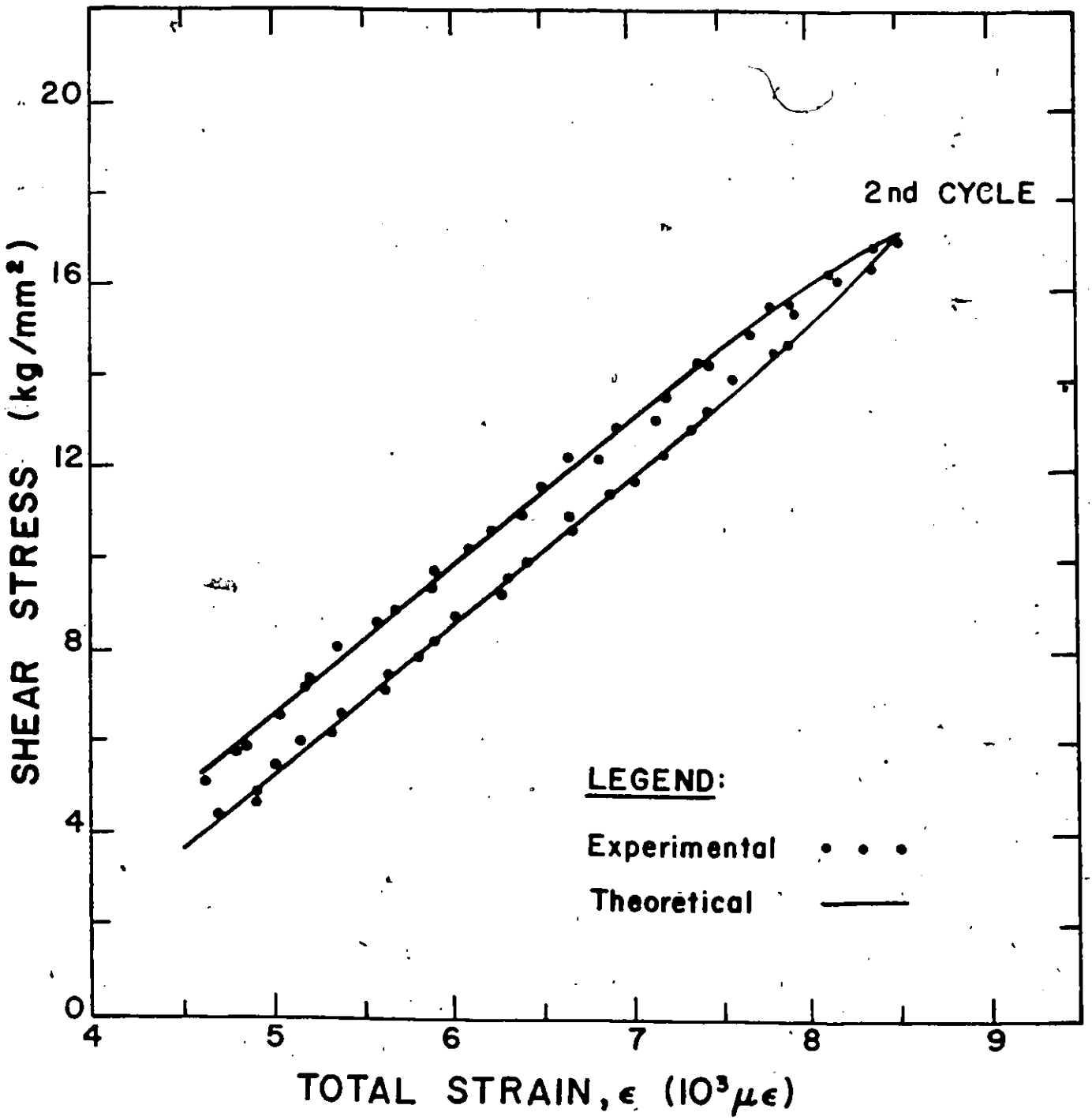

Figure A7(b).

Figure A7. Comparison of the calculated hysteresis loops (solid line) and the experimental data (symbols). The calculated hysteresis loops were replotted from Fig. A6.
(a) Hysteresis loop for the first cycle.
(b) Hysteresis loop for the 2nd cycle.

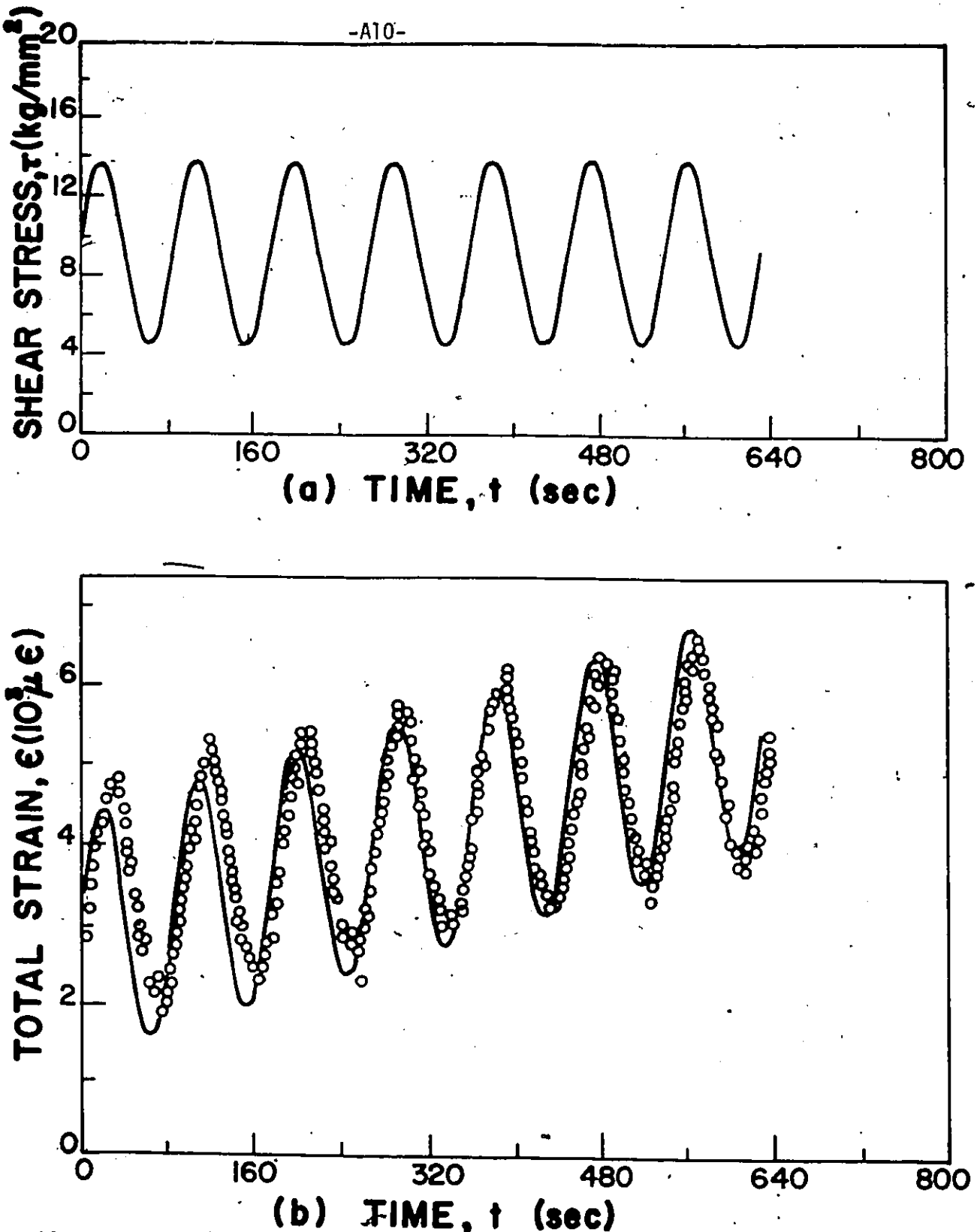

Figure A8. Strain-time response during load controlled cyclic deformation. (a) Input stress-time sinusoidal wave form (b) Strain-time response. The symbols represent experimental data and the solid line was calculated numerically using Eq. (2.37). The cycle period p=91 sec., and the other parameters are given in Fig. 4.13.

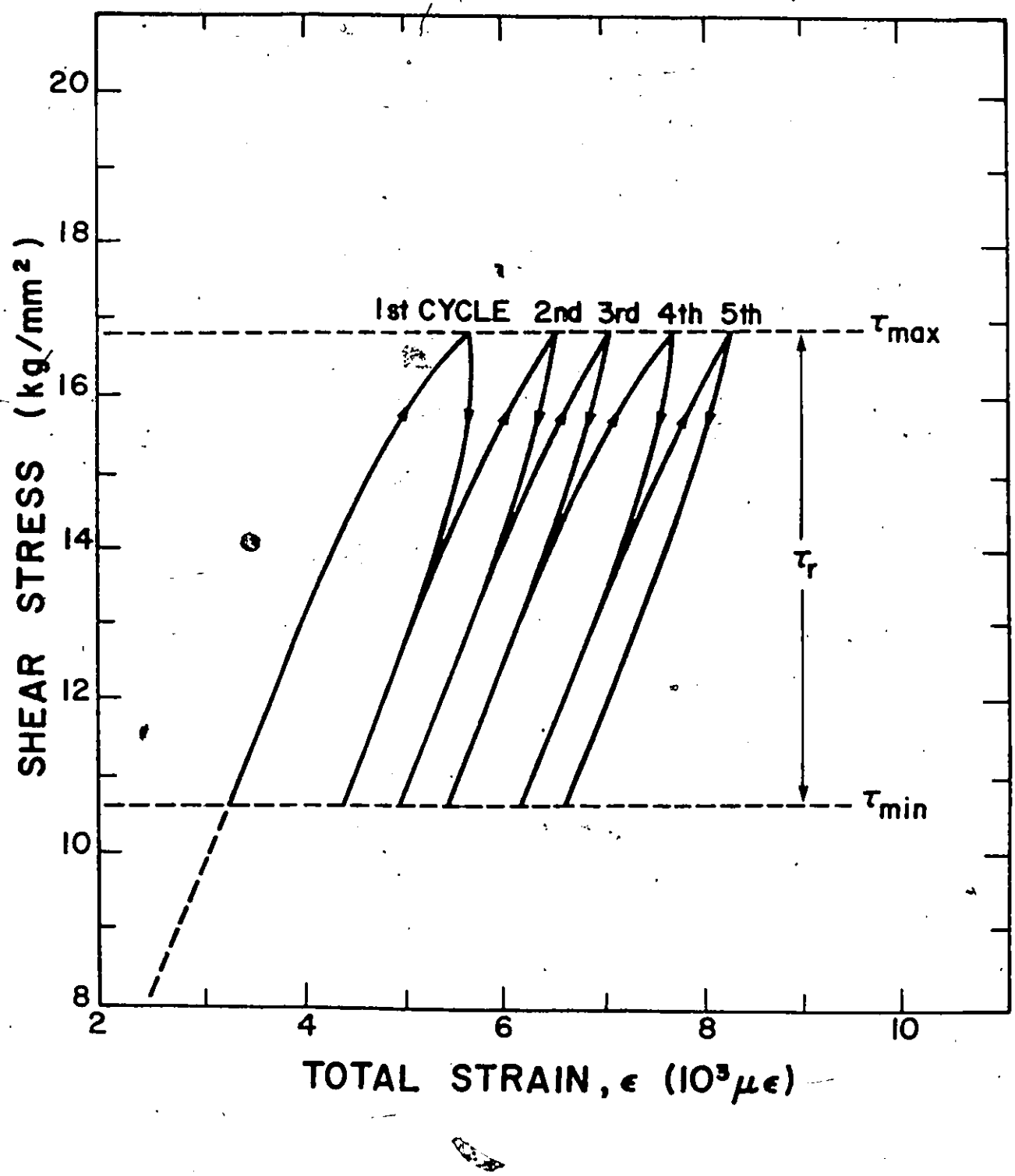

Figure A9. The figure shows the predicted hysteresis loops during the first few cycles of load controlled cyclic deformation. The strain-time response shown in Fig. 4.12 was replotted on stress-strain axes.

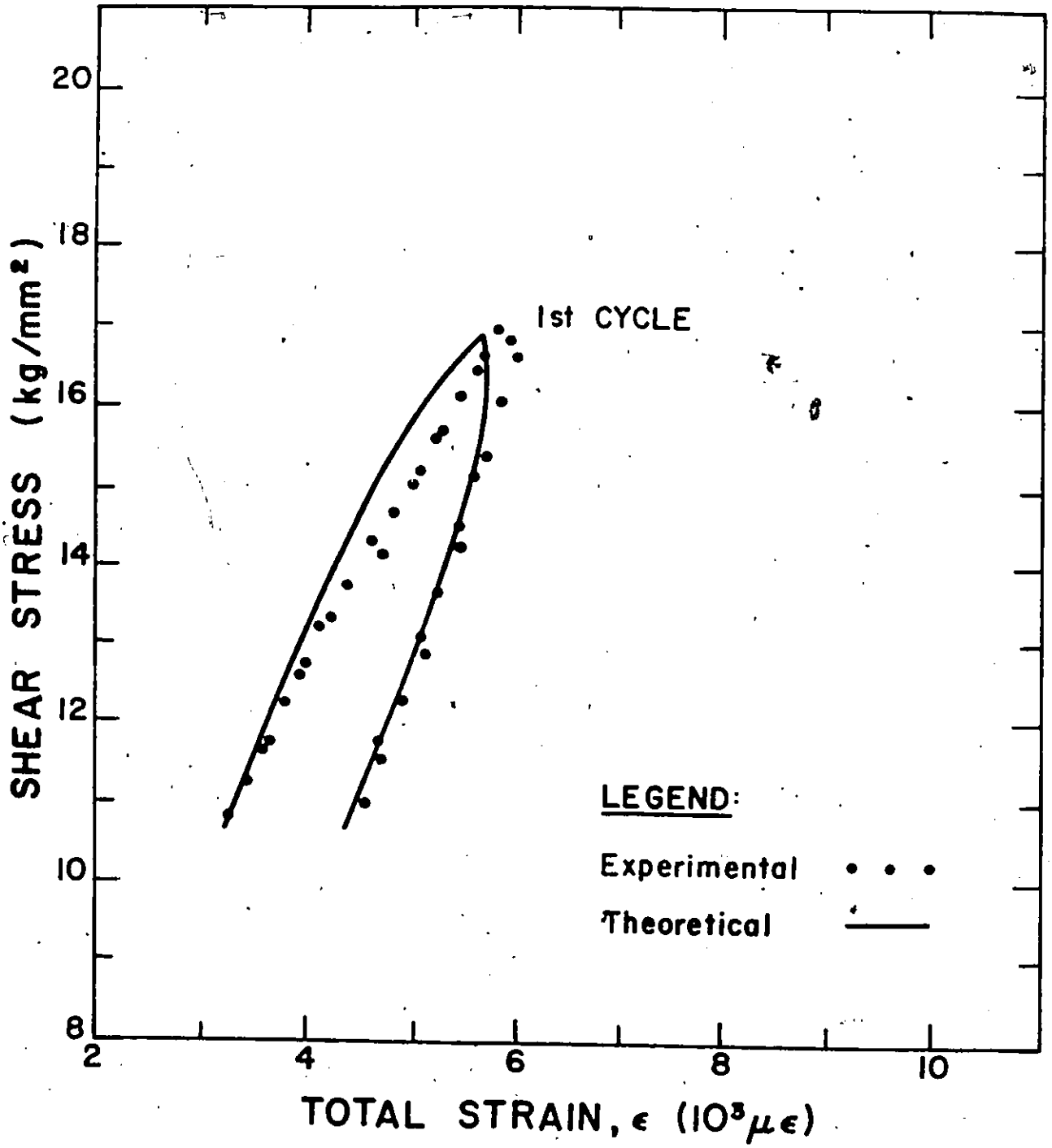
SHEAR STRESS (kg/mm²)
20
18
16
14
12
10
8
2
4
6
8
10
TOTAL STRAIN, ε (10³με)
1st CYCLE
LEGEND:
Experimental
Theoretical

Figure A10(a).

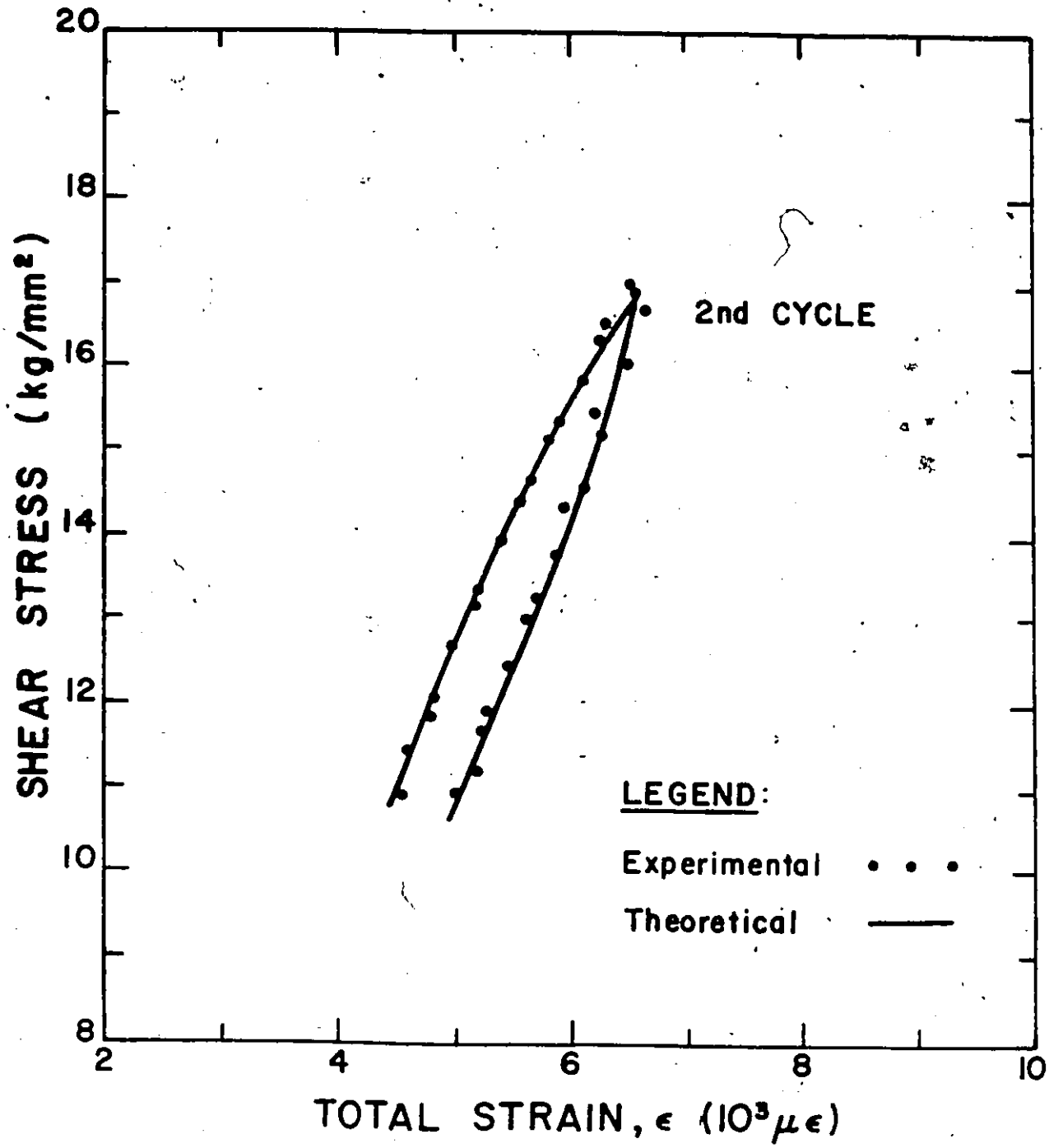

Figure A10(b).

Figure A10. Comparison of the calculated hysteresis loops (solid line) and the experimental data (symbols). The calculated hysteresis loops were replotted from Fig. A9. (a) Hysteresis loop for the first cycle. (b) Hysteresis loop for the second cycle.

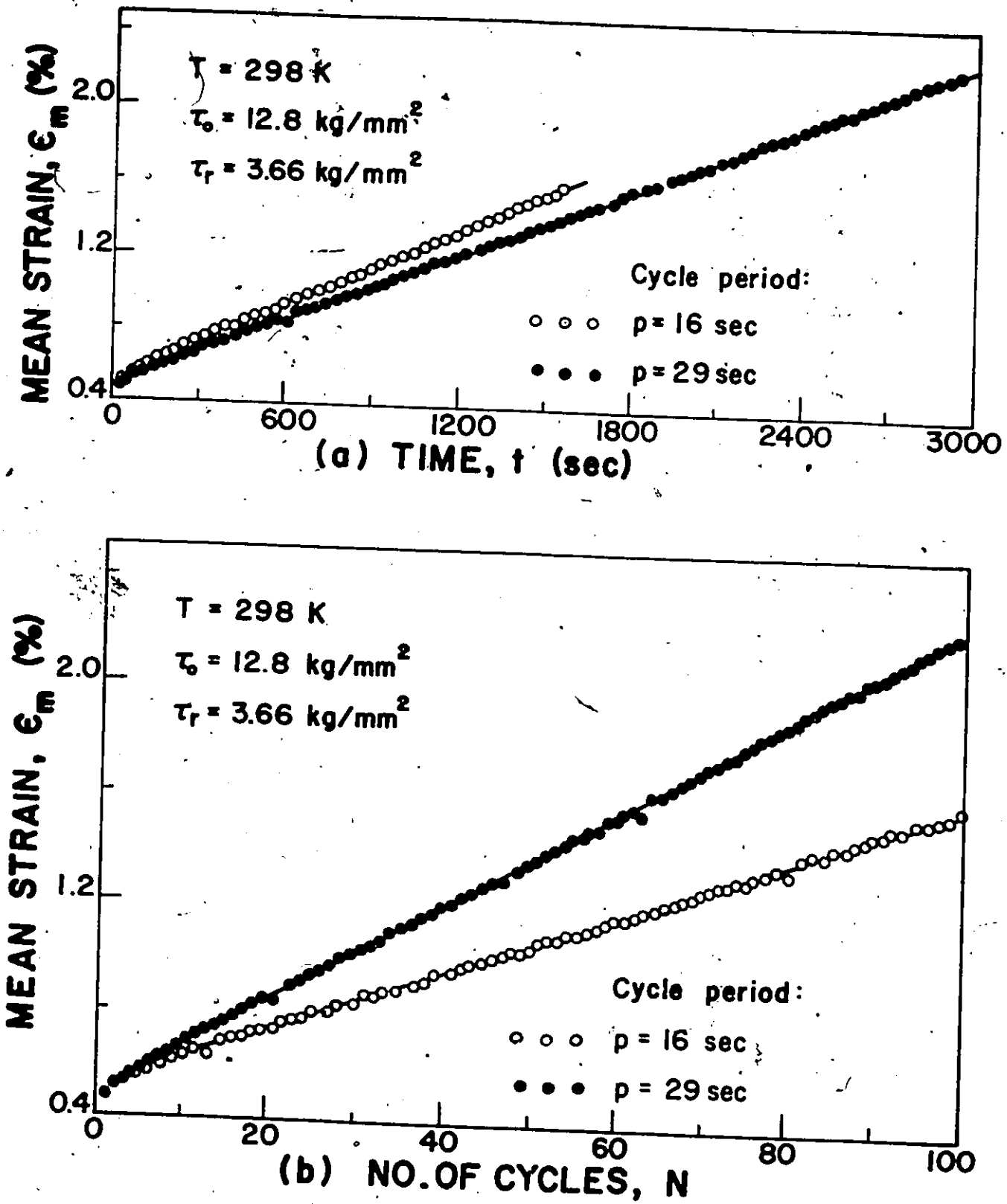

Figure A11. Effect of cycle period on the load controlled cyclic deformation. The symbols represent the experimental data while the lines were obtained from least square method using Eq. (4.7). (a) Strain versus time response (b) Strain-number of cycles response.

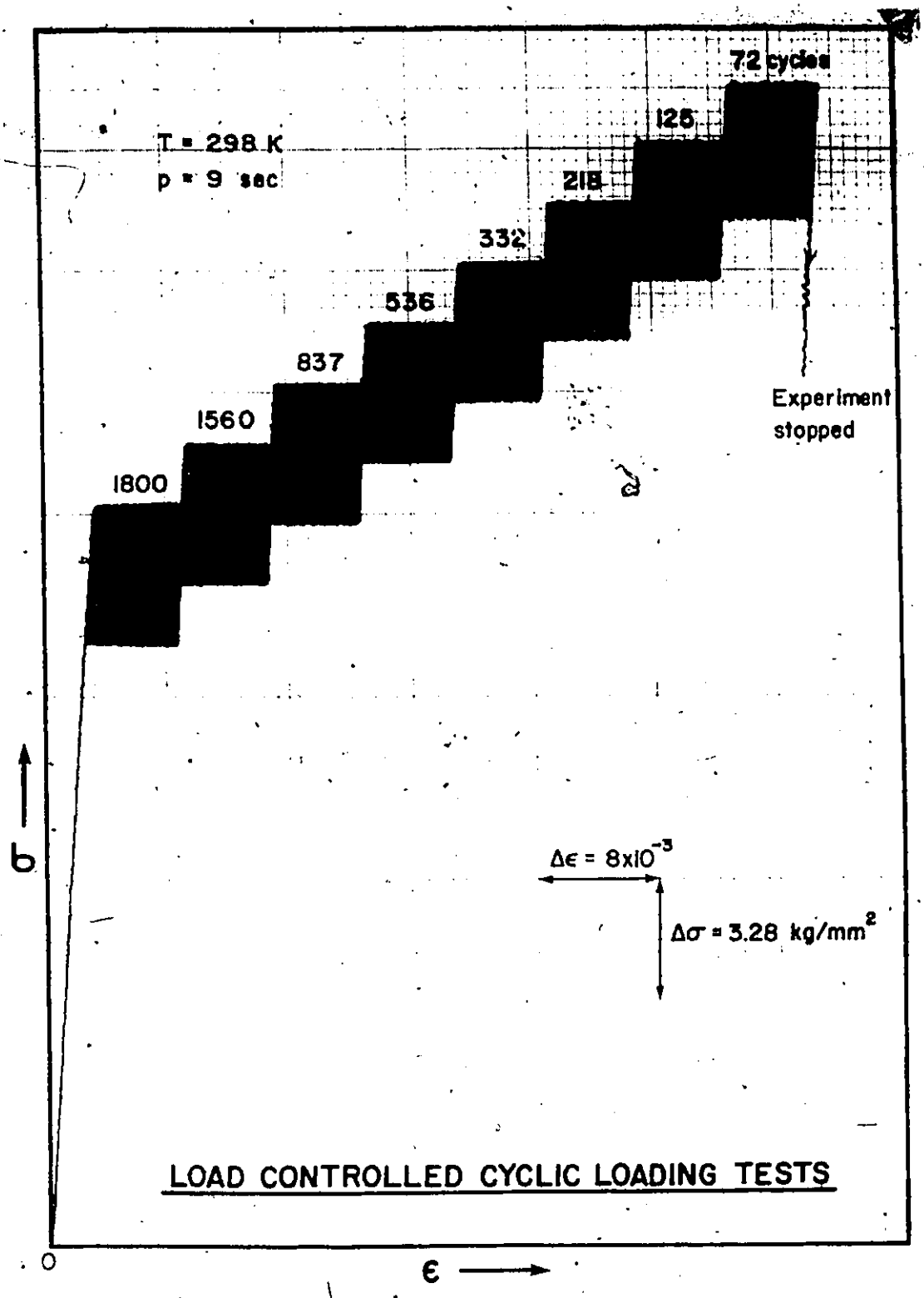
72 cycles
125
218
332
536
837
1560
1800
T = 298 K
p = 9 sec
Experiment stopped
b
Δε = 8x10⁻³
Δσ = 3.28 kg/mm²
LOAD CONTROLLED CYCLIC LOADING TESTS
O
ε

Figure A12.